

POLITECNICO DI TORINO

Master's Degree Course in Civil Engineering



Master's Degree Thesis

# INTERPRETATION OF AN EXPERIMENTAL CAMPAIGN OF AN ENERGY WALL

**Supervisors:**

Prof. Marco Barla

Dr. Matteo Baralis

**Candidate:**

Nguyen Quang Thien Buu

December, 2020



# Contents

|  |    |
|--|----|
| 1. <i>Chapter 1: INTRODUCTION</i> .....                                      | 1  |
| 2. <i>Chapter 2: SHALLOW GEOTHERMAL ENERGY</i> .....                         | 4  |
| 2.1. Introduction .....  | 4  |
| 2.1.1. Geothermal energy .....   | 4  |
| 2.1.2. Shallow geothermal system.....  | 5  |
| 2.2. Classification of geothermal resources.....                             | 6  |
| 2.2.1. Based on the depth .....  | 6  |
| 2.2.2. Based on the enthalpy .....   | 7  |
| 2.2.3. Based on the geothermal system .....                                  | 8  |
| 2.3. Utilization of geothermal resources.....                                | 8  |
| 2.3.1. Electric power production .....                                       | 8  |
| 2.3.2. Direct use.....   | 9  |
| 2.3.3. Geothermal heat pump .....  | 10 |
| 2.4. Principle of a geothermal heat pump.....                                | 10 |
| 2.5. Overview of ground systems for geothermal heat pump.....                | 12 |
| 2.5.1. Closed vertical loop.....   | 13 |
| 2.5.2. Closed loop horizontal systems.....                                   | 15 |
| 2.5.3. Open loop systems (groundwater systems).....                          | 16 |
| 3. <i>Chapter 3: ENERGY GEOSTRUCTURES</i> .....                              | 18 |
| 3.1. Introduction .....  | 18 |
| 3.2. Energy piles .....  | 19 |
| 3.3. Energy tunnels .....  | 22 |
| 3.4. Energy diaphragm walls .....  | 26 |
| 4. <i>Chapter 4: DESCRIPTION OF EXPERIEMENTAL SETUP (GEOTHERMSKIN)</i> ..... | 35 |
| 4.1. Prototype experimental site .....                                       | 35 |
| 4.1.1. Experimental site description.....                                    | 35 |

|        |   |     |
|--------|---|-----|
| 4.1.2. | GeothermSkin description.....                             | 36  |
| 4.1.3. | Experimental setup.....                                   | 38  |
| 4.1.4. | Monitoring system.....                                    | 43  |
| 4.2.   | Experimental results .....                                | 51  |
| 4.2.1. | Energy wall thermal performance .....                     | 52  |
| 4.2.2. | The impact of GeothermSkin on the surrounding ground..... | 58  |
| 4.2.3. | Structural effects on the wall.....                       | 62  |
| 5.     | <i>Chapter 5: NUMERICAL MODELLING</i> .....               | 64  |
| 5.1.   | Thermal-Hydraulic-Mechanical Analysis .....               | 64  |
| 5.1.1. | Mechanical field equations.....                           | 64  |
| 5.1.2. | Hydraulic field equations .....                           | 66  |
| 5.1.3. | Thermal field equations.....                              | 67  |
| 5.1.4. | Boundary conditions .....                                 | 68  |
| 5.2.   | Numerical Modelling.....                                  | 70  |
| 5.2.1. | Calculation software.....                                 | 70  |
| 5.2.2. | Geometry of the model.....                                | 70  |
| 5.2.3. | Parameters of materials .....                             | 73  |
| 5.2.4. | Boundary conditions (BC) .....                            | 75  |
| 5.2.5. | Results and discussion.....                               | 81  |
| 6.     | <i>Chapter 6: CONCLUSIONS</i> .....                       | 86  |
| A.     | APPENDICES.....   | 88  |
| 1.     | Test H_1+2_20200131_20200203 .....                        | 88  |
| 2.     | Test H_2+3_20200207_20200210.....                         | 101 |
| 3.     | Test H_1+3_20200214_20200217.....                         | 114 |
| 4.     | Test H_1+3_20200221_20200224.....                         | 127 |
| 5.     | Test H_1+2+3_20200228_20200302.....                       | 140 |
| 6.     | Test H_1_20200305_20200507 .....                          | 153 |

|                       |     |
|-----------------------|-----|
| Reference:.....       | 167 |
| Acknowledgments:..... | 169 |

**List of figures:**

|  |    |
|--|----|
| Figure 1.1: Global Carbon Dioxide Emissions, 1850–2040 (www.c2es.org).....   | 1  |
| Figure 1.2: Green-house gas emission due to Renewable Resources and Non-Renewable Resources (www.ucsusa.org) .....   | 2  |
| Figure 2.1: Sources, type and output of Geothermal Heat Pump (Geothermal Community) ....   | 5  |
| Figure 2.2: Diagram showing the different categories of geothermal resources. (Dickson and Fanelli, 2004) .....  | 6  |
| Figure 2.3: Scheme of a compression heat pump (Geothermal Community) .....   | 10 |
| Figure 2.4: Closed vertical loop system (Geothermal Community) .....   | 14 |
| Figure 2.5: Cross-sections of different bypass of boreholes heat exchangers (Geothermal Community) .....   | 14 |
| Figure 2.6: Ground heat exchanger a) Closed horizontal type and b) Trench type (Geothermal Community) .....  | 15 |
| Figure 2.7: Closed horizontal-Slinky loop (Geothermal Community) .....   | 16 |
| Figure 2.8: Open ground water loop system (Geothermal Community).....  | 17 |
| Figure 3.1 Scheme of a geothermal energy system (Brandl, 2006) .....   | 19 |
| Figure 3.2: Absorber pipes attached to the reinforcement cage (Brandl, 2006) .....   | 20 |
| Figure 3.3: Response mechanism of a pile heat exchanger, a) for heating and b) for cooling   | 21 |
| Figure 3.4: Clay/concrete interface behavior assessed using thermal borehole shear device (Pagola et al., 2018).....                                       | 21 |
| Figure 3.5: Schematic representation of a tunnel segmental lining equipped as ground heat exchanger (Barla et al., 2016) .....                             | 23 |
| Figure 3.6: Comparison between Enertun and previous configurations in terms of heat exchange obtained from numerical simulation (Barla et al., 2019) ..... | 23 |
| Figure 3.7: Preparation stages of energy segments: (a) moulding, (b) casting, (c) demoulding and (d) circulation test (Barla et al., 2019).....            | 24 |
| Figure 3.8: Efficiency of different configurations (Barla et al., 2016) .....  | 24 |
| Figure 3.9: Temperatures in the soil at different distance from the tunnel during three years of cycling heating and cooling (Barla et al., 2016) .....    | 26 |
| Figure 3.10: Annual operating cost savings with respect to other heating/cooling systems (Barla et al., 2016).....   | 26 |
| Figure 3.11: Feeding Geothermal Loop onto Reinforcement Cage (Amis et al., 2011).....  | 27 |

|  |    |
|--|----|
| Figure 3.12: Geothermal Loop and Reinforcement Cage Installation (Amis et al., 2011). ....   | 28 |
| Figure 3.13: Three types of underground heat exchangers: (a) W-shaped type, (b) improved W-shaped type and (c) single U-shaped type (Xia et al., 2012).....  | 30 |
| Figure 3.14: Relationship curves of heat exchange rate and time under different types of heat exchangers (Xia et al., 2012).....   | 31 |
| Figure 3.15: Normalized effect of each parameter in terms of heat exchanged (Di Donna et al., 2016).....   | 32 |
| Figure 3.16: Layout of the Base (a), Single-W (b) and Double-W (c) heat exchanger pipe (units m) (Sterpi et al., 2018) .....   | 33 |
| Figure 4.1: Render of the GeothermSkin energy system applied to a residential building basement (Baralis and Barla, 2019) .....  | 37 |
| Figure 4.2: Main components of the novel energy wall system GeothermSkin (Baralis and Barla, 2019).....  | 37 |
| Figure 4.3: Deployment of the pipes network in the experimental (Baralis and Barla, 2019) 39   |    |
| Figure 4.4: Trench shoring process: (a) early stage of excavation and (b) bottom of the excavation (Baralis and Barla, 2019) .....   | 39 |
| Figure 4.5: Pipe deployment fixed by regularly distant clamps (Baralis and Barla, 2019) .....  | 40 |
| Figure 4.6: Manifold connecting the pipes from/to the heat pumps with the heat exchanger modules (Baralis and Barla, 2019).....  | 41 |
| Figure 4.7: Scheme of the geothermal heat pump system (Baralis and Barla, 2019) .....  | 42 |
| Figure 4.8: Strain gauges installation (Baralis and Barla, 2019) .....   | 44 |
| Figure 4.9: Installation of the pressure cells on the wall surface (Baralis and Barla, 2019)....   | 44 |
| Figure 4.10: Heat exchangers prototype layout and monitoring stress and strain sensors on the wall surface (Baralis and Barla, 2019) .....   | 45 |
| Figure 4.11: (a)Temperature monitoring sensors for ground monitoring and (b) depth location of the sensors along planes (Baralis and Barla, 2019) .....  | 47 |
| Figure 4.12: Volumetric water content sensor installed at the experimental facility in Torino: (a) before installation and (b) once installed before burial on plane B where the green cables are connected to the temperature sensors while the thicker black ones are the hygrometer sensors cables (Baralis and Barla, 2019)..... | 48 |
| Figure 4.13: (a)Installation of hydraulics sensors above the plane at very shallow depths within plastic pipes filled with sand before ground backfilling. Sensors included 8 hygrometers and (b) 3 tensiometers (Baralis and Barla, 2019).....  | 48 |

|   |    |
|---|----|
| Figure 4.14: Temperature sensor location on (a)Plane A and (b) on Plane B along with their codification. Also some hygrometer sensors nominated as S0xx are depicted (Baralis and Barla, 2019)..... | 49 |
| Figure 4.15: Temperature sensor location on (a)Plane C and (b) on Plane D along with their codification. Also some hygrometer sensors nominated as S0xx are depicted (Baralis and Barla, 2019)..... | 50 |
| Figure 4.16: Thermal performance of experimental H_2+3_20200207_20200210 with parallel link of circuit 2 and 3 in heating mode.....   | 51 |
| Figure 4.17: Thermal performance comparison of different tests.....   | 55 |
| Figure 4.18: Comparison of thermal levels in heating tests depending on the supply temperature (Baralis and Barla, 2019) .....  | 55 |
| Figure 4.19: Peak power with respect to maximum temperature change in several tests.....  | 56 |
| Figure 4.20: Thermal performance interpretation of experimental test H_1+3_20200214_20200217 with parallel link of circuit 1 and 3 in heating mode .....  | 56 |
| Figure 4.21: Heat rates of different tests in comparison with previous literature .....   | 58 |
| Figure 4.22: Thermal records along string 2 (plane A) and string 12 (plane C) during experiment H_2+3_20200207_20200210.....  | 59 |
| Figure 4.23: Temperatures records from chain 2 of experimental test H_1+3_20200214_20200217.....  | 59 |
| Figure 4.24: Ground temperature at the beginning of tests in different positions near along the wall .....  | 60 |
| Figure 4.25: Temperature change between the beginning and the end of tests in different positions .....   | 61 |
| Figure 4.26: Volumetric water content and suction potential records from test H_2+3_20200207_20200210.....  | 61 |
| Figure 4.27: Strain gauges and pressure cells records from test H_2+3_20200207_20200210 .....   | 63 |
| Figure 4.28: Stresses and strain variations induced by GeothermSkin thermal activation during the heating experimental campaign. ....   | 63 |
| Figure 5.1: a) DXF model imported to FEFLOW (dimensions in m) (AUTOCAD); b) Mesh generation .....   | 71 |
| Figure 5.2:The piping system was modelled by discrete features.....   | 71 |
| Figure 5.3: Simulation-Time Control.....  | 72 |
| Figure 5.4: 3D model .....  | 72 |

|  |    |
|--|----|
| Figure 5.5: 3D Model - Hydraulic conductivity $K_{yy}$ .....   | 75 |
| Figure 5.6: Time series of surface temperature.....  | 76 |
| Figure 5.7: Time series of air temperature .....   | 77 |
| Figure 5.8: Time series of inlet fluid.....  | 77 |
| Figure 5.9: Temperature BC of the model: a) Temperature BC of nodes in different surfaces,<br>b) Temperature BC of the inlet fluid (red circles in the figure) ..... | 78 |
| Figure 5.10: Interpolation line of temperature .....   | 79 |
| Figure 5.11: Initial temperature of soil in Test 3.....  | 79 |
| Figure 5.12: Circuit 2 and 3 with fluid speed at entrances and ends, and a set of 2 observation<br>points (O2 and O3).....   | 80 |
| Figure 5.13: Variation over time of inlet and outlet temperatures .....  | 82 |
| Figure 5.14: Comparison of outlet temperatures between numerical and experimental methods<br>.....   | 82 |
| Figure 5.15: Temperature distribution in the slice of piping system at the end of duration ....  | 83 |
| Figure 5.16: Temperature distribution in 3D model at the end of duration .....   | 83 |
| Figure 5.17: Comparison of soil temperature between two method at sensor C3T1 .....  | 84 |
| Figure 5.18: Comparison of soil temperature between two method at sensor C9T1 .....  | 85 |
| Figure 5.19: Comparison of soil temperature between two method at sensor C13T1 .....   | 85 |
| Figure 5.20: Comparison of soil temperature between two method at sensor C19T1 .....   | 85 |

***List of tables:***

|   |    |
|---|----|
| Table 2.1: Classification of geothermal resources (°C) (Dickson and Fanelli, 2004) .....  | 7  |
| Table 3.1: Testing results with different input parameters (Barla et al., 2016) .....   | 25 |
| Table 3.2: Experimental schemes of heat transfer test in diaphragm walls (Xia et al., 2012).                                    | 29 |
| Table 3.3: A set of runs for a specific case study and results (Di Donna et al., 2016) .....                                    | 31 |
| Table 3.4: Energy performance of the three pipe layouts in December 2015 (Sterpi et al., 2018).....                             | 33 |
| Table 4.1: Heat exchanger circuits experimental setup details (Baralis and Barla, 2019).....                                    | 38 |
| Table 4.2: Location of stress and strain sensors on the wall surface with the direction of axis (Baralis and Barla, 2019) ..... | 45 |
| Table 4.3: List of tests carried out.....   | 52 |
| Table 4.4: Parameters' values for calculation of heat exchange rate in experiment H_2+3_20200207_20200210.....                  | 54 |
| Table 4.5: Thermal performances of the energy wall from experimental results interpretation .....                               | 54 |
| Table 5.1: Soil parameters.....   | 74 |
| Table 5.2: Parameters of geothermal probes .....  | 74 |
| Table 5.3: Air parameters.....  | 75 |
| Table 5.4: Concrete Parameters .....  | 75 |
| Table 5.5: Temperatures of different sensors .....  | 78 |
| Table 5.6: Parameters' values for calculation of heat exchange rate in numerical result. ....                                   | 81 |
| Table 5.7: The heat exchange rate result of numerical model .....   | 81 |
| Table 5.8: Thermal performance comparison between numerical and experimental methods  | 81 |
| Table 5.9: Location of the sensors (or observation points) .....  | 84 |

# 1. *Chapter 1: INTRODUCTION*

Since the dawn of the Industrial Revolution in the early 1800s, the burning of fossil fuels like coal, oil and gasoline have greatly increased the amount of greenhouse gases in the atmosphere, especially CO<sub>2</sub>. Atmospheric CO<sub>2</sub> levels have increased by more than 40 percent since the beginning of the Industrial Revolution, from about 280 parts per million (ppm) in the 1800s to 400 ppm today. The last time Earth's atmospheric levels of CO<sub>2</sub> reached 400 ppm was during the Pliocene Epoch, between 5 million and 3 million years ago, according to the University of California, San Diego's Scripps Institution of Oceanography ([www.c2es.org](http://www.c2es.org)). The amounts of CO<sub>2</sub> emission in the past and in the predicted future are showed in Figure 1.1.

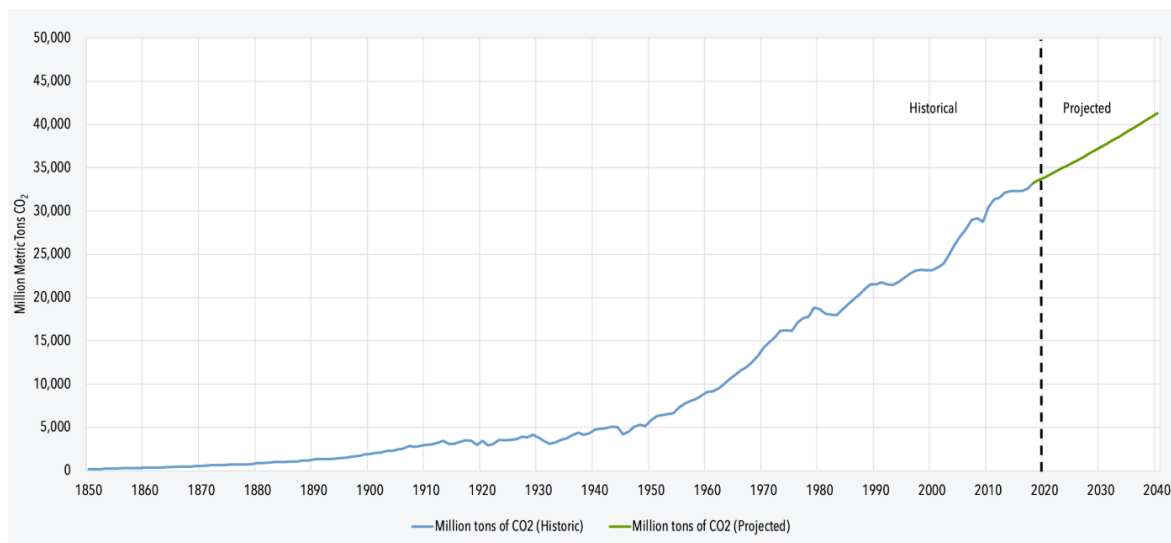


*Figure 1.1: Global Carbon Dioxide Emissions, 1850–2040 ([www.c2es.org](http://www.c2es.org))*

The increasing levels of greenhouse gases and the resulting global warming, is expected to have significant impact. If global warming continues unchecked, it will cause significant climate change, a rise in sea levels, increasing ocean acidification, extreme weather events and other severe natural and societal impacts which can lead to a huge influence to the life quality, health and environment.

In contrast, most renewable energy sources produce little to no global warming emissions. The term renewable energy refers to energy sources that are in nature and are renewed in whole or in part, in particular, the energy of watercourses, wind, non-accumulated solar energy, biomass, geothermal energy, and so on. The efficient use of these sources plays important role in energy production, reduction of greenhouse gas emissions, reduction of fossil fuel imports, development of local industry and job creation. Renewable energy technologies are clean and have a much lower environmental impact than conventional energy technologies.

Some numbers are represented in Figure 1.2 in order to show the difference between renewable and non-renewable resources. Burning natural gas for electricity releases between 0.270 and 0.910 kilograms of carbon dioxide equivalent per kilowatt-hour (CO<sub>2</sub>eq/kWh); coal emits between 0.640 and 1.630 kilograms of CO<sub>2</sub>eq/kWh. Wind, on the other hand, is responsible for only 0.009 to 0.018 kilograms of CO<sub>2</sub>eq/kWh on a life-cycle basis; solar 0.030 to 0.090; geothermal 0.045 to 0.090; and hydroelectric between 0.045 and 0.227 (www.ucsusa.org).

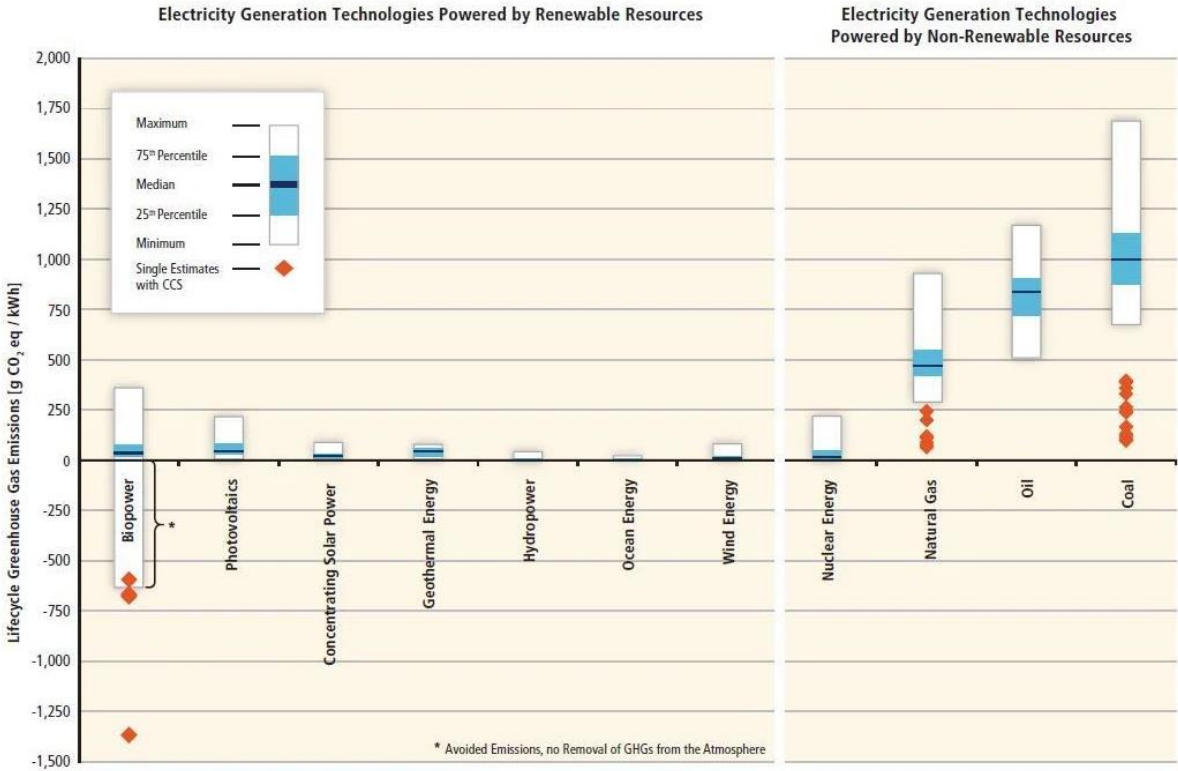


Figure 1.2: Green-house gas emission due to Renewable Resources and Non-Renewable Resources (www.ucsusa.org)

With renewables, the world can be led into a new age of sustainable development in which there is not any concern about the limitation of energy, the significant growth of energy prices and the environmental protection. In order to do that, the contributions of each person, region, country will play an important role in accelerating the rate of using renewable energy and decreasing the green-house gas emission. As engineers, we have enough knowledge and skills to be a part of this contributions by exploiting some geo-structures as a device to collect energy and use them for daily activities. In term of civil engineering, geothermal energy from the subsurface of the Earth can become an enormous potential of renewable energy that can be used for different kinds of purposes. So, ground-embedded structures such as shallow foundations, bored piles, diaphragm walls, tunnel linings, etc. can be used as absorber elements for ground

heat exchange. With heat carrier fluid circulating through the piping system attached within concrete elements, heat is extracted from the ground or stored in the ground for heating and cooling of associated buildings. One of the major strength of this method is that the geothermal system can be attached to the in-place geo-structures used for structural purpose, it results in the saving of initial cost for installation with respect to other systems. However, it is obvious that the structure will suffer from the significant change in stress and strain due to temperature variation, this point needs to be thoughtfully taken into account, then the thermal - hydraulic-mechanical problem will be discussed in this thesis.

Hence, the objective of this thesis is to study the energy performance of an innovative energy wall, called GeothermSkin and to evaluate the effects of some important factors to this performance, such as supply temperature, flow rate, direction and position of piping deployment, examining the environmental impact on the surrounding ground and structural effects on the supporting wall.

Content of the thesis:

- Chapter 1: The introduction of renewable energy and the need to employ the geo-structure as heat exchanger so as to exploit the heat from the ground.
- Chapter 2: The introduction of shallow geothermal energy and the principle of using heat pump to extract and inject geothermal energy from ground to provide them for heating/cooling system.
- Chapter 3: The introduction of energy geostructures as energy piles, energy tunnels, energy diaphragm walls.
- Chapter 4: A description about experimental campaign and an interpretation of its results is represented in order to introduce GeothermSkin system designed and installed by Prof Marco Barla and Dr Matteo Baralis in an office building in Torino (Italy), interpreting the thermal performance of this system as well as its effect on the wall and the surrounding ground.
- Chapter 5: Using FEFLOW software to build a numerical model with input data of a specific test, comparing the thermal performance of experimental results and numerical results.
- Chapter 6: Some conclusion related to thermal performance, its dependency upon different factors, thermal affection on ground temperature, water content of soil, stress and strain of the wall.

## **2. *Chapter 2: SHALLOW GEOTHERMAL ENERGY***

### **2.1. *Introduction***

#### **2.1.1. *Geothermal energy***

Geothermal Energy (from the ancient Greek "geo", earth, and "thermos", heat) is, in its broad definition, the thermal energy contained in our planet, the Earth. The heat can be extracted from a depth up to about 10 km, which is the maximum depth reached by human drilling. Part of this heat is continuously generated by the decay of the long-lived radioactive isotopes of uranium (U238, U235), thorium (Th232) and potassium (K40), which are present in the Earth, part, in uncertain proportions, are other potential sources of heat such as the primordial energy of planetary accretion (Dickson and Fanelli, 2004). Because the difference in temperature between deep hotter zones and shallow colder zones generates the conductive flow of heat from the former towards the latter, called Earth's heat flow that varies from place to place, and with time, depending on the geological and physical condition of the underground. On average, the heat flow from the continental crust is 65 mW/m<sup>2</sup> and from the oceanic crust is 101 mW/m<sup>2</sup> (Dickson and Fanelli, 2004).

The heat flow at the Earth's surface derives from the radiogenic decay within the upper crust, the heat generated in the most recent magmatic episode, and the heat coming from the mantle and inner Earth's structures. In continental crust, where the isotope heating is larger since granitic rocks rich of long-living radioactive isotopes are common, the heat flow is highest in areas having experienced "recent" (less than 65 million year) magmatic activity, whereas it decreases in older crusts. In oceanic crust, the concentration of radiogenic heating is negligible due to the rock composition (basaltic), but the crust thickness is smaller than in continents and the heat flow largely derives from heat flowing from the mantle. Most plate boundaries are below sea level and the young oceanic crust has very high heat flow values. Geothermal exploitation from continental areas is much more popular.

To extract energy from the ground, water can be used as a carrier of heat. The two main mechanisms involved are conduction and convection. Warm and hot fluids can be extracted from the underground in a wide range of temperature and discharge rate, and used directly for their heat content or to produce electric power. Even the modest temperatures at shallower depths, they can be used to extract or store heat by means of ground source heat pumps.

### 2.1.2. Shallow geothermal system

With developments of the ground-source heat pump application, the earth can be used as a heat source for heating in summer or as a heat sink for cooling in winter in all countries. The geothermal heat pump doesn't create electricity, but it greatly reduces consumption of it. As a result, one of the best way to reduce the operation cost of heating and cooling systems in building is the installation of a geothermal heat pump, an economical and energy-efficient technology for space heating and cooling and water heating. In winter, geothermal heat pump systems draw thermal energy from the shallow ground to warm the building. In summer, a cooling mode is active by reversing the process above, using the ground as a sink to store the heat within the building. The system uses electricity to move thermal energy between the building and the ground and change it to a higher or lower temperature to meet the heating or cooling requirements, rather than converting it to electricity. A lower amount of electricity is consumed compared to traditional heating and cooling systems.

Geothermal heat pumps use the earth as a heat source or sink by means of a circulating water loop. Since the heat pump supplies both heating and cooling, only one appliance is needed to satisfy both conditioning needs. There is no need of exterior equipment such as cooling towers or condensing units or heating plants. Each heat pump unit can heat or cool at any time and the part load performance is excellent. Maintenance is simpler and less costly than conventional fossil fuel and cooling tower systems.

Geothermal heat pump (also called Ground Source Heat Pumps, GSHP) is a system with three main components as in Figure 2.1:

- The ground side to get heat out of or into the ground,
- The heat pump to convert the heat to a suitable temperature level, and
- The building side transferring the heat or cold into the room.

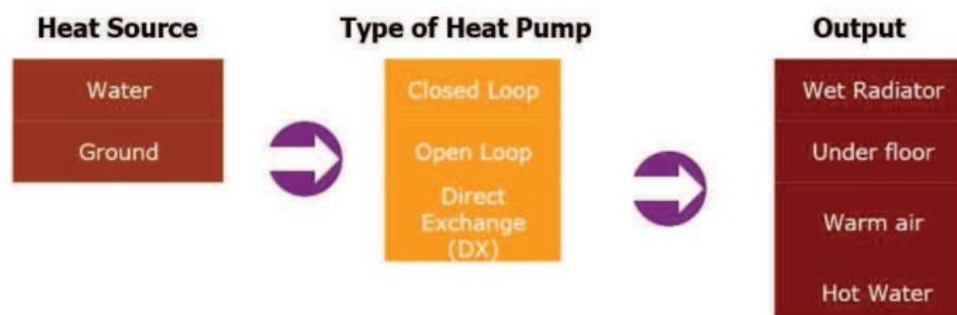


Figure 2.1: Sources, type and output of Geothermal Heat Pump (Geothermal Community)

## 2.2. Classification of geothermal resources

Standard international terminology classification is not clearly presented throughout the geothermal community. The following, however, are some of the most common classifications in this discipline.

### 2.2.1. Based on the depth

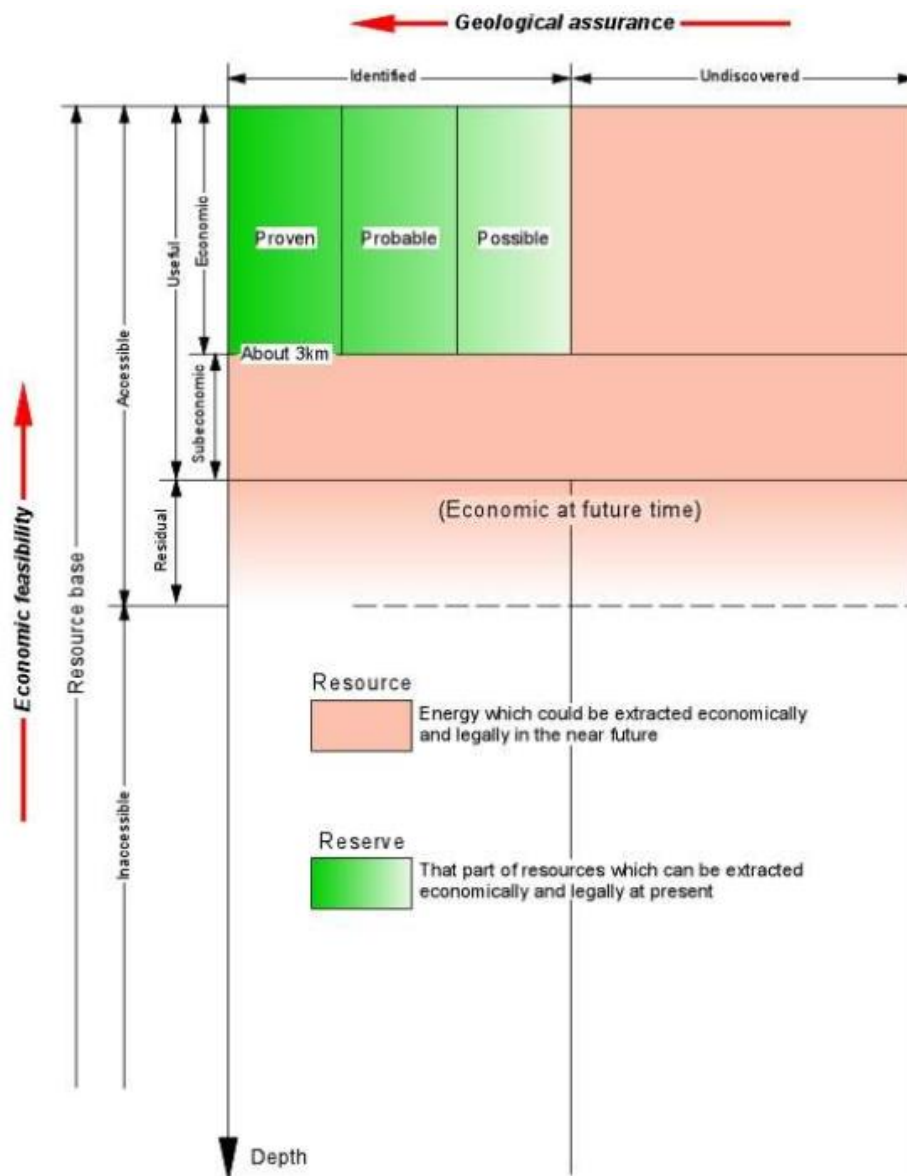


Figure 2.2: Diagram showing the different categories of geothermal resources. (Dickson and Fanelli, 2004)

Due to the limitation of drilling to a particular depth, only the thermal heat contained in this limited depth can be exploited, called accessible resource base; that is all of the thermal energy stored between the Earth's surface and a specified depth in the crust, beneath a specified area and measured from local mean annual temperature according to Muffler and Cataldi (1978).

The accessible resource base includes useful and residual resource bases. Part of useful resource base (Resource) that could be extracted economically and legally at some specified time in the near future (less than a hundred years) and the remaining part, called identified economic resource (Reserve), can be extracted legally at a cost competitive with other commercial energy sources and that are known and characterized by drilling or by geochemical, geophysical and geological evidence. Besides, residual resource base is the stored energy for further future. These and other terms that may be used in geothermal discipline are showed in Figure 2.2, in which the vertical axis is the degree of economic feasibility; the horizontal axis is the degree of geological assurance.

**2.2.2. Based on the enthalpy**

The most common criterion for classifying geothermal resources is based on the enthalpy of the geothermal fluids that act as the carrier transporting heat from the deep hot rocks to the surface. Enthalpy, which can be considered more or less proportional to temperature, is used to express the heat (thermal energy) content of the fluids. The resources are divided into low, medium and high enthalpy resources, according to criteria that are generally based on the energy content of the fluids and their potential forms of utilization. Table 2.1 reports the classifications proposed by a number of authors. Temperature values or ranges involved case by case should be indicated in each category, since terms such as low, intermediate and high can lead to the ambiguity and confusion.

*Table 2.1: Classification of geothermal resources (°C) (Dickson and Fanelli, 2004)*

|  | (a)    | (b)     | (c)     | (d)  | (e)  |
|--|--------|---------|---------|------|------|
| Low enthalpy resources   | <90    | <125    | <100    | <150 | <190 |
| Intermediate enthalpy resources  | 90-150 | 125-225 | 100-200 | -    | -    |
| High enthalpy resources  | >150   | >225    | >200    | >150 | >190 |
| Sources:<br>(a) Muffler and Cataldi (1978).<br>(b) Hochstein (1990).<br>(c) Benderitter and Cormy (1990).<br>(d) Nicholson (1993).<br>(e) Axelsson and Gunnlaugsson (2000) |        |         |         |      |      |

### **2.2.3. Based on the geothermal system**

A distinction is made between water- or liquid-dominated geothermal systems and vapor-dominated (or dry steam) geothermal systems (White, 1973). In water-dominated systems, liquid water is the continuous, pressure-controlling fluid phase. Some vapor may be present, generally as discrete bubbles. These geothermal systems, whose temperatures may range from 125 to 225 °C, are the most widely distributed in the world. Depending on temperature and pressure conditions, they can produce hot water, water and steam mixtures, wet steam and, in some cases, dry steam. In vapor-dominated systems, liquid water and vapor normally co-exist in the reservoir, with vapor as the continuous, pressure-controlling phase. Geothermal systems of this type are rare, and are high-temperature systems. They normally produce dry-to superheated steam.

Another division between geothermal systems is that based on the reservoir equilibrium state (Nicholson, 1993), considering the circulation of the reservoir fluid and the mechanism of heat transfer. In dynamic systems, the reservoir is continually recharged by water that is heated and then discharged from the reservoir either to the surface or into underground permeable formations. Heat is transferred through the system by convection and circulation of the fluid. This category includes high-temperature (>150 °C) and low-temperature (<150 °C) systems. In static systems (stagnant or storage systems), there is only minor or no recharge to the reservoir and heat is transferred only by conduction. This category includes low temperature and geo-pressured systems. The geo-pressured reservoirs consist of permeable sedimentary rocks, included within impermeable low-conductivity strata, containing pressurized hot water that remained trapped at the moment of deposition of the sediments. The geo-pressured reservoirs can also contain significant amounts of methane. The geo-pressured systems could produce thermal and hydraulic energy (pressurized hot water) and methane gas. These resources have been investigated extensively, but so far there has been no industrial exploitation.

## **2.3. *Utilization of geothermal resources***

### **2.3.1. Electric power production**

Electricity generation mainly needs steam to rotate a turbine that activates a generator, which produces electricity. Most power plants still use fossil fuels to boil water for steam, whereas geothermal power plants use steam produced from or heated by underground hot fluids. Three main types of technology are available: dry steam, flash steam and binary cycle, depending on the characteristics of the geothermal fluid.

In dry steam power plants, the steam is drawn from underground resources of steam, and is piped directly from underground wells to the power plant. The geothermal fluids must be in vapor state when they reach the surface. These systems, named vapor-dominated systems, are characterized by very high temperature.

Flash steam power plants are the most common and use geothermal reservoirs of water with temperatures greater than 182 °C. This very hot water flows up through wells in the ground under its own pressure. As it flows upward, the pressure decreases and some of the hot water boils into steam. The steam is then separated from the water and used to power a turbine/generator. Any leftover water and condensed steam are injected back into the reservoir, making this a sustainable resource.

Binary cycle power plants operate on water at lower temperatures of about 107-182 °C. Binary cycle plants use the heat from the hot water to boil a working fluid, usually an organic compound with a low boiling point. The working fluid is vaporized in a heat exchanger and used to turn a turbine. The water is then injected back into the ground to be reheated. The water and the working fluid are kept separated during the whole process, so there are little or no air emissions. ([www.nrel.gov](http://www.nrel.gov))

### **2.3.2. Direct use**

Low-temperature geothermal resources show a tremendous potential for direct-use applications, with temperature ranging between about 20 and 150 °C. The main types of direct applications of geothermal energy are space heating, bathing and swimming (including balneology), agricultural (greenhouses and soil heating), industry, and aquaculture (mainly fish farming).

Space condition refers to the alteration of the climate in an enclosed space by either heating or cooling. While the use of geothermal energy for space heating is popular in cold climates, in tropical climates, geothermal energy could be used to cool building. Although the initial investment cost is higher than the conventional system, the operation cost is comparatively lower than in conventional one. Some of the health benefits derived from bathing in geothermal water include treatment of high blood pressure, skin diseases, diseases of the nervous system and relieving the symptoms of rheumatism. The use of geothermal energy to heat swimming pools is a common practice, especially in the cold countries where almost all outdoor swimming pools are geothermally heated all year round. The major application of geothermal energy in agriculture is the heating of greenhouses in order to control the climate, mainly temperature and

relative humidity. The industrial uses of geothermal energy are numerous and involve mainly heating and cooling. Drying or dehydration of agricultural products is one of the major industrial applications of geothermal energy. For example, animal products need to be processed immediately after production in order to preserve them for later use.

### 2.3.3. Geothermal heat pump

To heat or cool a space we need to transfer heat. To this aim, the thermal energy stored in the ground at shallow depth may be used. Below a depth of a few meters from the ground surface, the temperature is not affected by the seasonal change of air temperature and is essentially constant and equal to the mean annual air temperature. The thermal energy of the ground can be exploited by using heat pumps, which convert the low-temperature geothermal energy to thermal energy at a higher temperature by exploiting the physical property of fluids to absorb and release heat when they vaporize or condense, respectively. This part will be discussed more in the following.

### 2.4. Principle of a geothermal heat pump

A heat pump is a device which allows the transport of heat from a lower temperature level to a higher one, by using external energy. The most common type of heat pump is the compression heat pump.

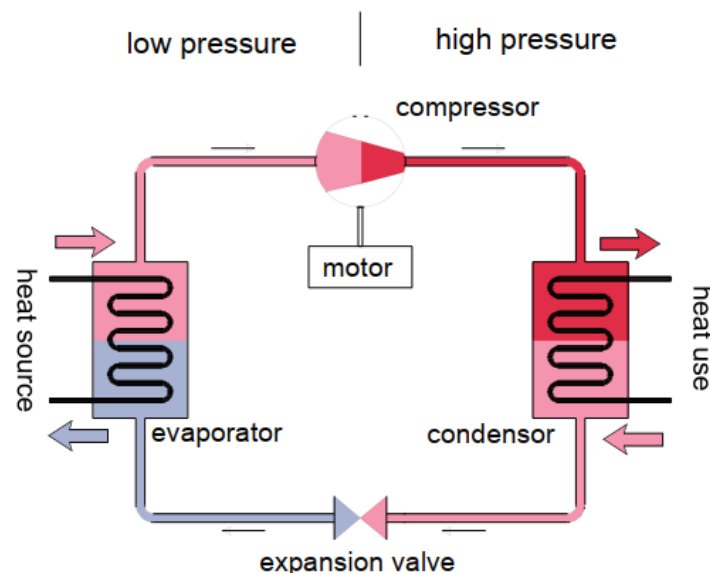


Figure 2.3: Scheme of a compression heat pump (Geothermal Community)

As the Second Law of Thermodynamics, heat will flow only from hotter to colder matter, but a heat pump will draw heat from the ground at, say, 5 °C and use it to warm a building to 21 °C. In a compression heat pump, the thermodynamic principle is the fact that a gas becomes

warmer when it is compressed into a smaller volume. In a heat pump, a medium with low boiling point (refrigerant) is evaporated by the ground heat, the resulting vapor (gas) is compressed (by using external energy, typically electric power) and thus heated, and then the hot gas can supply its heat to the heating system. Still being in the high pressure part, the vapor now condenses again to a liquid after the useful heat has been transferred. Finally, the fluid enters back into the low-pressure part through an expansion valve, gets very cold and can be evaporated again to continue the cycle as showed in Figure 2.3.

An alternative is the absorption heat pump (AHP) which is a heat pump driven by thermal energy such as combustion of natural gas, steam solar-heated water, air or geothermal-heated water, differently from compression heat pumps that are driven by electric energy. AHP really does a useful energy transfer from a lower temperature-level source of energy, free of cost (i.e., air, water, or soil) to a higher temperature level. The cycle is divided into two parts: the first part is a “working fluid” desorption from liquid absorbent at the highest temperature in the system. The second part happens at lower temperature and lower pressure for easy energy transfer. When “working fluid” goes in vapor phase with liquid absorbent (separated in the first part), then a heat delivering at intermediate temperature occurs. When vapor is condensed at the highest pressure, it delivers heat at intermediate temperature also. This useful heat is provided to the user.

In both cases, the amount of external energy input (electric power or heat) has to be kept as low as possible to make the heat pump ecologically and economically desirable. The measure for this efficiency is the COP (Coefficient of Performance). For an electric compression heat pump, it is defined as:

$$COP = \frac{\text{useful heat}}{\text{electric power input}}$$

The higher the COP, the lower the external energy input compared to the useful heat. COP is dependent on the heat pump itself (efficiency of heat exchangers, losses in compressor, etc.) and on the temperature difference between the low-temperature (ground) side and the high temperature (building) side. COP can be given for the heat pump under defined temperature conditions (e.g. 5 °C ground / 35 °C heating supply), or as an average annual COP in a given plant, also called SPF (Seasonal Performance Factor).

In heating mode, the heat pump works as follows: heat from the earth connection arrives at an earth connection-to refrigerant heat exchanger called the evaporator. The refrigerant is colder

than the temperature of the heat transfer fluid from the earth connection, so heat flows into the refrigerant. This heat causes the liquid refrigerant to evaporate; its temperature does not increase much. This gaseous, low pressure and low temperature refrigerant then passes into an electrically-driven compressor. This raises the refrigerant's pressure and, as a consequence, its temperature. The high temperature, high pressure, gaseous output of the compressor is fed into a second heat exchanger, called the condenser. In water-to-air heat pumps, a fan blows air to be heated through this "air coil". In water-to-water heat pumps, water which will heat the building flows through the condenser. Since the refrigerant is hotter than the air or water, it transfers heat to it. As it loses heat, the refrigerant's temperature drops and it condenses. This high temperature liquid refrigerant then passes through an expansion valve. The valve reduces the pressure of the refrigerant, and as a consequence, its temperature drops significantly. Now, this low temperature liquid flows to the evaporator and the cycle starts again. In this way, the heat from the water or other heat transfer fluid in the earth connection is transferred to the air or water in the building, hence the name "water-to-air heat pump" or "water-to-water heat pump".

For working fluid (refrigerant), suitable substances are those with large specific heat capacities and which evaporate at low temperatures. Today, only chlorine free refrigerants are permitted. These are non-ozone depleting refrigerants (Ozone Depletion Potential, ODP = 0). R134a, R407C, R410A, R404A and propane fulfill these conditions. The most used refrigerants are R134a and R407C and other blends as they are both non-flammable and nontoxic.

## ***2.5. Overview of ground systems for geothermal heat pump***

The ground system links the geothermal heat pump to the underground and allows for extraction of heat from the ground or injection of heat into the ground. These systems can be classified generally as open or closed systems.

To choose the right system for a specific installation, several factors have to be considered: geology and hydrogeology of the underground (sufficient permeability is a must for open systems), area and utilization on the surface (horizontal closed systems require a certain area), existence of potential heat sources like mines, and the heating and cooling characteristics of the building(s).

In the design phase, accurate data of the key parameters for the chosen technology are necessary; to size the ground system in such a way that optimum performance is achieved with minimum cost. Wells must be properly designed and developed, and periodic maintenance on the well and well pumps must be performed.

The terms “open” and “closed loop” systems are originated from the USA, and may be looked upon as practical descriptions of systems with boreholes with plastic pipes (closed) and systems where groundwater is pumped from and injected through water wells (open). These terms are also used in Europe.

The various shallow geothermal systems to transfer heat out of or into the ground comprise:

- Horizontal ground heat exchangers: 1.2 - 2.0 m depth (horizontal loops)
- Borehole heat exchangers: 10 - 250 m depth (vertical loops)
- Energy piles: 5 - 45 m depth
- Ground water wells: 4 - 50 m depth
- Water from mines and tunnels

Systems using a heat exchanger inside the ground are also called “closed” systems; systems producing water from the ground and having a heat exchanger (e.g. the evaporator) above ground are called “open” systems.

### **2.5.1. Closed vertical loop**

This system applied for single resident buildings consists of one or several boreholes in which borehole heat exchangers (BHE) are installed. The boreholes may commonly be up to 200 m deep and drilled into almost any type of soil and rock. The BHE is connected to a heat pump. By circulating a heat carrier fluid (water mixed with antifreeze), heat is extracted from the borehole surroundings and transferred to the heat pump from which heat at a higher temperature is distributed to the building, as illustrated in Figure 2.4.

Several types of borehole heat exchangers have been used or tested; the two possible basic concepts are (Figure 2.5):

- U-pipes, consisting of a pair of straight pipes, connected by an 180° - turn at the bottom. One, two or even three of such U-pipes are installed in one hole. The advantage of the U-pipe is low cost of the pipe material, resulting in double U-pipes being the most frequently used borehole heat exchangers in Europe.
- Coaxial (concentric) pipes, either in a very simple way with two straight pipes of different diameter, or in complex configurations.

During the winter season, the temperature of the fluid and the borehole surroundings will gradually get lower. The fluid will then often reach a temperature well below the freezing point. As a result, the COP of the heat pump will gradually drop. However, in a correctly designed

system, the temperature will not be as low as making the heat pump to stop. This is a great advantage of GSHP's compared to air as heat source.

In the summer, these systems may provide free cooling directly or the heat pump operates as a cooling machine and stores condenser heat in the ground. This is a great advantage, especially in warmer climates. By definition, using the system also for cooling, turns it into a borehole thermal energy storage (BTES) system.

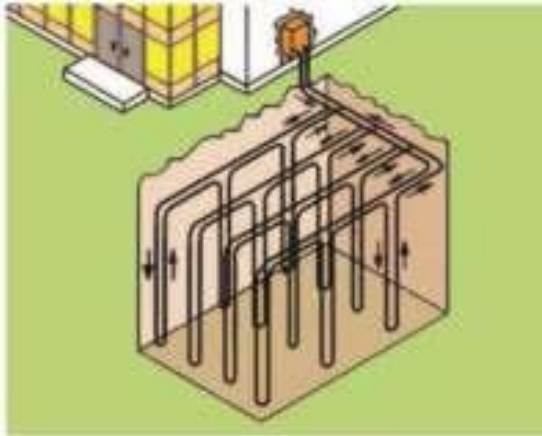


Figure 2.4: Closed vertical loop system (Geothermal Community)

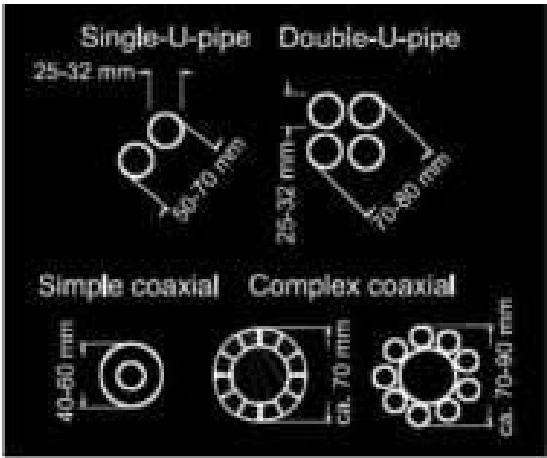


Figure 2.5: Cross-sections of different bypass of boreholes heat exchangers (Geothermal Community)

If the system is used for heat extraction only, which is the most common practice in colder climates, a single borehole recovers its normal temperature naturally during the summer season. If several boreholes are used, it is great importance that the boreholes are not too close to each other. The holes are drilled at a distance of about 6 m and depth between 30 and 120 m (Figure 2.4).

In terms of thermal properties of the ground, they are strongly influenced by the soil volumetric water content, volume fraction of solids and volume fraction of air. Air is a poor thermal

conductor and reduces the effectiveness of the solid and liquid phases to conduct heat. While the solid phase has the highest conductivity, it is the variability of soil moisture that largely determines thermal conductivity. As such soil moisture properties and soil thermal properties are very closely linked and are often measured and reported together. As a result, from a geological point of view, the best efficiency of vertical loops is obtained in crystalline rocks with a high content of silica, such as granites and gneisses. Among the sedimentary rocks, the best efficiency is achieved in quartzite and dense sandstones with a low porosity. However, it is important to know that almost any types of rocks are technically feasible, as well as any types of soil. This makes the vertical loops having a very high potential regardless the geological conditions at site.

**2.5.2. Closed loop horizontal systems**

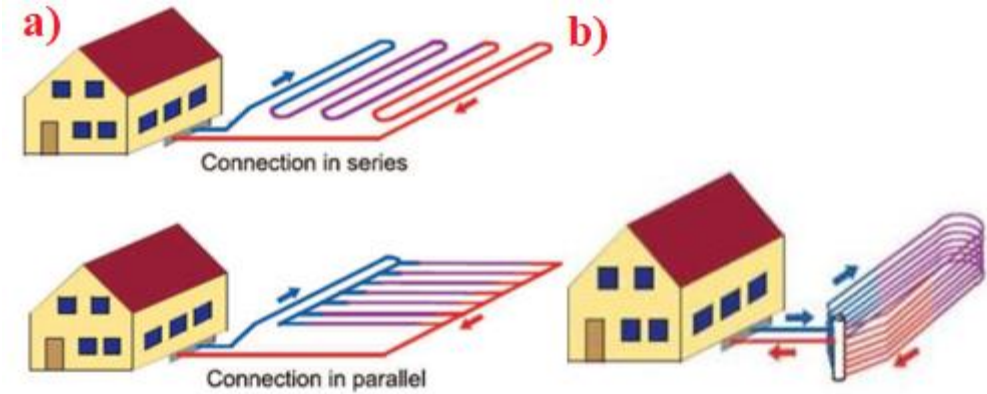


*Figure 2.6: Ground heat exchanger a) Closed horizontal type and b) Trench type (Geothermal Community)*

The shallowest system is the horizontal loop. This consists of a plastic pipe that is typically ploughed or dug down in the garden of a residential house as shown in Figure 2.6.a). This system may not be of interest for a driller, but may still be considered by an installer as an option of heat exchangers. Compared to vertical loops, this system takes a lower investment for construction. On the other hand, it is less efficient due to a lower working temperature of the fluid. This is partly due to the relatively lower thermal conductivity of the soil compared to a rock. Furthermore, the technique is based on freezing the moisture in the soil that requires a rather low fluid temperature over a long part of the winter season. The freezing process will continuously draw water towards the pipe, hence creating ice scaling around the plastic pipes. The ice itself will have a positive effect on the thermal conductivity. The pipes can be connected in series or parallel (Figure 2.6.a).

For the trench collector (Figure 2.6.b), a number of pipes with small diameter are attached to the steeply inclined walls of a trench. The main thermal recharge for all horizontal systems is provided mainly by the solar radiation to the earth's surface. It is important not to cover the surface above the ground heat collector, or to operate it as a heat store.

However, in later years a more compact system has been developed called “slinky”. This consist of coils of plastic pipes, that are placed vertical in dug ditches (Figure 2.7), one at each wall of the ditch. A slinky configuration would flatten a spiral of piping at the bottom of a wide trench or large scraped area. The slinky loops could be placed adjacent to each other in a large excavated area and then backfilled to a depth of 1,8 to 2,5 m.

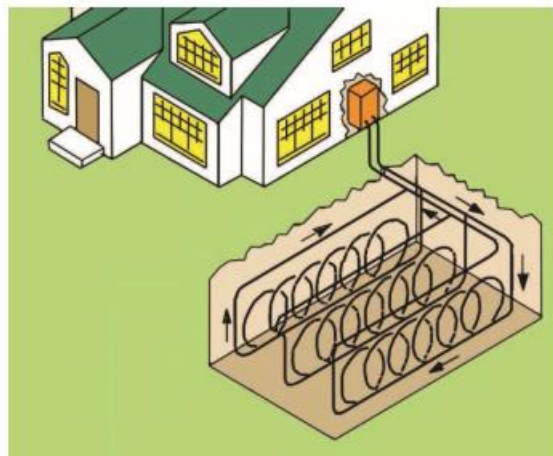


*Figure 2.7: Closed horizontal-Slinky loop (Geothermal Community)*

### **2.5.3. Open loop systems (groundwater systems)**

Ground water is a valuable natural source especially for drinking water. Still, using ground water for energy extraction is fairly common in many countries for both heating and cooling. The reason for this is that groundwater systems are more efficient than closed loop systems because the temperature of groundwater is practically constant all over the year (if pumped from a depth of 10 m or more) and that water is the best carrier of thermal energy (the highest heat capacity).

As illustrated in Figure 2.8, the technology “normal” groundwater wells are used for energy extraction. However, to create a system with extraction and injection is more challenging. Such systems have to be circulated under pressure and under perfectly airtight conditions to avoid problems with clogging and corrosion induced by chemical processes.

In the country side, a single well or even a dug well may be used. In these cases, the chilled water is disposed to surface water or infiltrated by a buried stone bed. However, in several

countries, due to environmental and legal issues, it is not possible to discharge chilled water in neither the surface water nor the different aquifer levels. As a result, doublet wells have normally to be used, one or several for production and approximately an equal number of wells for reinjection of chilled water.

Groundwater can also be used for direct cooling with great interest due to its very high efficiency. The maximum temperature requirements would typically be about 10 °C for comfort cooling and about 25 °C for process heating.

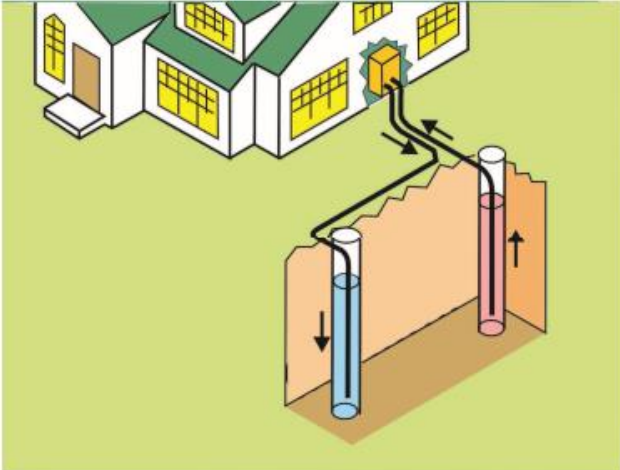


Figure 2.8: Open ground water loop system (Geothermal Community)

### **3. Chapter 3: ENERGY GEOSTRUCTURES**

#### **3.1. Introduction**

As discussed in the previous chapter, the geostructures are not only used to carry and transfer the loads to the soil, but they can be also designed as a part of heating system. Some practical examples of energy geostructures are: retaining wall, tunnels, foundation piles and diaphragm walls.

In the past, the awareness of environmental protection leads to the increasing need of utilizing renewable energy, then Ground Source Heat Pumps (GSHP) are efficient and environmental friendly systems for buildings. However, GSHP suffers from the economic barriers of the relatively high initial capital cost, which is significantly affected by the excavation cost of Ground Heat Exchanger (GHE). The drilling cost can be significant reduced or eliminated if GHE is embedded in the building foundations which is already required for structural purposes. So-called thermo-active foundations or energy geostructures work at the same time as structural elements and components of the GSHP system.

To explain how the thermo-active system works, Brandl (2006) interpreted as follow. Basically there are two circuits: the primary circuit contains closed pipework in earth-contact concrete elements (piles, barrettes, diaphragm walls, columns, base slabs, etc.) through which a heat carrier fluid is pumped to exchange energy between the building and the ground. The carrier fluid is a heat transfer medium of either water, water with antifreeze (glycol) or a saline solution. It is shown that glycol–water mixtures are the most suitable, especially because they contain also additives to prevent corrosion in the header block, valves, the heat pump, etc. The secondary pipework is a closed fluid-based circuit embedded in the floors and walls of buildings or bridge decks, road structures, platforms, etc. Commonly, a heat pump connects the two closed circuits, in which heat exchange occurs, as shown in Figure 3.1. The main charge of the pump is to increase the temperature level from 10-15 °C to 25-35 °C in heating mode. Therefore, a low electrical energy is required to raise the originally non-usable heat resources to a higher, usable temperature.

The use of energy geostructures has become more popular around the world, especially in some pioneering countries as Austria and Switzerland (1980s) with first application for base slabs, then piles (1984) and diaphragm walls (1996), and UK, Germany (Brandl, 2006). There are many researches that have been conducted by different authors around the world. Brandl (2006) described the projects of a rehabilitation center, and the first thermo-active traffic tunnel, called

Lainzer Tunnel in Vienna which involved the use of piles as heat-exchangers, while the absorber pipes are situated in diaphragm walls, in bottom slabs and between the primary and secondary lining of the station tunnels in Metro line U2, Vienna.

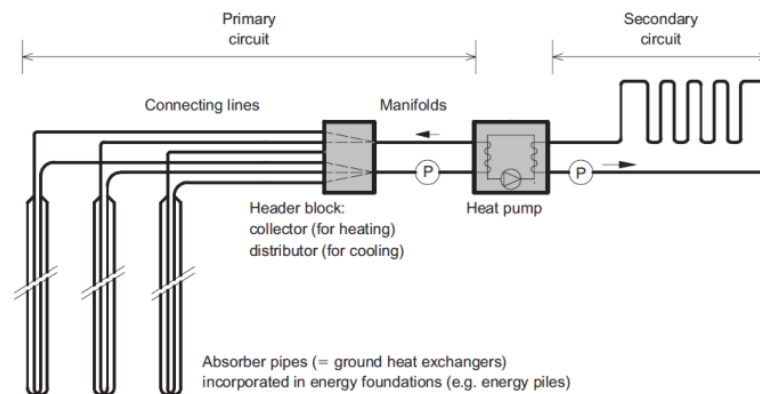


Figure 3.1 Scheme of a geothermal energy system (Brandl, 2006)

Di Donna et al. (2016) investigated how some important factors affect the energy performance of diaphragm walls equipped as heat-exchangers, in which different parameters (such as wall length, the ratio between the panel height and the excavation depth, the velocity of heat carrier fluid, number of pipes) were taken into consideration.

Sterpi et al. (2018) described a case study of 6-storey residential building located in Tradate, Varese, Italy, in which the field observation and optimization by numerical modelling were done for heat-exchanger systems embedded in diaphragm walls and base slab area to optimize their energy performance.

Suckling and Smith (2002) described the first use of energy walls in the United Kingdom where an installation at Keble College, Oxford included a thermally-activated, bored pile retaining wall in addition to thermally-activated bearing piles.

### 3.2. Energy piles

The plastic piping can be fixed to the reinforcement cage of the piles in a plant or on the site (Figure 3.2), the latter is more common.

According to Brandl (2006), the percentage of (large-diameter) bored piles has been steadily increasing since the year 2000. Austria is a pioneer to promote the use of this type of geostructures, since 1985 more than 1 million meters of cast iron piles have been installed. As known, the heat exchangers are inserted into the fresh concrete, and have to be secured against uplift until the concrete has sufficiently hardened. The standard diameter of such driven piles is  $d = 170$  mm, but this can be increased significantly by shaft grouting. Nevertheless, the

geothermal effectiveness of such thin energy piles is smaller than that of driven precast concrete piles or large-diameter bored piles, despite of the high thermal conductivity of cast iron. The small diameter enables the installation of only one pipe loop and no coiled piping. Moreover, the contact area with the ground is relatively small. In soft soils, buckling of the piles also has to be considered (Brandl, 2006).



*Figure 3.2: Absorber pipes attached to the reinforcement cage (Brandl, 2006)*

Energy piles will be subjected to a net change of the temperature relative to the initial condition over time, which causes thermal stresses and head displacements. Under thermo-elastic conditions, if the pile is a free body, i.e. it has no restraints, it will expand while heating and contract during cooling to yield a thermal free strain, then the length of piles will also change. If the pile is perfectly restrained, it will keep its length, but thermally induced stresses will be created. In reality, a pile will not expand or contract freely as it will be confined by the structure on top and the surrounding soil, at different levels of restraint (Figure 3.3). The restrained strain provokes a thermal stress in the pile and the thermally induced axial load which affects the verification of bearing capacity of piles.

When a thermal load is transmitted from the pile to the soil, the soil reacts by changing its volume (expansion or contraction of the pore water and soil structure) and by modifying the strength of contact between soil particles. Coarse-grained soils do not seem to be affected by temperature variations due to their drained behavior. On the other hand, fine-grained soils show a densification and a reduction in the undrained shear strength with increasing temperature due to an increase in the pore water pressure that cannot be dissipated. This results in a reduction in

effective stresses (short-term). Sutman (2016) reported that an excess pore water pressure of 0.7% of the effective stress is generated by 1°C increase in soil temperatures.

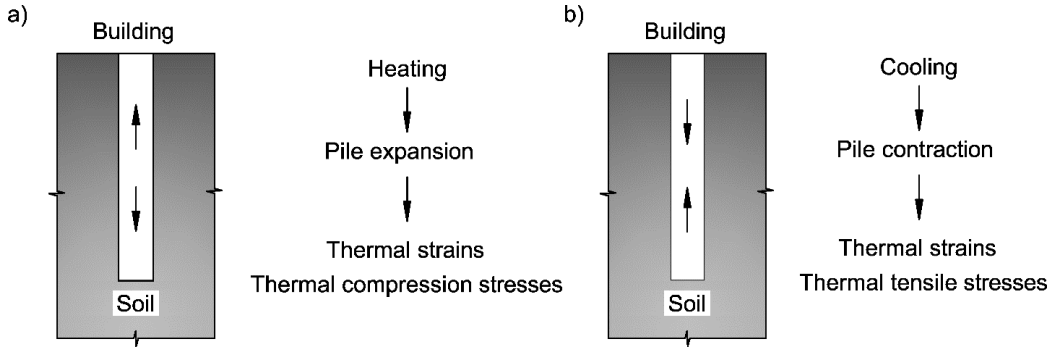


Figure 3.3: Response mechanism of a pile heat exchanger, a) for heating and b) for cooling

Pagola et al. (2018) reported that the pile bearing capacity is not reduced to a critical level in terms of structural integrity. They described an analysis of monotonic temperature variations in the range from 6 °C to 50 °C - 60 °C and they concluded that higher temperatures increase the strength of the clay-concrete contact. This is explained by the thermal consolidation of the clay that results in an increase of the contact surface, even though the interface friction angle is reduced. They also concluded that there was no impact of temperature on the interface shear strength (as described in Figure 3.4) between concrete and a low plasticity clay.

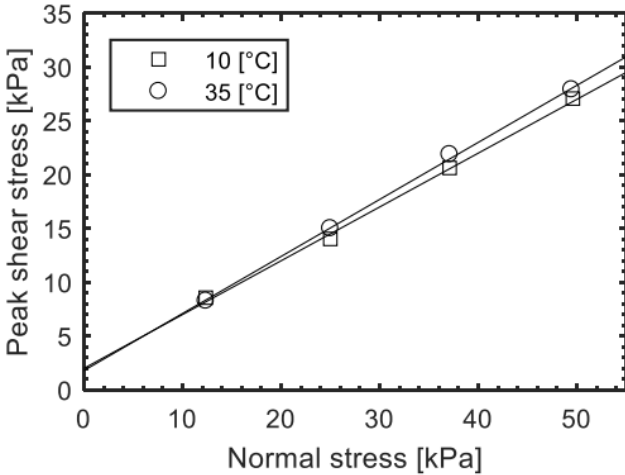


Figure 3.4: Clay/concrete interface behavior assessed using thermal borehole shear device (Pagola et al., 2018)

In order to characterize the degradation of the pile-soil interface under thermal cyclic loads, constitutive laws and numerical models can be applied to reproduce the cyclic behavior of energy piles. The main research programs covering the thermo-mechanical behavior of the energy pile-soil systems include full-scale, lab-scale and numerical studies.

### 3.3. *Energy tunnels*

The application of heat exchange in tunnels have become more popular due to its efficiency. In comparison with foundation, substantially larger ground volumes can be used for geothermal heat. In high overburden tunnels, significantly higher temperatures can also be utilized. Additionally, geothermal heat production can be based on shallow tunnels, like metros. The first application of this kind can be found in the Lainzer tunnel in Austria (Adam & Markiewicz, 2009).

Moreover, when mechanized tunneling is used, the tunnel segmental lining is precast in factory and then placed onsite by a tunnel boring machine (TBM), so the preparation and optimization for each segment can be done before. The system could also allow cooling the tunnel using the heat produced internally by fast moving trains or vehicles. These main characteristics allow a tunnel lining to become a mean of thermal exchange (Barla and Di Donna, 2018). The tunnels with different local conditions and features can be classified into two types: “cold” and “hot” tunnels. Referring to cold tunnels, the air temperature during the year is around 15°C that can be slightly increased due to the moderate frequency passage of trains. The diameters of this kind of tunnels are normally large, about 10-12m. The prevailing temperatures in the tunnel only have a limited effect on the temperature in the surrounding ground. Instead, hot tunnels usually present high internal temperatures. Extra heat can be added from starting and braking of trains with rapid cycle frequency and from the numerous stations. A schematic representation of a segmental lining equipped with geothermal heat exchangers is presented in Figure 3.5 (Barla et al., 2016).

Although enhancing thermal exchange and optimization could be done during design process of geostructures by changing some factors, such as surface and width of concrete members or choice of materials according to thermal conductivity, in most cases, the structural design has been already done, then followed by the thermal design. In this situation, the need to optimize heat exchanger elements is essential to make the geostructures as well as buildings more efficient and economical.

Based on the increasingly popular use of TBMs, Barla and Di Donna has designed a novel energy tunnel precast segmental lining, named Enertun which is patented at Politecnico di Torino. They suggest a layout of pipes perpendicular to the tunnel axis, thus implying a head losses reduction of 20-30% (Barla et al., 2019). Furthermore, it is clear that groundwater flow contributes significantly to the energy efficiency of geothermal systems that leads to the interest

in installing energy tunnels in zones with groundwater flow. Figure 3.6 shows the heat exchanged by a ring of energy tunnel lining, comparing Enertun configuration with the one employed in the past. If no difference is shown in the absence of groundwater flow, an increase of about 10% is found when considering Enertun in the case of groundwater flow perpendicular to the tunnel axis. (Barla et al., 2019).

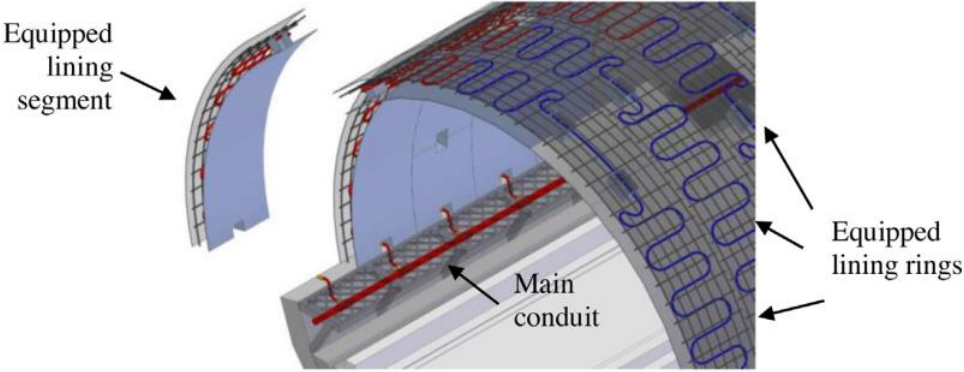


Figure 3.5: Schematic representation of a tunnel segmental lining equipped as ground heat exchanger (Barla et al., 2016)

Figure 3.7 shows the main steps that characterized the preparation of the segments. The primary circuit which is embedded in the ground connects with heat pump via header pipes, then the heat pump transfers the heat from an environment with a given temperature to another one characterized by a different temperature via the secondary circuit, represented by the building to be heated or cooled.

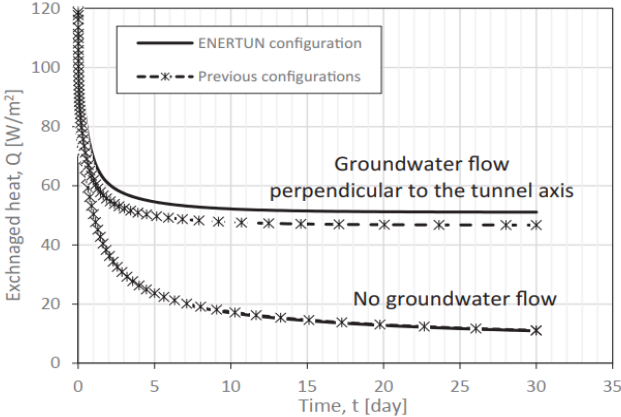


Figure 3.6: Comparison between Enertun and previous configurations in terms of heat exchange obtained from numerical simulation (Barla et al., 2019)



Figure 3.7: Preparation stages of energy segments: (a) moulding, (b) casting, (c) demoulding and (d) circulation test (Barla et al., 2019)

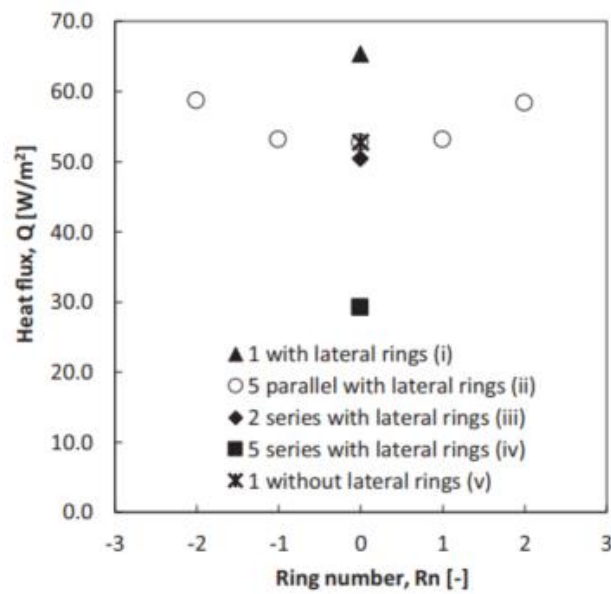


Figure 3.8: Efficiency of different configurations (Barla et al., 2016)

Table 3.1: Testing results with different input parameters (Barla et al., 2016)

|        | Fluid velocity, $v$ | Inlet temperature, $T_{in}$ | Inlet temperature, $T_{in}$ | $T_g-T_{wo}$ | $T_{wo}-T_{wi}$ | Reynolds number, $Re$ |
|--------|---------------------|-----------------------------|-----------------------------|--------------|-----------------|-----------------------|
|        | [m/s]               | [°C]                        | [°C]                        | [°C]         | [°C]            | [-]                   |
| Winter | 0.3                 | 4                           | 7.84                        | 6.16         | 3.84            | 6107                  |
|        | 0.4                 | 4                           | 7.05                        | 6.95         | 3.05            | 8143                  |
|        | 0.5                 | 4                           | 6.53                        | 7.47         | 2.53            | 10179                 |
|        | 0.6                 | 4                           | 6.16                        | 7.84         | 2.16            | 12215                 |
|        | 0.8                 | 4                           | 5.67                        | 8.33         | 1.67            | 16287                 |
|        | 1                   | 4                           | 5.36                        | 8.64         | 1.36            | 20359                 |
| Summer | 0.4                 | 28                          | 23.73                       | 9.73         | 4.27            | 8143                  |
|        | 0.5                 | 28                          | 24.46                       | 10.46        | 3.54            | 10179                 |
|        | 0.8                 | 28                          | 25.66                       | 11.66        | 2.34            | 16287                 |
|        | 1                   | 28                          | 26.1                        | 12.1         | 1.9             | 20359                 |

Regarding the efficiency of the system, firstly the most favorable ring configuration that was chosen had to be verified, followed by determining the most suitable inlet fluid velocity to optimize the plant performance, then the quantity of exchanged heat could be evaluated. By doing some numerical models of 5 different types of configuration, the rings connected in parallel solution is the most suitable (see Figure 3.8). On the other hand, the most suitable inlet fluid velocity can be defined based on the simulation with different values of fluid velocity ranging from 0.3 to 1 m/s, then  $Q$  extracted during winter and injected during summer can be computed based on the difference between the inlet and outlet temperature of the pipe circuit, see Table 3.1. It appears that the optimized inlet fluid velocity was 0.4 m/s.

Barla et al. (2016) suggested the optimized solution using the system both for heating and cooling to maintain the sustainability of the system, in which the temperature reduction induced by the winter heat extraction is recharged by the heat injection resulting from the use of the system for summer conditioning. The results obtained for the seasonally cyclic heating-cooling hypothesis are described in Figure 3.9.

In comparison with traditional heating plants, the annual cost in operating the energy tunnel system is significantly lower. Figure 3.10 shows the saving of annual cost with the same amount of produced energy.

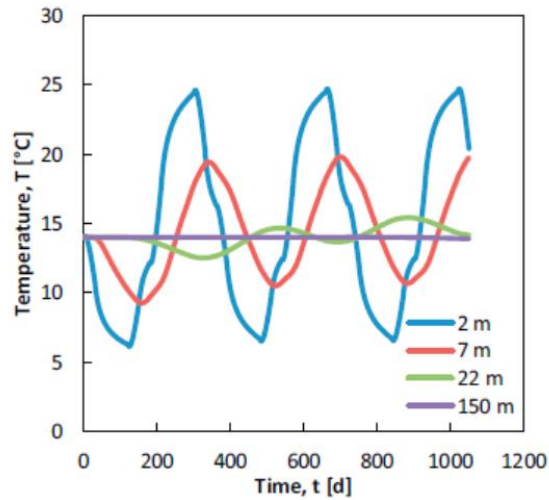


Figure 3.9: Temperatures in the soil at different distance from the tunnel during three years of cycling heating and cooling (Barla et al., 2016)

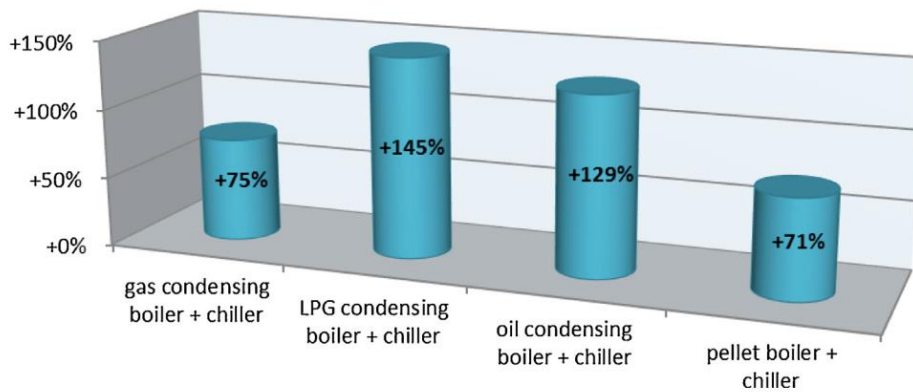


Figure 3.10: Annual operating cost savings with respect to other heating/cooling systems (Barla et al., 2016)

### 3.4. Energy diaphragm walls

Diaphragm wall is a continuous reinforced concrete wall which supports an underground structure, as a foundation or facilitate cut off provision in order to support deep excavation. Diaphragm wall forms a rectangular section constructed in-situ under the soil. These walls are constructed panel-by-panel each interlocked to ensure structural stability and water tightness. The diaphragm walls can have a thickness ranging from 60 cm to 150 cm with a width of 2.0 to 3.5 m. The diaphragm walls can be constructed up to a depth of 60 m.

The geothermal diaphragm walls, unlike conventional ones, have a system of polyethylene pipes which are necessary for transporting the heat transfer fluid. The loops are attached to the outside face of the reinforcement cage near external surface, the external cover need to be increased to maintain 75 mm of cover to the loops. However, the bending and shear capacity of

the wall have minor effect due to relatively small diameters of the geothermal loops and the effective area of the concrete wall is only marginally reduced by the introduction of geothermal loops and can be ignored in the capacity calculation (Amis et al., 2011).

In comparison with the construction sequences of normal diaphragm wall, those for geothermal one are a little bit different:

- Quality control and pre-installation testing;
- Lifting of the diaphragm armature cage;
- Installation of the pipes;
- Fixing the pipes to the cage as it is lowered;
- Cutting of excess pipes and their protection;
- Aptitude test of the pipes before casting concrete;
- Casting (of the diaphragm) of concrete.

The geothermal loops are fabricated at the factory under controlled conditions, then are coiled ready for dispatch to site. On site the coiled loops are then placed onto a drum arrangement (as shown in Figures 3.11 and 3.12) to enable the loops to be fed out and fixed onto the reinforcement cage as it is lowered into the prepared panel. Unlike other geostructures which will be surrounded by soil on all faces, the energy diaphragm walls will have one face permanently partially exposed to the basement.



*Figure 3.11: Feeding Geothermal Loop onto Reinforcement Cage (Amis et al., 2011).*

The integration of the GSHP system into the diaphragm wall has to be assured, although this system would not have any adverse impact on the construction process and quality of the completed diaphragm wall panels. Normally, the heat exchanger system should be used in both conditions (heating in winter season and cooling in summer season), so the heat carrier fluid inside the pipes is always changing, and the maximum and minimum temperature of the liquid must be set for any possible evolutions. With a variable temperature during the year and the

temperature difference between the fluid and the concrete, a thermal stress is generated around the pipes, but quite limited.



*Figure 3.12: Geothermal Loop and Reinforcement Cage Installation (Amis et al., 2011).*

Furthermore, in areas away from heat exchangers, the thermal stress in the structure is mainly caused by the change of temperature of surrounding soil, but its range caused by geothermal energy utilization is rather small. A thermal expansion of pore water increases the pore water pressure, and consequently decreases the effective stress of the soil. Besides, an increasing temperature reduces the internal viscosity, and hence the shear resistance.

The efficiency of an energy diaphragm wall depends on many factors such as: the arrangement of the loops inside the cage, the spacing between two consecutive pipes, the concrete and soil thermal properties, the presence of groundwater flow, the velocity of heat carrier fluid, boundary conditions and the temperature difference between the soil and the heat carrier fluid of loops in the diaphragm walls. Almost all these parameters were taken into account from different authors during the last years.

Xia et al. (2012) analyzed the new technology on the Shanghai Museum of Nature History by attempting to investigate the heat transfer performance of heat exchangers embedded in diaphragm walls based on field experiment. The influential factors to heat transfer performance were further studied, such as heat exchanger types, inlet water temperature, water velocity and operation modes (presented in Table 3.2). Some heat exchanger types were investigated and their sizes are shown in Figure. 3.13. Type (a) (b) were in W-shape, consisted of two single U-shaped tubes in series connection with a distance of 15 cm and 75 cm respectively. Type (c) included only one single U-shaped tube with the distance of branch tubes being 75 cm.

Table 3.2: Experimental schemes of heat transfer test in diaphragm walls (Xia et al., 2012)

| No. | Influence factors            | Factor levels                                      | Other conditions  |
|-----|------------------------------|--|---|
| 1   | Heat exchanger types         | Tubes type (a), (b), (c)                           | Velocity 0.6 m/s; inlet temperature 35 °C                 |
| 2   | Water velocity (m/s)         | 0.25, 0.45, 0.6, 0.75, 0.90, 1.05, 1.30, 1.5       | Tubes type (b); inlet temperature 7 °C                    |
| 3   | Inlet water temperature (°C) | 32.0, 35.0, 38.0                                   | Tubes type (a), (b), (c); velocity 0.6 m/s                |
| 4   | Operation modes              | Intermittent operation (1:1), Continuous operation | Tubes type (b); velocity 0.6 m/s, inlet temperature 35 °C |

In comparison with the heat exchangers in boreholes, firstly the heat exchange rate per meter in diaphragm wall is higher. The buried depth of the heat exchangers in boreholes is about 80-100 m compared to about 20-40 m in diaphragm wall, however the heat exchange rate is relevant to the buried depth with adverse proportion (the smaller the buried depth of heat exchangers, the higher the heat exchange rate per meter). Secondly, due to the unlimited size of diaphragm wall, the two single U-shaped absorber tubes in series connection (W-shaped) with larger intervals can perform better than double U-shaped heat exchangers in borehole while all other conditions being equal. Thirdly, a lot of heat is released due to the hydration of concrete which may lead to the rise of temperature of concrete to 60-70 °C at the most, and its recovery speed is very slow.

The temperature of underground is a very important factor which influences the heat exchange rate, i.e., the higher the temperature of underground, the lower the heat exchange rate for space cooling, and the higher the heat exchange rate for space heating. Fourthly, the surrounding medium of absorber tubes in diaphragm wall is concrete, while the surrounding of absorber tubes in borehole is backfills and soil. Because of the higher thermal conductivity and heat capacity of concrete, heat exchangers in diaphragm wall may perform better than those in borehole while all other conditions being equal. As a result, it is obvious that the heat exchangers in diaphragm wall are very different from those in borehole, so the research results and experience of heat exchangers in borehole cannot be used directly in diaphragm wall (Xia et al., 2012).

Considering the effect of heat exchanger types on the energy performance, the heat exchange rate of type (b) is higher than that of type (a) and the heat exchange rate of type (c) is the lowest at any time as presented in the Figure 3.14. Compared with single U-shaped heat exchangers in the same condition, the heat transfer rate of W-shaped heat exchanger in diaphragm walls is 25-40% higher (Xia et al., 2012).

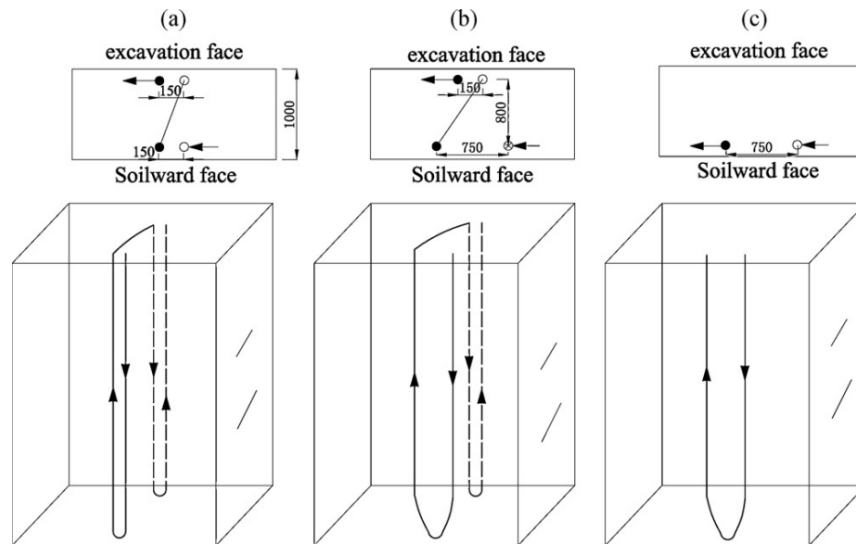


Figure 3.13: Three types of underground heat exchangers: (a) W-shaped type, (b) improved W-shaped type and (c) single U-shaped type (Xia et al., 2012)

The effective water velocity is 0.6–0.9 m/s, so a reasonable velocity should be determined, instead of pursuing an extensive high water velocity. The heat transfer rate changes linearly with the temperature of inlet water with the rate of 1°C increase with respect to 15% rise of heat exchange rate (Xia et al., 2012).

Di Donna et al. (2016) applied statistically based parametric analysis techniques to the energy assessment of diaphragm walls and suggested an optimization of their energy efficiency. The most important parameters affecting energy performance could be: thermal conductivity concrete ( $\lambda_{con}$ ), the difference between the soil and excavation air temperature ( $\Delta T$ ), the wall length (L), the ratio between the panel height and the excavation depth (R), the width of wall (W), concrete cover (C), the velocity of heat carrier fluid (v) and the number of pipes (or pipe spacing, sp), besides the diameter of pipes and panel length do not significantly affect the energy efficiency. In order to do this, 8 cases could be defined with different values of input parameters (see Table 3.3). Then, 8 numerical models were set to compute the heat transfer rates at four different time frames corresponding to 3, 5, 30 and 60 days after the activation of geothermal system.

Increasing the concrete thermal conductivity is a positive way to improve the energy efficiency. In contrast, the embedment ratio, as well as concrete cover seem to have a minor effect on the energy efficiency. The panel width is the third most influential parameter in the short term, but its influence decreases in the long term. See Figure 3.15 to have a better illustration which compares the effect of each factor normalized by the largest effect in the same time frame.

Observing the variation of the parameters' influence with time, it is clear to distinguish those that play an important role in the short or long term.

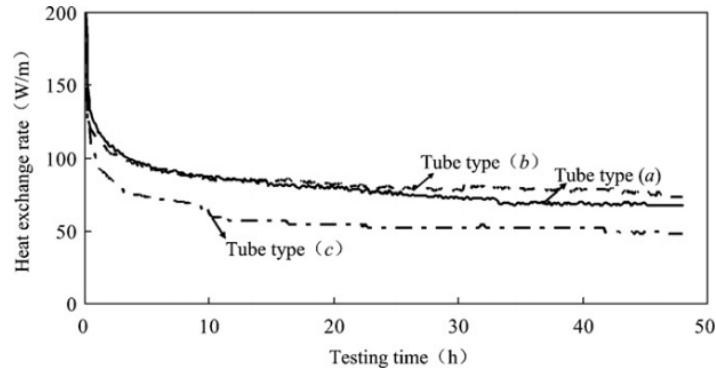


Figure 3.14: Relationship curves of heat exchange rate and time under different types of heat exchangers (Xia et al., 2012)

Table 3.3: A set of runs for a specific case study and results (Di Donna et al., 2016)

| Run No | Parameter |       |         |        |         |                 |                       | Results     |             |              |              |
|--------|-----------|-------|---------|--------|---------|-----------------|-----------------------|-------------|-------------|--------------|--------------|
|        | W [m]     | R [m] | sp [cm] | C [mm] | v [m/s] | $\Delta T$ [oC] | $\lambda_{con}$ [(*)] | q-3d [(**)] | q-5d [(**)] | q-30d [(**)] | q-60d [(**)] |
| 1      | 0.8       | 1.25  | 25      | 50     | 0.2     | 2               | 1.5                   | 30.8        | 24.6        | 15.1         | 13.3         |
| 2      | 0.8       | 1.25  | 25      | 100    | 1.2     | 6               | 3                     | 33.5        | 24.8        | 13.9         | 11.8         |
| 3      | 0.8       | 2     | 75      | 50     | 0.2     | 6               | 3                     | 23.2        | 19.0        | 9.8          | 7.7          |
| 4      | 0.8       | 2     | 75      | 100    | 1.2     | 2               | 1.5                   | 22.0        | 19.3        | 11.7         | 9.8          |
| 5      | 1.2       | 1.25  | 75      | 50     | 1.2     | 2               | 3                     | 31.8        | 26.8        | 15.7         | 14.0         |
| 6      | 1.2       | 1.25  | 75      | 100    | 0.2     | 6               | 1.5                   | 18.8        | 15.9        | 7.2          | 5.5          |
| 7      | 1.2       | 2     | 25      | 50     | 1.2     | 6               | 1.5                   | 37.2        | 27.6        | 10.9         | 8.1          |
| 8      | 1.2       | 2     | 25      | 100    | 0.2     | 2               | 3                     | 38.8        | 30.7        | 16.8         | 18.4         |

Unit: (\*): [W/(mK)], (\*\*): [W/m<sup>2</sup>]

In conclusion, for short term considerations, the pipe spacing is the most important factor affecting energy efficiency and this suggests that maximizing the number of pipes installed is one route to get the optimization, however the pipe spacing influence reduces with time and hence other factors including long term payback periods need to be considered for finalizing design spacings. In the long term, the temperature excess between the wall and the excavation is the single most important factor governing energy efficiency.

The field observation results done by Sterpi et al. (2018) were compared with those of Brandl (2006) and Xia et al. (2012) in terms of the average heat rate. By normalizing the overall area of the diaphragm walls or the base slab, Brandl (2006) reported 30 W/m<sup>2</sup> for diaphragm walls fully embedded in the soil and 10-30 W/m<sup>2</sup> for base slabs, while 33.6-43.2 W/m is the range of

the heat rates per unit depth depending on the heat exchanger layout into the diaphragm wall, for 32°C fluid inlet temperature by normalizing the diaphragm wall depth (Xia et al., 2012).

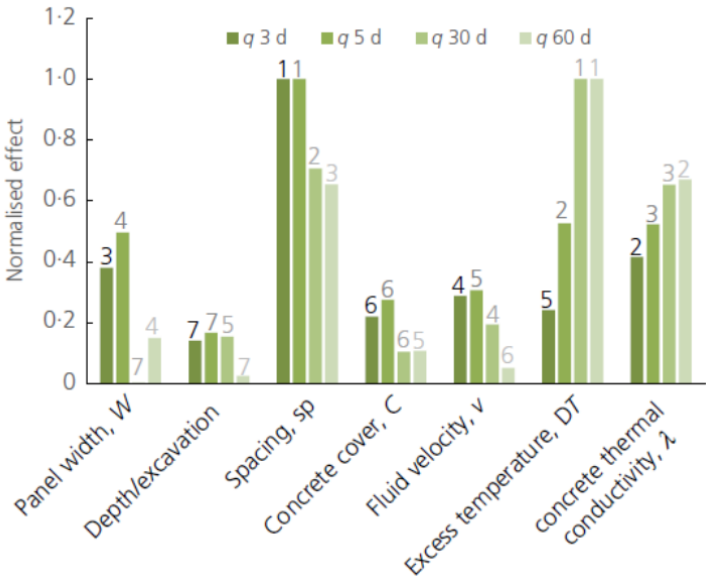


Figure 3.15: Normalized effect of each parameter in terms of heat exchanged (Di Donna et al., 2016)

Meanwhile, Sterpi et al. (2018) gave the seasonal average heat rate per unit depth of 33.4 W/m, in good agreement with Xia et al. (2012) with similar boundary conditions in both cases. In contrast, the seasonal average heat rates per unit surface are 13.9 W/m<sup>2</sup> and 5.2 W/m<sup>2</sup> for the diaphragm walls and the base slab respectively (Sterpi et al., 2018), which are much lower than the references of Brandl (2006), so ground heat exchangers installed in those geostructures that are only partially embedded in the soil may behave sensibly worse. However, if the overall resulting performance of 13.9 W/m<sup>2</sup> is considered as the average of the performance of the two parts (below and over excavation level), weighed by their pertinence areas (one third for below part and two third for over part), the performance of the portion below excavation results in 31.5 W/m<sup>2</sup>, namely very close to 30 W/m<sup>2</sup>.

There are two aspects to enhance the heat exchange, namely the increase of the distance between pipe branches circulating the fluid at different temperatures and the minimization of the length of the path exposed to the excavation that, in some conditions, can negatively affect the heat exchange. In the numerical analysis, Sterpi et al. (2018) suggested three models to make the comparison and see the advantages, they are base layout (total length is 90 m), two enhanced layouts which are single W-shaped and double W-shaped loops with 40 m and 60 m of total length respectively, see Figure 3.16 for more detail.

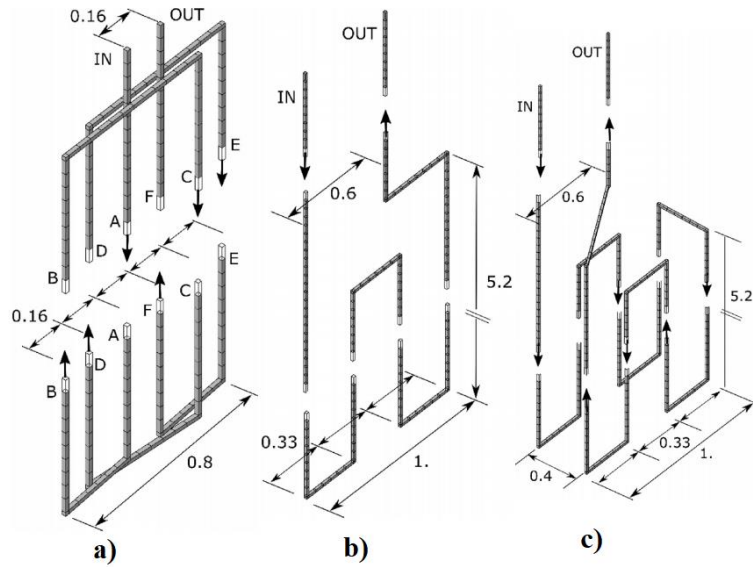


Figure 3.16: Layout of the Base (a), Single-W (b) and Double-W (c) heat exchanger pipe (units m) (Sterpi et al., 2018)

For both enhanced layouts, the fluid temperature undergoes a rather continuous increase as a result of the negligible interference between branches at very different temperatures, especially the first and the last, now being 0.6 m apart from each other. In both cases, the negative influence of a low thermal condition at the excavation side is confirmed by the lower temperature increase (or lower energy) observed in the calibrated model with respect to the initial model as showed in Table 3.4. In calibrated models, a boundary condition with a seasonally varying damping factor was used to simulate the effect of excavation sides, whereas this damping factor was kept constant in initial models.

Table 3.4: Energy performance of the three pipe layouts in December 2015 (Sterpi et al., 2018)

| Layout   | Length [m] | E [kWh] |     | q [W] |     | q/S <sub>dw</sub> [W/m <sup>2</sup> ] |      | ΔT with respect to base layout [%] |      |
|----------|------------|---------|-----|-------|-----|---------------------------------------|------|------------------------------------|------|
|          |            | I       | C   | I     | C   | I                                     | C    | I                                  | C    |
| Base     | 90         | 223     | 157 | 371   | 263 | 20.6                                  | 14.6 | -                                  | -    |
| Single-W | 40         | 238     | 173 | 395   | 289 | 22                                    | 16.1 | 6.6                                | 10   |
| Double-W | 60         | 255     | 182 | 425   | 304 | 23.6                                  | 16.9 | 14.5                               | 15.8 |

Note: I: Initial model, C: Calibrated model

The energy performances of the three different layouts are compared in Table 3.4, in terms of total exchanged heat E, average heat rate q, and specific average heat rate q/S<sub>dw</sub> per unit panel wall surface, in December 2015. The slightly better performance of the Single-W layout compared to the base one (+6.6% in the initial model, +10% in the calibrated model, as average heat rate) demonstrates that a long piping is unnecessary if the thermal interference among

branches is not minimized and the fluid circulates mostly above the excavation level. The markedly better performance of the Double-W layout (+14.5% in the initial model, +15.8% in the calibrated model) basically is the result of a longer pipe and of using both embedded faces of the wall. In conclusion, Single-W layout and the Double-W layout can exchange 10.0% and 15.8% more heat than the base layout, with a pipe length equal to 45% and 67% of the base layout respectively.

## **4. Chapter 4: DESCRIPTION OF EXPERIMENTAL SETUP (GEOTHERMSKIN)**

Many advantages of geothermal system are described in parts above, besides in contemporary world, policies are pushing the building sector to a higher efficiency imposing high standards in the primary supply (European Parliament, European Council, 2009). However, the existing energy solutions still present some weakness, i.e. in dense urban areas, especially in central districts where available surfaces are limited for solar energy installation or horizontal geothermal systems to generate enough energy. On the other hand, vertical geothermal systems usually require high initial costs related to drillings and excavation. It is clear that thermal activation of earth-contact area of the buildings can be considered as a proper solution without drilling or excavation costs related to borehole heat exchanger installation.

It is clear that the depths reached by the underground parts of buildings is directly proportional to the number of stories above the ground level, so the foundation of buildings with limited number of stories (8-10 floors) do not reach to the homoeothermic zone where the temperature profiles commonly show a constant temperature, suggesting that the temperature is uniform in space and constant in time. As a result, the temperatures of the ground at these depths are slightly less favorable than those of vertical shallow geothermal systems. However, the cost-benefit balance is still of great interest because the expected efficiency of a system installed at these depths is relatively low and the low installation cost of very shallow geothermal system.

In this perspective, Baralis and Barla (2019) suggested a novel energy system, called GeothermSkin, conceived to minimize the installation-related costs. This system is intended to be installed during building construction or refurbishment. The basic idea of this system is to provide a full or at least a partial fulfilment of the renewable energy requirements of building by transforming the earth-contact area of a building into a heat exchanger for heating and cooling of the building itself.

### **4.1. Prototype experimental site**

#### **4.1.1. Experimental site description**

The first realization was designed for experimental purposes intended to test the system energy performance and thermal impact that is exerted on the surrounding ground. Based on components available on the market, a setup was designed in a small scale and not used to fulfill the energy needs of the served building, but used to test a set of different conditions and

configurations in the same location with sufficient heat supply for a small size commercial heat pump.

This kind of system has been applied for the building of the Energy Center Laboratory in Torino (Italy) in 2019. The building was recently built and hosts private and academic research offices and laboratories. An auditorium is also present at the ground level of the building for a total gross floor area of about 7000 m<sup>2</sup>. The building was conceived as a smart energy building with high efficiency standards to control and monitor energy consumption. An extremely large number of smart sensors monitor indoor environment and energy consumption on all the 4 elevated stories and on the basement level, including the 2000 m<sup>2</sup> underground car park. A wide monitoring system was designed and put in place during prototype construction.

#### **4.1.2. GeothermSkin description**

The energy GeothermSkin system covers as a skin structural elements which are in contact with the ground as presented in the Figure 4.1. The GeothermSkin system can be put in place by fixing to the reinforcement cages of the earth-contact structural elements or to the outer surface and then buried by backfilling, but there is a little difference in installation process between new and existing building. In the case of new construction, the system can be installed once the structural works are completed which means just after the removal of formworks and before the backfilling of the ground or attached directly to reinforcement cage. In contrast, in the case of existing buildings, an excavation need to be done to have enough external space next to the walls for setting up the system. Therefore, the horizontal area occupancy is obviously avoided in this case.

The whole system of GeothermSkin is constituted of many modular panels with maximum width of 2.5 m which allow these modules to be assembled directly on site without the need of special transportation. The modules compose a network of polymeric pipes (crosslinked polyethylene PE-Xa or high density polyethylene PE-D) with proper resistance to high temperatures, high pressures and corrosion. These panels are bounded to the vertical elements by a proper support and fixing system, namely common anchoring system used for radiant panel-based heating systems.

Figure 4.2 summarizes the main components of the GeothermSkin system, in which the modular panels are placed at preferable positions with a minimum spacing of 30 cm from the digging bottom and 10 cm from the edges. Moreover, the internal diameters of pipes are from 20 to 30 mm, with the thickness of 2 to 4 mm, while the heat carrier fluid within the pipes is a mixture

of water and glycol that allows to operate safely the system in a range of temperatures down to  $-20\text{ }^{\circ}\text{C}$  (freezing point of  $-30\text{ }^{\circ}\text{C}$ ). The single modules (i.e. element indicated as 20, 30, 40) can present different shapes differentiated by the preferential direction in pipe deployment and placed on the outer surface of the underground walls (indicated as 10). They can be oriented horizontally (module 20, 30) and vertically (module 40) and work independently, namely parallel, but it is possible to make connections between them.



Figure 4.1: Render of the GeothermSkin energy system applied to a residential building basement (Baralis and Barla, 2019)

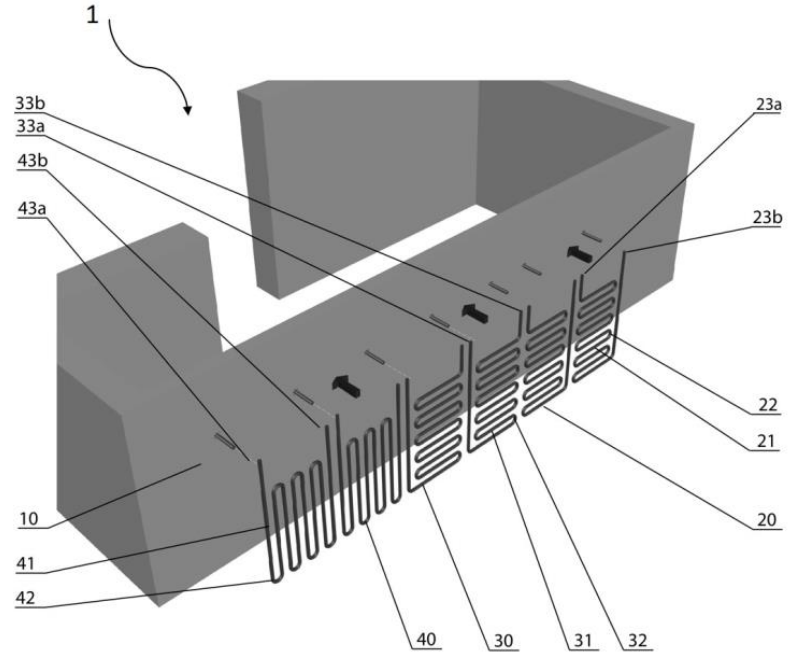


Figure 4.2: Main components of the novel energy wall system GeothermSkin (Baralis and Barla, 2019)

The first kind of connection to the collector pipes is to bring them to the inner side of the building by using appropriate holes, then these pipes are in turn connected to the

heating/cooling distribution system through a heat pump. Differently, the second configuration is the direct connection between the exit end of a circuit and the entrance end of the neighboring one which is established directly on the exterior wall surface. The deployment of manifolds is conceived to facilitate inspection and intervention. Due to the modularity of the system and its easily inspected ability, the failure detection of single modules and exclusion of damaged pipes from the network could be done actively to keep the system's functionality even in the case of local damages.

### 4.1.3. Experimental setup

#### *a/ Pipe layout*

The thermal energy is not involved in the building demand, but it just provides a sufficient energy supply for a heat pump. Designing process of this layout had to take into account the minimum space required for installation of the system without any interference with daily activities of the building. The ground heat exchanger system was located on the south-eastern facade of the building at the most distant corner in order to reduce significantly the thermal effect exerted by the building and the car park on the ground to this system. The layout, direction, length, entrance and exit ends the panel are shown in the Figure 4.3 and Table 4.1.

*Table 4.1: Heat exchanger circuits experimental setup details (Baralis and Barla, 2019)*

| Circuit | Pipe direction | Pipe length [m] | Entrance end | Exit end |
|---------|----------------|-----------------|--------------|----------|
| 1       | Horizontal     | 26.6            | H2           | H1       |
| 2       | Horizontal     | 27              | H3           | H2       |
| 3       | Vertical       | 29.3            | H4           | H3       |

A set of three different modules (the first two panels in horizontal and the third one in vertical direction) allows to comparatively test at identical working conditions in both configurations. A properly designed manifold connection hence allows to select the modules to be tested with parallel rather than sequential connection. Hydraulic circuit was driven to the inner side of the wall by means of four small diameter holes with a 130 mm diameter (indicated with letter H in Figure 4.3). Besides, another larger core was realized in the middle circuit in order to bring the sensor cables of the monitoring system to the acquisition unit. Figure 4.3 describes the deployment of the pipes network in the experimental site with the identification of the modules and of the drilled holes H1 - H2 - H3 - H4 for manifold connection and HM for monitoring sensors wires (dimensions are indicated in centimeters).

In order to reduce the thermal influence of the air temperature at the ground level, the heat exchanger coil covered the wall from about 150 cm below ground surface up to the maximum depth of the basement level of approximately 4.60 m below ground surface. An area of 210 cm width per 300 cm height resulted in an effective exchanging area of 6.3 m<sup>2</sup> per module while neglecting the relatively small shallower parts reaching the ends.

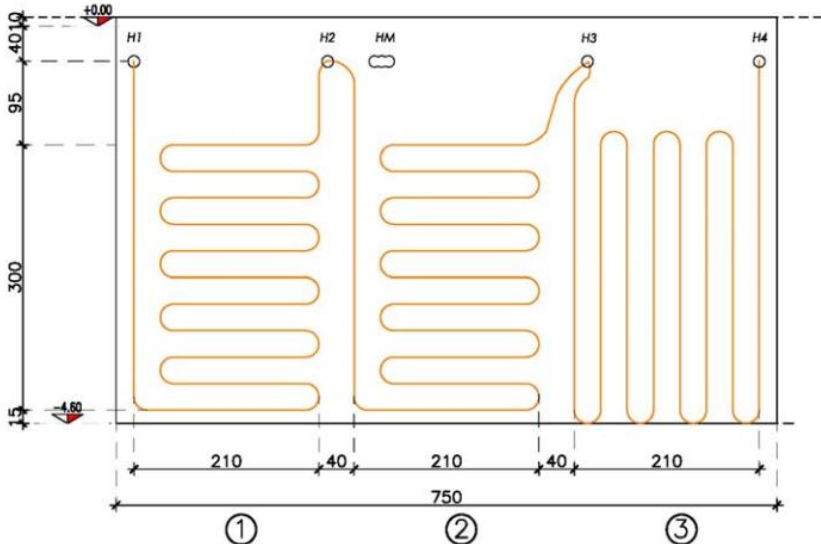


Figure 4.3: Deployment of the pipes network in the experimental (Baralis and Barla, 2019)



Figure 4.4: Trench shoring process: (a) early stage of excavation and (b) bottom of the excavation (Baralis and Barla, 2019)

The excavation was done to install the modules into the exterior surface of the walls. However, as mentioned above, there would be no need to do the excavation in case of new construction, while the ground surrounding the existing walls need to be excavated to generate space for modular setup. In the experimental site, due to the small available area for the excavated material and facilities, excavation faces were built vertical. Because of the shape of the excavation and the depth reached, the shaft was secured by means of relevant iron trench shores (Figure 4.4). Once the excavation was completed, the pipes network was fixed to the exterior

surface of the wall and the three circuits were manually put in place by a series of simple metal clamps with approximately 75 cm spacing (Figure 4.5).

The protection of the pipe system from damages during soil compaction process had to be considered. One of the proper methods is providing thin sand layers limited to the very narrow surroundings of the walls, which reduces shear forces on the pipe network. However, the compaction process had to be done carefully.

#### *b/ The system distribution*

Hydraulic circuit brings the fluid to the heat exchangers and vice versa by a series of connection valves that are in turn attached to the main flow and return pipes of the heat pump. In particular, the hydraulic circuit has been equipped with a manifold that allow to test different configurations of the heat exchangers (see Figure 4.6), the series of valves mounted on the manifolds allow to singularly exclude from circulation one or more modules. Consequently, the modules are connected in parallel rather than sequentially. The flow in these main flow and return pipes has to be able to feed multiple heat exchanger circuit simultaneously. These pipes were made of high density polyethylene with a larger nominal diameter of 32 mm and to be tested properly against leakage before connecting to the manifold system. Furthermore, the system was pressurized up to 2 bar and pressure decrease over time was measured by means of an appropriate pressure gauge.



*Figure 4.5: Pipe deployment fixed by regularly distant clamps (Baralis and Barla, 2019)*

Nominal heat power of currently installed heat pump is of 3.15 kWt with a declared COP of 4.72. Thus electric supply is about 0.67 kWe including consumption from the two circulation pumps which are embedded in the heat pump. Each of the circulation pumps is conceived to serve separately the user side rather than the ground side. While on the ground side nominal flow rate is 0.65 m<sup>3</sup>/h, a significantly lower flow rate (0.29 m<sup>3</sup>/h) is set up at the user side. Flow

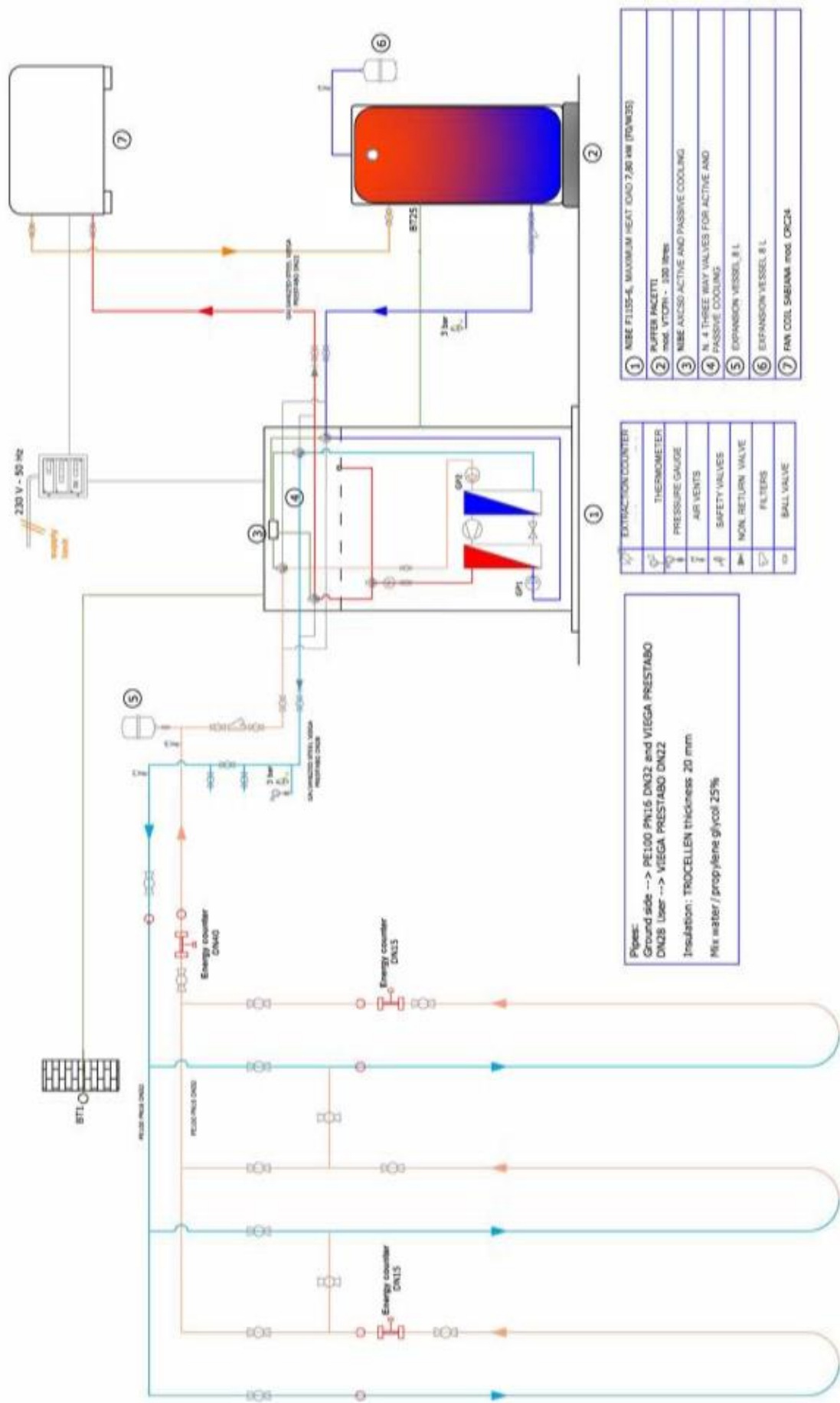
rate is also directly measured at the heat exchanger side where some energy meters were installed in proximity to the manifold in the cavaedium.



*Figure 4.6: Manifold connecting the pipes from/to the heat pumps with the heat exchanger modules (Baralis and Barla, 2019)*

The heat pump internally performs a thermodynamic cycle on R407C type refrigerant fluid (working volume 1.16 kg) which is composed by HFC components (mixture of 23% R32, 25% R125 and 52% R134A) that allows to provide water at high temperatures up to 65 °C at the hot side of the cycle. In particular, the user (secondary) circuit is composed of a fan coil to dissipate the refrigerant/heating energy and a buffer accumulator tank (Figure 4.7).

Secondary circuit pipes are 22 mm diameter galvanized steel pipes with the same thermal insulation as the primary circuit. The use of a fan coil can dissipate the heat produced by the heat pump during winter season, while during the summer season the fan coil heats up the temperature of the heat carrier fluid. The internal fan coil can be fed with heat carrier fluid at temperatures in the range of 5 °C to 85 °C. Electrical ventilation engine allows to produce a flow rate of 340 m<sup>3</sup>/h.



- ① NIBE FL135-E, MAXIMUM HEAT LOAD 7.80 kW (70kW35)
- ② RUPPERT PACETTI mod. VTOPN - 320 litres
- ③ NIBE ANCO-ACTIVE AND PASSIVE COOLING
- ④ N. 4 THREE WAY VALVES FOR ACTIVE AND PASSIVE COOLING
- ⑤ EXPANSION VESSEL 8 L
- ⑥ EXPANSION VESSEL 8 L
- ⑦ FAN COIL SABIANA mod. CRCC4

|   |                    |
|---|--------------------|
| ⊘ | EXTRACTION COUNTER |
| ⊘ | THERMOMETER        |
| ⊘ | PRESSURE GAUGE     |
| ⊘ | AIR VENTS          |
| ⊘ | SAFETY VALVES      |
| ⊘ | NON RETURN VALVE   |
| ⊘ | FILTERS            |
| ⊘ | BALL VALVE         |

Pipes:  
 Ground side -> PE100 PN16 DN22 and VIEGA PRESTABO DN28 User -> VIEGA PRESTABO DN22  
 Insulation: TROCELLEN thickness 20 mm  
 Mix water / propylene glycol 25%

Pipes Rehau 20 mm - sp. 2 mm

Figure 4.7: Scheme of the geothermal heat pump system (Baralis and Barla, 2019)

#### 4.1.4. Monitoring system

An extensive monitoring system was designed to analyze thermo-mechanical induced effects on the wall and thermal alteration, water content and pore pressures in the ground volume facing the GeothermSkin prototype.

##### *a/ Stress-strain monitoring system*

In natural conditions, the temperature of the wall external surface and of the surrounding ground are almost the same, but slightly different from the temperature in free field conditions. The ground close to the wall over excavation level suffers from the thermal change due to the influence of the air inside, especially, the presence of a heat exchanger within the structure generates the thermal alteration beyond the external surface of the equipped wall. The heat carrier fluid is circulated in the pipes of ground side and user side (outdoor and indoor units of the heat pump), it arrives at the heat pump from ground loop and carries heat at low temperature during heating, or enters the circuit of ground side and carries heat at high temperature during the cooling season. This is especially true at the entrance end of the circuit, while along the path the temperatures drop/increase respect to the wall temperature decreases as a result of the heat exchange with the ground (Baralis and Barla, 2019). It is clear that the changes in temperature lead to deformation that is proportional to the temperature variation, then strains are in turn related and cause stresses acting on the structural elements. However, in this work the thermo-mechanical aspects have been neglected because of the main interest in the thermal and hydraulic coupled analysis directly involved in the determination of the geothermal performances. Nonetheless, a brief qualitative description of collected data will be given.

Strains were measured by a series of 5 gauges that were firmly fixed to the wall by two dowels (for each gauge) glued by chemical anchoring agent in specifically drilled holes, see Figure 4.8: (a) fixing dowels positioning prior to installation and (b) after the installation. Besides, 4 pressure cells sensors were put in place in addition to the previously mentioned strain gauges to measure the stress field acting at the wall surface in different directions. Pressure is recorded by converting it through a transducer into an electrical signal conveyed to the acquisition unit and data-logger. The instrument detects the pressure acting on the direction normal to the measure plate. In particular, sensor Cp2 allows to measure the normal direction to the wall, so some concrete was cast behind the plate filling the 5.5 cm thick void space in order to provide a perfect contact between plate and wall surface (see Figure 4.9 with (a) Cp2 with backfilling to guarantee perfect contact and (b) Cp4 positioning).

Placement and accurate positioning of the sensors was performed according to the scheme of Figure 4.10 and Table 4.2



Figure 4.8: Strain gauges installation (Baralis and Barla, 2019)

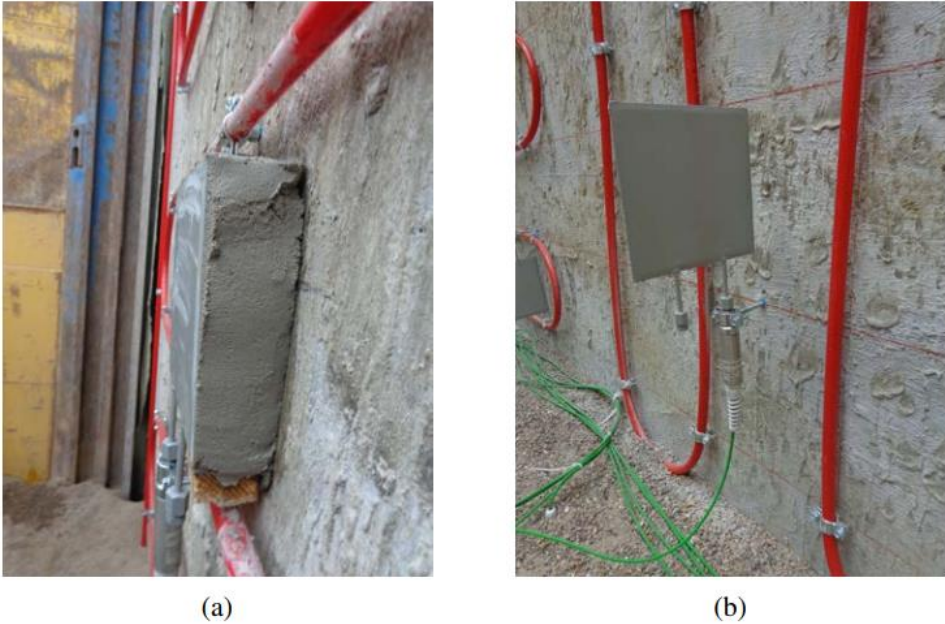


Figure 4.9: Installation of the pressure cells on the wall surface (Baralis and Barla, 2019)

*b/ Temperature and hygrometric monitoring system*

Regarding to the temperature measurement, a large number of PT-100 (see Figure 4.11a) were positioned on four planes at different depths that were materialized during backfilling operations. The thermal resistances are specifically designed for ground monitoring. Some potential damages to the sensors or their cables could be caused by the possible aggressive environment in the ground and problems related to soil compaction, i.e. impacts with larger

particles or boulders in the heterogeneous ground at the site. As a result, these sensors and cables need to be used together with a metallic protection.

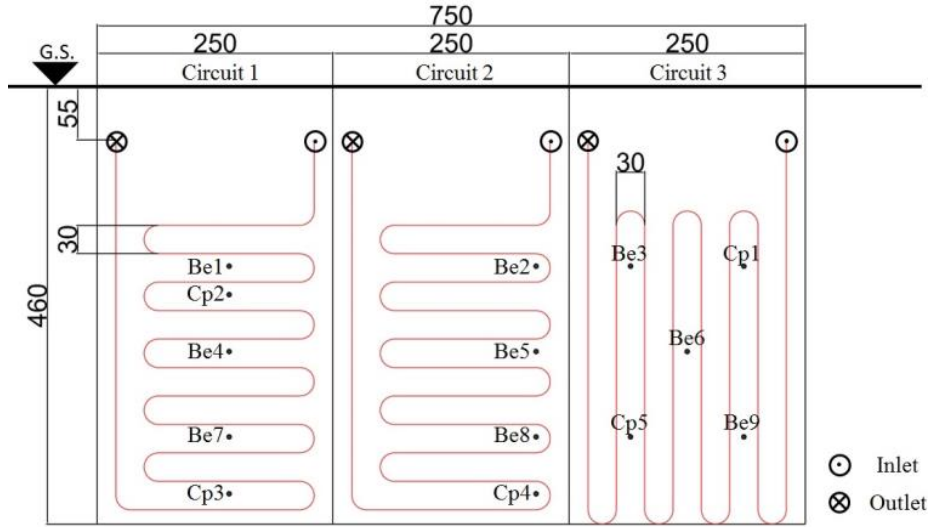


Figure 4.10: Heat exchangers prototype layout and monitoring stress and strain sensors on the wall surface (Baralis and Barla, 2019)

Table 4.2: Location of stress and strain sensors on the wall surface with the direction of axis (Baralis and Barla, 2019)

| Loop | Instrument    | Depth [cm] | Axis | Code |
|------|---------------|------------|------|------|
| 1    | Strain gauge  | 170        | H    | Be1  |
| 1    | Pressure cell | 200        | N    | Cp2  |
| 1    | Strain gauge  | 260        | V    | Be4  |
| 1    | Strain gauge  | 350        | H    | Be7  |
| 1    | Pressure cell | 410        | V    | Cp3  |
| 2    | Strain gauge  | 170        | V    | Be2  |
| 2    | Strain gauge  | 260        | H    | Be5  |
| 2    | Strain gauge  | 350        | V    | Be8  |
| 2    | Pressure cell | 410        | H    | Cp4  |
| 3    | Strain gauge  | 170        | H    | Be3  |
| 3    | Pressure cell | 170        | V    | Cp1  |
| 3    | Strain gauge  | 260        | V    | Be6  |
| 3    | Pressure cell | 350        | H*   | Cp5  |
| 3    | Strain gauge  | 350        | H    | Be9  |

Note: V = vertical, N = normal, H = horizontal, H\* = due to excavation backfilling, accidental hit induced a 15° counter-clockwise rotation of the plate

Backfilling process was done in stages with planes being shown in Figure 4.11b. Each materialized plane was executed consecutively by roughly compacting and equalizing to designed depths. Temperature sensors were positioned in strings composed of 4 or 8 sensors in

each plane, depending on the depth and on the specific alignment. It is expected that along the depth of the wall, the thermal gradient tends to be bigger and bigger, so the maximum distance between measurement points and the wall should be smaller at deeper planes. The accuracy of the collected data might be assured by perfect contact between the sensors' bodies and the ground. Installing the sensors by digging correctly at desired positions as designed with small holes did not only retain perfectly the mentioned contact, but it resulted in smaller differences between the part subjected to sensor insertion and the rest of the plane in terms of compaction in comparison with larger digs. As mentioned in the part above, the sensor protection from the upper parts or compaction process could be done by covering these sensors with a thin sand layer. There were still little shifts of sensor positions because of the presence of pebbles within the compacted soil that obstructed the exact placement of the sensors. Although the positions of the sensors were accurately measured just after installation, acceptable shifts of 5cm in magnitude with respect to the designed location could be allowed, see Figure 4.14 and Figure 4.15.

Apart from the thermal monitoring apparatus, a total of 18 hydrometers were included in the monitoring system up to the maximum depth (4.6 m below ground surface) reached by the wall. They measure the volumetric content of water as a percentage of the total volume investigated by the probe with 0.03% volume of precision and also temperature measurement is embedded in the 10-cm long sensor (see Figure 4.12) with 2 °C accuracy. Since the shallower plane was at 0.75 m below ground surface and the infiltration due to rainfalls (or garden watering) starts from the ground surface with significant gradients in the very shallower layers, 8 sensors were installed above plane A. The cables, sensors were protected before final ground backfilling by placing them in resistant plastic tubes which were filled with finer ground parts (mainly sands) and have been removed only after the ground levelling (Figure 4.13).

All the sensors cables, as mentioned above, are driven to specifically drilled hole HM in the wall (shown in Figure 4.3) and headed over the cavaedium where they were carefully arranged with excess length to avoid straps due to ground settlements during the consolidation phase. In the cavaedium, the acquisition unit was operated by the electrical system of the building, but there was still a backup battery remaining in the system as well in order to ensure continuous operations and avoid data losses. All process of data collection can be uploaded on the internet for remote consultation and download.

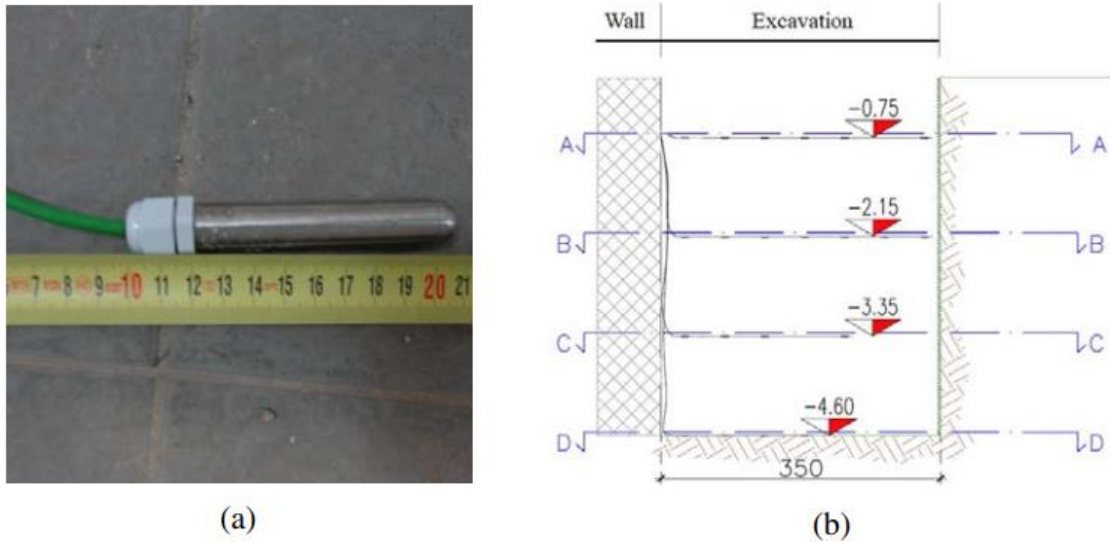


Figure 4.11: (a) Temperature monitoring sensors for ground monitoring and (b) depth location of the sensors along planes (Baralis and Barla, 2019)

Other significant information related to the energy system is the amount of heat exchange. Measurement could be done by three different energy meters installed on the collector manifold. Each meter is made up of two separate pieces: the first one functions as a monitor of the flow rate of the heat carrier fluid with an ultrasonic flow meter on the return pipe. The second one couples the flow rate measurement with the temperatures at two distinct points (the inlet and outlet ends of the circuits) measured by PT-500 thermal resistances, see Figure 4.7 for detail distribution. In order to compare the differences in energy performance of two different directional configurations at the same conditions, the two first meters were set up to measure the data from circuit 1 and 3 respectively. Besides, the energy performance of the whole GeothermSkin system can be evaluated based on the data measurement of the third meter installed on the main flow and return pipes of the system. Data collected were the circulation pump speed of both the primary and secondary circuit, the inlet and outlet temperatures of both the circuits, the temperature of the buffer tank on the secondary circuit and the cavaedium air temperature. In order to delineate heat pump efficiency and the unit energy cost of the system, it is planned to acquire further parameters as the power consumption of the heat pump through a dedicated electricity meter and the flow rate on the secondary circuit through the installation of an additional energy meter.



(a)

(b)

Figure 4.12: Volumetric water content sensor installed at the experimental facility in Torino: (a) before installation and (b) once installed before burial on plane B where the green cables are connected to the temperature sensors while the thicker black ones are the hygrometer sensors cables (Baralis and Barla, 2019)



(a)

(b)

Figure 4.13: (a) Installation of hydraulics sensors above the plane at very shallow depths within plastic pipes filled with sand before ground backfilling. Sensors included 8 hygrometers and (b) 3 tensiometers (Baralis and Barla, 2019)

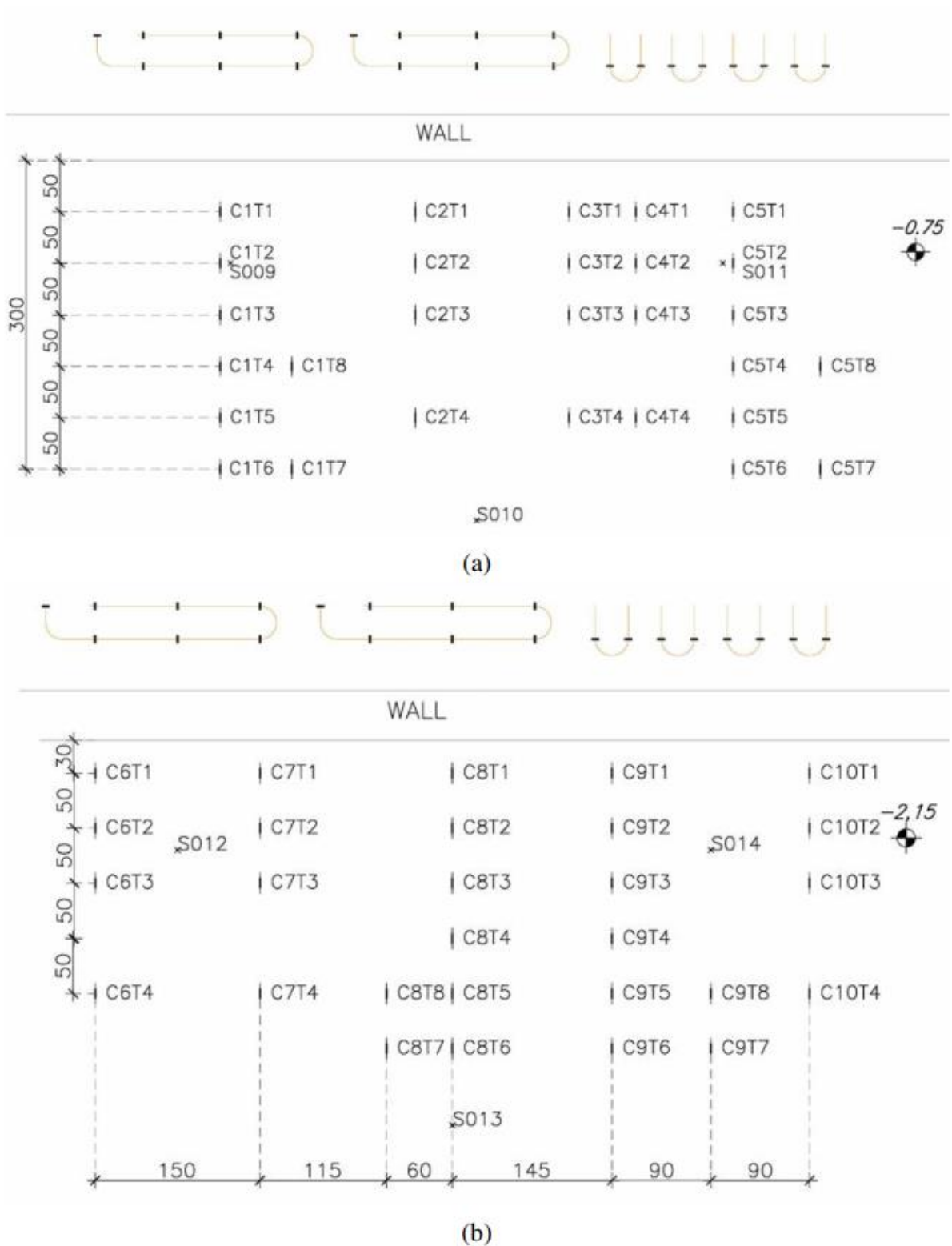


Figure 4.14: Temperature sensor location on (a) Plane A and (b) on Plane B along with their codification. Also some hygrometer sensors nominated as S0xx are depicted (Baralis and Barla, 2019)

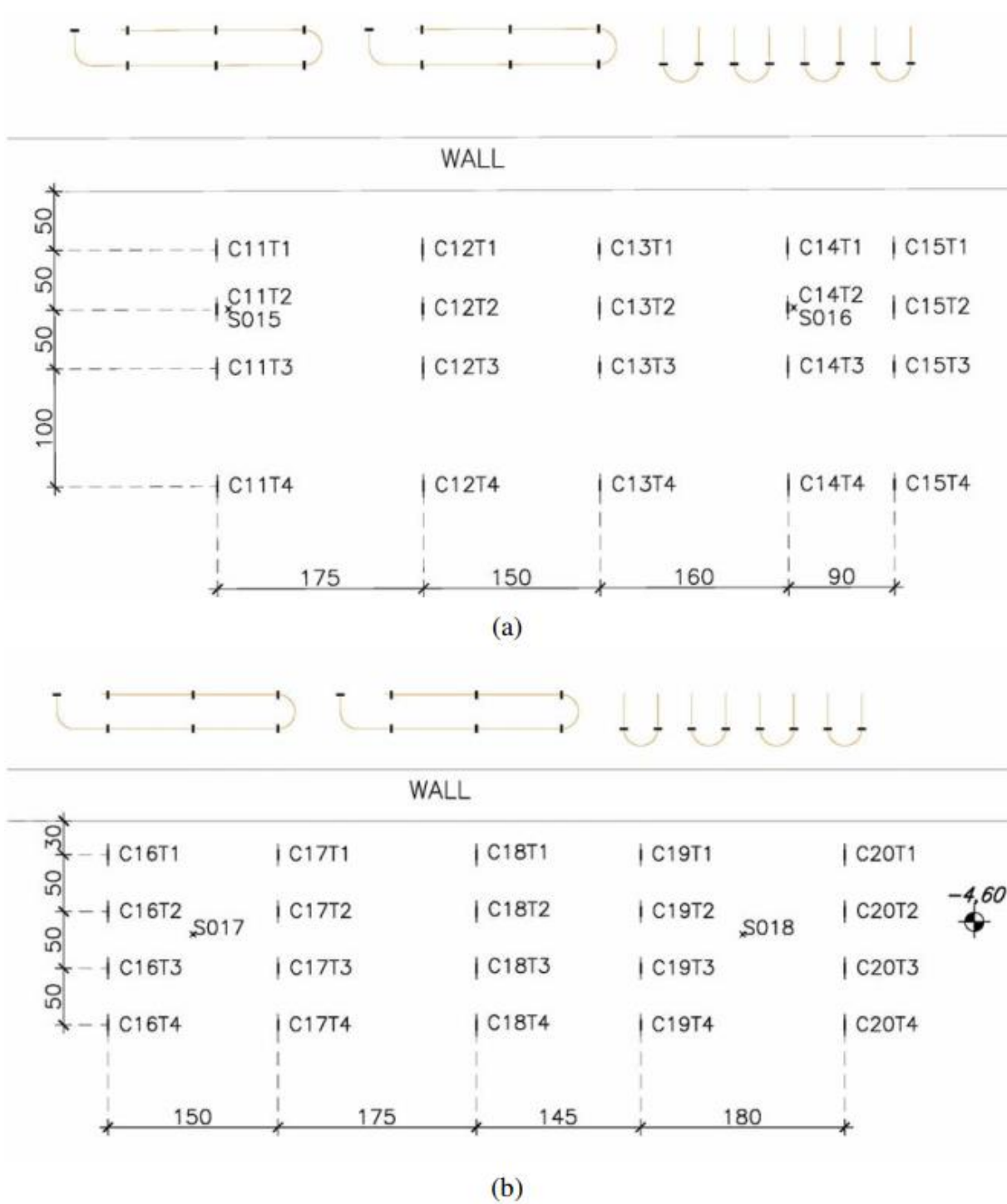


Figure 4.15: Temperature sensor location on (a) Plane C and (b) on Plane D along with their codification. Also some hygrometer sensors nominated as S0xx are depicted (Baralis and Barla, 2019)

## 4.2. Experimental results

The ground heat exchangers installation, together with the thermo-hydro-mechanical monitoring system, was completed in July 2019. The hydraulic circuit was completely saturated with the water-glycol mixture in August 2019 and thus the experimental campaign started in September 2019.

For this thesis, a set of 6 different tests in heating mode were analyzed from the end of January to the beginning of May. These results particularly illustrate the thermal performances of the installation, the ground thermal affection and the mechanical actions on the wall. Test information can be found in Table 4.3. The tests cover a variety of possible configuration from the heat exchanger geometry point of view. In fact, the links between different circuits in all tests were parallel, but the various number of circuits and different sets of circuits employed was performed. The thermal performances during the tests conducted with different couples of circuits (1 and 2, 1 and 3, 2 and 3) allow to comparatively define the more efficient solution from the thermal point of view. Besides, the activation of single, double or triple circuits will enable to test the relevance of thermal interference among neighboring modules.

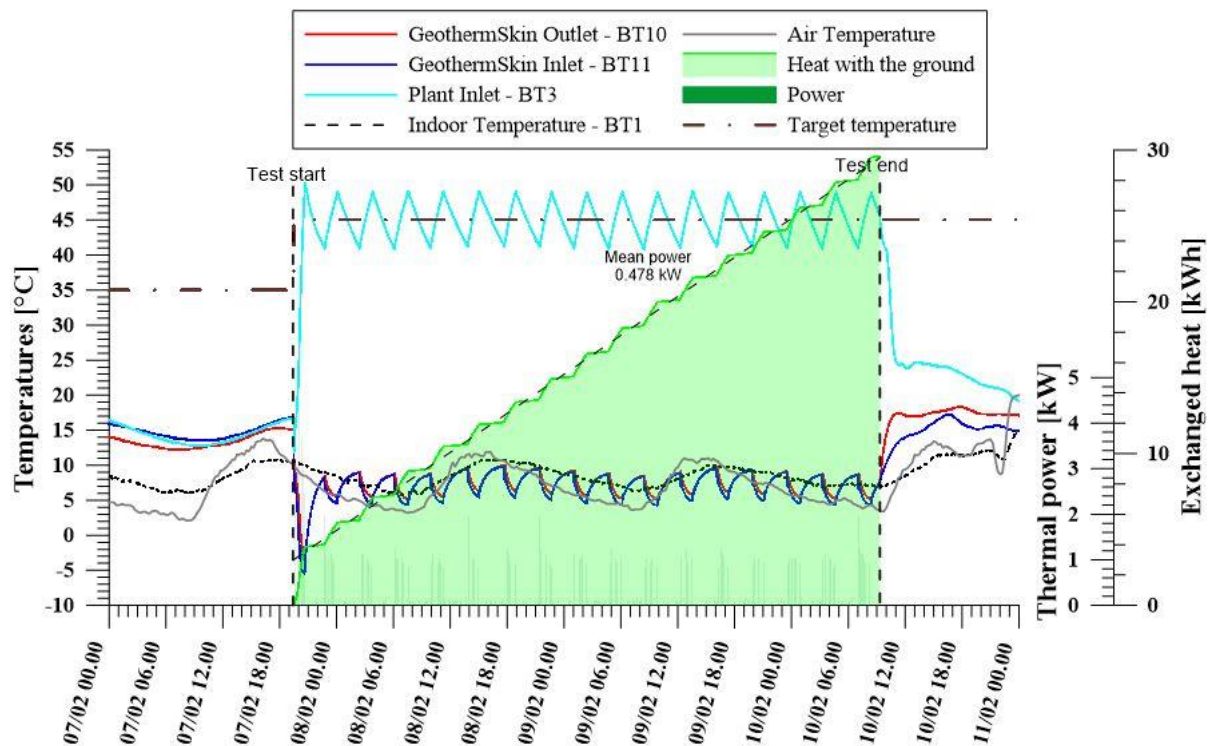


Figure 4.16: Thermal performance of experimental  $H_{2+3}_{20200207\_20200210}$  with parallel link of circuit 2 and 3 in heating mode.

Although the heat carrier fluid circulation is continuous, the thermal cycle operates discontinuously, so the parametrization of target temperature should be considered carefully in

order to optimize the overall system performances. Discontinuous thermal cycle is driven by the temperature of the fluid delivered to the fan coil user (namely BT3 in the Figure 4.16). The relationship between the cavaedium air temperature and the supply one was presented by means of a curve that can be adjusted manually on the heat pump, in which the thermal cycle starts when the difference between the calculated target temperature  $T_{target}$  and the real one  $T_{real}$  (the outlet temperature at user side, BT3) exceeds an imposed value in specific time.

$$DegreeMinute = \sum (T_{real} - T_{target}) \cdot t \quad (4.1)$$

Table 4.3: List of tests carried out

| No   | Test code                   | Link (**) | Starting time       | Ending time         | Duration | Target Temp |
|--|-----------------------------|-----------|---------------------|---------------------|----------|-------------|
|  |                             |           |                     |                     | [h]      | [°C]        |
| 1  | H_1+2_20191220_20200113 (*) | P         | 20/12/2019<br>19.30 | 13/01/2020<br>10.53 | 567.4    | 45          |
| 2  | H_1+2_20200131_20200203     | P         | 31/01/20<br>18.00   | 03/02/20<br>09.20   | 63.3     | 35          |
| 3  | H_2+3_20200207_20200210     | P         | 07/02/20<br>19.30   | 10/02/20<br>09.20   | 61.8     | 45          |
| 4  | H_1+3_20200214_20200217     | P         | 14/02/20<br>19.20   | 17/02/20<br>9.20    | 62.0     | 45          |
| 5  | H_1+3_20200221_20200224     | P         | 21/02/20<br>18.04   | 24/02/20<br>10.04   | 64.0     | 45          |
| 6  | H_1+2+3_20200228_20200302   | P         | 28/02/20<br>18.40   | 02/03/20<br>9.25    | 62.8     | 45          |
| 7  | H_1_20200305_20200507       | -         | 05/03/20<br>19.25   | 07/05/20<br>10.00   | 1502.6   | 45          |
| (*): Tests taken from Baralis and Barla (2019)<br>(**): The letter P indicates an in parallel connection. Tests are identified with the first letter "H" indicating the heating and the following numbers indicate the activated heat exchangers (Circuit 1, 2 or 3) |                             |           |                     |                     |          |             |

#### 4.2.1. Energy wall thermal performance

Monitoring systems allowed to determine the thermal performance during different tests in terms of instantaneous and mean exchanged thermal power, temperature range of the inlet and outlet of the system. The heat losses in the main collector/distributor pipes in the cavaedium can be neglected because of the small temperature gradient between the heat carrier fluid and the cavaedium ambient temperature, together with the complete and heavy insulation of the pipes. As a result, these temperatures mentioned above should be taken into account as outlet and inlet of the heat pump.

One example of experimental interpretation of test H\_2+3\_20200207\_20200210 (Test 3) with parallel link of circuit 2 and 3 in heating mode is showed in Figure 4.16 in order to see thermal performance of the system. Heat exchange is calculated on the basis of the temperature difference at the inlet and outlet ends of the ground loop, according to Equation 4.2:

$$q = Q \cdot \rho_f \cdot c_f \cdot (T_{in} - T_{out}) \quad (4.2)$$

where Q is the flow rate, registered by the flow meter mounted on the main collector pipe,  $\rho_f$  is the unit weight of the fluid,  $c_f$  is its specific heat capacity,  $T_{in}$  and  $T_{out}$  are the inlet and the outlet heat pump temperatures on the ground loop respectively. All parameters used for the interpretation are listed in Table 4.4.

These values are referred to the mixture of the propylene glycol to water mixture at the specified proportions in volume and considering the mean temperature of the fluid of 8 °C. The dependency of the unit weight and the specific heat capacity was neglected due to the limited temperature ranges experienced. As regards system performance, instantaneous heat exchange rate peak value was recorded during the initial heating ramp and was equal to 5.25 kW, corresponding to a temperature difference of 5.1 °C. Beside this starting point of the ramp, maximum heat exchange rate was 2.15 kW corresponding to a temperature change of 2.1 °C. During the compressor activation phase, the power generated was about 1-1.4 kW (as clearly shown in Figure 4.16). However, the main interest is to define the mean thermal power that can be exchanged by the system. This can be evaluated as the ratio of the total amount of heat provided by the system over the test time as in Equation 4.3:

$$q_{mean} = \frac{\int_{t_{start}}^{t_{stop}} q dt}{t_{stop} - t_{start}} = \frac{\sum q \cdot \Delta t}{t_{stop} - t_{start}} \quad (4.3)$$

Where  $t_{start}$  and  $t_{stop}$  are the start and ending times of the test respectively and q is calculated according to Equation 4.2 for each time step. This means that power can also be interpreted as the slope of the interpolating line of the cumulated exchanged energy depicted in Figure 4.16. In the test, mean thermal power reached the approximate value of 478 W, then the heat exchange rate was computed by the ratio of the mean thermal power and the area of activated circuits (11.5 m<sup>2</sup> per each circuit). Table 4.5 reports the heat exchanges for the tests carried out. Detailed information and graphs regarding the tests carried out are extensively reported in Appendix A.

Table 4.4: Parameters' values for calculation of heat exchange rate in experiment

H\_2+3\_20200207\_20200210

| Quantity                              | Value   |
|---------------------------------------|---------|
| Propylene Glycol to water mixture [%] | 25      |
| Flow rate [l/s]                       | 0.26    |
| Unit weight [kg/m <sup>3</sup> ]      | 1028.31 |
| Specific heat capacity [kJ/kg°C]      | 3.889   |

Table 4.5: Thermal performances of the energy wall from experimental results interpretation

| No | Test code                   | Flow rate<br>[l/h] | Peak  |              | Average |                     |
|----|-----------------------------|--------------------|-------|--------------|---------|---------------------|
|    |                             |                    | Power | Temp. change | Power   | Exchange rate       |
|    |                             |                    | [kW]  | [°C]         | [kW]    | [W/m <sup>2</sup> ] |
| 1  | H_1+2_20191220_20200113 (*) | 910.0              | 2.13  | 2.1          | 0.492   | 21.39               |
| 2  | H_1+2_20200131_20200203     | 925.0              | 2.67  | 2.6          | 0.333   | 14.48               |
| 3  | H_2+3_20200207_20200210     | 925.8              | 2.26  | 2.2          | 0.478   | 20.78               |
| 4  | H_1+3_20200214_20200217     | 282.0              | 1.75  | 5.6          | 0.115   | 5.00                |
| 5  | H_1+3_20200221_20200224     | 930.7              | 2.48  | 2.4          | 0.445   | 19.35               |
| 6  | H_1+2+3_20200228_20200302   | 1006.0             | 2.46  | 2.2          | 0.476   | 13.80               |
| 7  | H_1_20200305_20200507       | 713.4              | 3.25  | 4.1          | 0.363   | 31.57               |

(\*): tests taken from Baralis and Barla, 2019

Based on the Figure 4.17, in terms of mean heat exchange rates, the results from different tests in the case circuits with different pipe main direction are almost the same. It is evident that the heat rates were approximately 20 W/m<sup>2</sup> when comparing three tests of Test 1 (both circuits 1 and 2: horizontal), Test 3 (circuit 2: horizontal, circuit 3: vertical) and Test 5 (circuit 1: horizontal, circuit 3: vertical) which were conducted in similar conditions (similar values of flow rate, the same properties of fluid, target temperature of 45 °C). Furthermore, the same results of two latter tests which included two circuits with the same direction deployment, but different positions also showed that the heat exchange rate is independently from position of circuits.

On the other hand, Test 2 was also conducted in similar conditions with Test 1, but the target temperature was lower with 35 °C compared to 45 °C of the latter. The heat rate of this test was around 5 W/m<sup>2</sup> smaller than that of the Test 1, which can be explained by considering the temperature range of the fluid in the heat exchanger. Baralis and Barla (2019) conducted the Test H\_1+2 in three different values of target temperatures which were 35 °C, 45 °C as mentioned above and 55 °C for the other one. In Figure 4.18, temperature ranges of the brine

in the heat exchanger are almost stable, independently from the temperature to be delivered to the user, which is presented by the blue and green line in Figure 4.18. Indeed, tests carried out with circuit 1 and 2 with parallel connection in heating mode highlight only slight differences in the thermal range. However, this slight difference also led to a decrease in heat rate. As a result, this finding might suggest that the expected temperature at user side plays an important role in the heat exchange rate of the system: the higher is the target temperature, the bigger is the amount of heat rate exchanged.

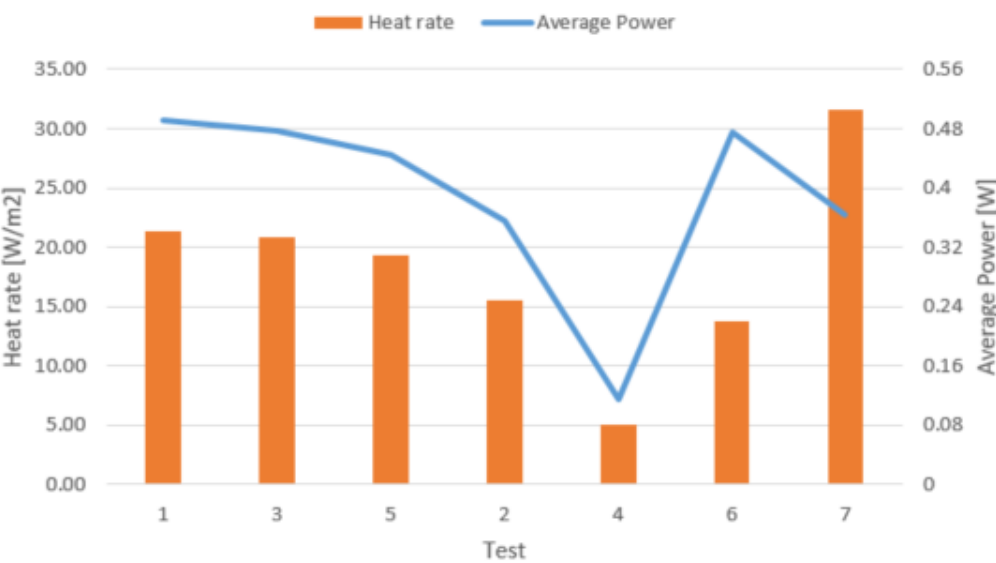


Figure 4.17: Thermal performance comparison of different tests

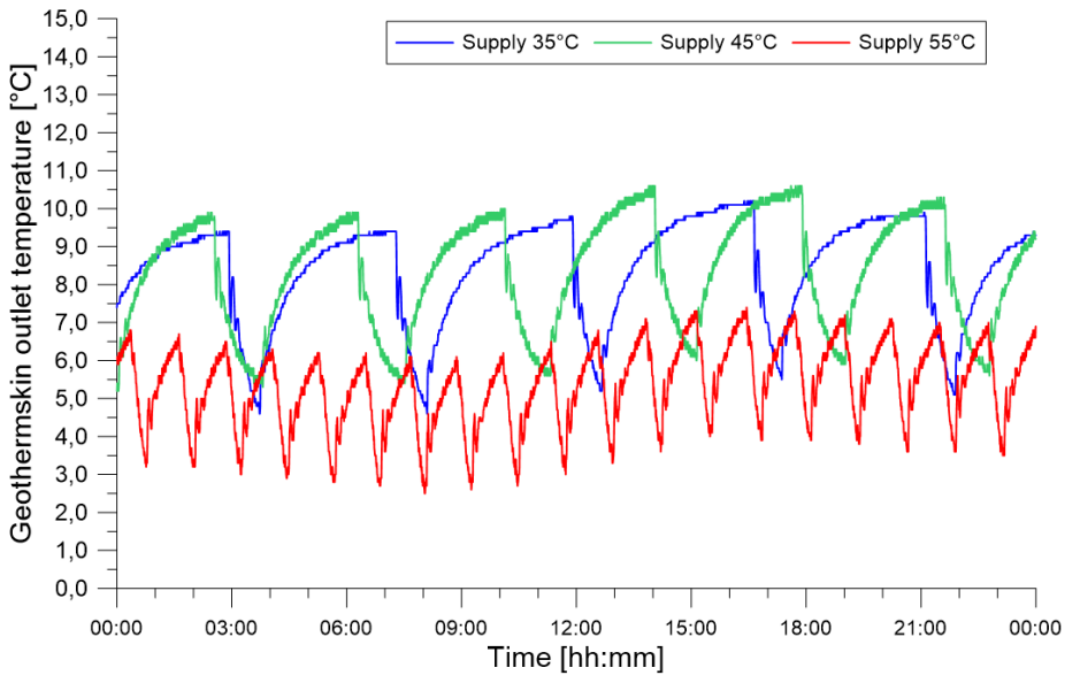


Figure 4.18: Comparison of thermal levels in heating tests depending on the supply temperature (Baralis and Barla, 2019)

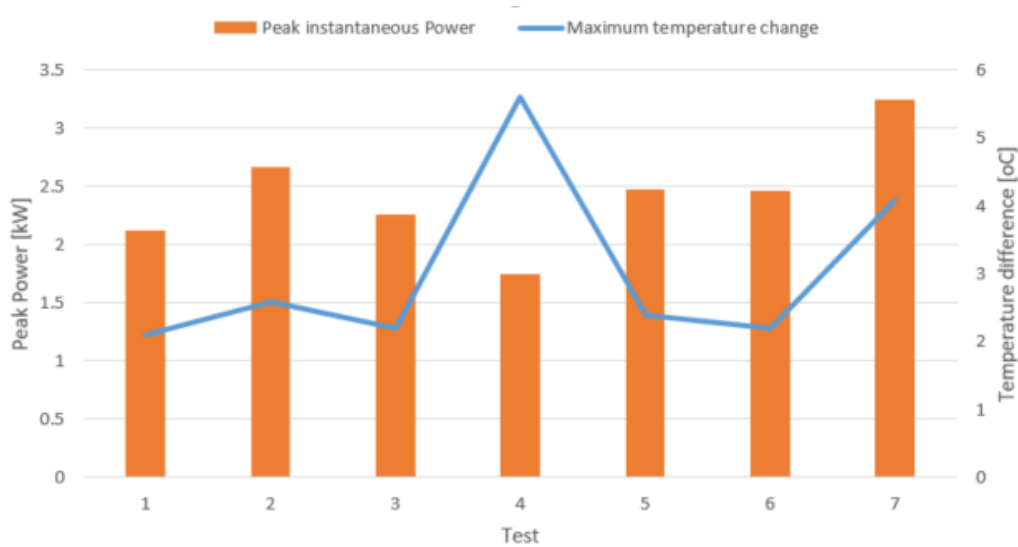


Figure 4.19: Peak power with respect to maximum temperature change in several tests.

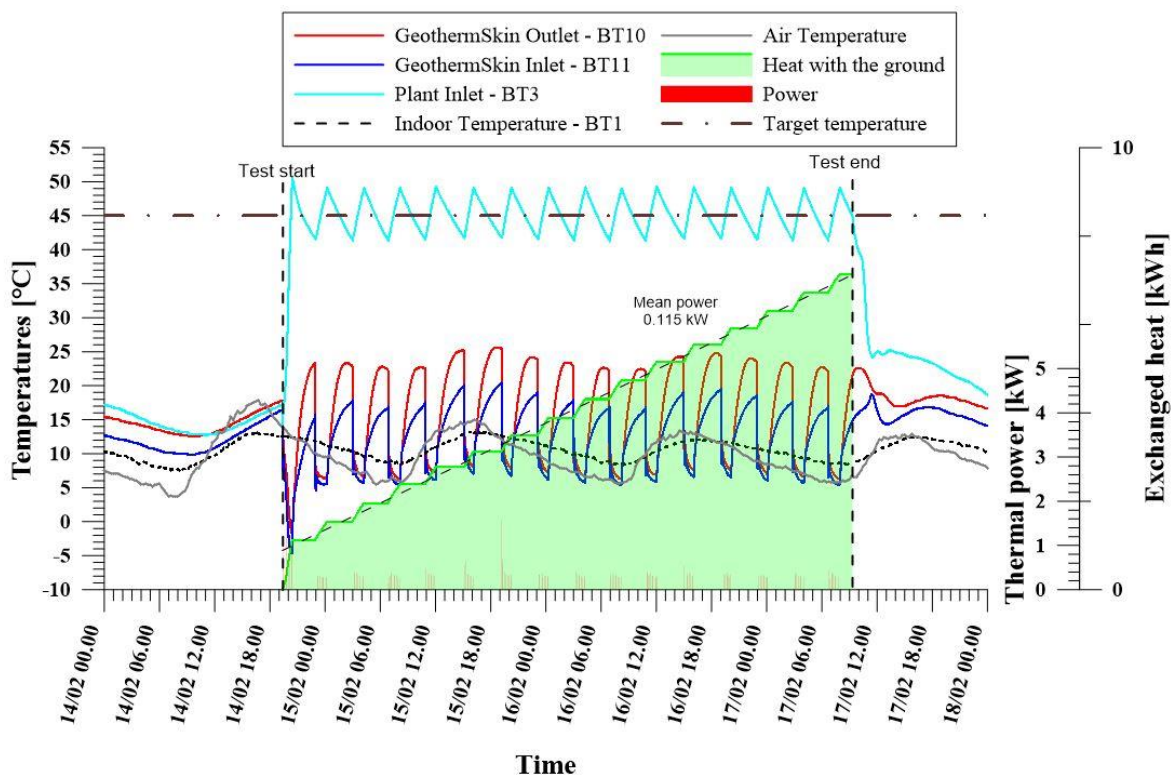


Figure 4.20: Thermal performance interpretation of experimental test

H\_1+3\_20200214\_20200217 with parallel link of circuit 1 and 3 in heating mode

Regarding Test H\_1+3\_20200214\_20200217 (Test 4), maximum heat exchange rate was only 1.75 kW although a temperature change was biggest in all tests, comprising 5.6 °C, while these values of other tests were virtual identical, with more or less 2.4 kW and 2.6 °C (Figure 4.19). During the compressor activation phase the power generated is about 0.4-0.8 kW (as clearly shown in Figure 4.20). Furthermore, its heat rate was significantly smaller than those of others, accounting for only 5 W/m<sup>2</sup>. These much smaller values resulted from the much lower flow

rate with only 282 l/s in comparison with more than 900 l/s of other tests. As a conclusion, the thermal performance is significantly affected by flow rate.

Results from Test H\_1+2+3\_20200228\_20200302 (Test 6) with the activation of three circuits showed an identical average power with respect to those of other tests with two activated circuits, but the larger activated area of three circuits led to a decrease in the heat rate. Similarly, although the average power of Test H\_1\_20200305\_20200507 (Test 7) was lower than those of other tests due to a smaller value of flow rate, the heat rate obviously increased because of the small activated area of one circuit. This finding might be associated with heat flux as a function of the pipe length, it can be observed that: (i) pipes of different lengths and same inlet and outlet locations exchange the same heat flux, and also: (ii) pipes of the same length but different distance between inlet and outlet exchange the same heat flux (Sterpi et al., 2014). For example, Test H\_1+3 and Test H\_2+3 (Test 3 and Test 5) have the same pipe length, different position of inlet and outlet, but the heat flux in both tests witnessed little difference which may be due to the difference of time period. Another example is the comparison of Test H\_1+3 and Test H\_1+2+3 (Test 5 and Test 6), they have the same position of inlet and outlet, different pipe length, but the heat flux in both tests were similar with a slightly larger value belonging to Test 6 due to its slightly higher flow rate. In conclusion, in order to reduce the initial investment cost, but still assure a sufficient heat exchange rate, the less number of circuits or even single circuit should be used rather than using more circuits with parallel linking if all other conditions are the same.

Mean thermal power values were normalized by the wall area interested by each circuit. In particular, the shallower portion of the wall that was not equipped with the heat exchanger was computed too. The inclusion of this area leads to conservative evaluation of the heat exchange rate. Results show a thermal efficiency of about 13-22 W per unit area in heating mode. It is clear in Figure 4.21, these values are almost consistent with previous literature referred to classical energy wall (15 W/m<sup>2</sup> of Bourne-Webb et al. (2016), around 20 W/m<sup>2</sup> of Di Donna et al. (2016), 14 W/m<sup>2</sup> of Sterpi et al. (2018)), except the result of Test 7 which is also in line with the suggested value for feasibility studies of Brandl (2006).

The thick concrete wall has a significant thermal resistance, the hydraulic circuit is not directly connected to the external facade as the support system ensures a minimum distance (about 5 cm) and soil is interposed between the circuit and the wall. As a result, the heat flux towards the inner facade of the wall seemed to be relatively small and negligible, there was no measurement there.

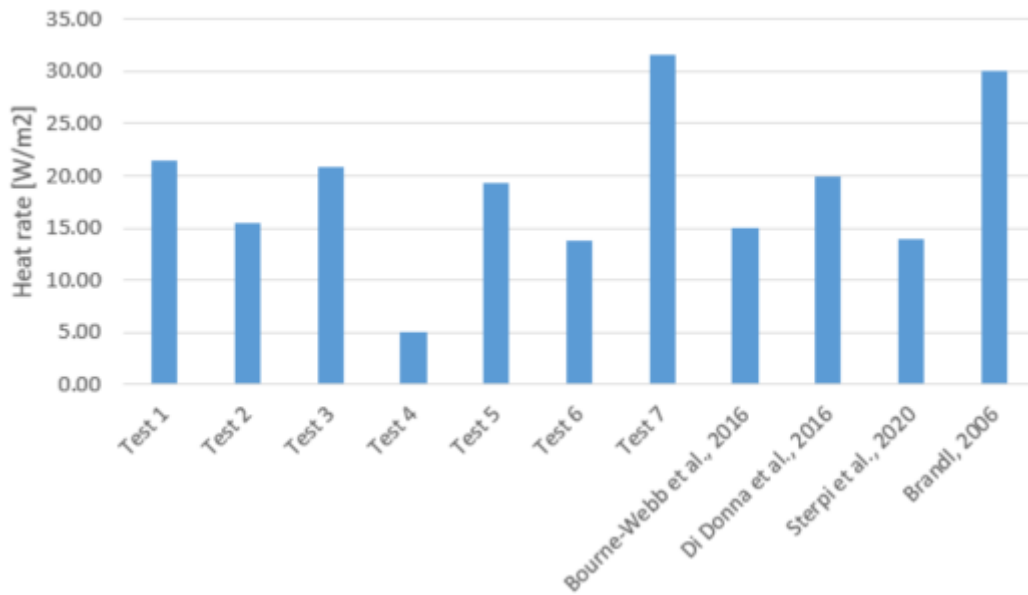


Figure 4.21: Heat rates of different tests in comparison with previous literature

#### 4.2.2. The impact of GeothermSkin on the surrounding ground

As mentioned in Chapter 2, geothermal systems use the subsurface as a heat source/sink depending on the operative mode. Injection or extraction of thermal energy thus can negatively impact on the temperatures at the site, affecting the resource either in the short or the long term. Source affection can be concisely represented by the heat plume generated. Thus the characterization of its magnitude, extension and position plays an important role in design process of geothermal structures.

##### *a/ Thermal impact of GeothermSkin system*

An extensive network of PT-100 sensors was installed in the experimental site with the sensors deployment being presented in previous paragraphs. All data resulting from the experimental campaign has been collected, processed and reported in Appendix A. Some typical and representative results only are shown in this part, in particular reported results refer to Test H\_2+3\_20200207\_20200210 (Test 3).

As it can be seen from Figure 4.22, the ground temperature is more stable than the outdoor air temperature. At shallower depths and at the nearest location to the wall (C2T1, C12T1), daily temperature of the ground fluctuated slightly. In contrast, at bigger distances from the cold boundaries (upper surface and wall facade, like C2T4, C12T4), the temperature trend kept almost unchanged during the whole test. During the experimental campaign in heating mode, the mean thermal level resulted to be hotter at higher depths, which was clearly indicated by comparing the records of paired sensors on string 2 and string 12 that are located at same

planimetric position but different depths (0.75 m and 3.35 m below ground surface respectively). On the other hand, the ground temperature experienced a slight decrease by the thermal activation (the small difference in temperature between the starting point and ending point).

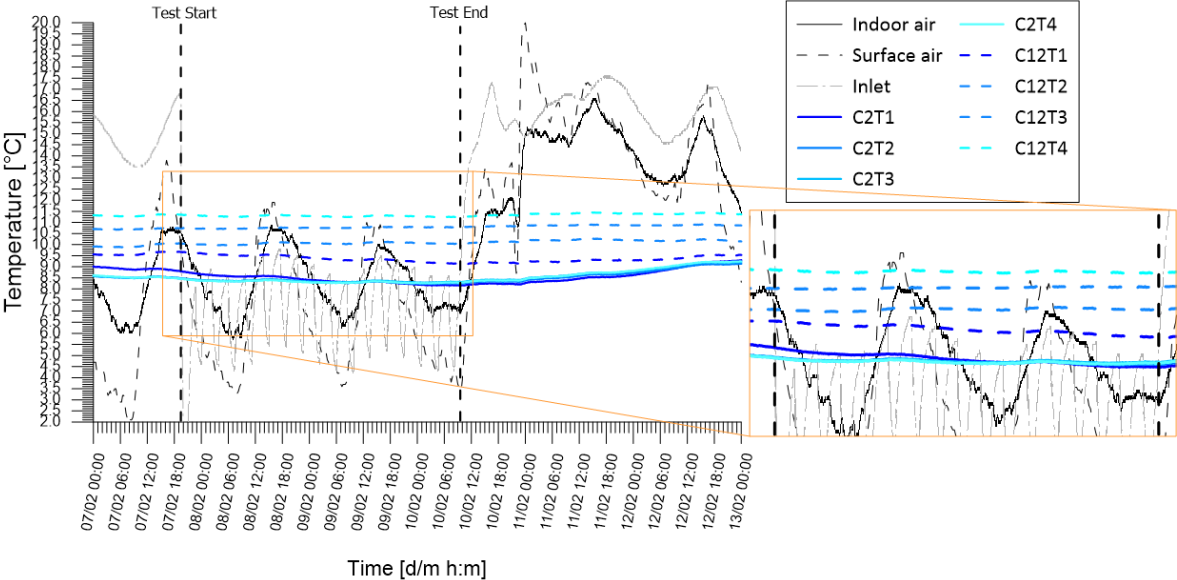


Figure 4.22: Thermal records along string 2 (plane A) and string 12 (plane C) during experiment H\_2+3\_20200207\_20200210

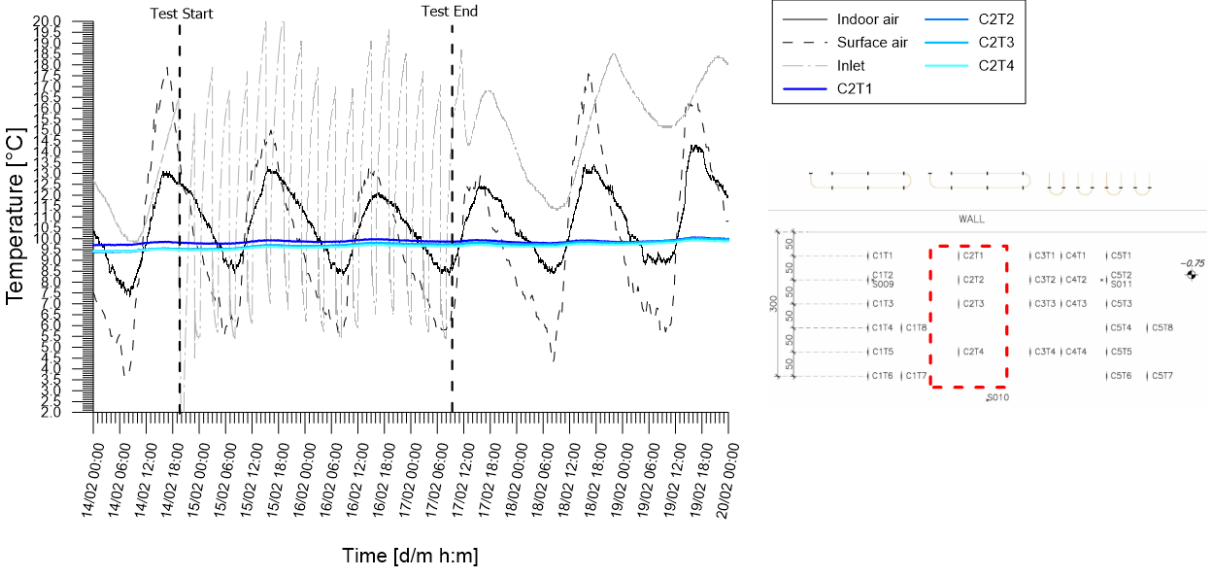


Figure 4.23: Temperatures records from chain 2 of experimental test H\_1+3\_20200214\_20200217

Regarding Test 4, the inlet temperature of circuit in this test changed significantly overtime. As in Figure 4.23, this temperature change ranged from 5 °C to more than 20 °C, 15 °C of difference was much higher than those of the Test 3 or Test 5 with only 5 °C changes for both of them.

Furthermore, the maximum temperature of inlet of circuit in Test 4 was about 10 °C higher than those of others, which resulted in the lower amount of heat carried by the fluid. However, the effect of thermal system on the ground temperature in this case was also minor because the temperature kept almost unchanged during the test as illustrated in Figure 4.23.

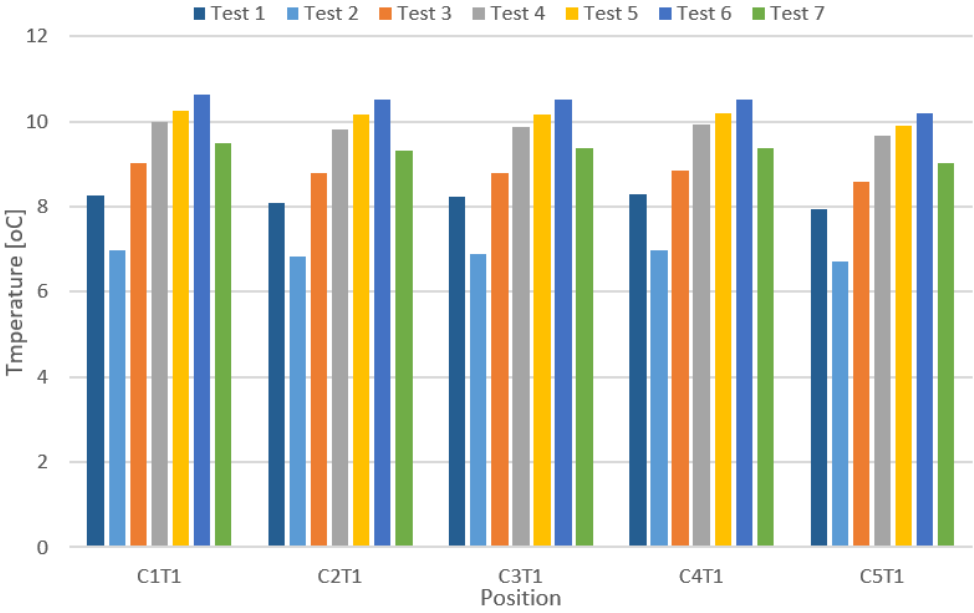


Figure 4.24: Ground temperature at the beginning of tests in different positions near along the wall

Figure 4.24 shows that ground temperatures at the beginning of tests were the same in different positions near along the wall. These temperatures varied between different tests which means that they changed in time due to the affection of environment. Furthermore, the temperature change during the test is reported in Figure 4.25, where it is clear that the variations of the ground temperature in all tests were similar in different positions. Additionally, the ground temperature of Test 4 and 5 was unchanged, while a small change of around 0.5 °C was recorded in Test 2, 3 and 6. In contrast, the ground temperature of Test 1 and 7 experienced a significant change with about 2.5 °C and 10 °C respectively, however this seems to result from the affection of the external temperature and environmental affection such as rainfall as these tests were operated in a long period of time (around 24 and 63 days respectively).

Thus, the experimental results seem to suggest that there is a minor impact or even no influence on the ground temperature exerted by the system when it is used in heating mode during winter season. As a result, the thermal status of the ground is virtually equal to the undisturbed conditions.

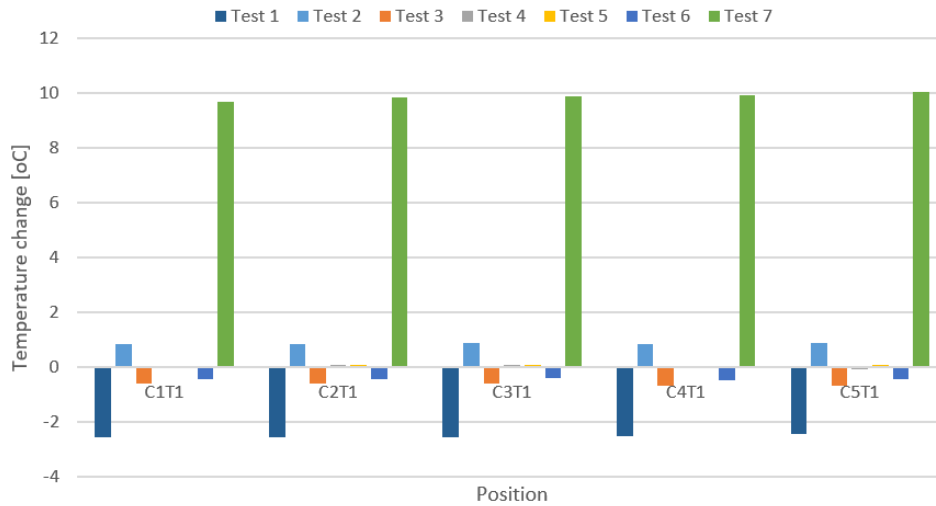


Figure 4.25: Temperature change between the beginning and the end of tests in different positions

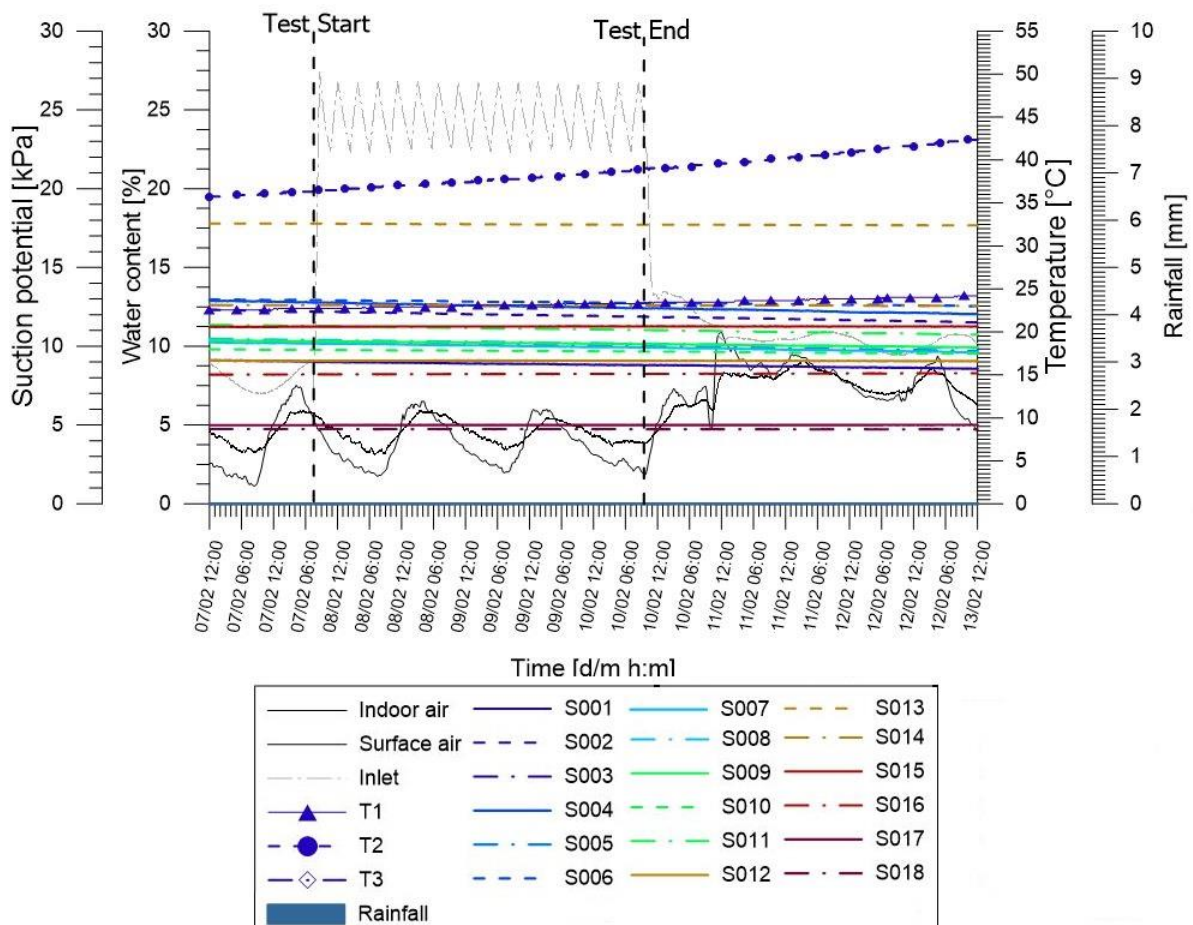


Figure 4.26: Volumetric water content and suction potential records from test H\_2+3\_20200207\_20200210

#### *b/ Impact on the ground partial saturation*

Due to the low influence also from the thermal point of view, there was also no significant alteration caused by the thermal activation on the hygrometric equilibrium of the ground near the wall. It can be clearly seen from Figure 4.26 that the water content seemed to be virtually unaffected by any external influence. Furthermore, the absence of water infiltration due to rainfall led to a limited volumetric water content, slightly decreasing in time. Additionally, the water content felt with depth with 5% at the base of the wall and around 10% at plane A (0.75 m below ground surface). Similarly, the water tension witnessed little rise recorded by the tensiometers, with the difference of 2 kPa compared to the start of the test.

#### **4.2.3. Structural effects on the wall**

Similar to the environmental aspects, the structural impact of thermal system on the supporting wall structure seemed to be extremely low. Data collected by strain gauges and pressure cells of the monitoring system revealed an extremely low change due to the thermal activation. In Figure 4.27, all strain gauges and pressure cells rose slightly at the beginning of test and almost remained unchanged later, even backed to the original values after the halt of test. As a result, it can be considered that there was no influence of thermal system on the wall in terms of structural effects. This finding is confirmed by the rest of the experimental campaign (see Appendix A), in which both stress and strain were almost stable during the test duration, except some cases witnessing variations due to the rainfall affection. It is clearer in Figure 4.28, the impact in term of deformation is extremely limited (from almost null to a maximum of about 90  $\mu\epsilon$ , excluding Test 7). Also stresses variations are extremely limited (from 40 to 200 kPa), confirming that the impact that is exerted on the wall because of the thermal activation is minor. This evidence seems to suggest that from the technical point of view, structural design of such structures might be carried out without taking into consideration the application of the GeothermSkin system. Associating with all comments above, collected data suggest that no relevant impacts are exerted by the system both from the wall structural point of view and on the surrounding ground.

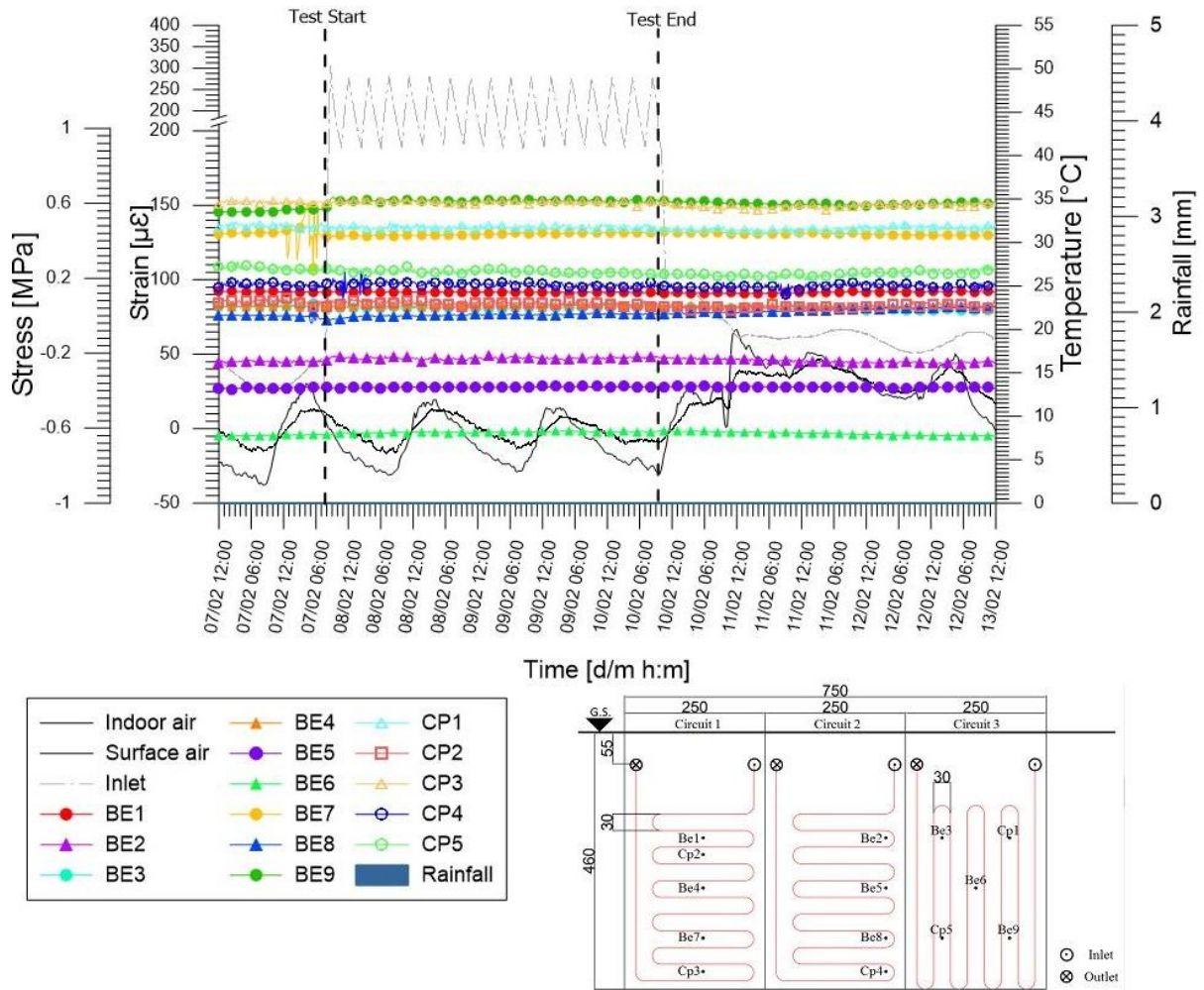


Figure 4.27: Strain gauges and pressure cells records from test H\_2+3\_20200207\_20200210

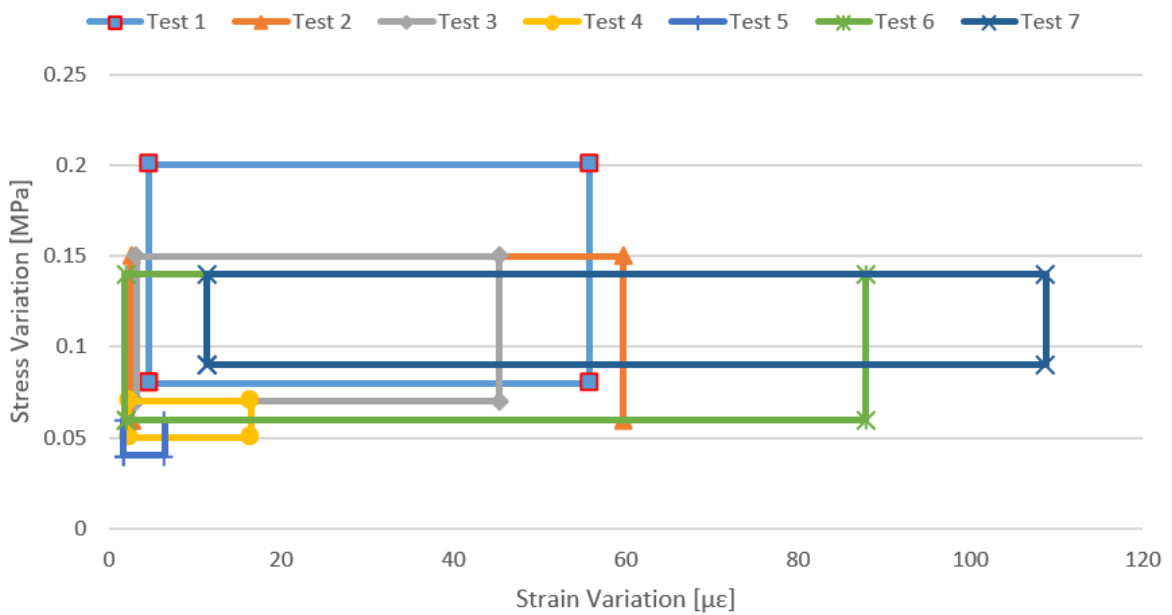


Figure 4.28: Stresses and strain variations induced by GeothermSkin thermal activation during the heating experimental campaign.

## 5. Chapter 5: NUMERICAL MODELLING

### 5.1. Thermal-Hydraulic-Mechanical Analysis

A numerical modeling of coupled thermo-hydro-mechanical (THM) analysis is required in order to predict the distribution of stresses, strains, displacements and interstitial pressure around an energy geostructure.

Energy geostructures are made up of elements in reinforced concrete, such as piles, foundation slabs, walls. They are not only subjected to a mechanical component of stress given by the load, but they are also able to exchange heat with the surrounding environment. The three aspects, thermo-hydro-mechanical, are coupled since the variations of the solid volume are influenced by the presence of temperature gradient, the heat exchanged depends on the presence of water flow, the density of the water varies with the heat load and the mechanical response of the materials depends both on the fluid pressure (effective stress) and on the variation in temperature. All the equations that governs a THM analysis will be introduced:

- Mechanical field:
  - Equilibrium equations
  - Congruence equations
  - Constitutive laws
- Hydraulic field:
  - Mass conservation equation
  - Darcy's laws
- Thermal field:
  - Energy conservation equation
- Boundary conditions

#### 5.1.1. Mechanical field equations

- Equilibrium equations

Timoshenko and Goodier (1951) equations must be satisfied by the soil:

$$\text{div}(\sigma_{ij}) + \rho g_i = 0$$

Where the div operator is the divergence,  $\sigma_{ij}$  is the tensor of the total stresses,  $g_i$  the gravity vector and  $\rho$  the density of the material, which includes the density of the water  $\rho_w$  and the solid particles  $\rho_s$ .

The definition of effective stress allows to consider the hydraulic component, thus the hydro-mechanical coupling is introduced and the equation is transformed as:

$$\text{div}(\sigma'_{ij}) + \nabla p_w + \rho g_i = 0$$

$\nabla$  is the gradient,  $p_w$  the pore water pressure and  $\sigma'_{ij}$  the effective stress tensor that can be written in incremental form by introducing the constitutive law.

➤ Compatibility equations

The deformations  $\varepsilon$  can be written in terms of displacements  $u$  along  $x$  axis, displacement  $v$  along  $y$  axis and displacement  $w$  along  $z$  axis:

$$\begin{aligned}\varepsilon_x &= \frac{\partial u}{\partial x}; \varepsilon_y = \frac{\partial v}{\partial y}; \varepsilon_z = \frac{\partial w}{\partial z} \\ \gamma_{xy} &= \frac{\partial u}{\partial y} + \frac{\partial v}{\partial x}; \gamma_{yz} = \frac{\partial v}{\partial z} + \frac{\partial w}{\partial y}; \gamma_{zx} = \frac{\partial w}{\partial x} + \frac{\partial u}{\partial z}\end{aligned}$$

Since deformations are a function of only three displacements, these are not independent. Mathematically it can be demonstrated that for the existence of a compatible displacement field, all the above mentioned deformation components and their derivatives must exist and be continuous for at least the second derivative.

➤ Constitutive laws

In order to obtain a solution for the system, other equations must be introduced: constitutive laws relate stresses to strains. For an elastic material, they are:

$$\begin{aligned}\sigma_x &= \frac{E \left[ (1-\nu)\varepsilon_x + \nu\varepsilon_y + \nu\varepsilon_z \right]}{(1+\nu)(1-2\nu)} \\ \sigma_y &= \frac{E \left[ (1-\nu)\varepsilon_y + \nu\varepsilon_x + \nu\varepsilon_z \right]}{(1+\nu)(1-2\nu)} \\ \sigma_z &= \frac{E \left[ (1-\nu)\varepsilon_z + \nu\varepsilon_x + \nu\varepsilon_y \right]}{(1+\nu)(1-2\nu)} \\ \tau_{xy} &= G\gamma_{xy}; \tau_{yz} = G\gamma_{yz}; \tau_{zx} = G\gamma_{zx}\end{aligned}$$

Where, for homogeneous, linear, isotropic, elastic materials,  $E$  is Young's modulus,  $\nu$  is the Poisson coefficient, while  $G$  is the Lamè constant (shear modulus).

In order to consider the thermal coupled effects, the vector form is introduced:

$$d\sigma'_{ij} = C_{ijkl} (d\varepsilon_{kl} + d\varepsilon^T_{kl})$$

Where  $C_{ijkl}$  is the stiffness matrix composed by 36 elements, which can be written in function of only  $E$  and  $\nu$  in case of isotropic, linear, elastic material:

$$C_{ijkl} = \frac{E(1-\nu)}{(1+\nu)(1-2\nu)} \begin{bmatrix} 1 & \frac{\nu}{1-\nu} & \frac{\nu}{1-\nu} & 0 & 0 & 0 \\ \frac{\nu}{1-\nu} & 1 & \frac{\nu}{1-\nu} & 0 & 0 & 0 \\ \frac{\nu}{1-\nu} & \frac{\nu}{1-\nu} & 1 & 0 & 0 & 0 \\ 0 & 0 & 0 & \frac{1-2\nu}{2(1-\nu)} & 0 & 0 \\ 0 & 0 & 0 & 0 & \frac{1-2\nu}{2(1-\nu)} & 0 \\ 0 & 0 & 0 & 0 & 0 & \frac{1-2\nu}{2(1-\nu)} \end{bmatrix}$$

Thermal deformation is defined as:

$$d\varepsilon_{kl}^T = \beta_{kl} dT$$

Where  $\beta$  is the linear coefficient of thermal expansion [ $^{\circ}\text{C}^{-1}$ ] and  $dT$  is the temperature increment.

### 5.1.2. Hydraulic field equations

➤ Mass conservation equation

The mass conservation equation was obtained using some theorems of fluid mechanics and using Darcy's law. The latter describes the motion of a fluid within a porous material and it is expressed as:

$$\vec{v} = -K \vec{\nabla} h$$

$v$  is the velocity,  $K$  the permeability of the soil and  $\vec{\nabla} h$  the hydraulic load.

The mass conservation equation in transitory conditions can be mathematically described by Poisson's equations:

$$K \left( \frac{\partial^2 h}{\partial x^2} + \frac{\partial^2 h}{\partial y^2} + \frac{\partial^2 h}{\partial z^2} \right) = \frac{\partial \varepsilon_v}{\partial t}$$

$\varepsilon_v$  is the volumetric deformations.

If the conditions of stationary regime exist, the volume does not change over time and the previous equation is reduced to that of Laplace:

$$\left( \frac{\partial^2 h}{\partial x^2} + \frac{\partial^2 h}{\partial y^2} + \frac{\partial^2 h}{\partial z^2} \right) = 0$$

The latter one describes a decoupled problem, since there are no mutual influences between the mechanical problem and the hydraulic one, therefore the field of interstitial pressure can be

determined independently from the solution of the mechanical problem. In vector form, the Poisson equation becomes:

$$\begin{aligned} \text{div}(K\vec{\nabla}h) &= \frac{\partial \varepsilon_v^M}{\partial t} \\ K\vec{\nabla}^2 h &= \frac{\partial \varepsilon_v^M}{\partial t} \end{aligned}$$

Where the Laplacian operator  $\vec{\nabla}^2 h$  is defined as divergence of the gradient. Adding the thermal rate, the final equation is:

$$K\vec{\nabla}^2 h = \frac{\partial \varepsilon_v^M}{\partial t} + \frac{\partial \varepsilon_v^T}{\partial t}$$

Where the thermal deformation is defined as:

$$\varepsilon_v^T = 3\beta\Delta T$$

### 5.1.3. Thermal field equations

#### ➤ Energy conservation equation

The heat transmission is a complex phenomenon which involves many material properties where the transmission takes place. However, there are three different ways or better mechanisms of transmission, described in the following.

- Conduction is an energy transporting way which is proper of solid or liquid phase in a porous material, no fluid's macroscopic movement is required. Fourier's law governs this mechanism where the transfer of kinetic energy takes place from high temperature zones to the adjacent low ones, and the heat transfer [W/m<sup>2</sup>] expressed as:

$$q_{cond} = -\lambda\vec{\nabla}T$$

Where  $\lambda$  is the thermal conductivity of the material [W/mK] and  $\vec{\nabla}T$  is the temperature gradient. The sign “-“ is related to the way of decreasing temperatures.

- Convection happens through a fluid in movement, hypothesis of saturated material was made, always with different temperature; the transfer energy with macroscopic transportation is equal to:

$$q_{conv} = c_w \rho_w \vec{v}_w \Delta T$$

Where  $c_w$  is the specific heat of water [J/kgK] and  $\Delta T$  is the difference of temperature between the two systems.

- Radiation is the mechanism of transfer between two surfaces with different temperatures. Its contribution to heat transfer is minor, so it will not be taken into account in our analysis.

The equation of conservation of energy under steady-state conditions in the case of only conduction is provided by the Laplace equation:

$$\vec{\nabla}^2 T = 0$$

On the other hand, in the case of transitory conditions, always only by conduction, the mass conservation equation can be described mathematically by the Poisson equation:

$$\lambda \vec{\nabla}^2 T = \rho c \frac{\partial T}{\partial t}$$

The second member is the accumulation of heat and it is formed from:

$$\rho c = n \rho_w c_w + (1-n) \rho_s c_s$$

That is the specific heat of the soil in which water specific heat  $c_w$  and solid skeleton one  $c_s$  are included; Conduction and convection can be blended together and, in the case of transitory conditions, the final equation would be:

$$\lambda \vec{\nabla}^2 T + \text{div}(\rho_w c_w \vec{v}_w \vec{\nabla} T) - \rho c \frac{\partial T}{\partial t} = 0$$

#### 5.1.4. Boundary conditions

It is known that, to solve a problem that can be expressed in the form of differential equations, boundary conditions are necessary firstly to reproduce a real condition, secondly to reduce the unknowns to have a determinated system. The choice of the boundary condition is more important in our analysis in order to create an appropriate model and reduce costs, rather than the complicated and long-time calculation related to equations above or even may lead to the divergence of the solution or to the convergence to a wrong solution.

There are several types of boundary conditions:

##### ➤ Dirichlet Boundary Condition

This condition specifies the value that the unknown function needs to take on along the boundary of the domain. For example, the Laplace equation, the boundary value problem with the Dirichlet boundary conditions is written as:

$$\begin{aligned} \Delta \varphi(x) &= 0, \forall x \in \Omega \\ \varphi(x) &= f(x), \forall x \in \partial\Omega \end{aligned}$$

where  $\varphi$  is the unknown function,  $x$  is the independent variable (e.g. the spatial coordinates),  $\Omega$  is the function domain,  $\partial\Omega$  is the boundary of the domain, and  $f$  is a given scalar function defined on  $\partial\Omega$ .

➤ Neumann Boundary Condition

It specifies the values that the derivative of a solution is going to take on the boundary of the domain. For example, the Laplace equation, the boundary value problem with the Neumann boundary conditions is written as:

$$\Delta\varphi(x) = 0, \forall x \in \Omega$$

$$\frac{\partial\varphi(x)}{\partial n} = f(x), \forall x \in \partial\Omega$$

Where  $n$  is the unit normal to the boundary surface, if  $\Omega \subset \mathbb{R}^n$

➤ Robin Boundary Condition

It consists of a linear combination of the values of the field and its derivatives on the boundary. For example, the Laplace equation, the boundary value problem with the Robin boundary conditions is written as:

$$\Delta\varphi(x) = 0, \forall x \in \Omega$$

$$a\varphi(x) + b\frac{\partial\varphi(x)}{\partial n} = f(x), \forall x \in \partial\Omega$$

where  $a$  and  $b$  are real parameters. This condition is also called “impedance condition”.

➤ Mixed Boundary Condition

It consists of applying different types of boundary conditions in different parts of the domain. It is important to notice that boundary conditions must be applied on the whole boundary: the “free” boundary is anyway subjected to a homogeneous Neumann condition. The mixed boundary condition differs from the Robin condition because the latter consists of different types of boundary conditions applied to the same region of the boundary, while the mixed condition implies different types of boundary conditions applied to different parts of the boundary.

➤ Cauchy Boundary Condition

The Cauchy boundary condition is a condition on both the unknown field and its derivatives. It differs from the Robin condition because the Cauchy condition implies the imposition of two constraints (1 Dirichlet boundary condition + 1 Neumann boundary condition), while the Robin

condition implies only one constraint on the linear combination of the unknown function and its derivatives.

Particularly, boundary conditions are referred to:

- In mechanical field: displacements applied for given points (Dirichlet), stress and strain tensors and external loads applied for given points (Neumann)
- In hydraulic field: hydraulic conditions such as hydraulic head, or velocity or/and pressure to be taken by a certain set of nodes (Dirichlet), some constraints on the derivative of velocity or pressure fields (Neumann)
- In thermal field: surface at fixed temperature (Dirichlet), heat flux across the boundaries (Neumann).

## ***5.2. Numerical Modelling***

A numerical model was built to evaluate the thermal performance of GeothermSkin system, particularly all information of Test H\_2+3\_20200207\_20200210 (Test 3) could be applied for this model to make a comparison between the numerical result and the experimental result.

### **5.2.1. Calculation software**

In this thesis, the FEFLOW software was used to compute the Thermo-Hydro analyses. FEFLOW (Finite Element subsurface FLOW simulation system) is a computer program for simulating groundwater flow, mass transfer and heat transfer in porous media and fractured media. The program uses finite element analysis to solve the groundwater flow equation of both saturated and unsaturated conditions as well as mass and heat transport, including fluid density effects. The software was firstly introduced by Hans-Jörg G. Diersch in 1979. In 1992, FEFLOW became a registered trademark, after that FEFLOW has been developed further, continuously improved and extended as a commercial simulation package.

### **5.2.2. Geometry of the model**

The geometry of the model was created through the AutoCAD software (Figure 5.1.a) and imported DXF file into the FEFLOW software, then elements in CAD file can be converted into points, lines and polygons. As a result, based on these elements, numerical software can generate of the geometry of the domain (polygon elements) and of the heat exchange systems (line elements). The geothermal probes in which the heat transfer fluid circulates, were located on the outside surface of the wall, with a 5 cm of distance from the wall surface due to clamps. The external geometry of the 2D model was defined as follow: the edges of the 2D geometry

are located at a distance of 20 cm from the pipes. Furthermore, 10 m in the direction of the ground and 1.5 m towards the building were added in model from the wall to take into account for the effect of the ground and the air. Additionally, the model was limited to a depth of 15 m from ground surface, where the temperature is believed to keep unchanged throughout the year.

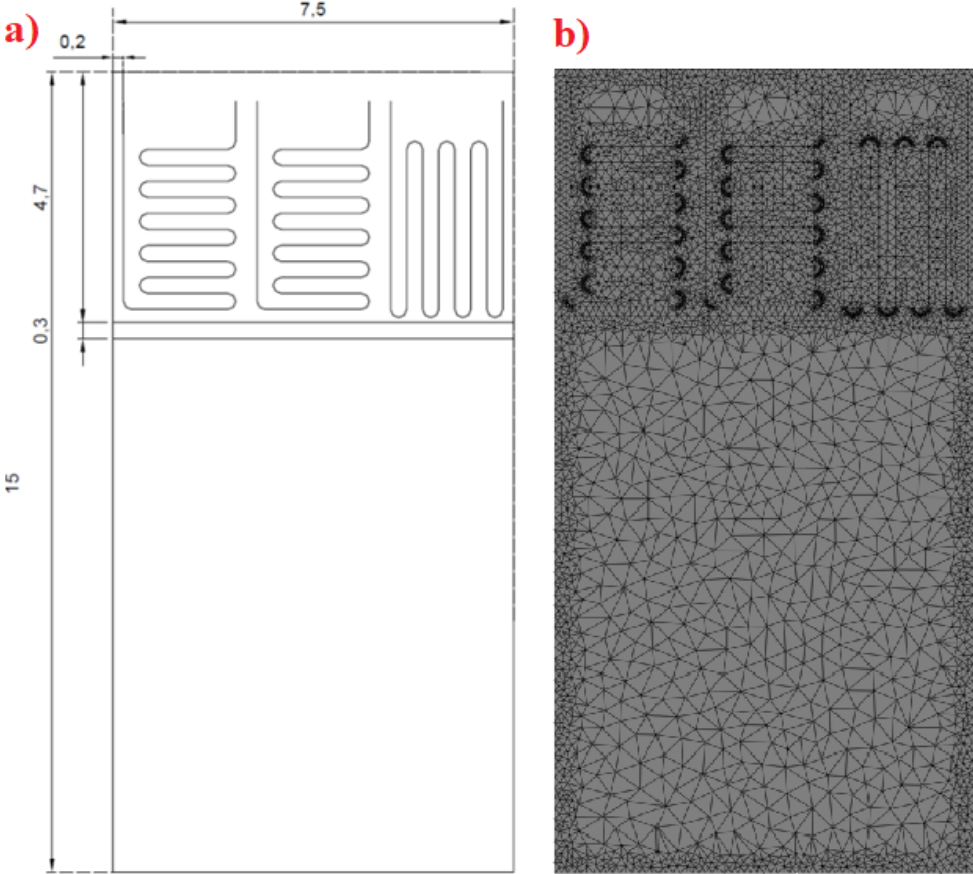


Figure 5.1: a) DXF model imported to FEFLOW (dimensions in m) (AUTOCAD); b) Mesh generation

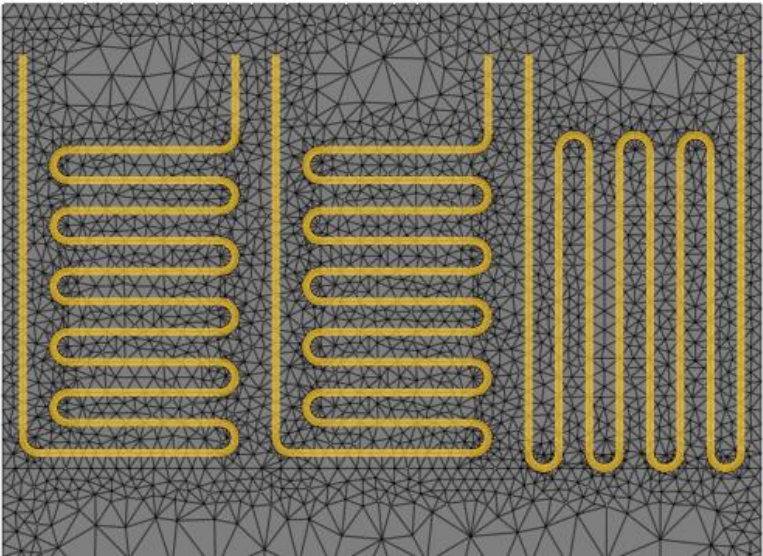


Figure 5.2: The piping system was modelled by discrete features

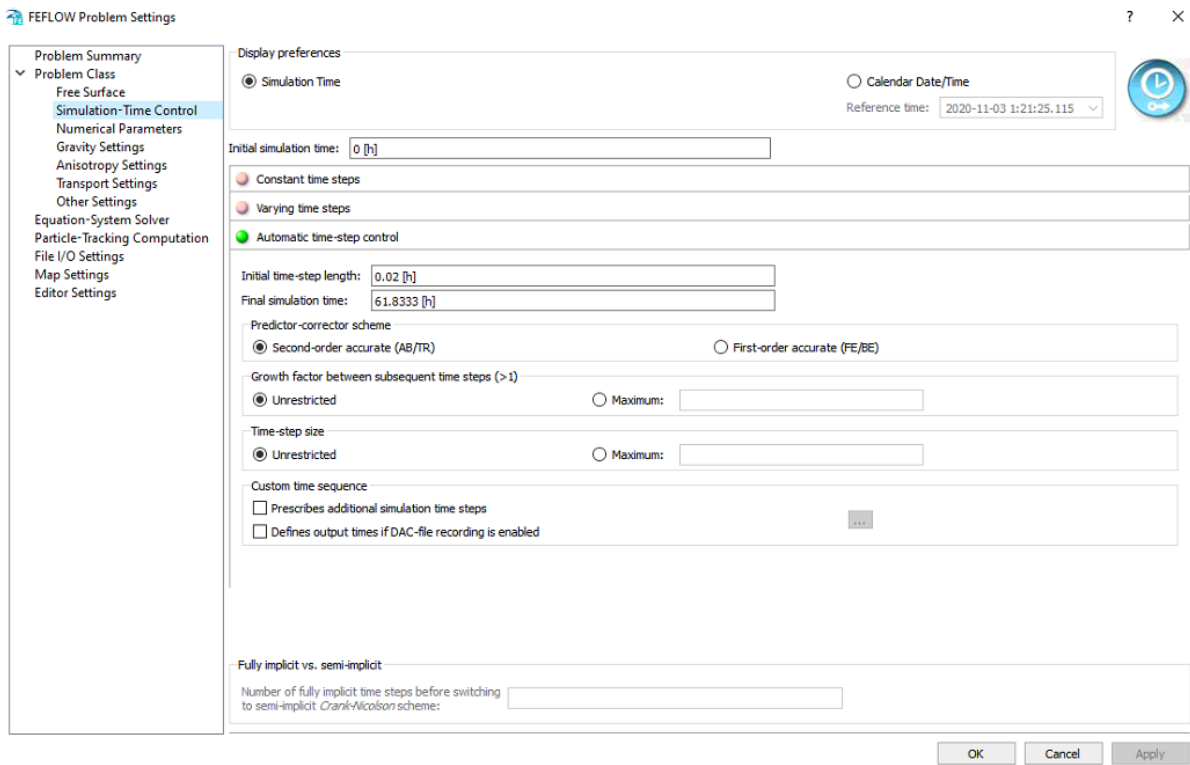


Figure 5.3: Simulation-Time Control

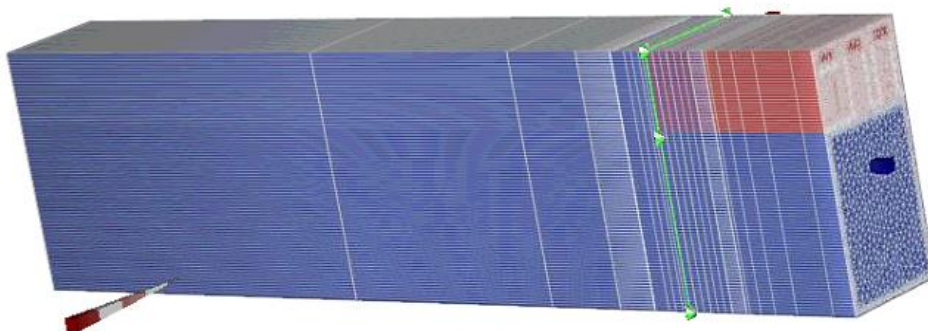


Figure 5.4: 3D model

Then, the mesh was generated thanks to the Supermesh and the Mesh Generator toolbar of the FEFLOW software which determined the domain limits of the Finite Element Mesh. In the case of flow analysis, a mesh with triangular elements is more suitable, some modification of mesh size of polygons, lines and points in the Supermesh (Figure 5.1.b) was done with denser mesh close to the geothermal probes. In 2D mesh, the number of nodes is 5912, the number of elements is 11502.

Using the Problem Settings command to define the simulation time, for Test 3, the duration lasted from 19:30 07/02/2020 to 9:20 10/02/2020, which was about 61.83 hours, so the simulation time was set from time  $t = 0$  [h] to  $t = 61.83$  [h] (Figure 5.3), direction of gravity according to the negative y axis.

The 3D Layer Configurator toolbar was used to create a 3D model from 2D: the number of layers and slices were equal to 22, and 23 respectively as showed in Figure 5.4. In 3D model, the number of nodes is 135976, the number of elements is 253044. The pipes of the three circuits were modeled through discrete features (Figure 5.2) which are present within the software. Discrete features can be added to models to represent highly conductive one-dimensional features, for each discrete feature, geometry and flow and possibly also mass, age- and heat-transport properties need to be defined, its concept is similar to beam elements in structural FE softwares. For the simulation within discrete features, three different flow laws can be chosen: Darcy, Hagen-Poiseuille, Manning-Strickler. In this case, the most suitable formulation for small diameter pipes is Hagen-Poiseuille which neglects the thermal properties of the material that constitutes the pipe. In Test 3, the circuits 2 and 3 were connected by parallel linking, so it was not necessary to define the connection between them. For parallel connection, 2 circuits were run separately by imposing the inlet fluid at entrances and measuring the temperature of ends of both circuits. In order to do that, 2 observation points needed to be set at 2 end points of the circuits.

### 5.2.3. Parameters of materials

The characteristics of the subsoil and the materials have to be defined, in particular thermal, geolithological and textural properties of the materials. The properties that most influence the thermal behavior of the subsoil are the water content, the physical characteristics and the thermal properties of the solid matrix. The main parameters that were used to describe the model are mentioned as below:

- Porosity  $n$ : the ratio between volume of voids ( $V_v$ ) and total volume ( $V_t$ )
- Thermal conductivity  $K$ : ability of a material to transmit heat; it increases as the water content increases. 
$$K = k \frac{\rho g}{\mu}$$

with  $\rho$  and  $\mu$  respectively density and viscosity of the fluid,  $g$  the acceleration of gravity and  $k$  the permeability of the porous medium.
- Thermal capacity  $C_v$ : quantity of heat that must be released or taken away from a unit volume of a substance to raise (or decrease) its temperature by 1 K: 
$$C_v = \frac{Q}{\Delta T}$$

- Thermal diffusivity  $\alpha$ : measure of how quickly a material is able to diffuse heat inside it;

it is the ratio:  $\alpha = \frac{K}{C_v}$

- Storage coefficient S: amount of water per unit volume of a saturated formation that is stored or expelled from storage due to the compressibility of the mineral skeleton.

In terms of thermal properties of materials, for small plants, the parameters are estimated from the presumed stratigraphy, while for plants with higher thermal potential, the thermal properties are measured on site. The most commonly used technique for the in-situ study of the heat exchanger's thermal properties is the GRT (Geothermal Response Test). The following tables (Table 5.1, 5.2, 5.3, 5.4) show the thermal properties used in the model, associated respectively with the ground of the Energy Center site, air, concrete and geothermal probes.

In particular, the hydraulic, hydro-dispersive and thermal parameters of the aquifer are the result of pumping tests, with temperature monitoring, conducted for three consecutive months (Barla et al., 2013).

*Table 5.1: Soil parameters*

| Parameter                         | Value                 | Unit                   |
|-----------------------------------|-----------------------|------------------------|
| Hydraulic conductivity $K_{xx}$   | $4.15 \cdot 10^{-3}$  | [m/s]                  |
| Hydraulic conductivity $K_{yy}$   | $2.075 \cdot 10^{-4}$ | [m/s]                  |
| Hydraulic conductivity $K_{zz}$   | $4.15 \cdot 10^{-3}$  | [m/s]                  |
| Storage coefficient               | $10^{-4}$             | [m <sup>-1</sup> ]     |
| Porosity                          | 0.25                  | [-]                    |
| Thermal capacity of the fluid     | 4.2                   | [MJ/m <sup>3</sup> /K] |
| Thermal capacity of the solid     | 2                     | [MJ/m <sup>3</sup> /K] |
| Thermal conductivity of the fluid | 0.65                  | [W/m/K]                |
| Thermal conductivity of the solid | 2.8                   | [W/m/K]                |
| Longitudinal heat loss            | 3.1                   | [m]                    |
| Transverse heat loss              | 0.3                   | [m]                    |

*Table 5.2: Parameters of geothermal probes*

| Parameter                         | Value     | Unit                   |
|-----------------------------------|-----------|------------------------|
| Storage coefficient               | $10^{-4}$ | [m <sup>-1</sup> ]     |
| Cross area                        | 3.14      | [cm <sup>2</sup> ]     |
| Hydraulic radius                  | 0.5       | [cm]                   |
| Thermal capacity of the fluid     | 4.2       | [MJ/m <sup>3</sup> /K] |
| Thermal conductivity of the fluid | 0.65      | [W/m/K]                |

Table 5.3: Air parameters

| Parameter                         | Value     | Unit                   |
|-----------------------------------|-----------|------------------------|
| Hydraulic conductivity $K_{xx}$   | $10^{-2}$ | [m/s]                  |
| Hydraulic conductivity $K_{yy}$   | $10^{-2}$ | [m/s]                  |
| Hydraulic conductivity $K_{zz}$   | $10^{-2}$ | [m/s]                  |
| Storage coefficient               | $10^{-4}$ | [m <sup>-1</sup> ]     |
| Porosity                          | 1         | [-]                    |
| Thermal capacity of the fluid     | $10^{-3}$ | [MJ/m <sup>3</sup> /K] |
| Thermal conductivity of the fluid | 0.53      | [W/m/K]                |
| Longitudinal heat loss            | 5         | [m]                    |
| Transverse heat loss              | 0.5       | [m]                    |

Table 5.4: Concrete Parameters

| Parameter                         | Value      | Unit                   |
|-----------------------------------|------------|------------------------|
| Hydraulic conductivity $K_{xx}$   | $10^{-16}$ | [m/s]                  |
| Hydraulic conductivity $K_{yy}$   | $10^{-16}$ | [m/s]                  |
| Hydraulic conductivity $K_{zz}$   | $10^{-16}$ | [m/s]                  |
| Storage coefficient               | $10^{-4}$  | [m <sup>-1</sup> ]     |
| Porosity                          | 0          | [-]                    |
| Thermal capacity of the solid     | 1.05       | [MJ/m <sup>3</sup> /K] |
| Thermal conductivity of the solid | 1.12       | [W/m/K]                |

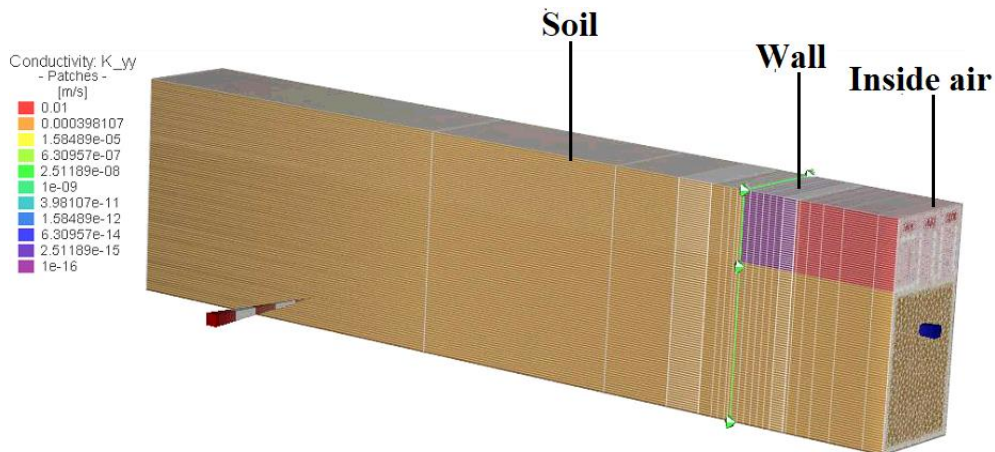


Figure 5.5: 3D Model - Hydraulic conductivity  $K_{yy}$

Figure 5.5 shows the 3D model in which it is possible to distinguish the air part, the wall and the ground, particularly the vertical hydraulic conductivity  $K_{yy}$  of different materials.

#### 5.2.4. Boundary conditions (BC)

To carry out a simulation of the heating test involving circuits 2 and 3 in parallel linking, it was necessary to provide the model with specific initial conditions and boundary conditions.

*a/ Temperature BC of soil at the depth of 15 m*

Soil at this depth can be considered as undisturbed soil, so its temperature is almost constant throughout the year. Additionally, as discussed above, the temperatures recorded in all sensors were not affected by the thermal system and seemed to be the temperatures of undisturbed soil, the temperature at sensor C18T4 which was the furthest and deepest position from the ground surface and the wall surface could be considered to apply for the soil at 15 m depth. In Test 3, the temperature at sensor C18T4 remained at 13.5 °C throughout the duration. Therefore, a temperature BC of 13.5 °C was set in the model at a depth of 15 m (Figure 5.9.a).

*b/ Temperature BC of soil at ground surface*

Regarding the upper surface of the domain (the ground surface), it was not possible to set constant BC temperatures because of its dependency on season. In this case, a definition of time series was introduced to define time variations of temperature. Time series consist of a unique ID as an identifier, a name, a curve type, a time mode, and a set of value pairs (time vs. value) and the interpolation law between the data pairs. Temperature values were measured by the thermo-hygro-pluvio anemometric station with radiometer located in Via della Consolata, 10, the site that is closest to the location of the Energy Center. In Test 3, the surface temperatures varied from 19:30 07/02/2020 to 9:20 10/02/2020 with duration being 61.83 hours, so by setting the starting point and the ending point of the test corresponding to  $t = 0$  [h] and  $t = 61.83$  [h] in the model, the time series curve could be plotted as in Figure 5.6. Then, the temperature BC of the nodes of the upper surface was set as in Figure 5.9.a.

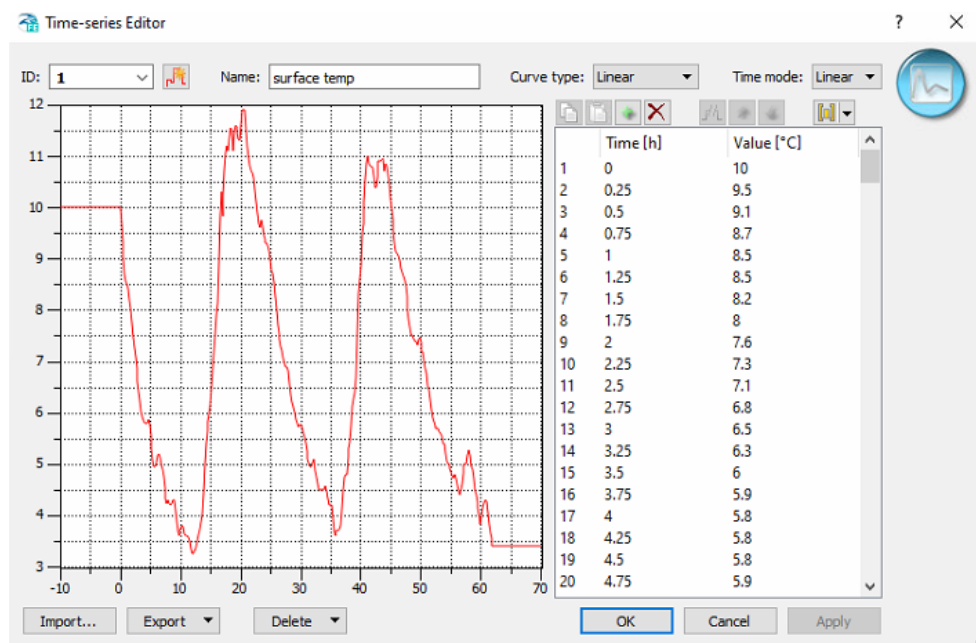
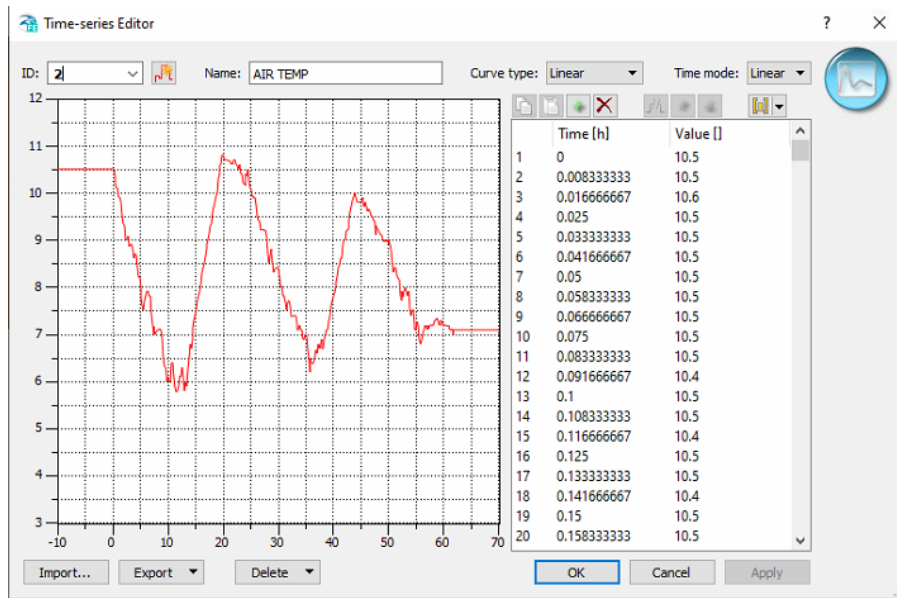


Figure 5.6: Time series of surface temperature

*c/ Temperature BC of air part*

The temperatures of the air inside building also varied with time, and this data was collected in site during the test, namely BT1. Also, using time series to define the temperature variation and plot it as in Figure 5.7. Then, the nodes in the surface separating the soil and air parts and in the slice near the wall (slice 18) were applied by the time series for temperature BC (Figure 5.9.a).



*Figure 5.7: Time series of air temperature*

*d/ Temperature of the heat fluid at the entrance points (inlet temperature)*

Moving to the BC of the geothermal probes, in the same way as the previous BC temperature, the time series was created as in Figure 5.8, it was then also applied for the inlet fluid at the entrances of circuit 2 and 3 (see Figure 5.9.b)

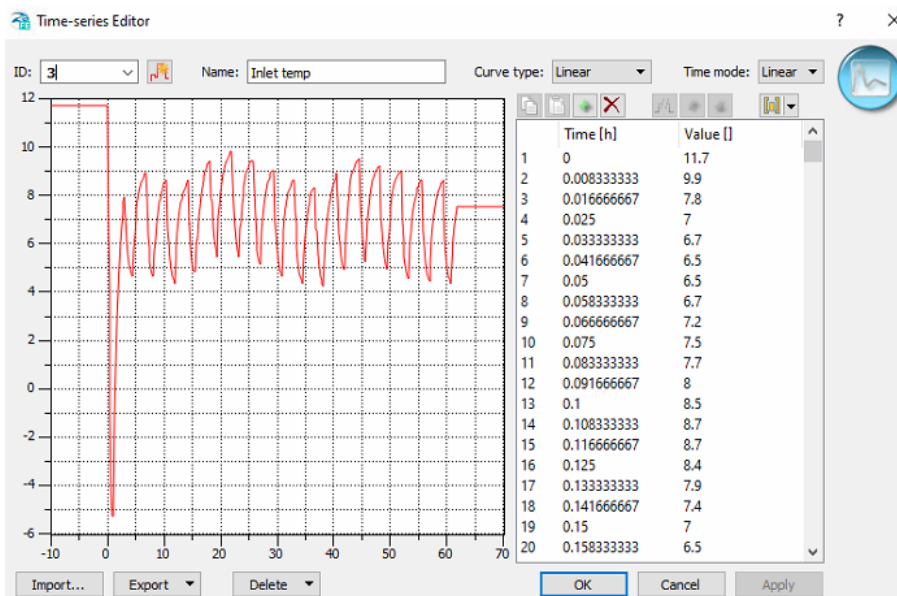


*Figure 5.8: Time series of inlet fluid*

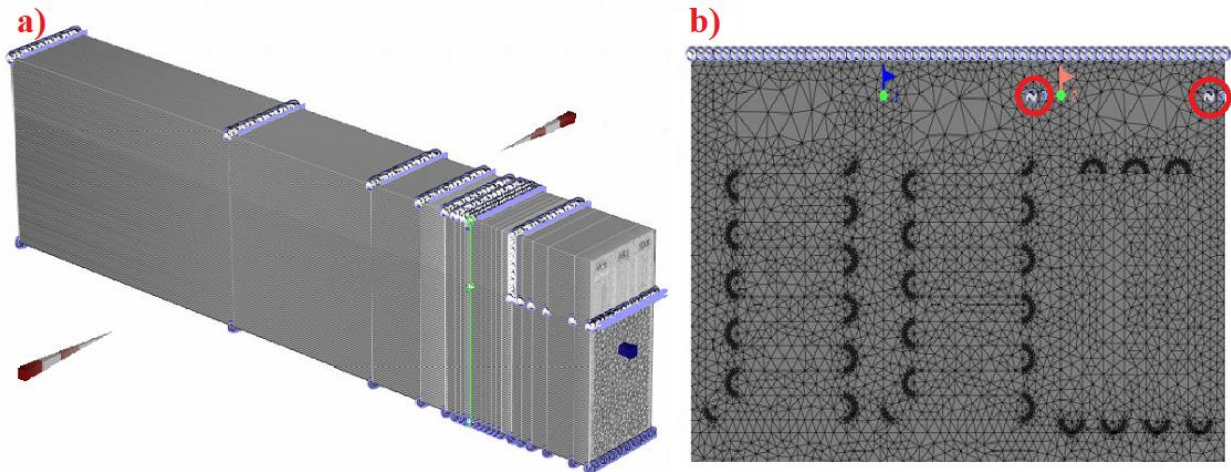


Figure 5.9: Temperature BC of the model: a) Temperature BC of nodes in different surfaces, b) Temperature BC of the inlet fluid (red circles in the figure)

e/ Initial temperature of soil

An initial temperature condition was set on the ground of the domain. These temperatures which could be considered as the temperatures of undisturbed soil were taken from sensors at the time before starting time of the test (07/02/2020 19:30). It can be seen from the test, these temperatures almost kept unchanged during the duration of test and they varied with depth. In this case, the values from the sensors at furthest distances from the wall could be selected for reference, because they were the least affected positions by the geothermal system, particularly sensors C3T4 at plane A, C8T5 at plane B, C13T4 at plane C, C18T4 at plane D as showed in Table 5.5. From this, the interpolating logarithmic function is obtained by using excel to describe the variation of soil temperature with depth (see Figure 5.10)

Table 5.5: Temperatures of different sensors

| Sensor | Depth [m] | Distance [m] | Temperature [°C] |
|--------|-----------|--------------|------------------|
| C3T4   | -0.75     | 0.75         | 9.16             |
| C8T5   | -2.15     | 2.15         | 9.75             |
| C13T4  | -3.35     | 3.35         | 11.65            |
| C18T4  | -4.6      | 4.6          | 13.34            |

The interpolation function is:  $Temp = 2.1354 \times \ln\left(\text{abs}\left(y_{global}\right)\right) + 9.2631$

Where, Temp is the temperature of soil node [°C],  $y_{global}$  is the depth of soil node or coordinate of node in y-direction [m]. Finally, initial temperature of each soil node were then applied this function by using expression tool. See Figure 5.11 for graphical point of view.

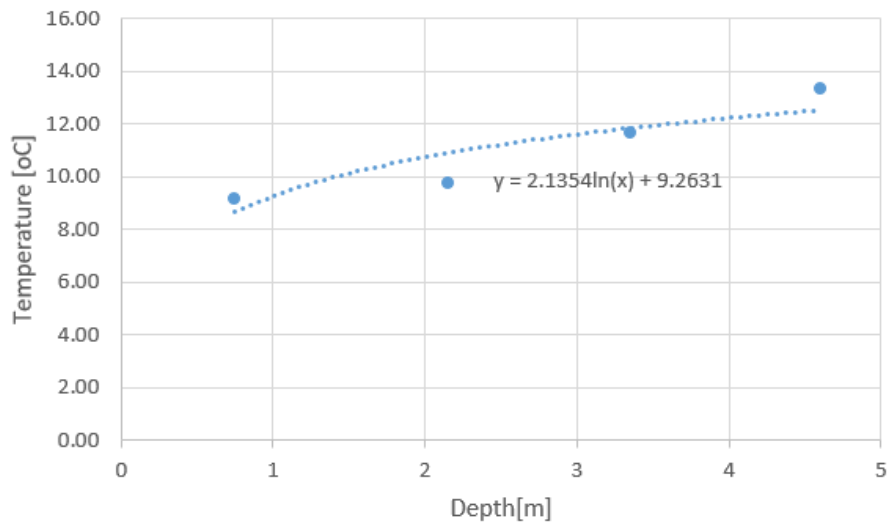


Figure 5.10: Interpolation line of temperature

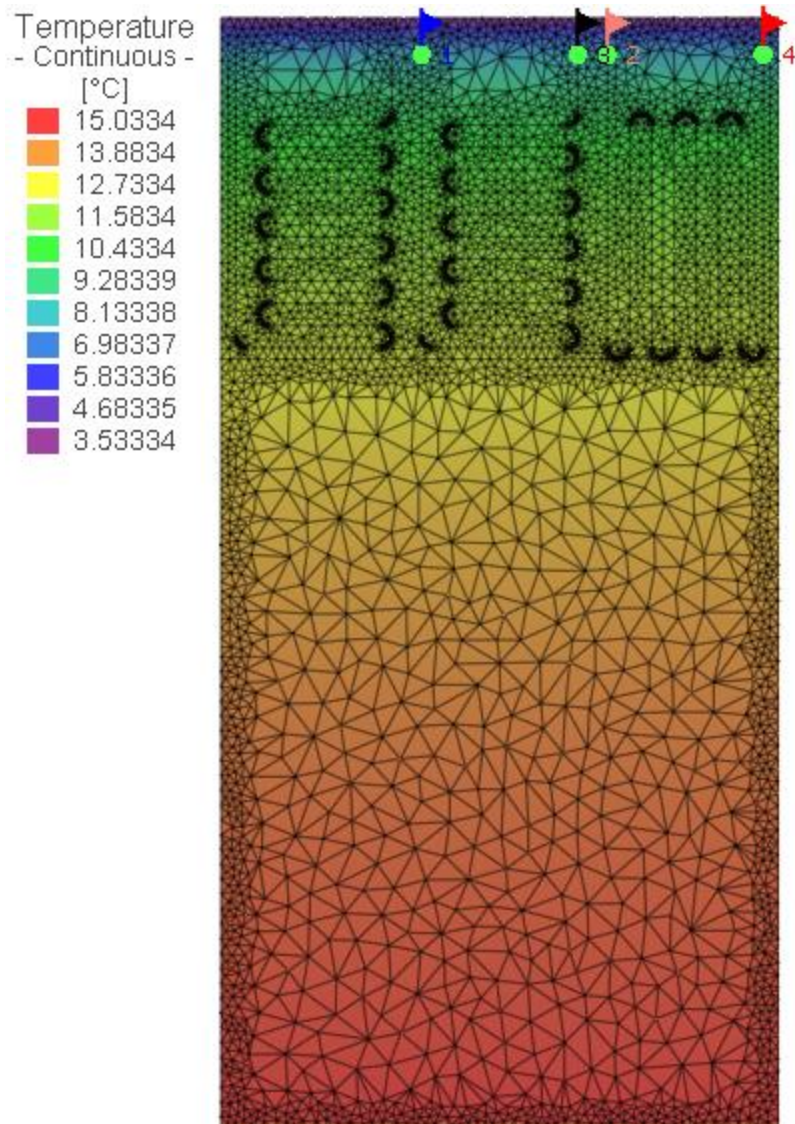


Figure 5.11: Initial temperature of soil in Test 3

*f/ The speed of fluid in the circuit 2 and 3*

Firstly, the speed of fluid had to be calculated based on the flow rate ( $Q$ ) of Test 3 and the area ( $S$ ) of pipe. In this test, the flow rate kept constant at 925.8 [l/h] or 0.257 [l/s] during the duration, the diameter of the pipe was 20 mm and the area of pipe was:

$$S = \pi \frac{\phi^2}{4} = 0.000314 \text{ [m}^2\text{]}$$

Therefore, the velocity of fluid was:

$$v = \frac{Q}{S} = \frac{0.257 \times 10^{-3}}{0.000314} = 0.8186 \text{ [m/s]}$$

However, this velocity was the one of main pipe, in this case, the fluid velocity of Circuit 2 and 3 were different from above because the linking of them was parallel. Regarding detail data of Test 3, the flow rate in both circuit were almost the same, so the input velocity of Circuit 2 and 3 were set to be equal to a haft of main fluid velocity (0.4093 [m/s]).

Using the Fluid-flux BC function, the speed of the fluid inside circuits 2 and 3 was set: entering circuit 3, the assigned speed was equal to -0.4093 m/s and at the output of circuit 2, it was equal to 0.4093 m/s (the negative sign indicates the incoming fluid, the positive sign is the outgoing fluid), see Figure 5.10 for a graphical point of view.

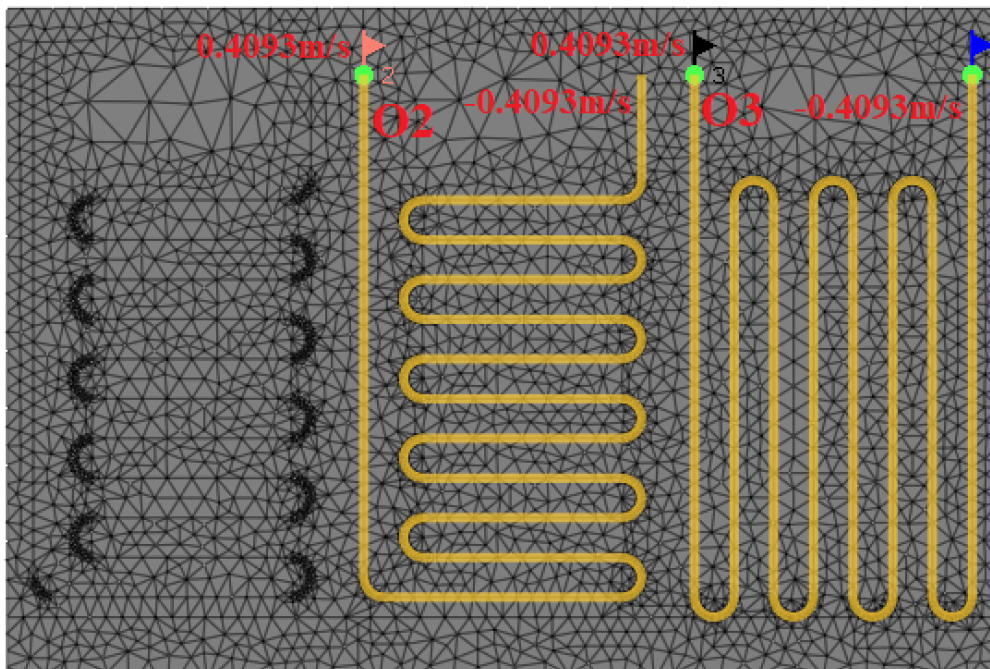


*Figure 5.12: Circuit 2 and 3 with fluid speed at entrances and ends, and a set of 2 observation points (O2 and O3)*

## 5.2.5. Results and discussion

### *a/ Thermal performance*

After running the model, the outlet temperatures of Circuit 2 and 3 were collected by 2 observation points at the points O2 and O3 as presented in Figure 5.12. Also, the inlet temperature was recorded by interpretation process of input data at each time step with respect to the time step of outlet temperature. The variation of inlet, outlet temperatures of both circuits were plotted in Figure 5.13. Also, the temperature distribution in the slice of piping system is showed in Figure 5.15, and in 3D model as showed in Figure 5.16.

The quantification of the heat exchange was also calculated by using Equation 4.2, but the flow rate was equal to a half of main fluid in experiment (see Table 5.6). At each time step, after calculating the heat exchanges, the instantaneous powers were also computed by multiplying the heat exchange by the time step. Then, the average power was defined by dividing the total power of the system by the duration of time. The process above was done separately in Circuit 2 and 3, and the final average power of the system was the summation of both circuits. With 23 m<sup>2</sup> area of both circuits, the heat exchanged rate was equal to 22.68 W/m<sup>2</sup>. The result is presented in Table 5.7.

*Table 5.6: Parameters' values for calculation of heat exchange rate in numerical result.*

| Quantity                              | Value   |
|---------------------------------------|---------|
| Propylene Glycol to water mixture [%] | 25      |
| Flow rate [l/s]                       | 0.13    |
| Unit weight [kg/m <sup>3</sup> ]      | 1028.31 |
| Specific heat capacity [kJ/kg°C]      | 3.889   |
| Duration [h]                          | 61.8333 |

*Table 5.7: The heat exchange rate result of numerical model*

| Total Energy [kWh] |           | Mean power [kW] |           | Mean power [kW] | Heat exchange rate [W/m <sup>2</sup> ] |
|--------------------|-----------|-----------------|-----------|-----------------|--|
| Circuit 2          | Circuit 3 | Circuit 2       | Circuit 3 | Two circuits    | Two circuits                           |
| 20.579             | 11.679    | 0.333           | 0.189     | 0.522           | 22.68                                  |

*Table 5.8: Thermal performance comparison between numerical and experimental methods*

| Mean power [kW]  |                     | Heat exchange rate [W/m <sup>2</sup> ] |                     |
|------------------|---------------------|--|---------------------|
| Numerical result | Experimental result | Numerical result                       | Experimental result |
| 0.522            | 0.478               | 22.68                                  | 20.78               |

In Table 5.8, the mean power of numerical result was almost 0.05 kW larger than that of experimental one. This minor difference between experimental and numerical results may be due to the neglect of thermal resistance of probe material and concrete wall, the 2 °C accuracy of soil temperature of monitoring systems, besides the numerical model could be considered as an ideal condition which was not affected by environmental factors. In conclusion, the numerical results seem to have a good agreement with the experimental results.

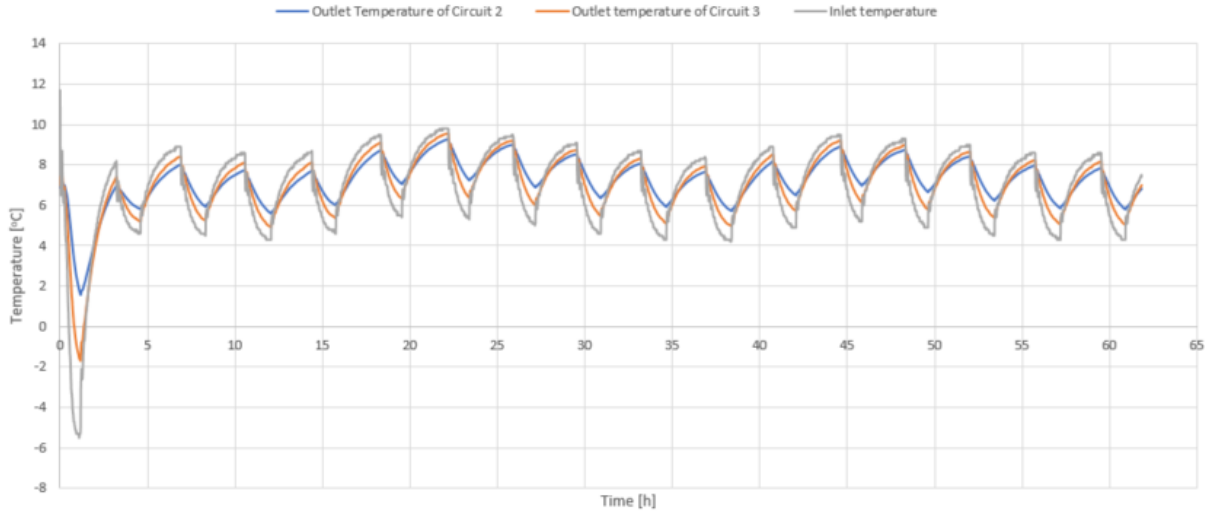


Figure 5.13: Variation over time of inlet and outlet temperatures

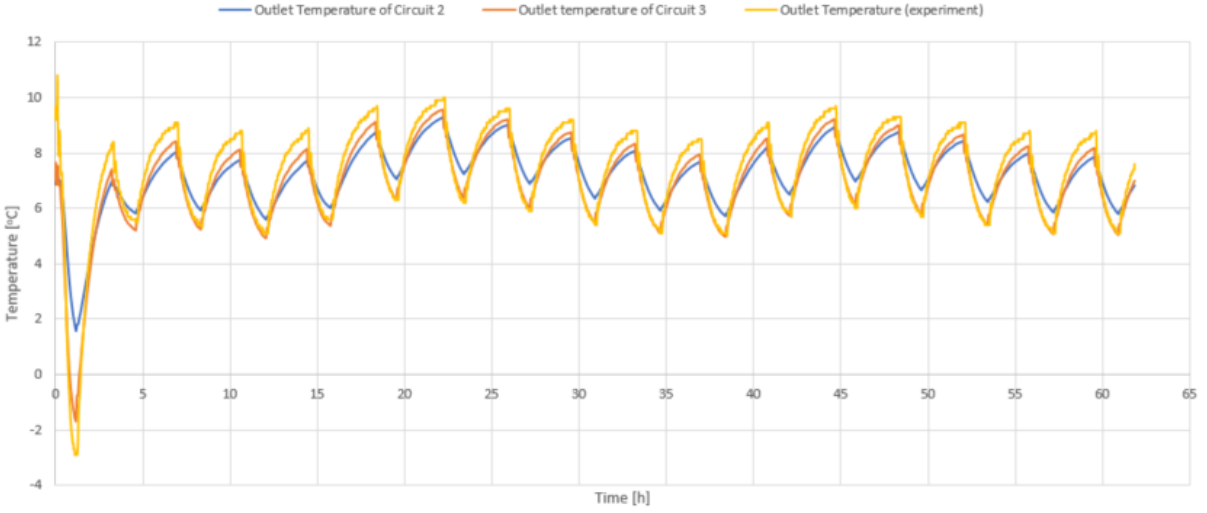


Figure 5.14: Comparison of outlet temperatures between numerical and experimental methods

The outlet temperatures in experiment were recorded at the main pipe, while these values in numerical model were collected separately at the ending points of two circuits. As a result, there were some temperature differences as seen in Figure 5.14. However, the variations of outlet temperature of numerical and experimental methods had the same shape during the time, it also confirms the agreement between both methods.

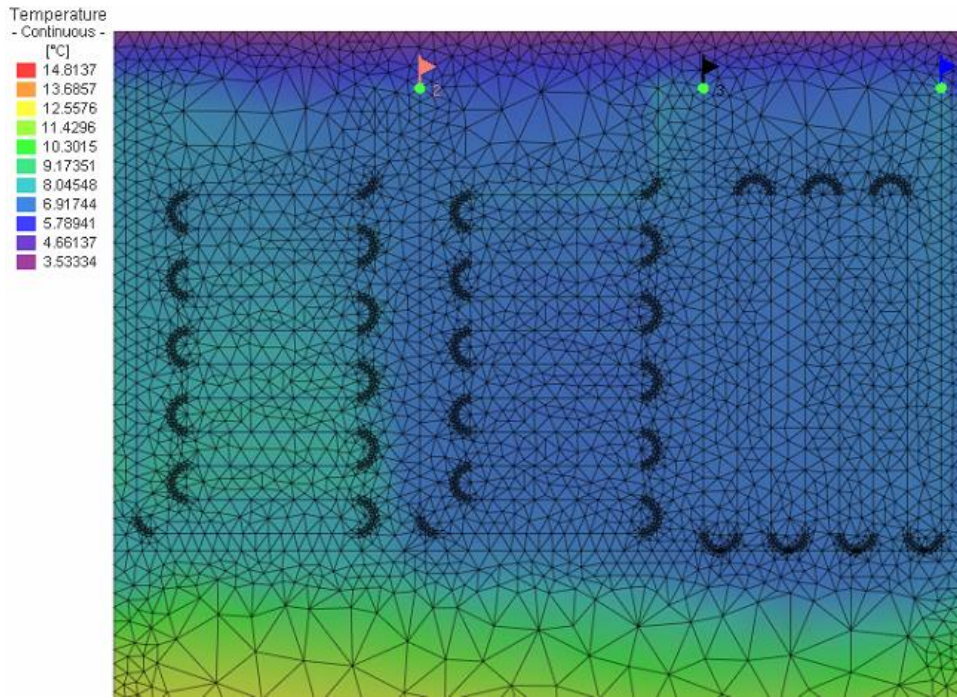


Figure 5.15: Temperature distribution in the slice of piping system at the end of duration

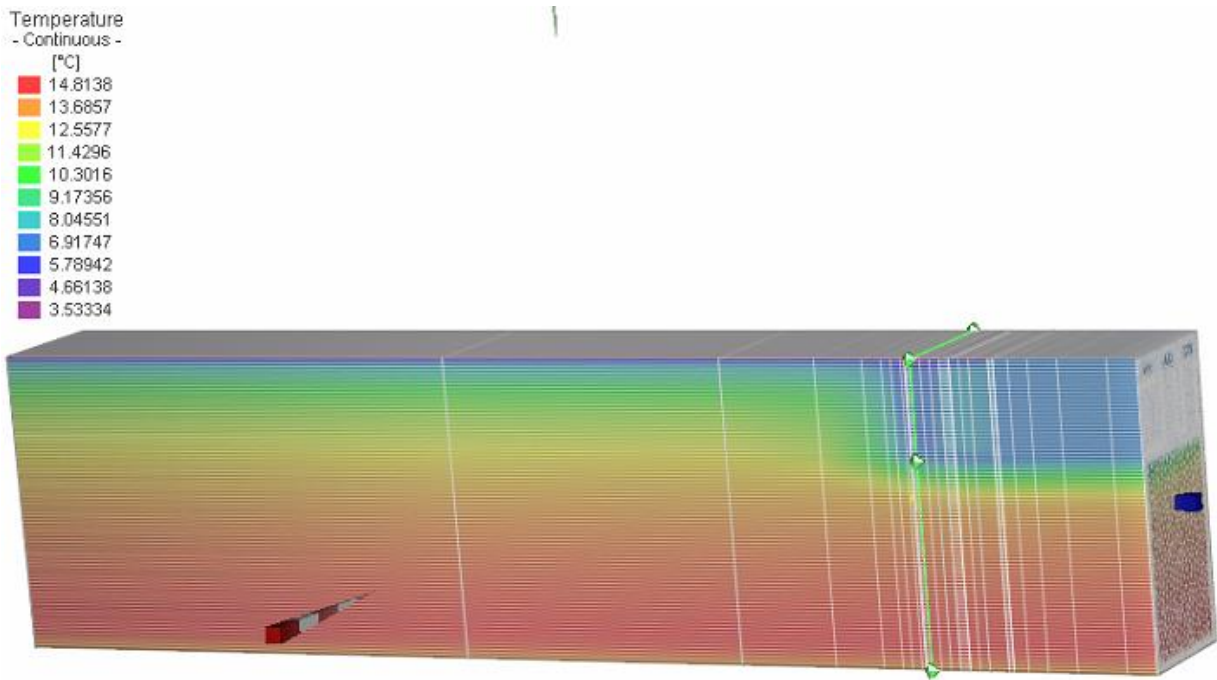


Figure 5.16: Temperature distribution in 3D model at the end of duration

*b/ Temperature of soil*

In order to test the affection of thermal system on the surrounding soil in terms of temperature, some observation points were set at positions with respect to the sensors C3T1, C9T1, C13T1, C19T1 to collect soil temperatures at these points during Test 3 with exact location in Table 5.9.

Then, the comparisons of both methods are presented in Figure 5.17, 5.18, 5.19, 5.20. In each sensor point, although the temperature values experienced little differences between two methods with the largest one belonging to the sensor C19T1 (3 °C), both methods shared the similar trend regarding temperature variation. The reason for these differences could be from the initial temperature condition that was set in the numerical model by setting a logarithmic function for temperature distribution with depth. However, the main interest in this case is the change of temperature during the test, both methods also confirmed that there is no or minor effect of the thermal system to the soil temperature.

Table 5.9: Location of the sensors (or observation points)

| Sensor | Depth [m] | Distance from the wall surface [m] |
|--------|-----------|------------------------------------|
| C3T1   | 0.75      | 0.50                               |
| C9T1   | 2.15      | 0.30                               |
| C13T1  | 3.35      | 0.50                               |
| C19T1  | 4.60      | 0.30                               |

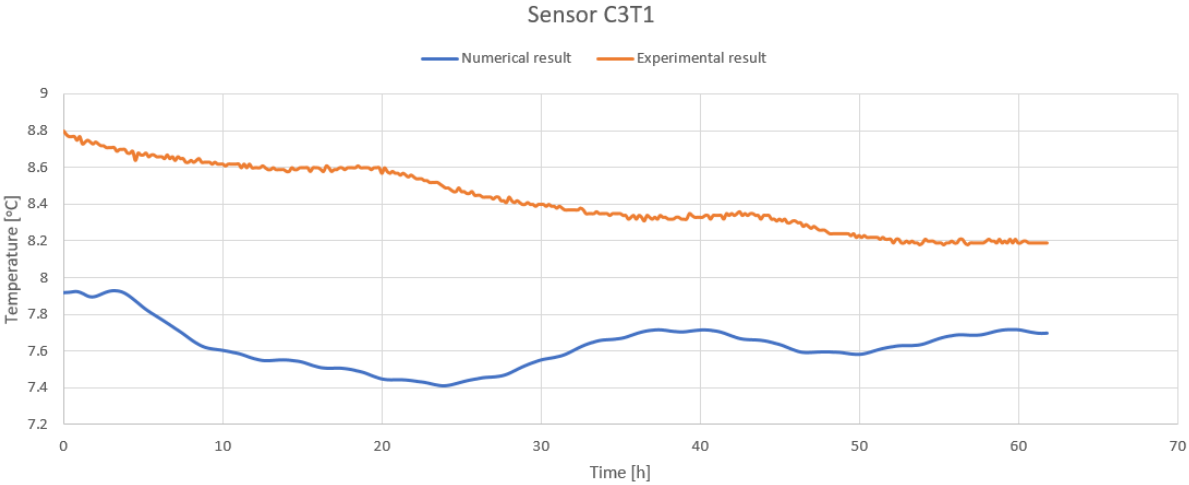


Figure 5.17: Comparison of soil temperature between two method at sensor C3T1

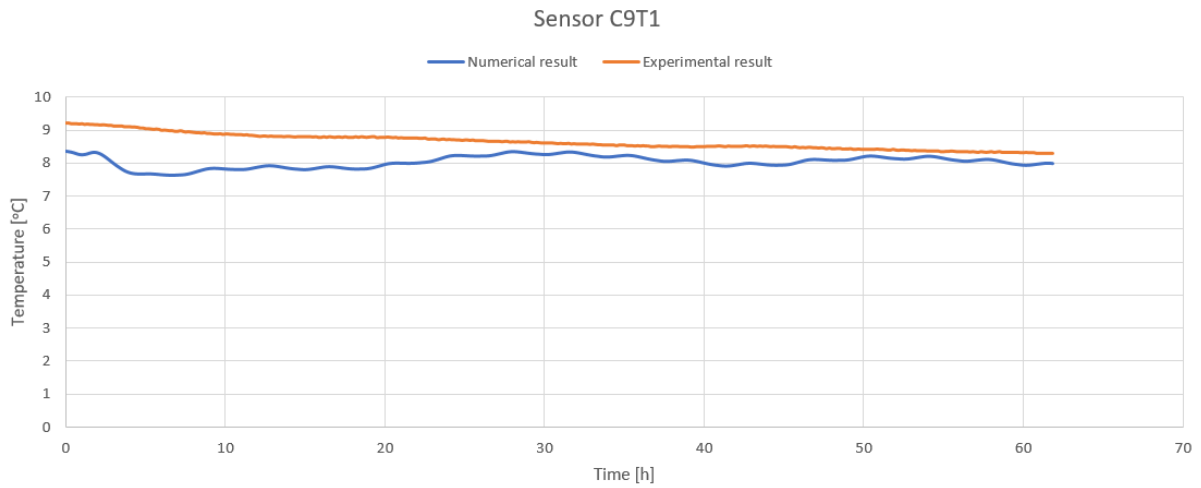


Figure 5.18: Comparison of soil temperature between two method at sensor C9T1



Figure 5.19: Comparison of soil temperature between two method at sensor C13T1

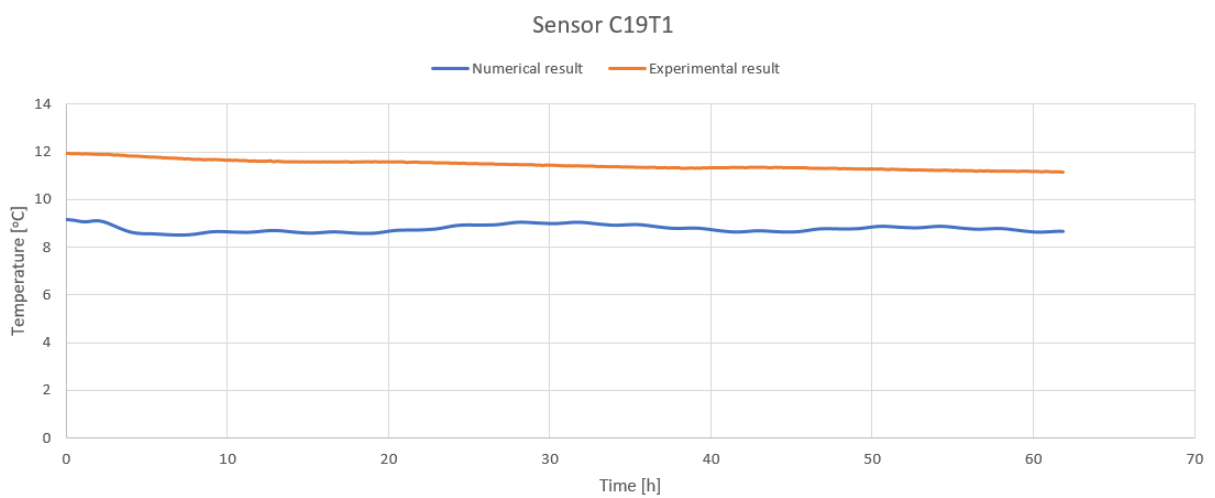


Figure 5.20: Comparison of soil temperature between two method at sensor C19T1

## 6. *Chapter 6: CONCLUSIONS*

This thesis is based on the experimental campaign of an energy wall system at the Energy Center Laboratory in Torino (Italy).

Firstly, introducing the concept of geothermal energy and its different forms is fundamental to understand how the technology works and what is the principle of heat pump system. At the base of this, energy geostructure has been described. Thanks to the huge surface in contact with the ground, tunnels are perhaps the ones that can best exploit the geothermal system. Nevertheless, energy piles and energy diaphragm wall are widely used around the world.

The main aim of this thesis is to introduce the concept and the realization of a very shallow geothermal system that exploits the earth-contact area of the buildings was presented. The system, called GeothermSkin, allows to employ the geothermal energy avoiding the high initial costs related to excavation and drilling needed in normal geothermal systems. This system is conceived as an external application of modular heat exchangers. These modules can be applied on the underground walls of buildings and interest extremely limited depths, so not to interfere with deeper systems.

The realization of a prototype system made up of three modules of various configuration reaching 4.6 m depth, allowed to test the thermal performance of the system. The impact on the structure and the surrounding ground in terms of stresses, strains, temperatures and water content was studied as well thanks to the extensive monitoring system which allowed to collect numerous data during the experimental campaign. At this stage, only data related to the heating mode has been recorded, more tests in cooling mode will be done in order to have an overall interpretation of the system.

A total of 6 tests were driven, in addition to 1 test taken from M. Baralis and M. Barla (2019), all of them were in heating operative mode and in parallel linking between circuits. As regards the heating operations, it resulted that the system can continuously produce 13 up to 22 W per equipped unit area, in good agreement with expectation from similar systems known in literature. This heat exchange rate is equivalent in all kinds of direction of the circuit deployment and position. The temperature at user side plays important role in thermal performance of the system with being proportional to the heat exchange rate. Although higher exchange rate can be obtained by rise of supply temperature, the more frequent activation may induce premature wear of the heat pump. Additionally, appropriate flow rate allows to obtain higher value of heat rate, in particular a much lower value of flow rate leads to the significant

decrease in heat rate even in the case of high difference temperature between inlet and outlet of the ground loop. The heat flux is almost independent from the number of circuits, their direction, their deployment, so in order to reduce the initial investment cost, but still assure a sufficient heat exchange rate, the less number of circuits or even single circuit should be used rather than using more circuits with parallel linking if all other conditions are the same. On the other hand, a numerical model was built by using FEFLOW software to simulate the behavior of the system from the thermal point of view, it resulted in an agreement in the comparison of the heat flux and heat rate obtained from experimental campaign and from numerical model.

On the basis of thermal performances, the system is expected to provide a valuable contribution to the fulfilment of clean energy production from new and refurbished buildings. Furthermore, the system may be used in combination with other renewable energy sources (as the solar thermal panels) to make the housing completely self-sustaining. It means that the electricity used by the system can be supplied by renewable energy.

The extensive monitoring plan allowed to identify the extremely low effect of the thermal system to the temperature, the water content, tension of the ground and from the structural point of view of the wall. Indeed, the ground temperature changes during the test were so small with the maximum value being only approximately 0.7 °C. It could be considered that minor impact or even no influence on the ground temperature is exerted by the system when it is used in heating mode during winter season. As a result, the thermal status of the ground is virtually equal to the undisturbed conditions. Furthermore, due to the low influence also from the thermal point of view, no significant alteration seems to be exerted by the thermal activation on the hygrometric equilibrium of the ground near the wall. Also strains on the equipped walls surface were found to be limited below 90  $\mu\epsilon$ . It was moreover detected virtually no affection on hygrometric values and on stresses at wall-ground contact.

As mentioned above, the GeothermSkin system did not result in any impact on temperature of soil in general. The preliminary experimental results suggest that this very shallow geothermal system allows to obtain a satisfying amount of energy and virtually not affecting the geothermal energy of deeper systems. As a result, the system may be adopted as a supplementary energy supplier beyond deeper installations as Borehole Heat Exchangers, open loop wells, energy piles and tunnels. This kind of energy system may play a role in exploiting geothermal resources, especially in densely inhabited areas.

## A.APPENDICES

### 1. Test H\_1+2\_20200131\_20200203

*Table A.1: Main features of the test*

|                                    |                |
|------------------------------------|----------------|
| Test start time                    | 31/01/20 18.00 |
| Test end time                      | 03/02/20 09.20 |
| Duration [h]                       | 63.3           |
| Operative mode                     | Heating        |
| Active circuit(s)                  | 1;2            |
| Circuit link                       | Parallel       |
| Target temperature user [°C]       | 35             |
| Flow rate at the ground side [l/h] | 923            |

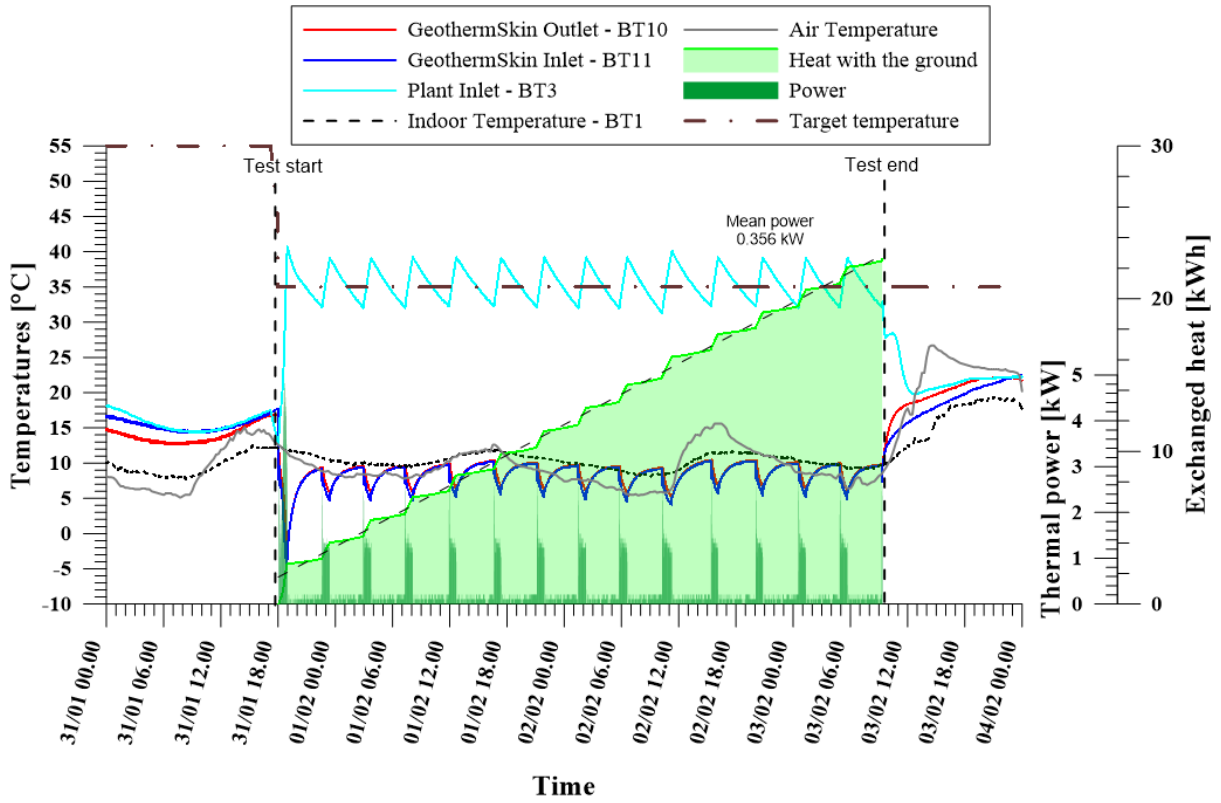


Figure A.1: Thermal performance interpretation of experimental test  $H_{1+2\_20200131\_20200203}$  with parallel link of circuit 1 and 2 in heating mode.

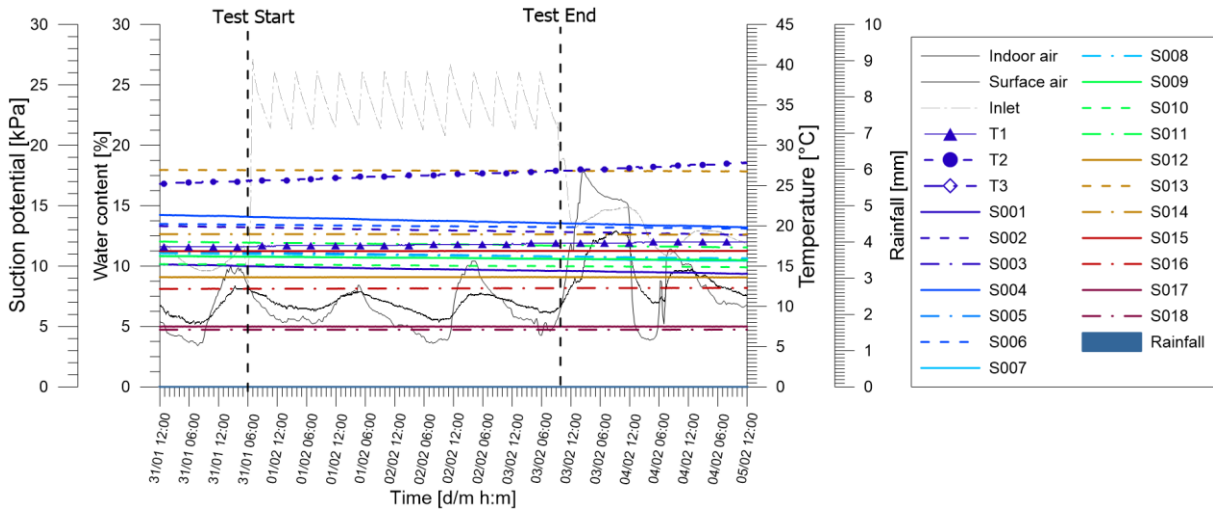


Figure A.2: Tensiometer and hygrometers records of experimental test  $H_{1+2\_20200131\_20200203}$  together with monitored rainfall from Politecnico weather station.

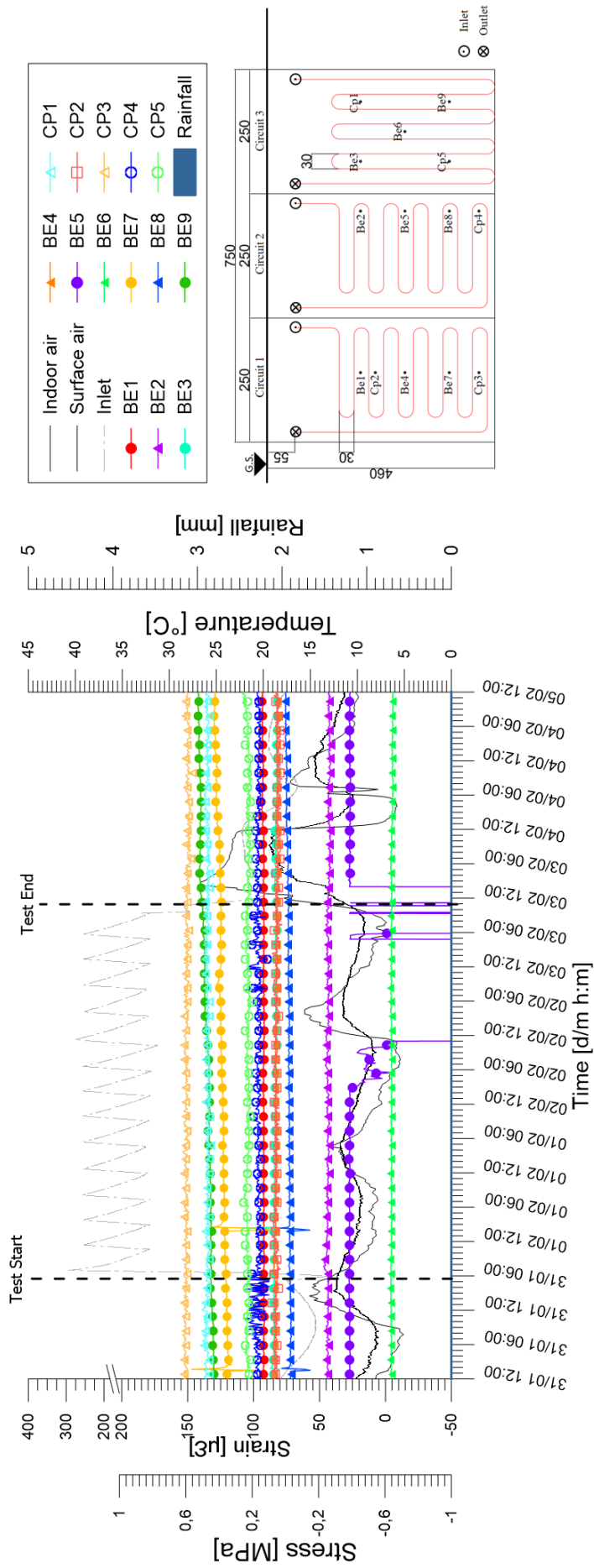


Figure A.3: Stresses and strains monitored at the wall external facade during experimental

test H\_I+2\_20200131\_20200203

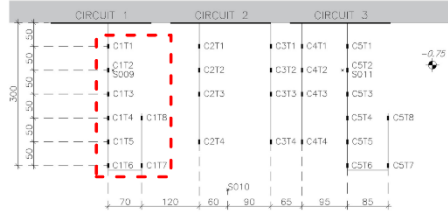
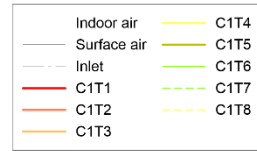
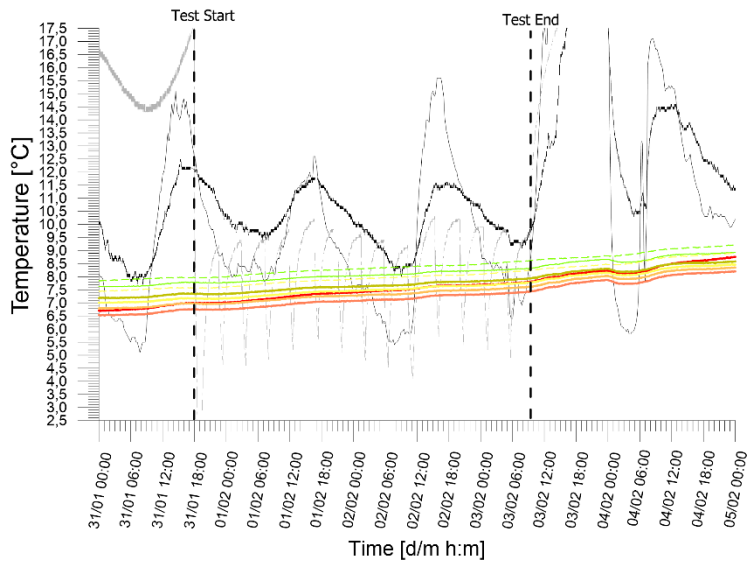


Figure A.4: Temperatures records from chain 1 of experimental test  
H\_1+2\_20200131\_20200203

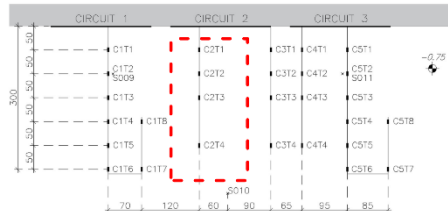
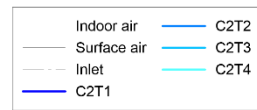
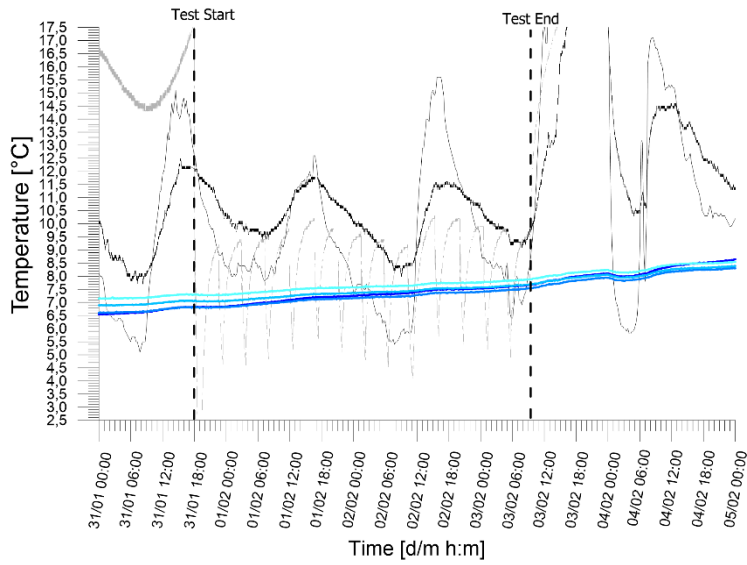


Figure A.5: Temperatures records from chain 2 of experimental test  
H\_1+2\_20200131\_20200203

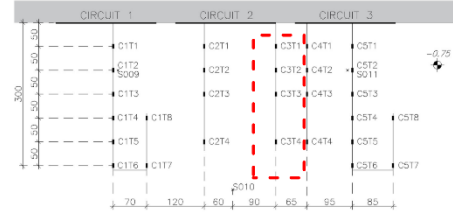
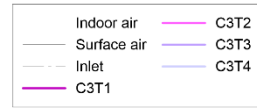
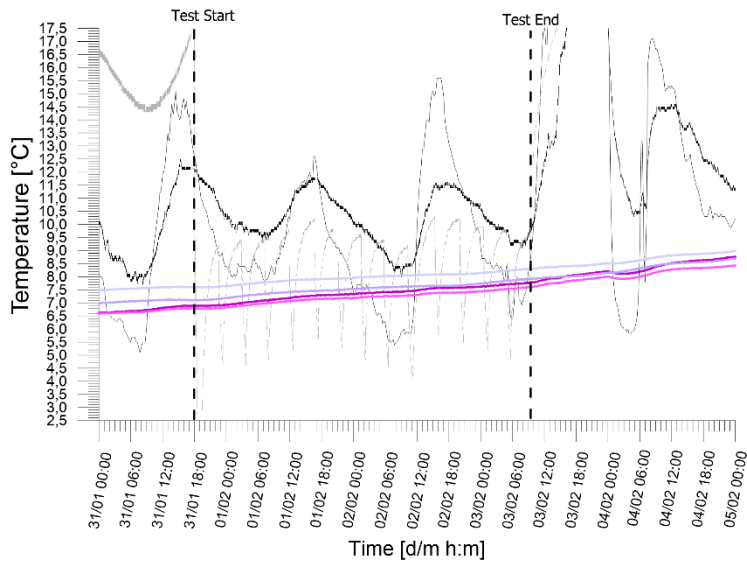


Figure A.6: Temperatures records from chain 3 of experimental test  
H\_1+2\_20200131\_20200203

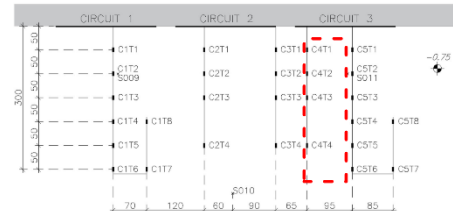
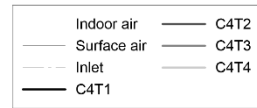
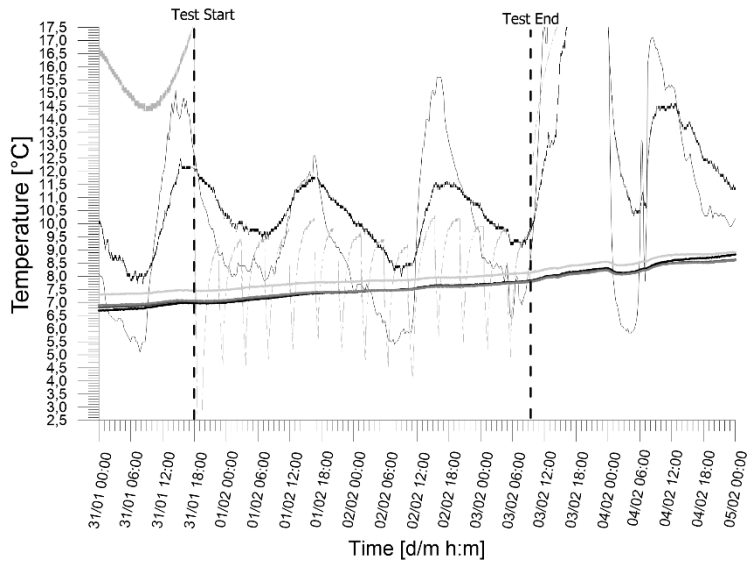


Figure A.7: Temperatures records from chain 4 of experimental test  
H\_1+2\_20200131\_20200203

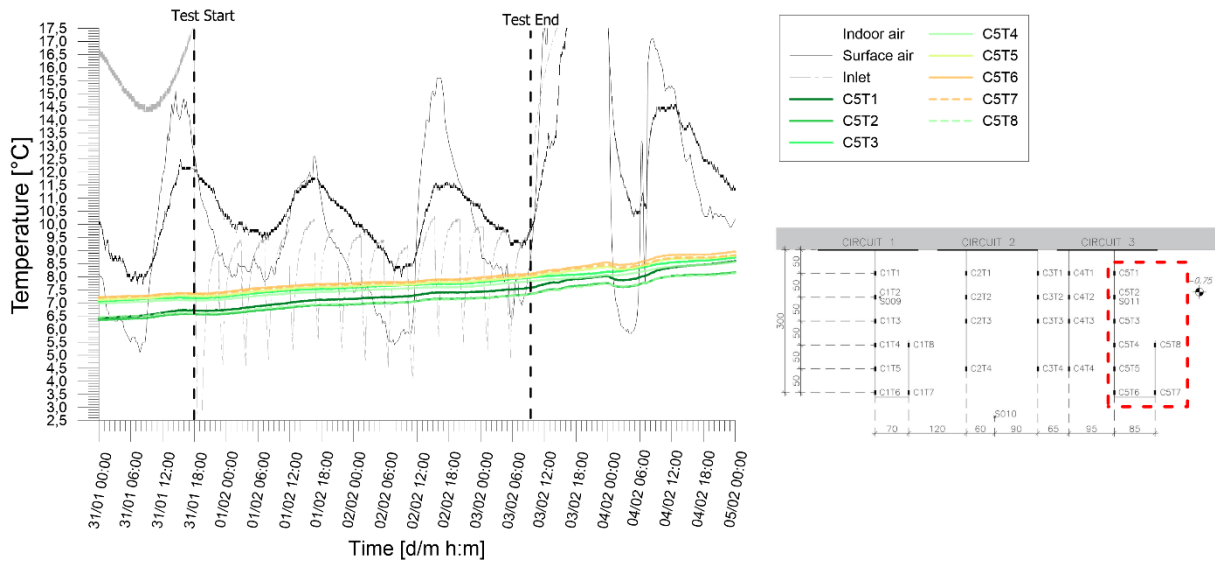


Figure A.8: Temperatures records from chain 5 of experimental test  
*H\_1+2\_20200131\_20200203*

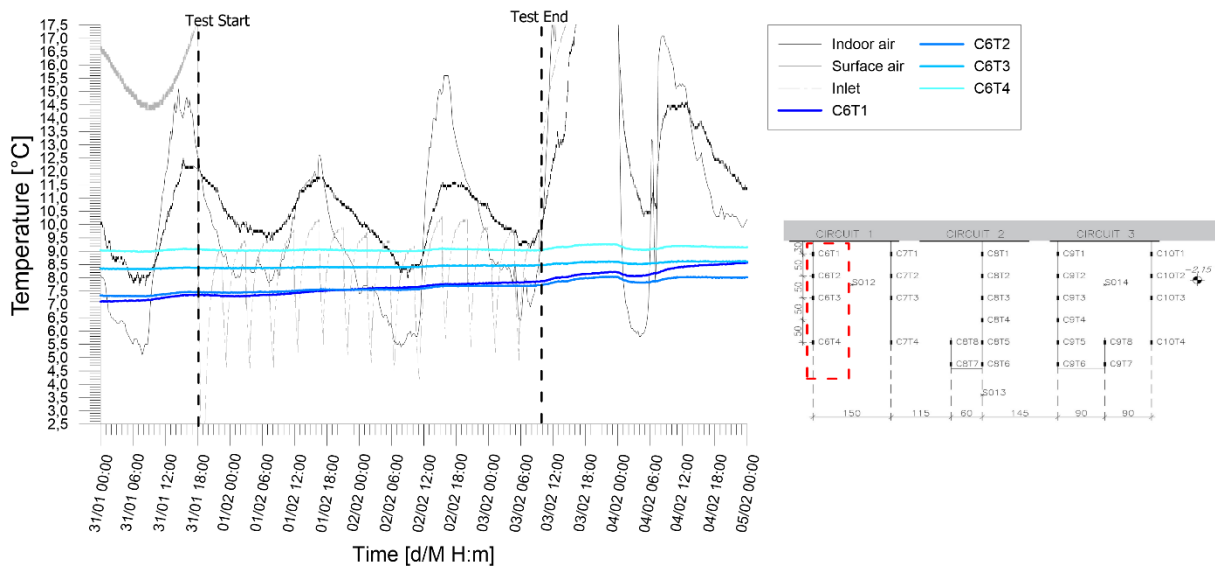


Figure A.9: Temperatures records from chain 6 of experimental test  
*H\_1+2\_20200131\_20200203*

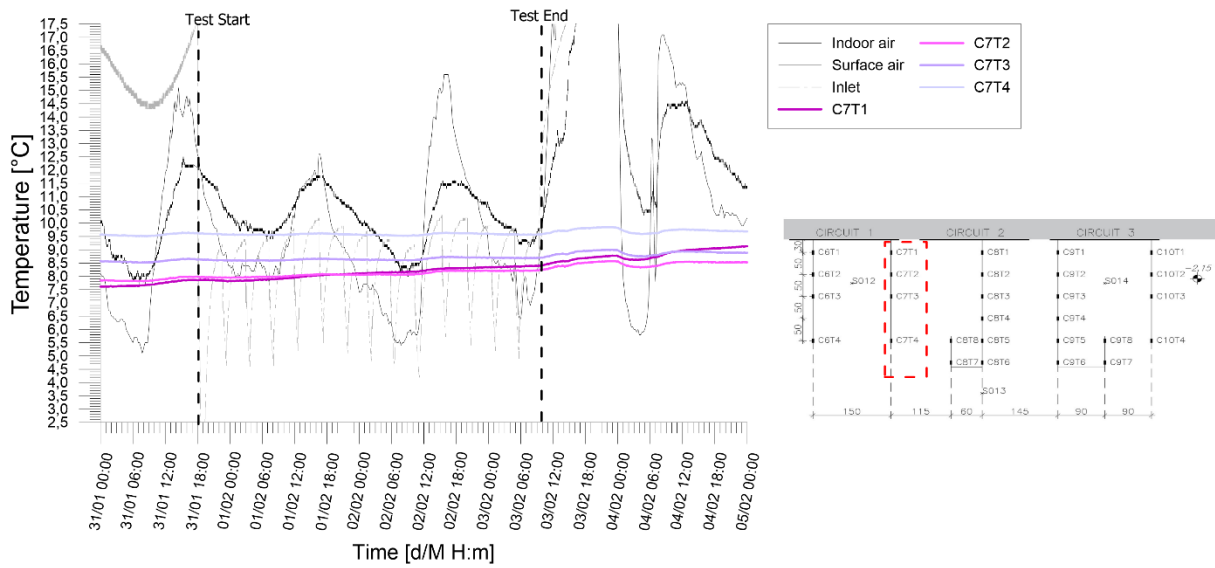


Figure A.10: Temperatures records from chain 7 of experimental test  
*H\_1+2\_20200131\_20200203*

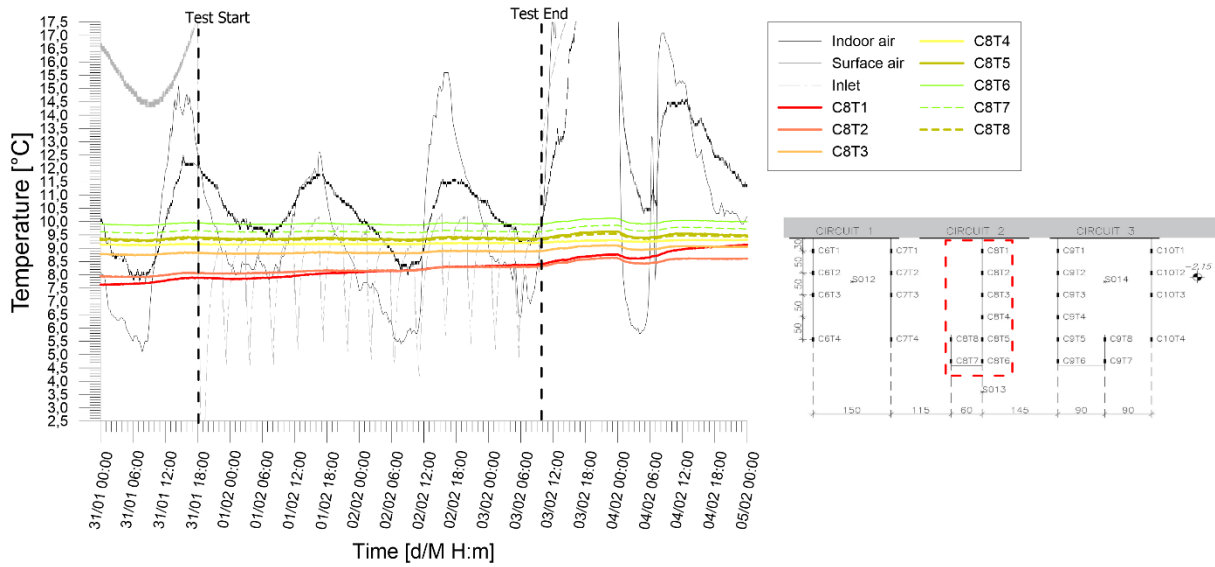


Figure A.11: Temperatures records from chain 8 of experimental test  
*H\_1+2\_20200131\_20200203*

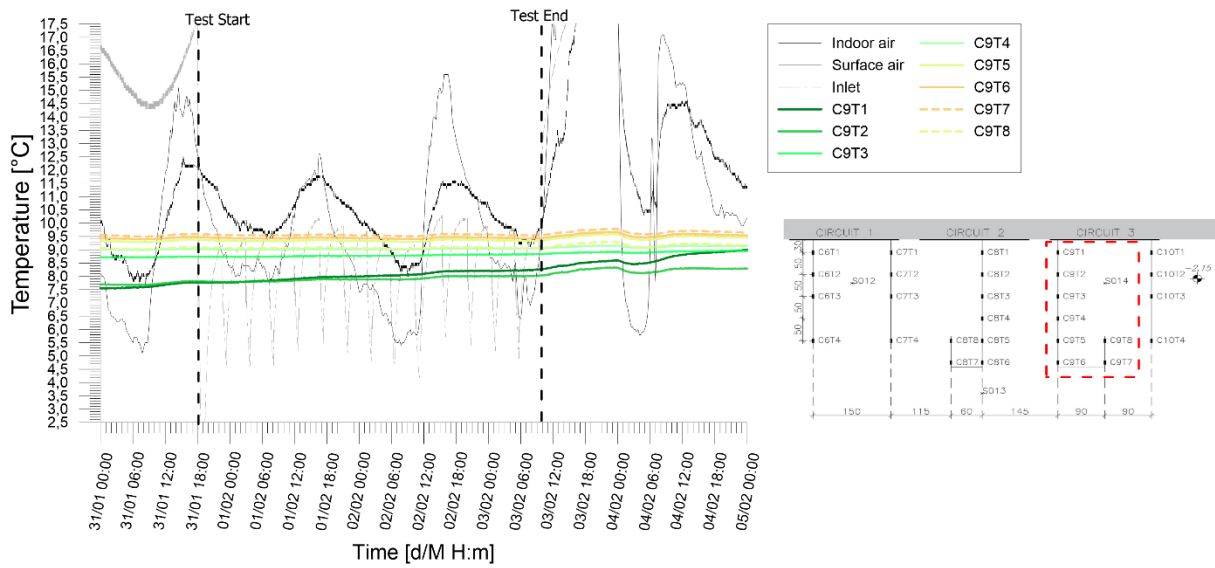


Figure A.12: Temperatures records from chain 9 of experimental test  
*H\_1+2\_20200131\_20200203*

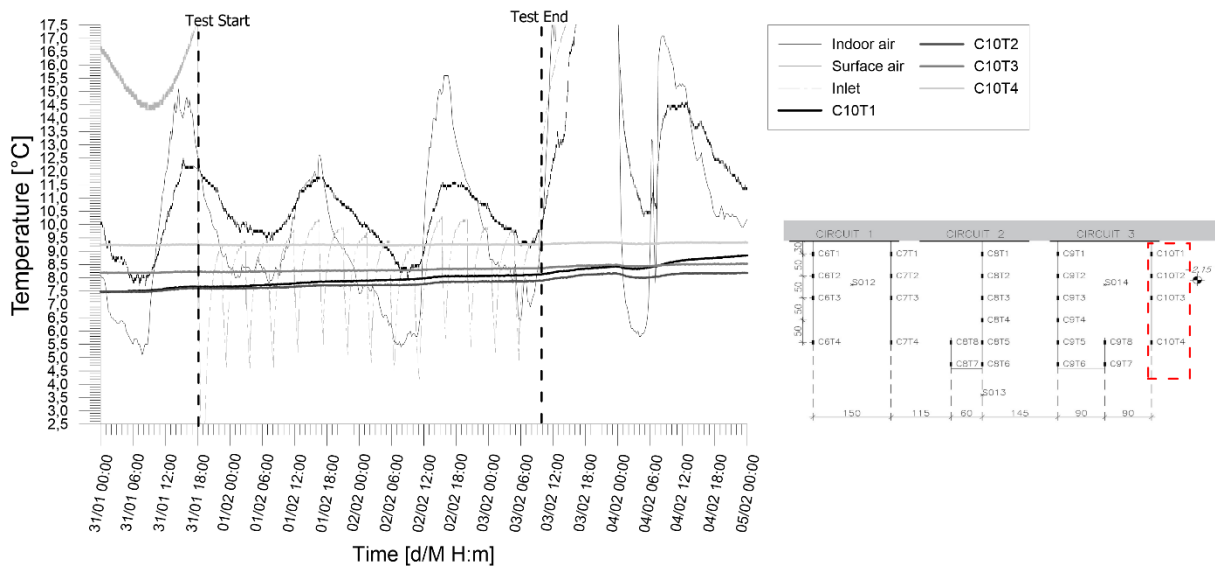


Figure A.13: Temperatures records from chain 10 of experimental test  
*H\_1+2\_20200131\_20200203*

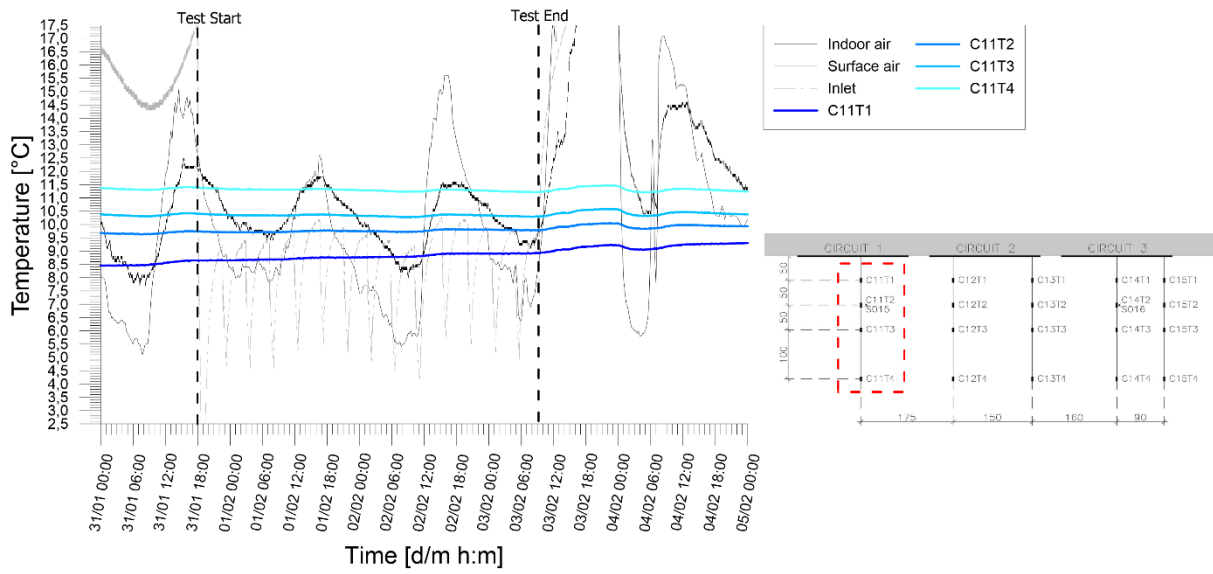


Figure A.14: Temperatures records from chain 11 of experimental test  
*H\_1+2\_20200131\_20200203*

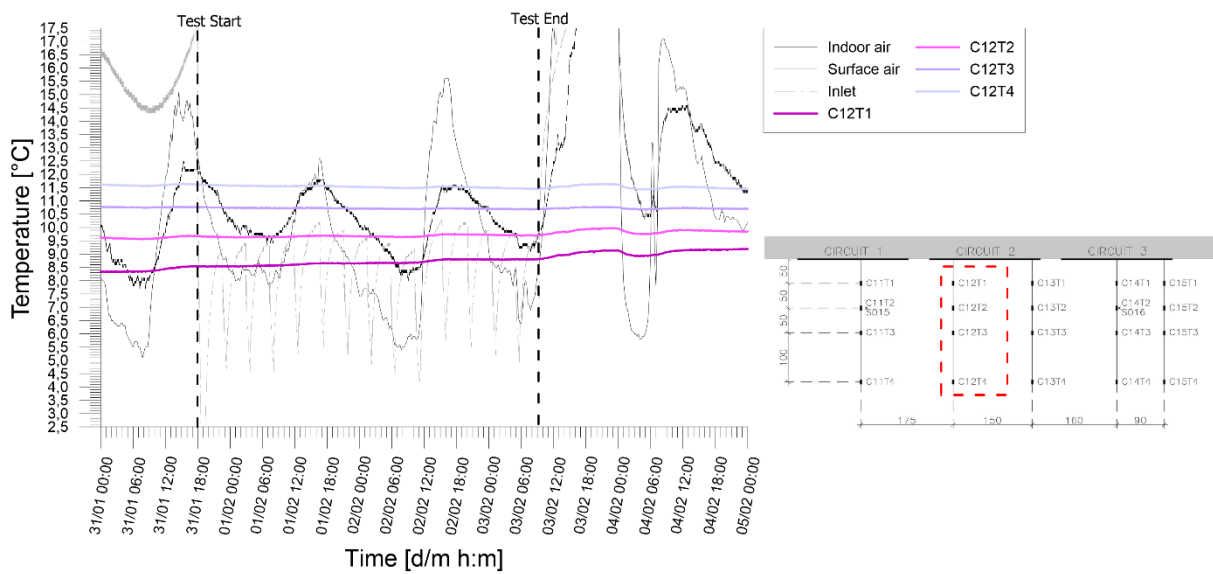


Figure A.15: Temperatures records from chain 12 of experimental test  
*H\_1+2\_20200131\_20200203*

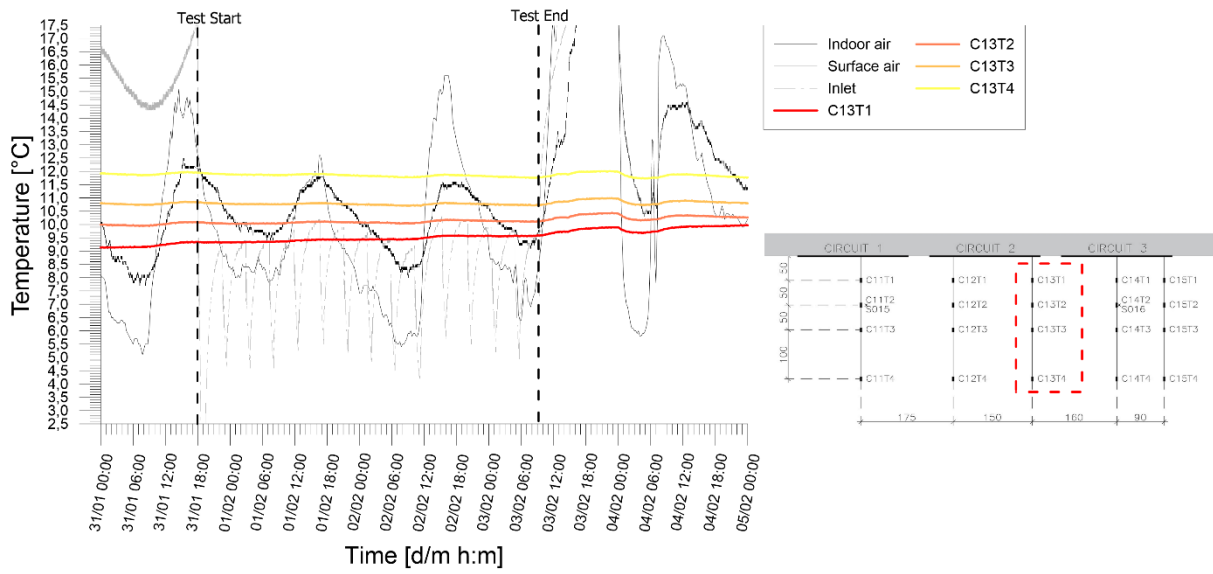


Figure A.16: Temperatures records from chain 13 of experimental test

H\_1+2\_20200131\_20200203

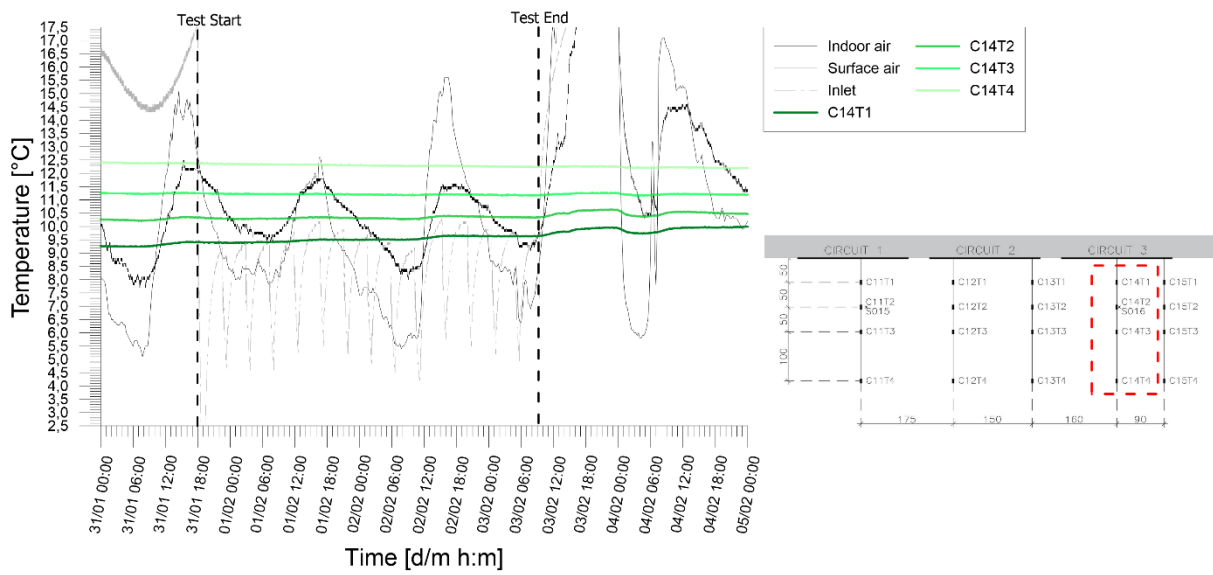


Figure A.17: Temperatures records from chain 14 of experimental test

H\_1+2\_20200131\_20200203

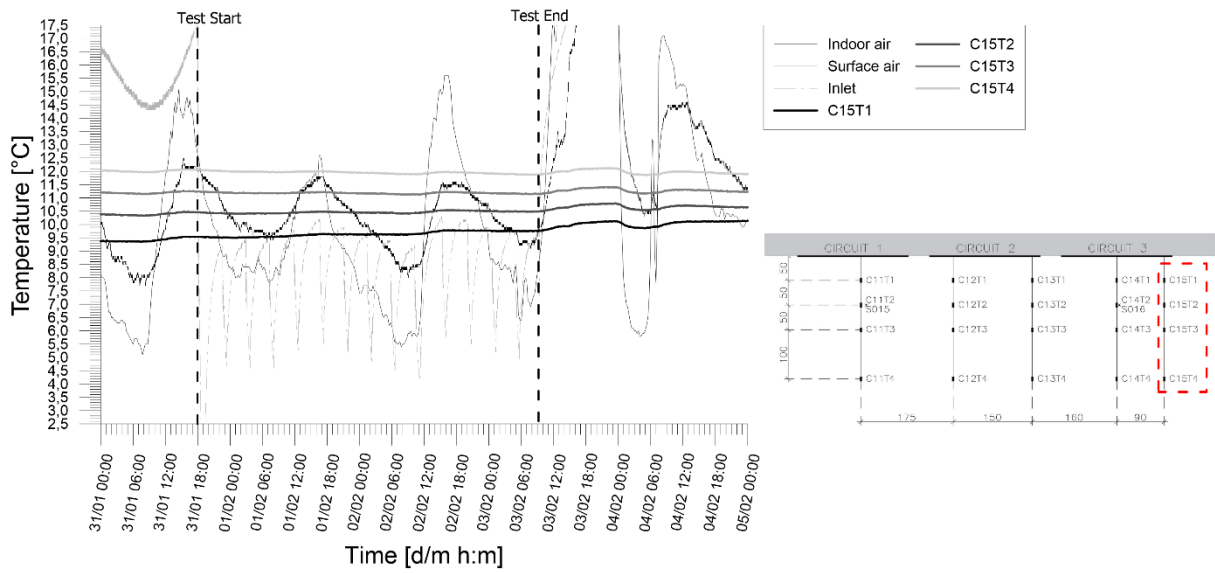


Figure A.18: Temperatures records from chain 15 of experimental test  
*H\_1+2\_20200131\_20200203*

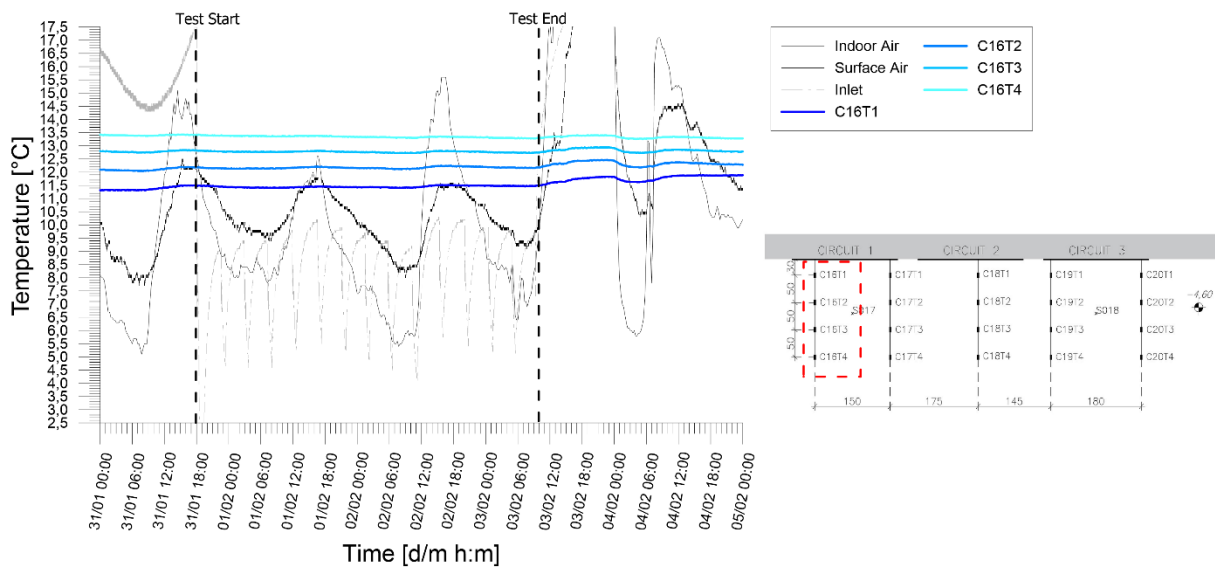


Figure A.19: Temperatures records from chain 16 of experimental test  
*H\_1+2\_20200131\_20200203*

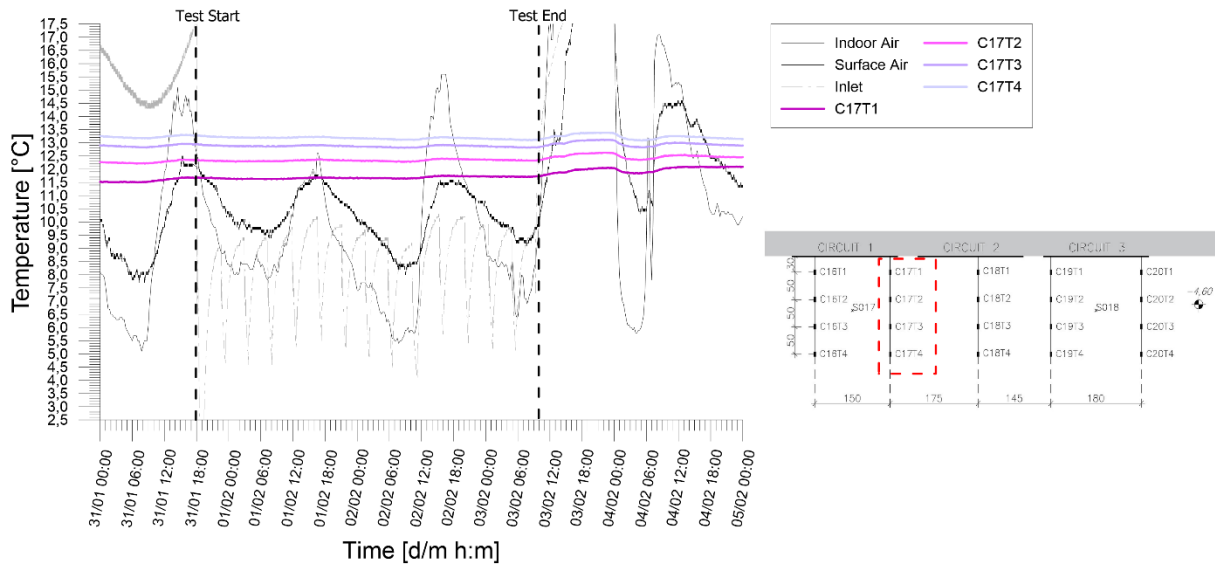


Figure A.20: Temperatures records from chain 17 of experimental test  
*H\_1+2\_20200131\_20200203*

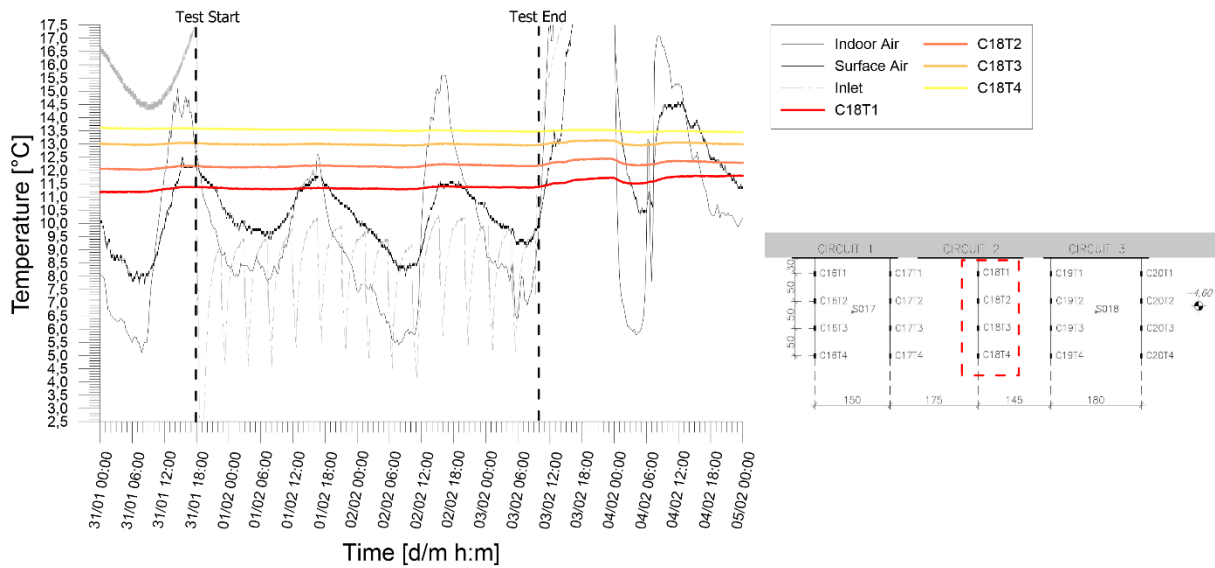


Figure A.21: Temperatures records from chain 18 of experimental test  
*H\_1+2\_20200131\_20200203*

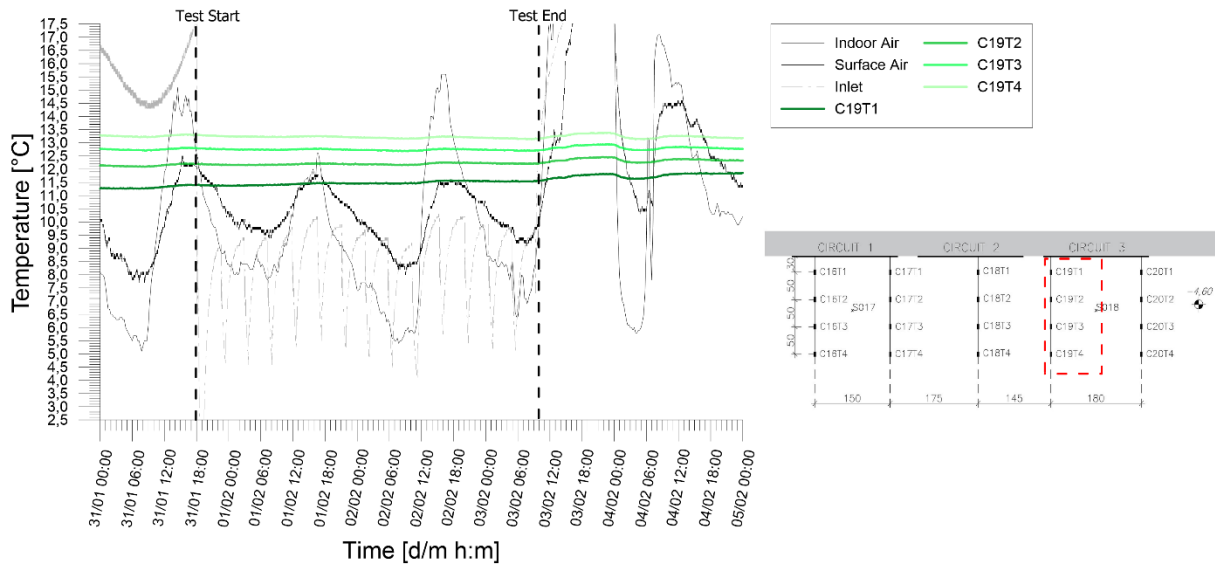


Figure A.22: Temperatures records from chain 19 of experimental test  
*H\_1+2\_20200131\_20200203*

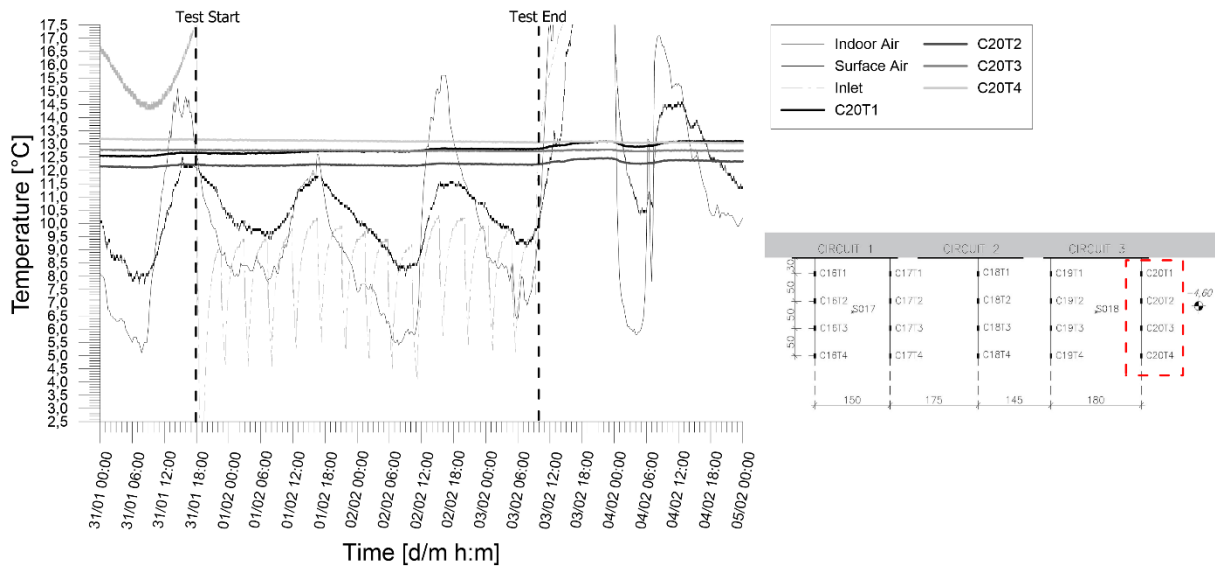


Figure A.23: Temperatures records from chain 20 of experimental test  
*H\_1+2\_20200131\_20200203*

## 2. Test H\_2+3\_20200207\_20200210

Table A.2: Main features of the test

|                                    |                |
|------------------------------------|----------------|
| Test start time                    | 07/02/20 19.30 |
| Test end time                      | 10/02/20 09.20 |
| Duration [h]                       | 61.8           |
| Operative mode                     | Heating        |
| Active circuit(s)                  | 2;3            |
| Circuit link                       | Parallel       |
| Target temperature user [°C]       | 45             |
| Flow rate at the ground side [l/h] | 925.8          |

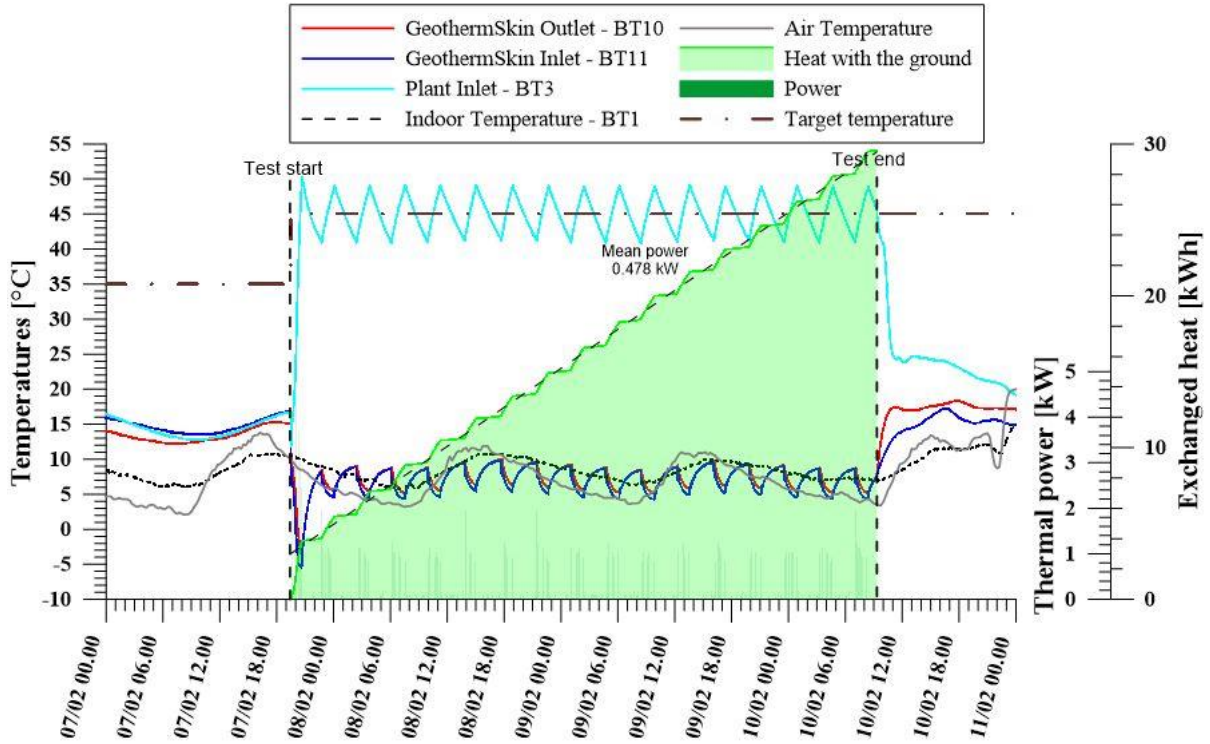


Figure A.24: Thermal performance interpretation of experimental test *H\_2+3\_20200207\_20200210* with parallel link of circuit 2 and 3 in heating mode.

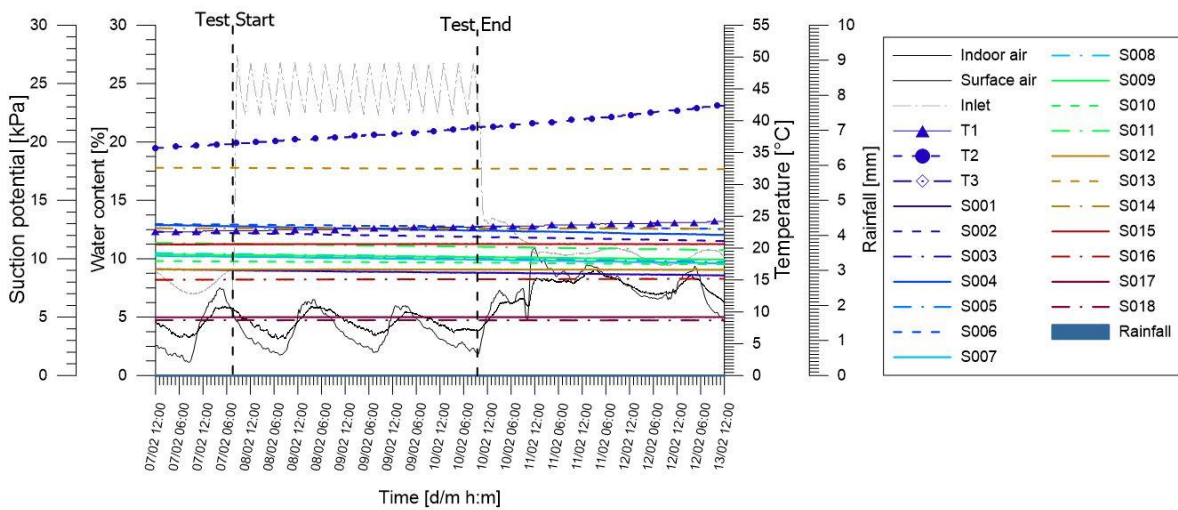


Figure A.25: Tensiometer and hygrometers records of experimental test *H\_2+3\_20200207\_20200210* together with monitored rainfall from Politecnico weather station.

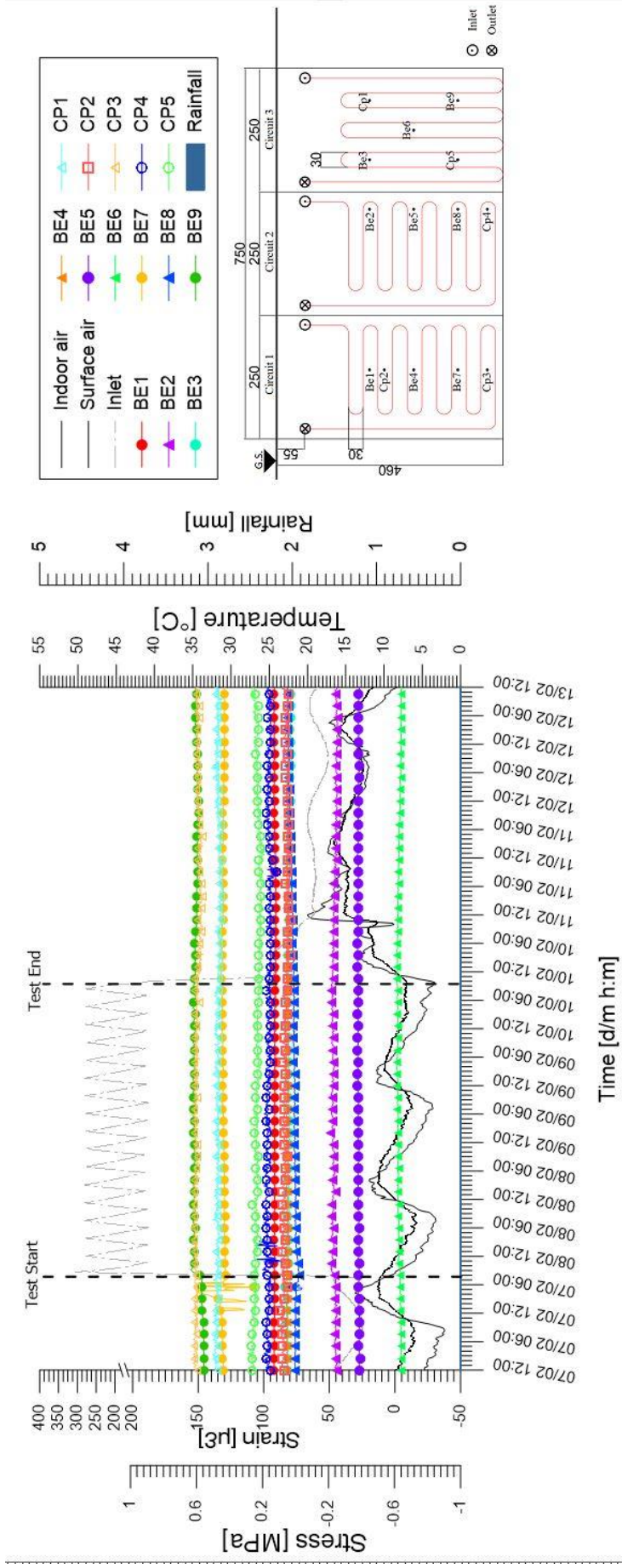


Figure A.26: Stresses and strains monitored at the wall external facade during experimental

test H\_2+3\_20200207\_20200210



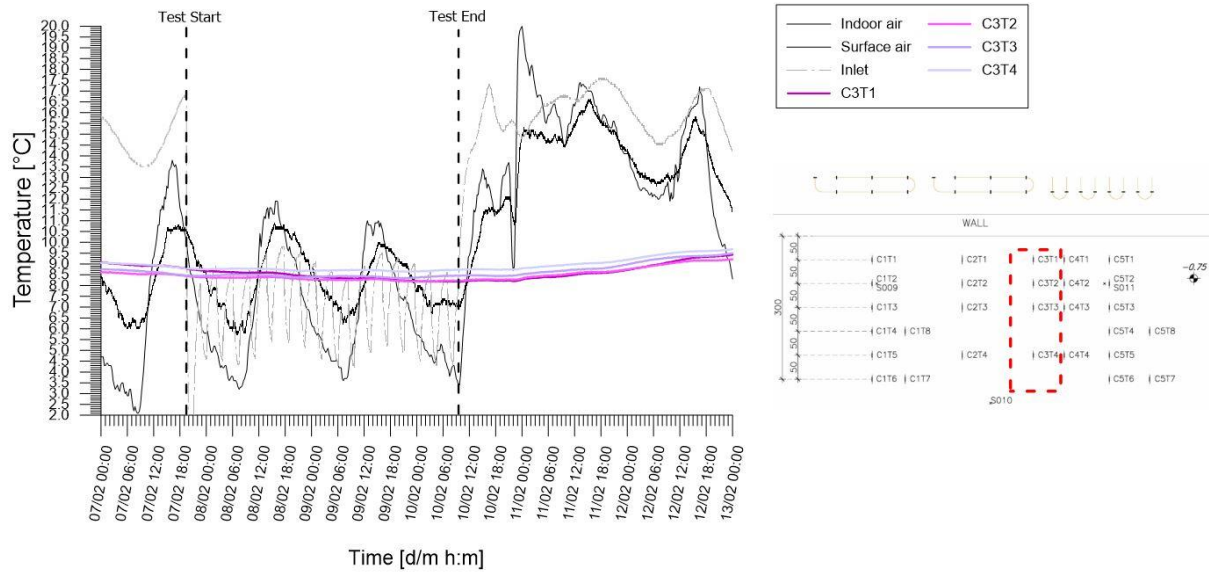


Figure A.29: Temperatures records from chain 3 of experimental test  
*H\_2+3\_20200207\_20200210*

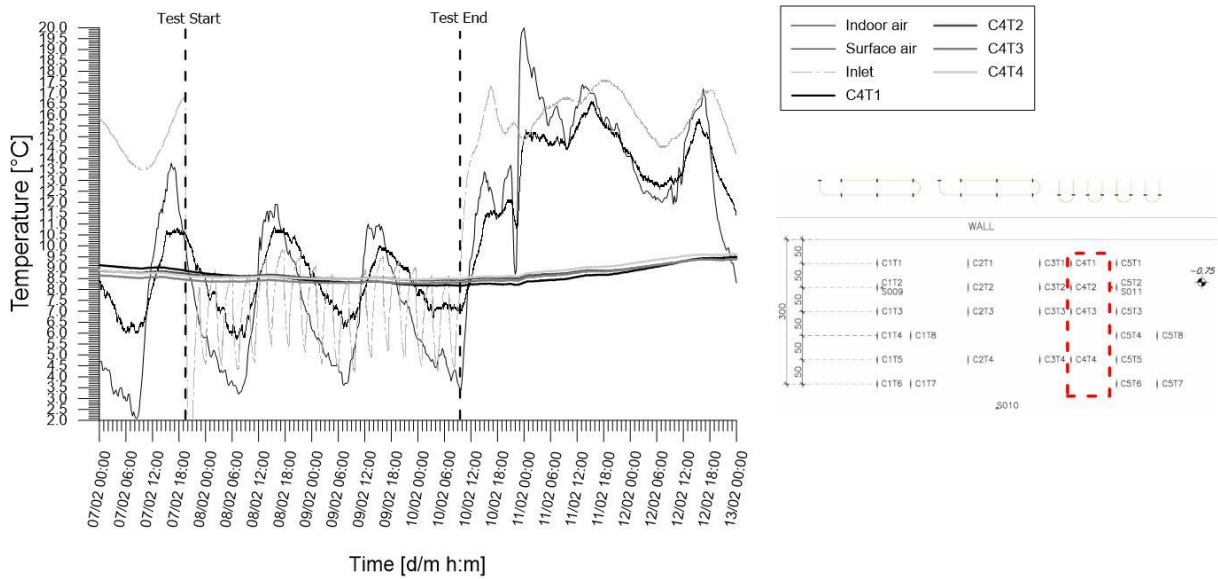


Figure A.30: Temperatures records from chain 4 of experimental test  
*H\_2+3\_20200207\_20200210*

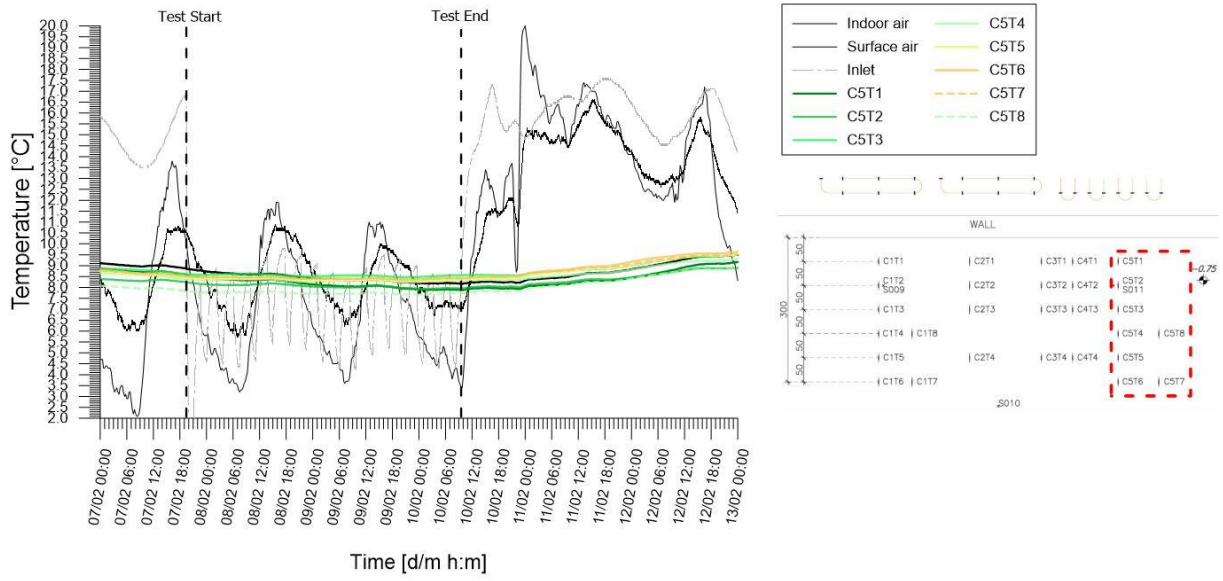


Figure A.31: Temperatures records from chain 5 of experimental test

H\_2+3\_20200207\_20200210

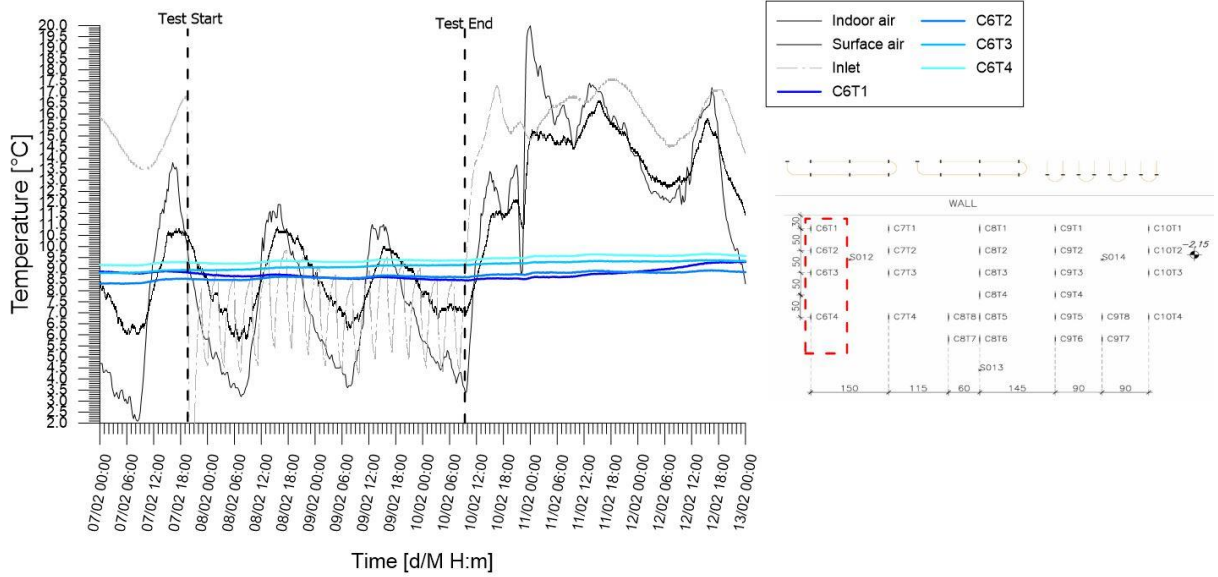


Figure A.32: Temperatures records from chain 6 of experimental test

H\_2+3\_20200207\_20200210

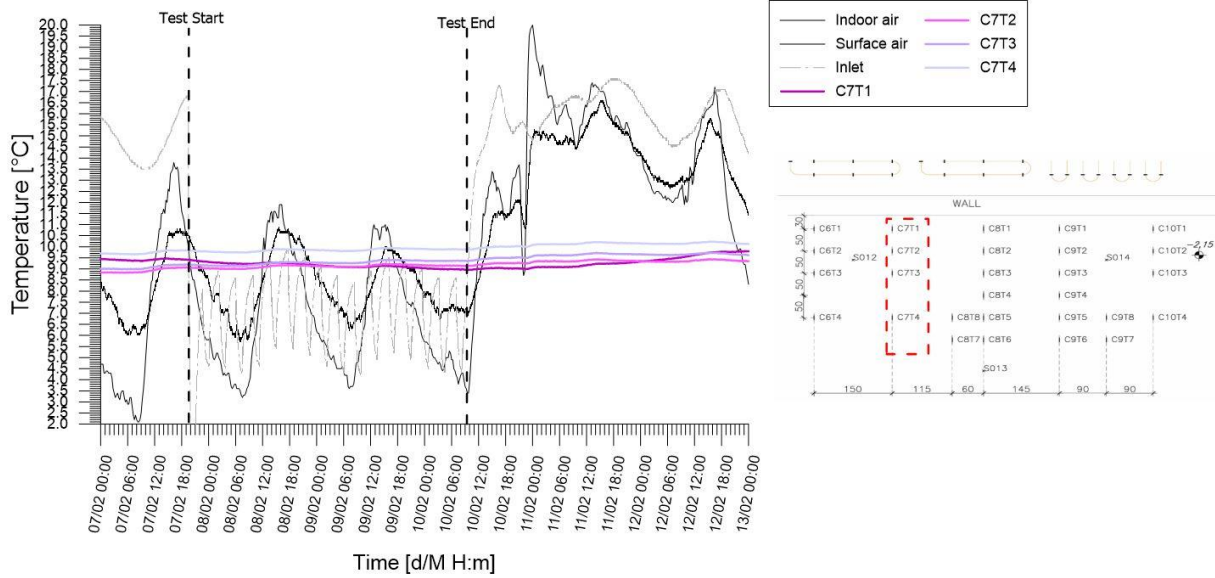


Figure A.33: Temperatures records from chain 7 of experimental test  
*H\_2+3\_20200207\_20200210*

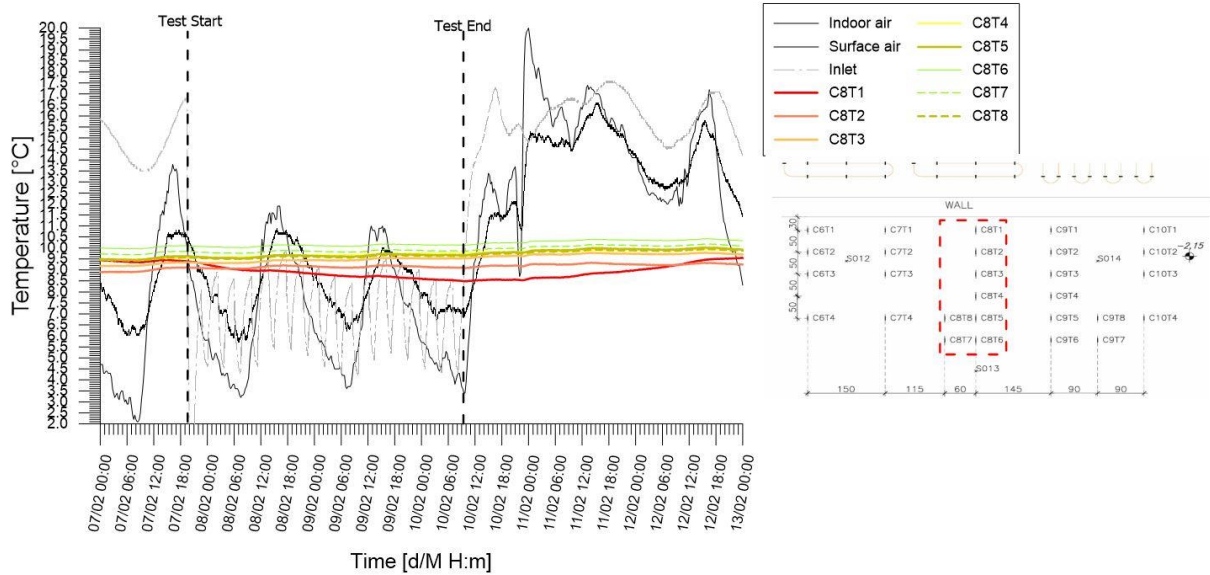


Figure A.34: Temperatures records from chain 8 of experimental test  
*H\_2+3\_20200207\_20200210*

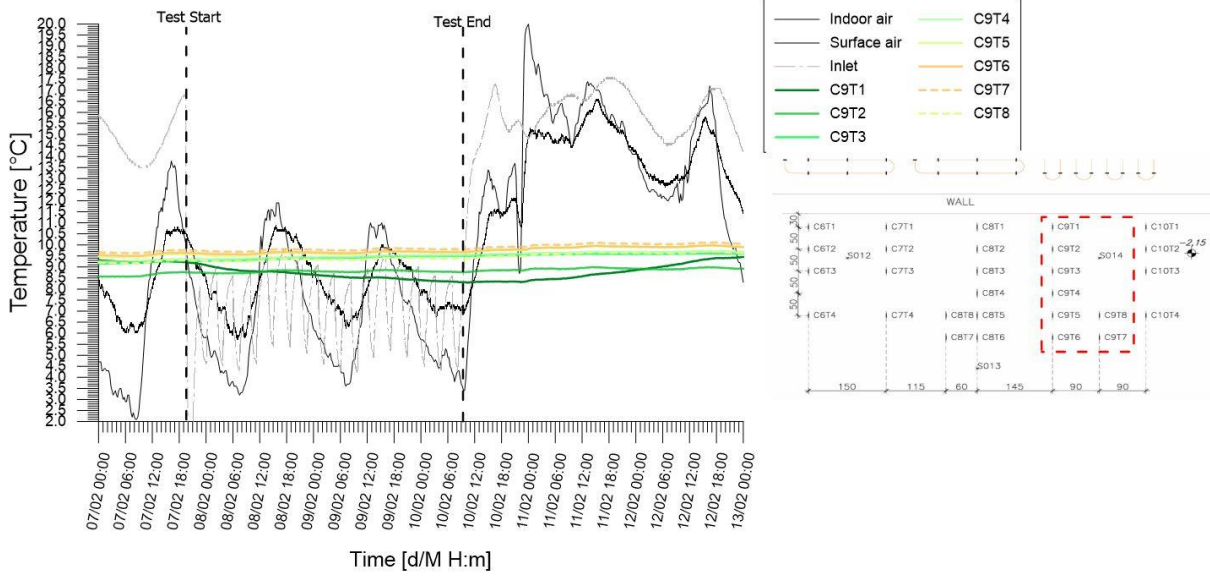


Figure A.35: Temperatures records from chain 9 of experimental test

H\_2+3\_20200207\_20200210

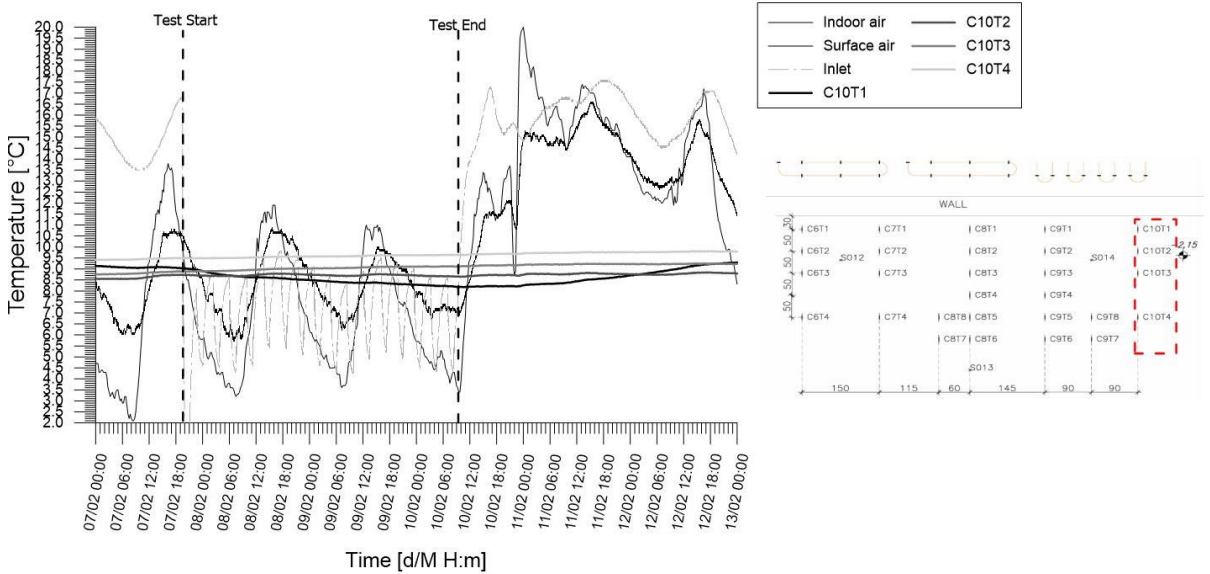


Figure A.36: Temperatures records from chain 10 of experimental test

H\_2+3\_20200207\_20200210

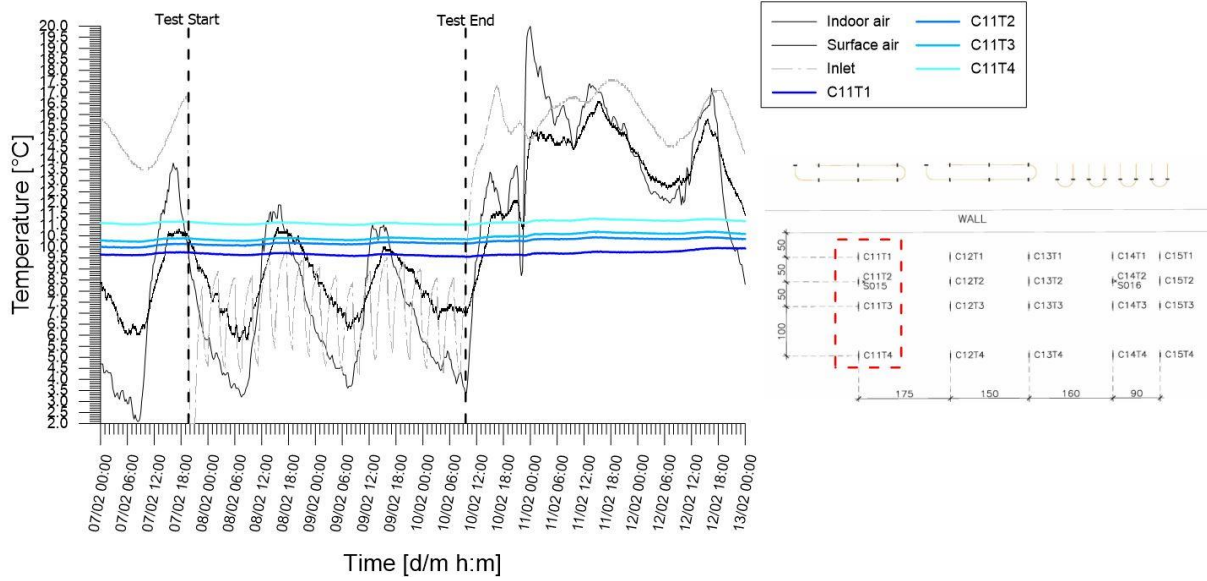


Figure A.37: Temperatures records from chain 11 of experimental test

H\_2+3\_20200207\_20200210

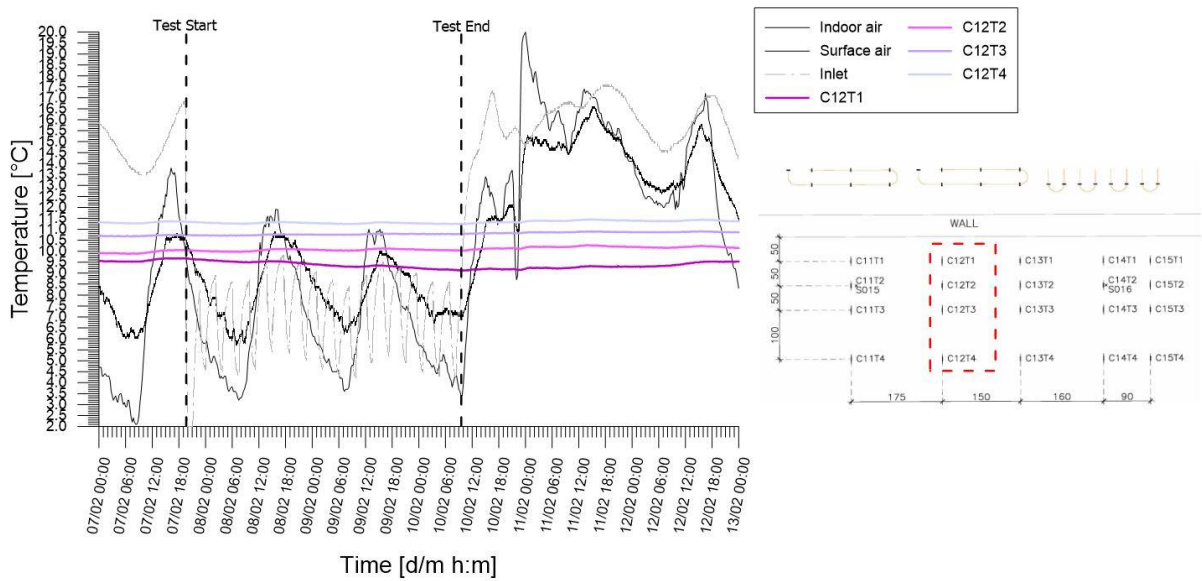


Figure A.38: Temperatures records from chain 12 of experimental test

H\_2+3\_20200207\_20200210

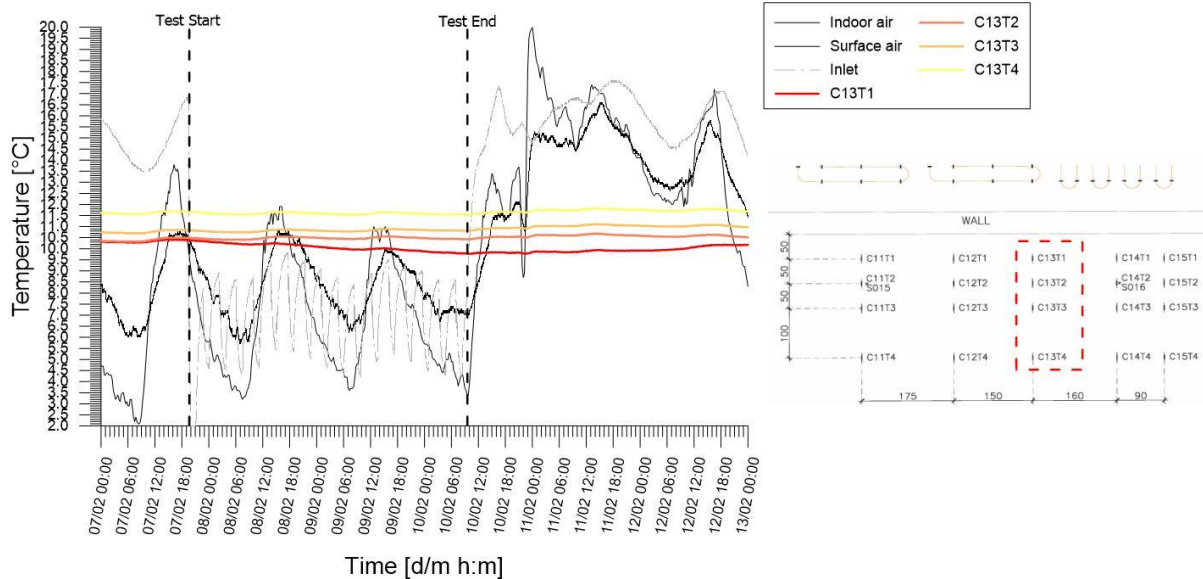


Figure A.39: Temperatures records from chain 13 of experimental test  
*H\_2+3\_20200207\_20200210*

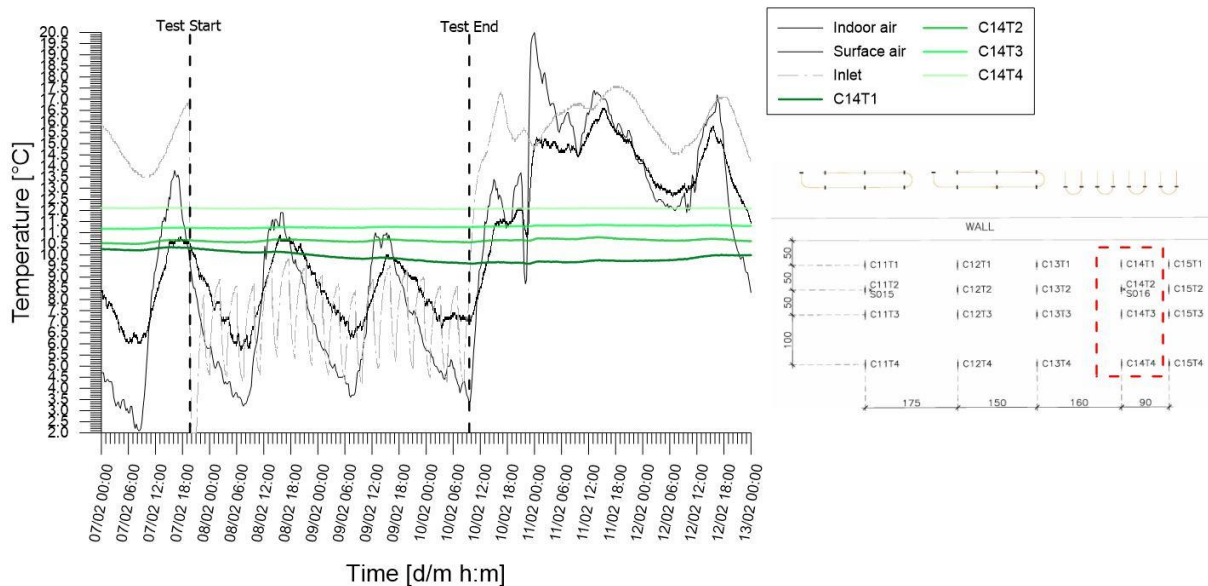


Figure A.40: Temperatures records from chain 14 of experimental test  
*H\_2+3\_20200207\_20200210*

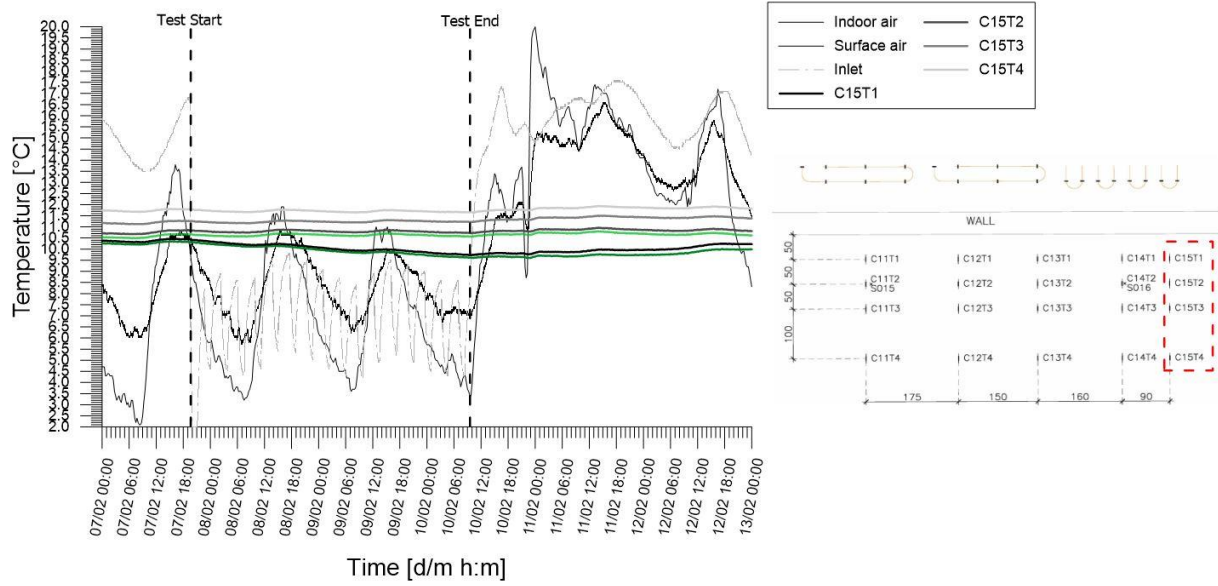


Figure A.41: Temperatures records from chain 15 of experimental test

H\_2+3\_20200207\_20200210

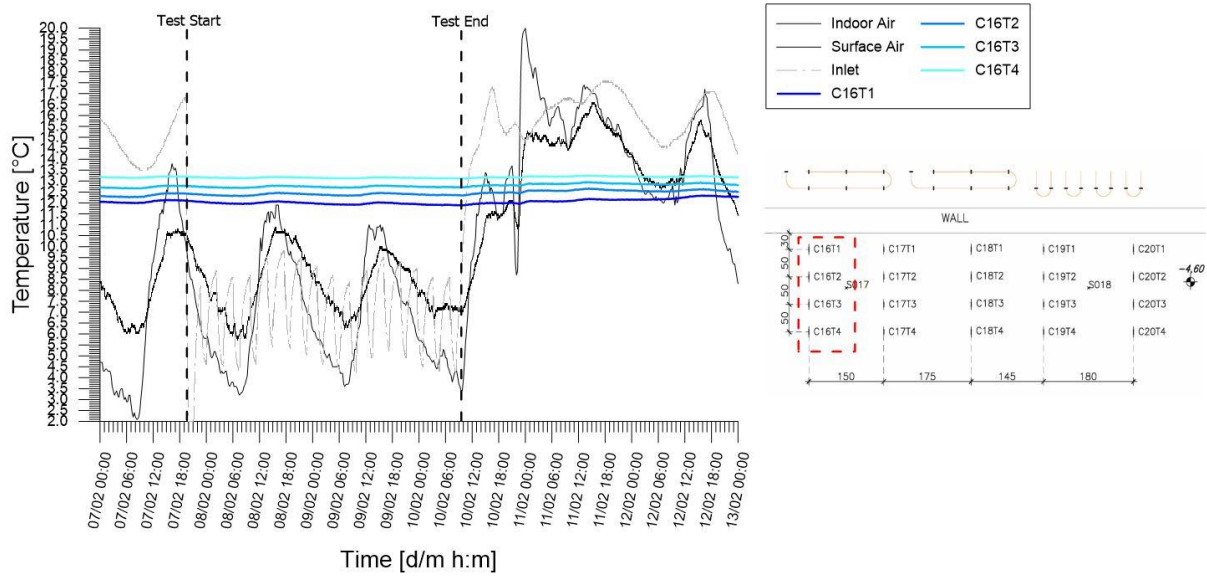


Figure A.42: Temperatures records from chain 16 of experimental test

H\_2+3\_20200207\_20200210

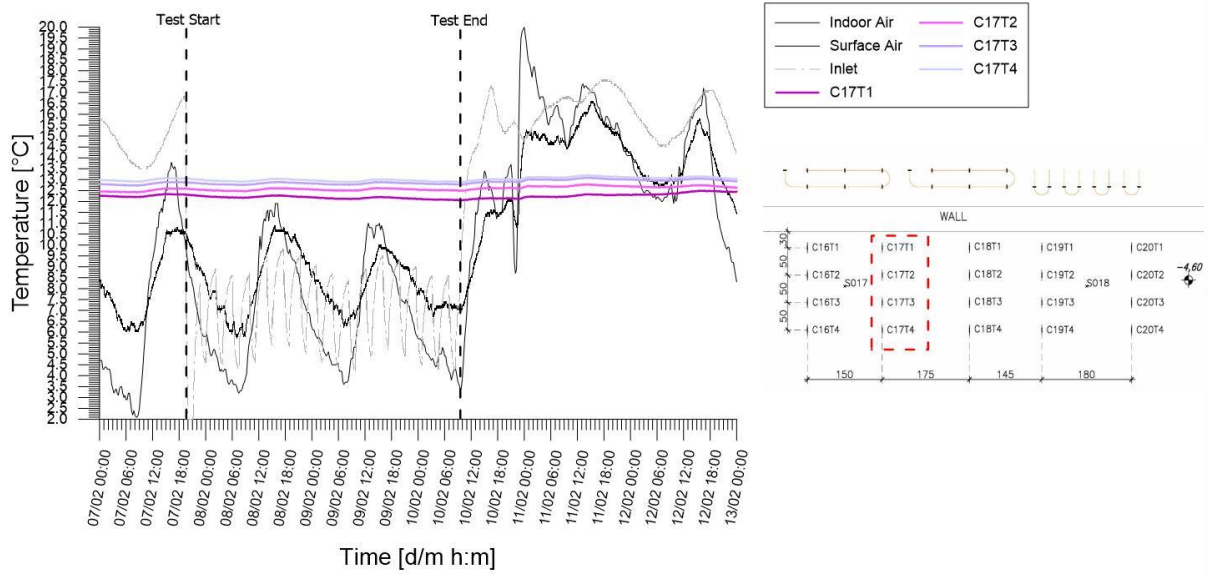


Figure A.43: Temperatures records from chain 17 of experimental test  
*H\_2+3\_20200207\_20200210*

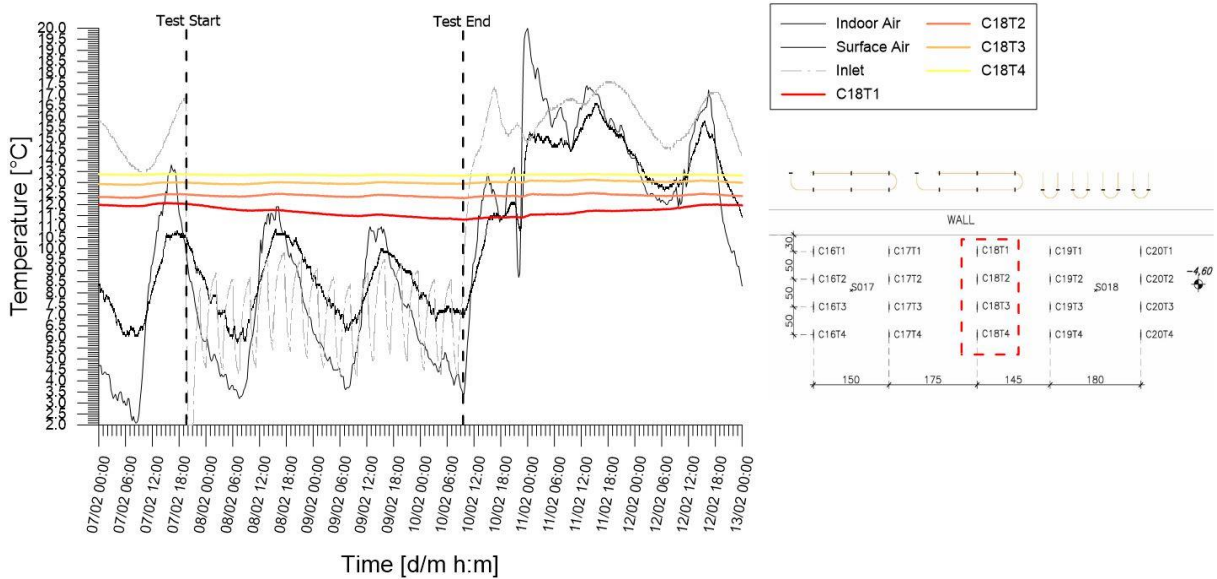


Figure A.44: Temperatures records from chain 18 of experimental test  
*H\_2+3\_20200207\_20200210*

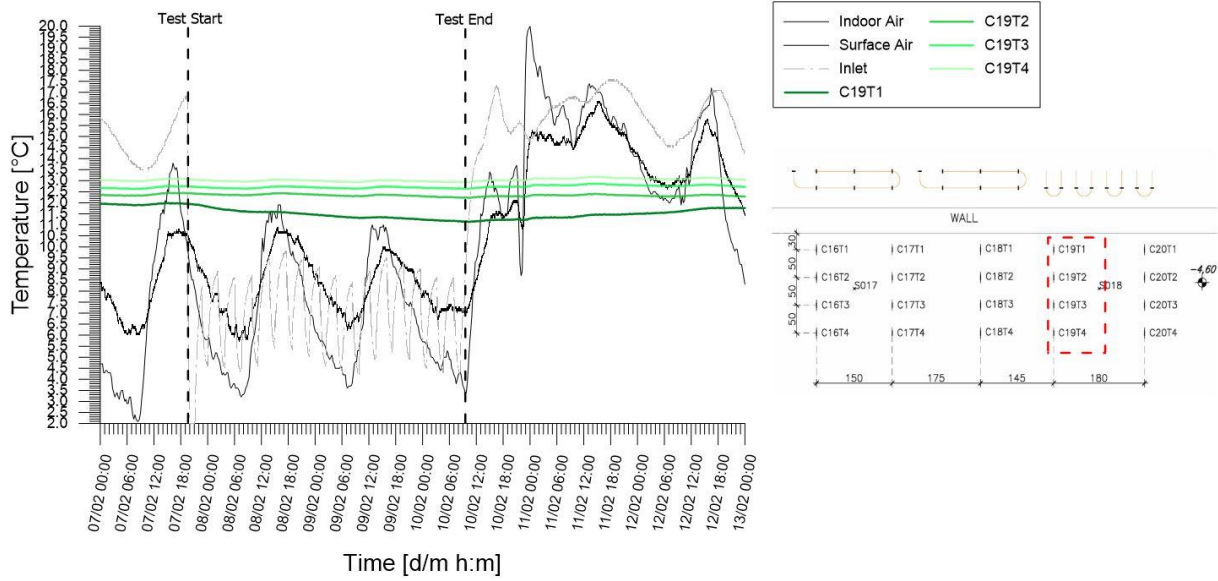


Figure A.45: Temperatures records from chain 19 of experimental test  
 H\_2+3\_20200207\_20200210

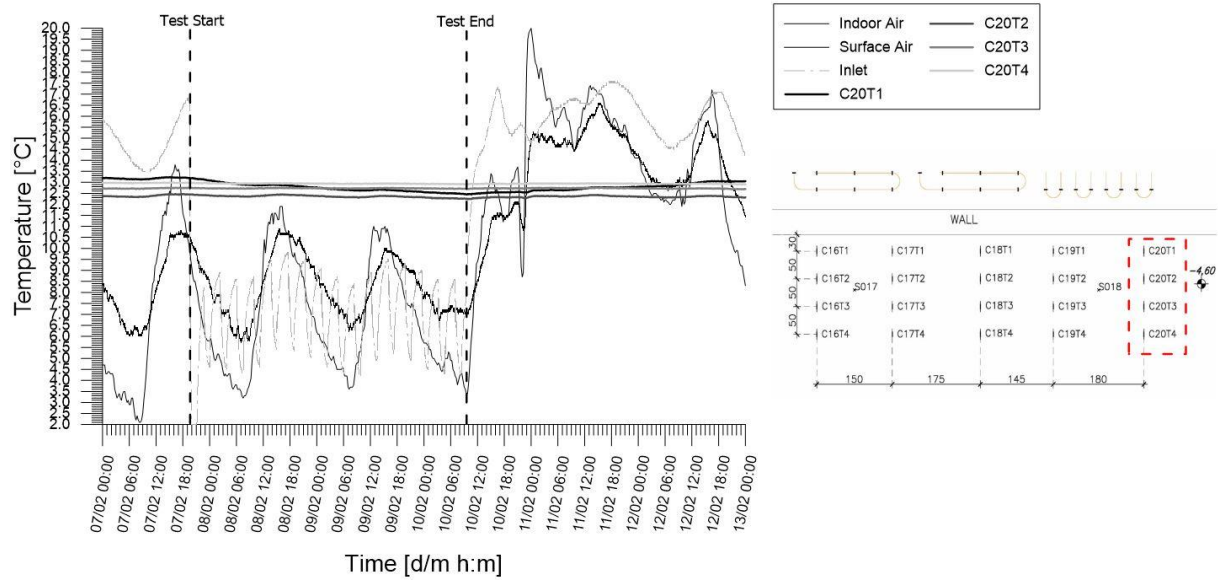


Figure A.46: Temperatures records from chain 20 of experimental test  
 H\_2+3\_20200207\_20200210

### 3. Test H\_1+3\_20200214\_20200217

*Table A.3: Main features of the test*

|                                    |                |
|------------------------------------|----------------|
| Test start time                    | 14/02/20 19.20 |
| Test end time                      | 17/02/20 9.20  |
| Duration [h]                       | 62             |
| Operative mode                     | Heating        |
| Active circuit(s)                  | 1;3            |
| Circuit link                       | Parallel       |
| Target temperature user [°C]       | 45             |
| Flow rate at the ground side [l/h] | 282            |

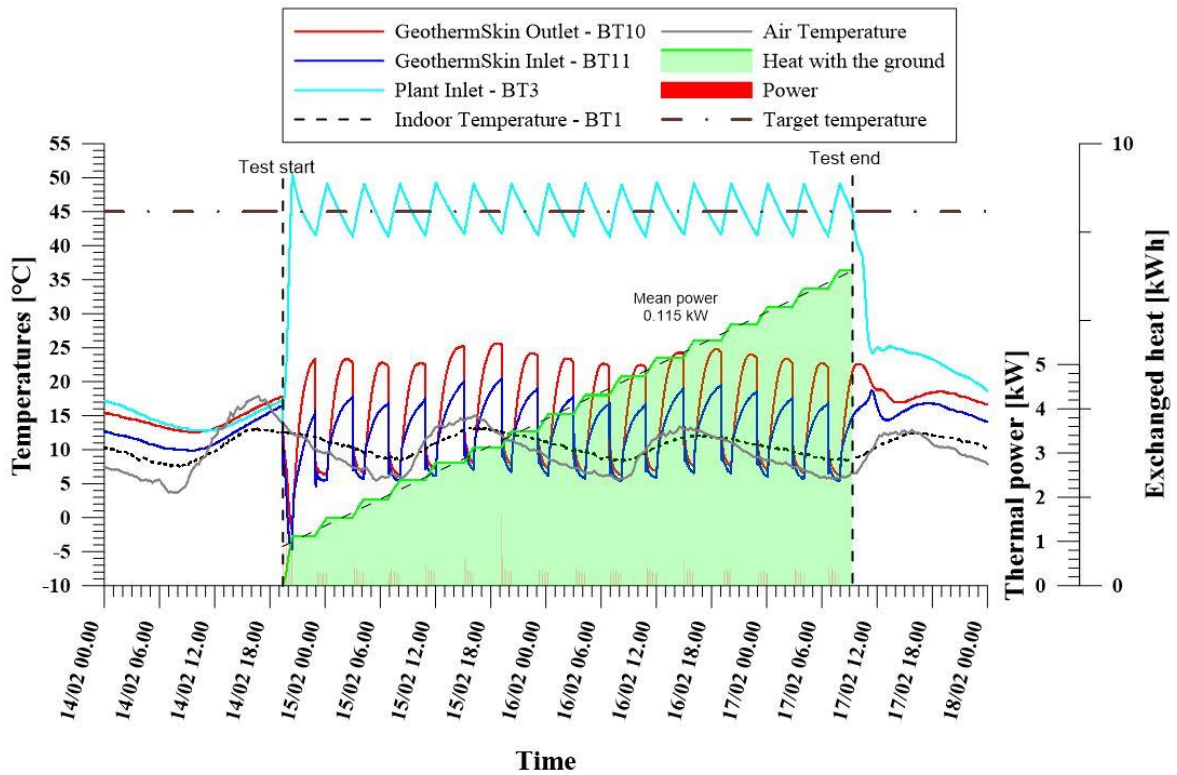


Figure A.47: Thermal performance interpretation of experimental test *H\_1+3\_20200214\_20200217* with parallel link of circuit 1 and 3 in heating mode.

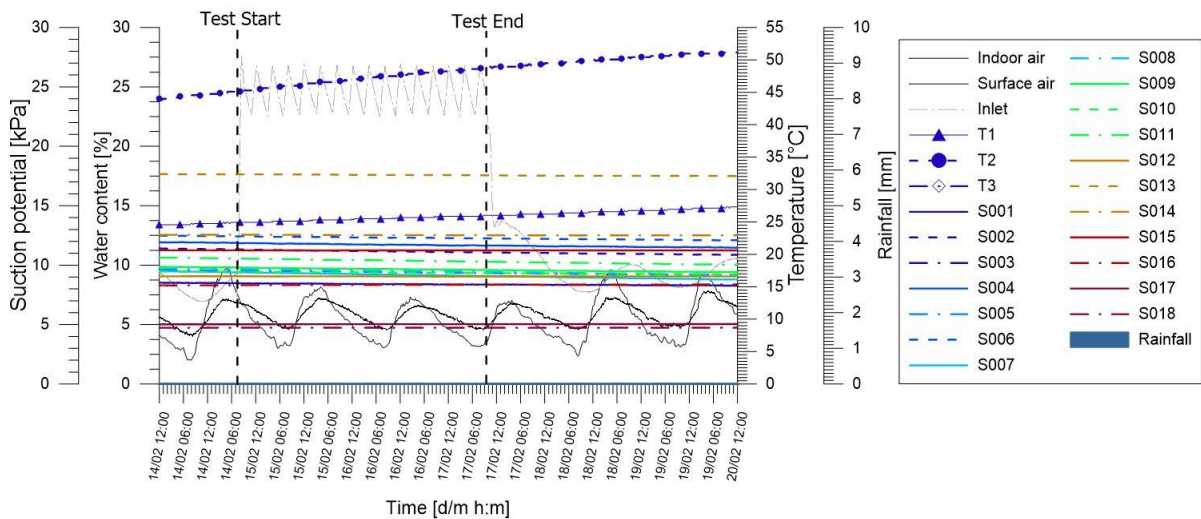


Figure A.48: Tensiometer and hygrometers records of experimental test *H\_1+3\_20200214\_20200217* together with monitored rainfall from Politecnico weather station.

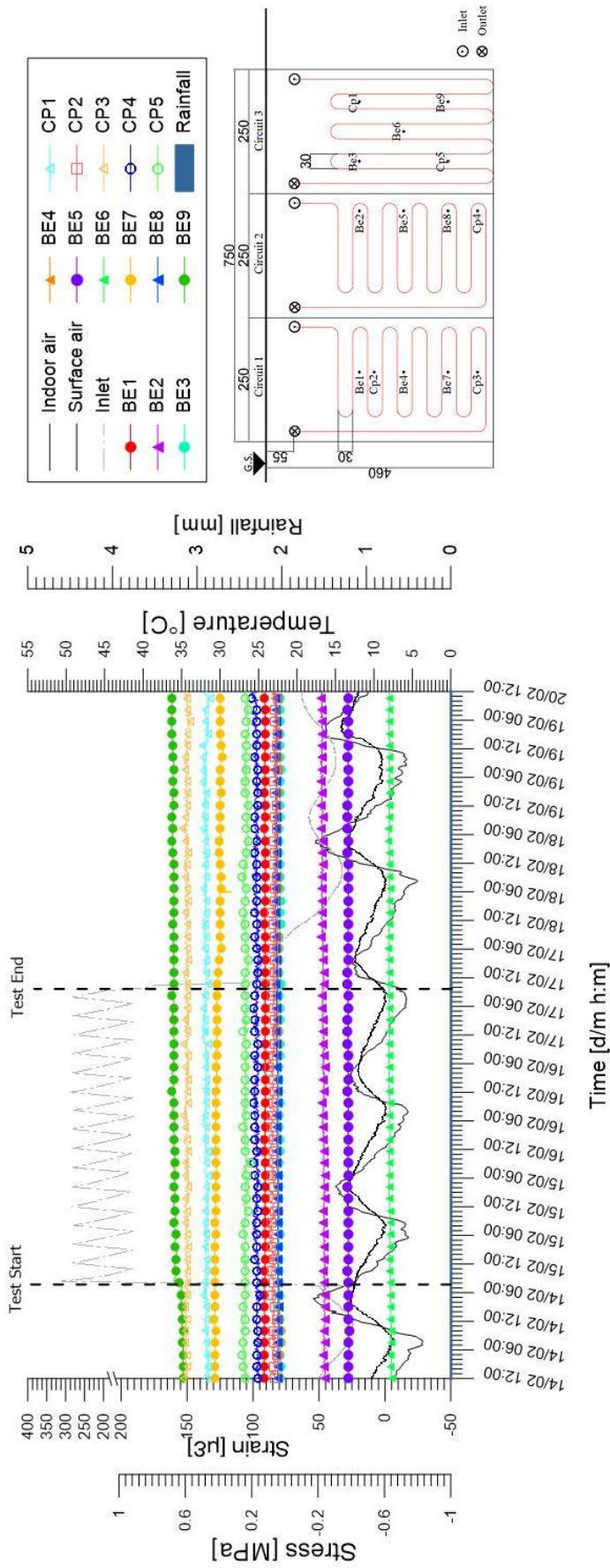


Figure A.49: Stresses and strains monitored at the wall external facade during experimental test  
 H\_I+3\_20200214\_20200217

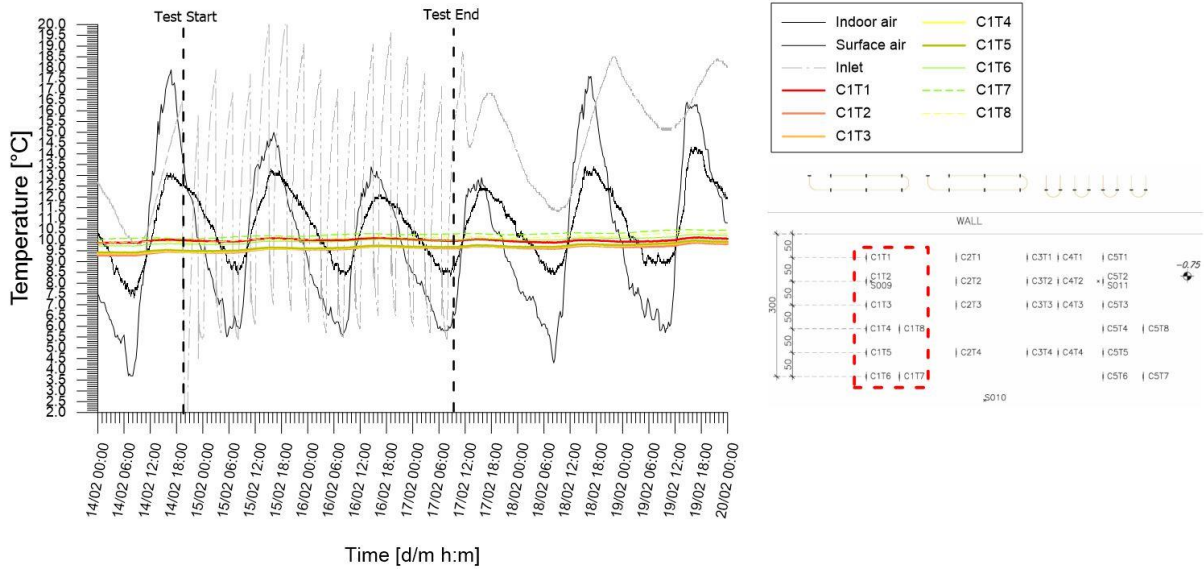


Figure A.50: Temperatures records from chain 1 of experimental test  
 H\_1+3\_20200214\_20200217

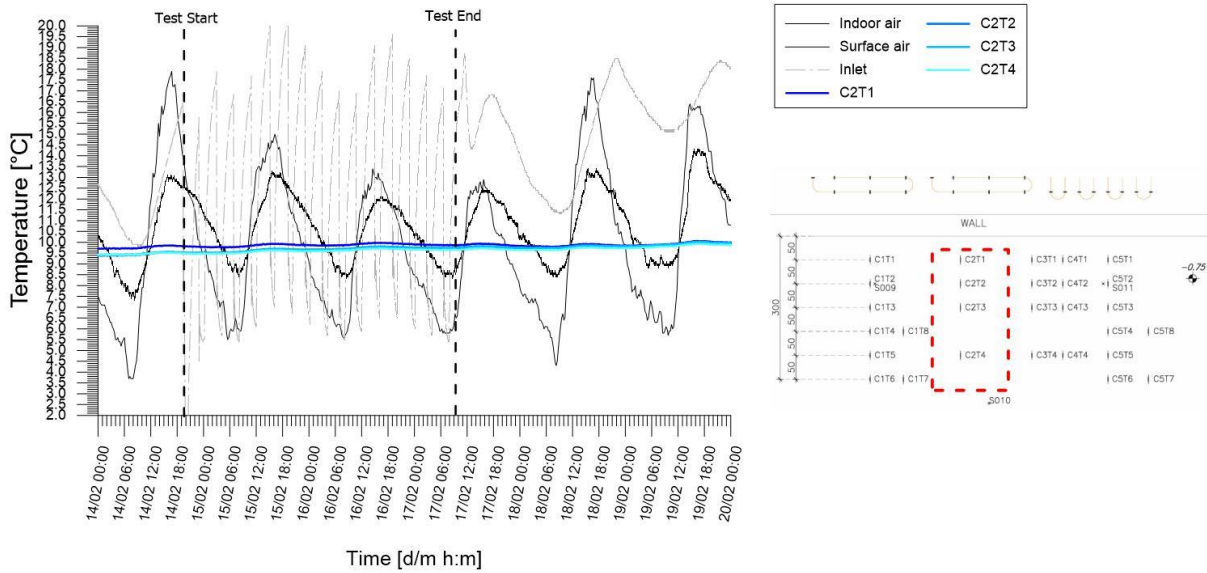


Figure A.51: Temperatures records from chain 2 of experimental test  
 H\_1+3\_20200214\_20200217

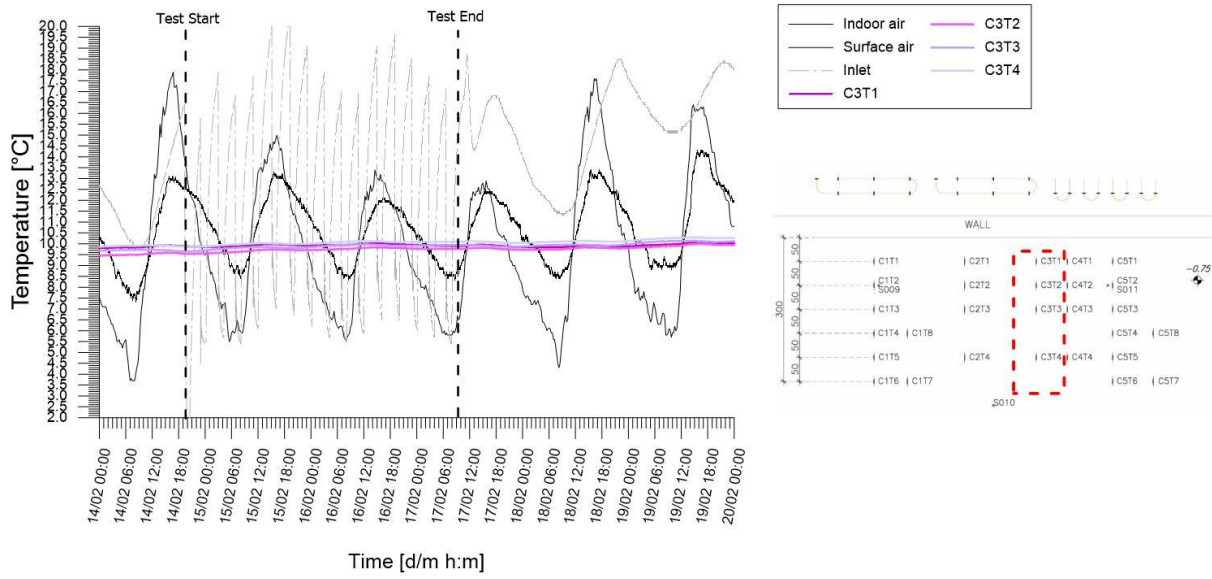


Figure A.52: Temperatures records from chain 3 of experimental test  
 H\_1+3\_20200214\_20200217

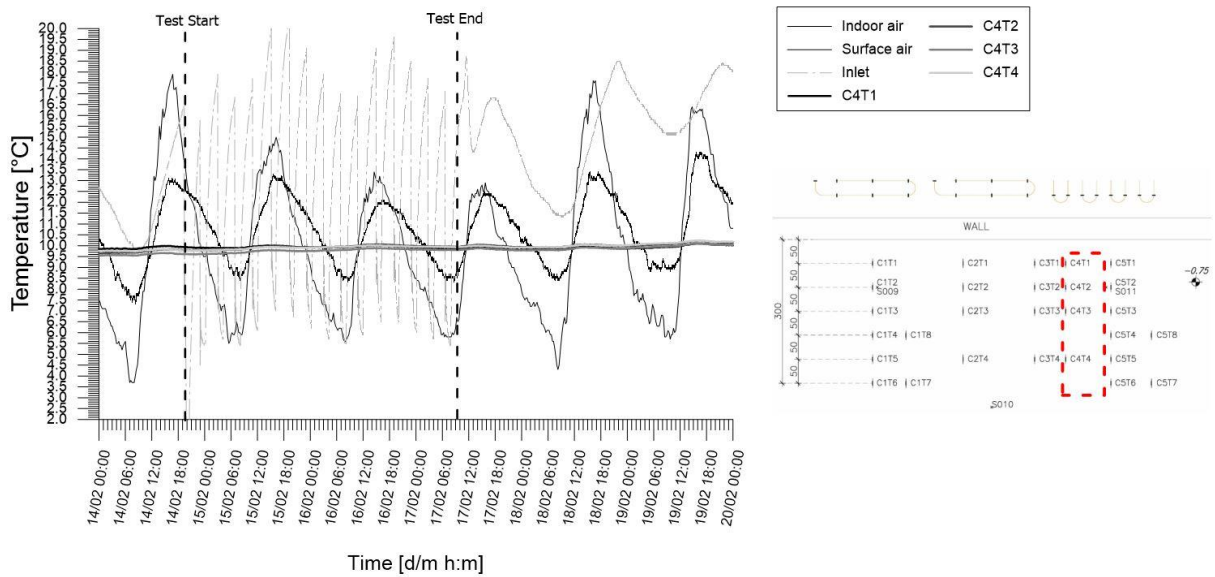


Figure A.53: Temperatures records from chain 4 of experimental test  
 H\_1+3\_20200214\_20200217



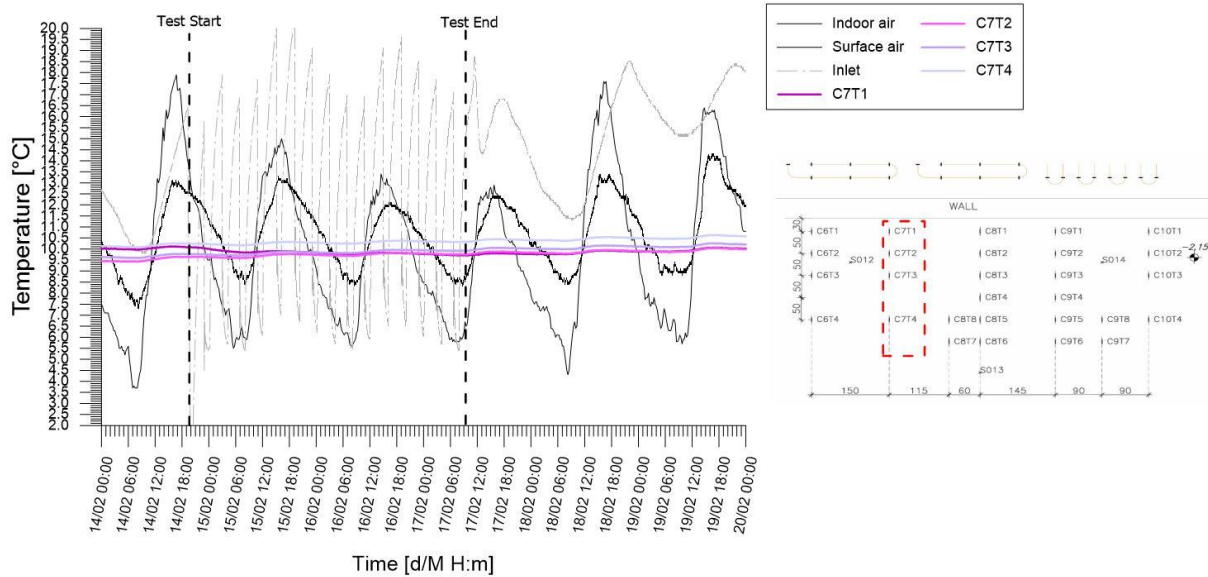


Figure A.56: Temperatures records from chain 7 of experimental test  
 H\_1+3\_20200214\_20200217

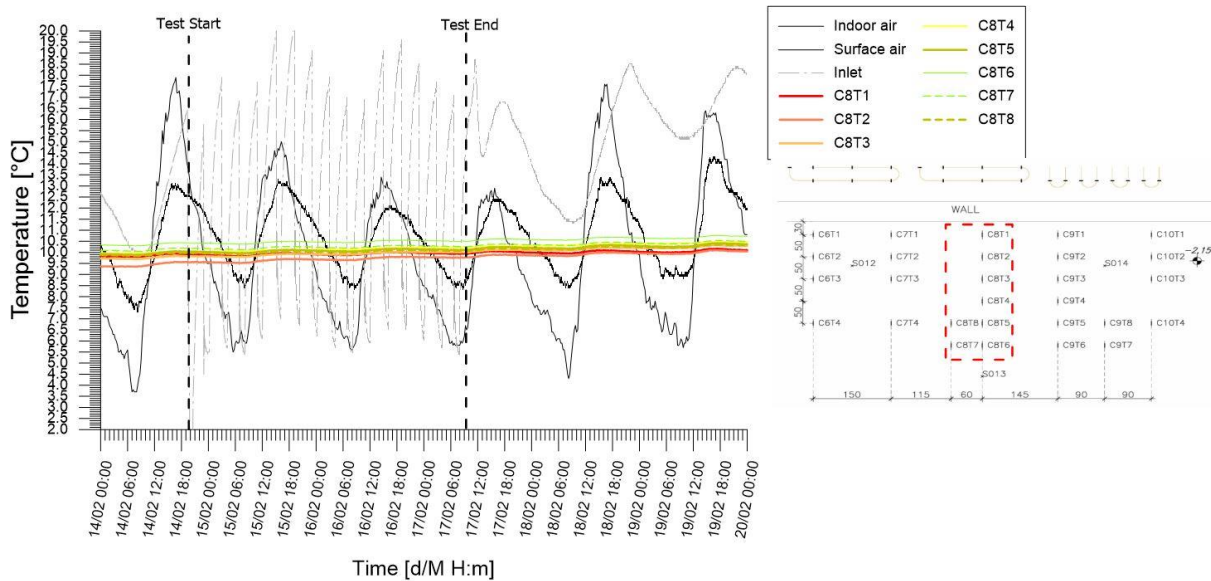


Figure A.57: Temperatures records from chain 8 of experimental test  
 H\_1+3\_20200214\_20200217

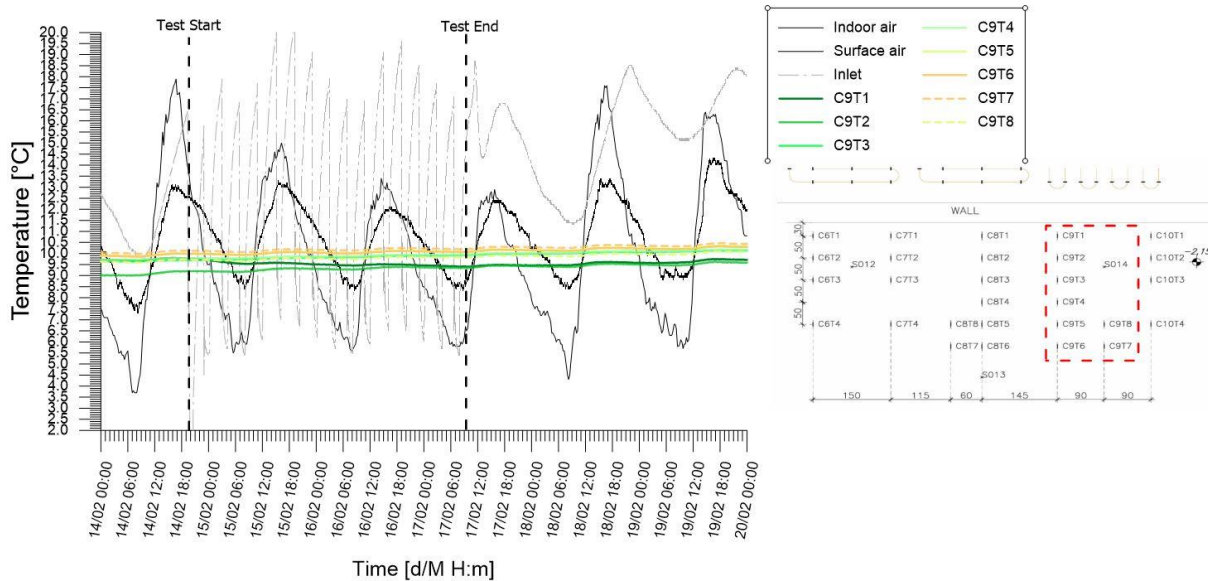


Figure A.58: Temperatures records from chain 9 of experimental test  
 H\_1+3\_20200214\_20200217

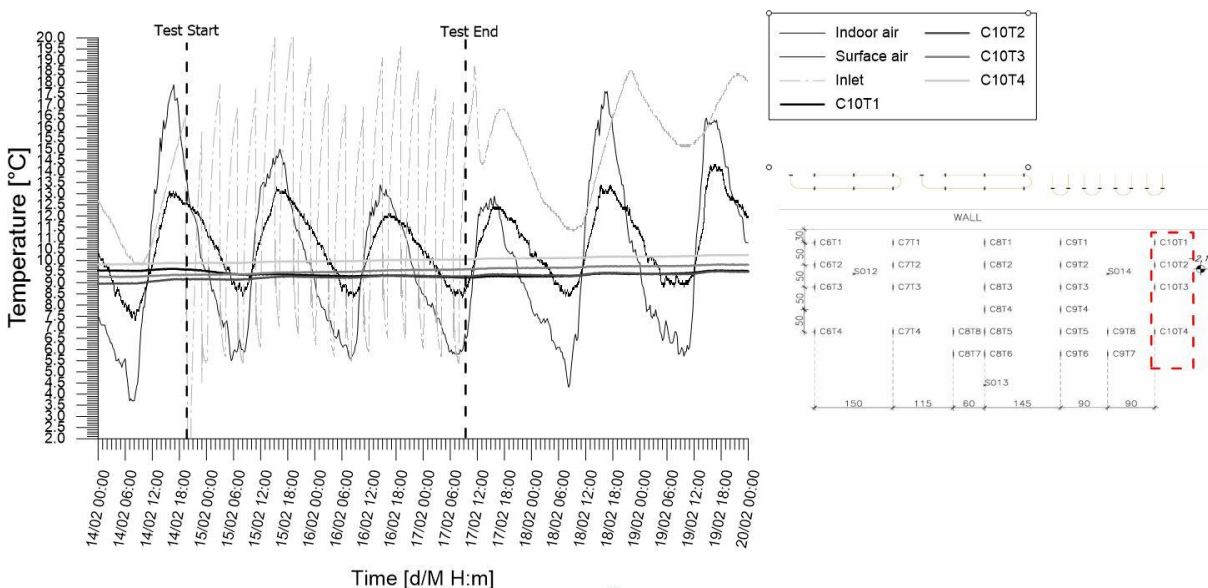


Figure A.59: Temperatures records from chain 10 of experimental test  
 H\_1+3\_20200214\_20200217

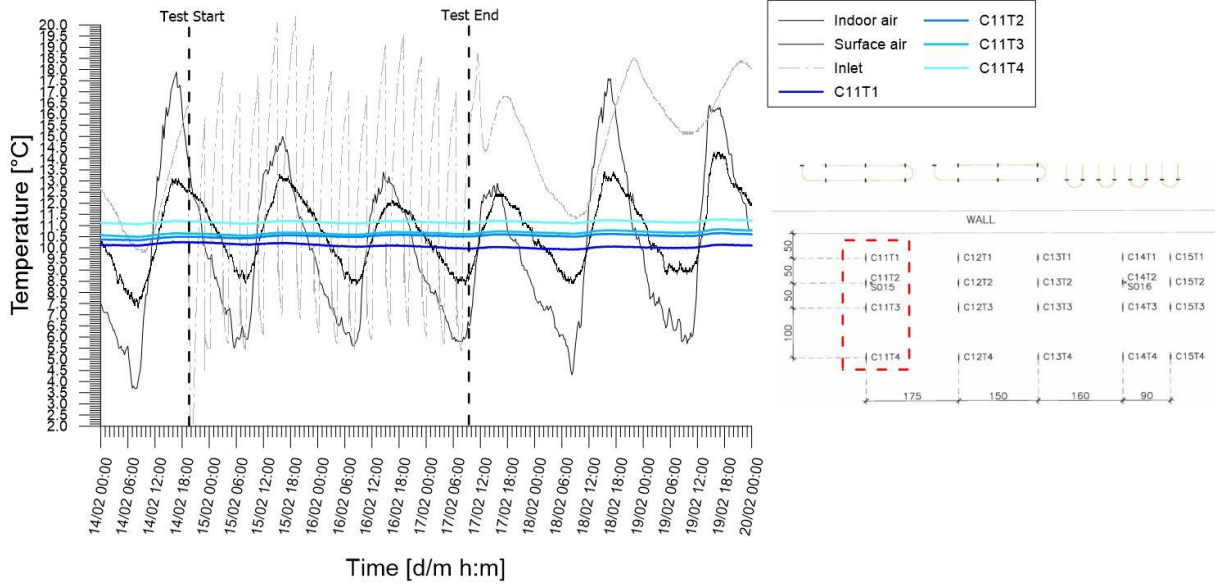


Figure A.60: Temperatures records from chain 11 of experimental test  
*H\_1+3\_20200214\_20200217*

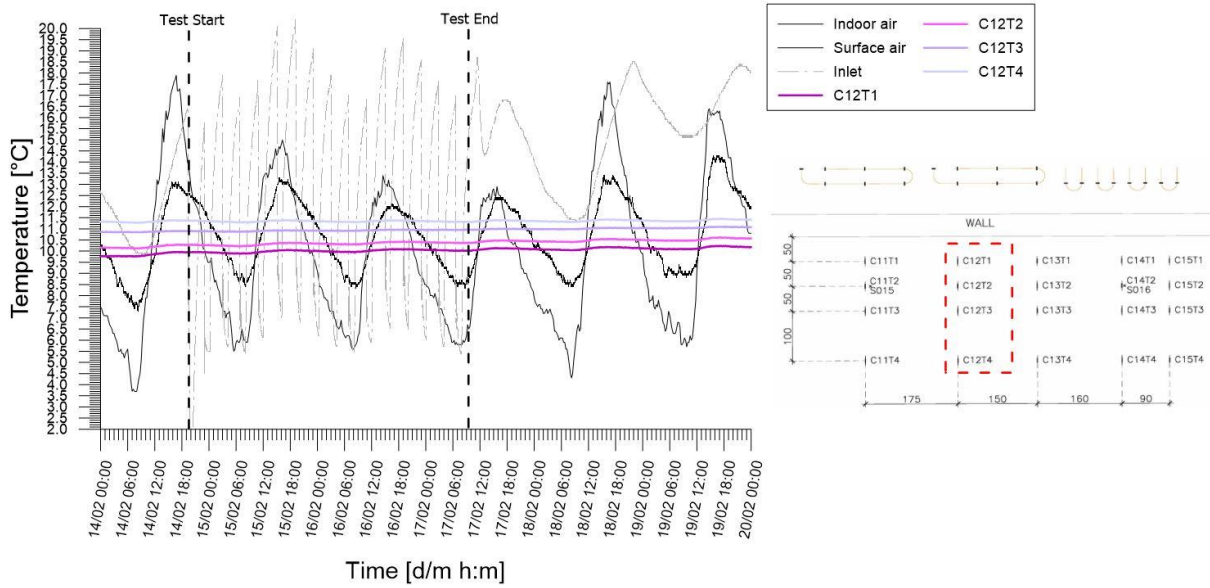


Figure A.61: Temperatures records from chain 12 of experimental test  
*H\_1+3\_20200214\_20200217*

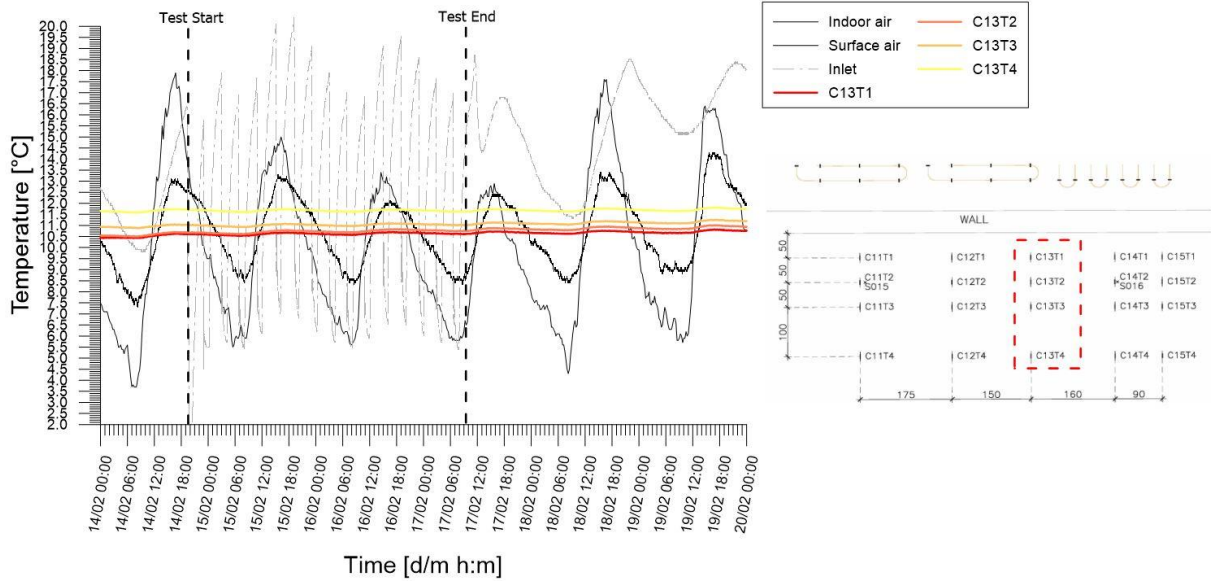


Figure A.62: Temperatures records from chain 13 of experimental test  
 H\_1+3\_20200214\_20200217

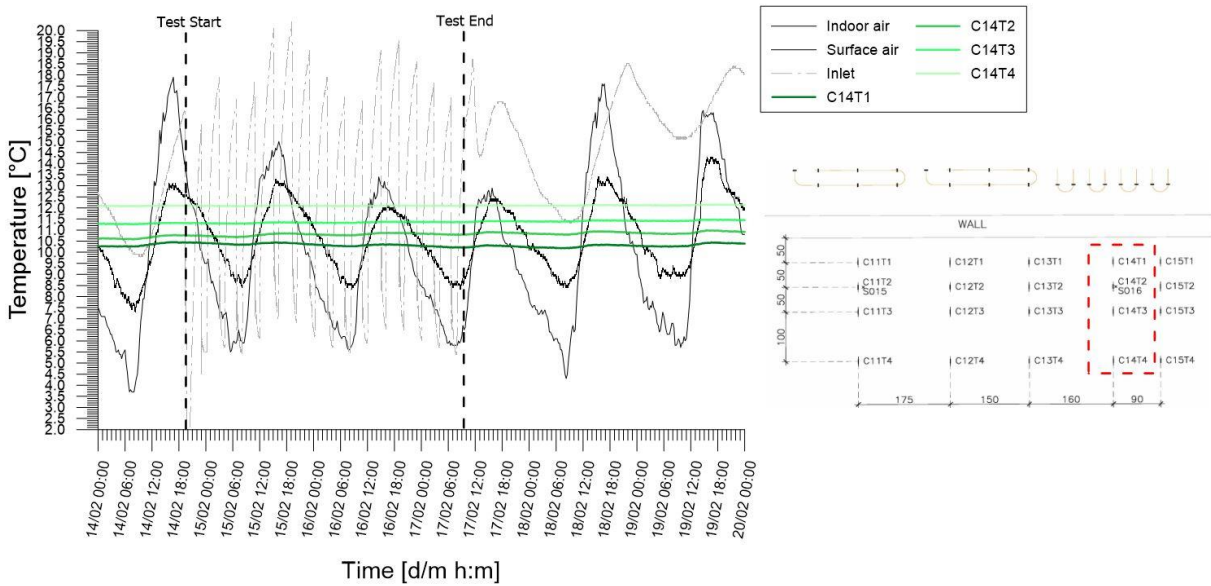


Figure A.63: Temperatures records from chain 14 of experimental test  
 H\_1+3\_20200214\_20200217

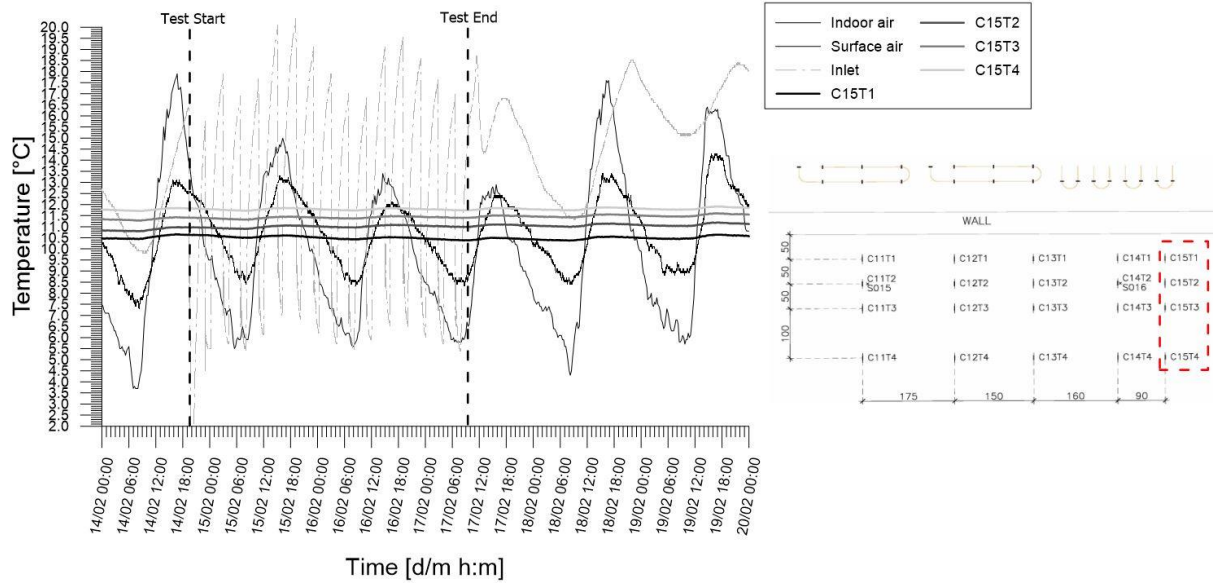


Figure A.64: Temperatures records from chain 15 of experimental test  
 H\_1+3\_20200214\_20200217

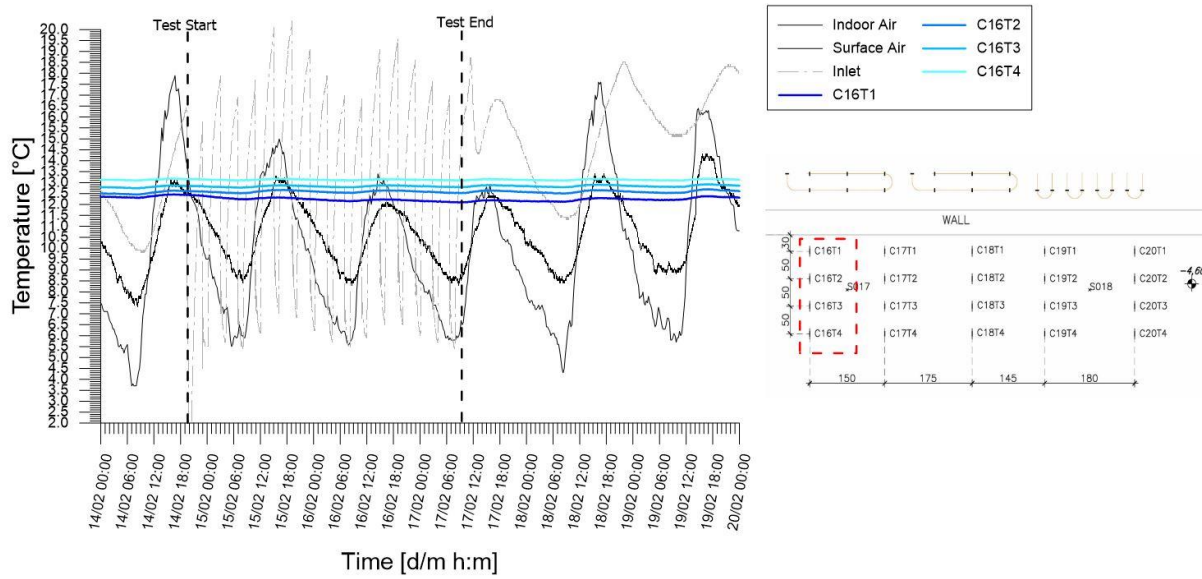


Figure A.65: Temperatures records from chain 16 of experimental test  
 H\_1+3\_20200214\_20200217

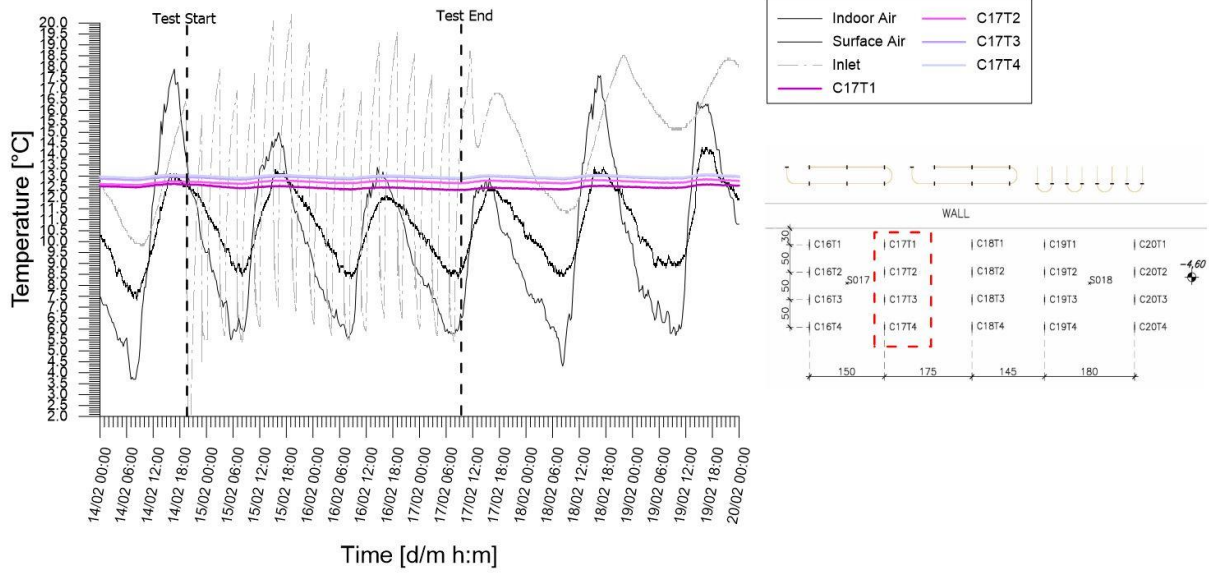


Figure A.66: Temperatures records from chain 17 of experimental test  
*H\_1+3\_20200214\_20200217*

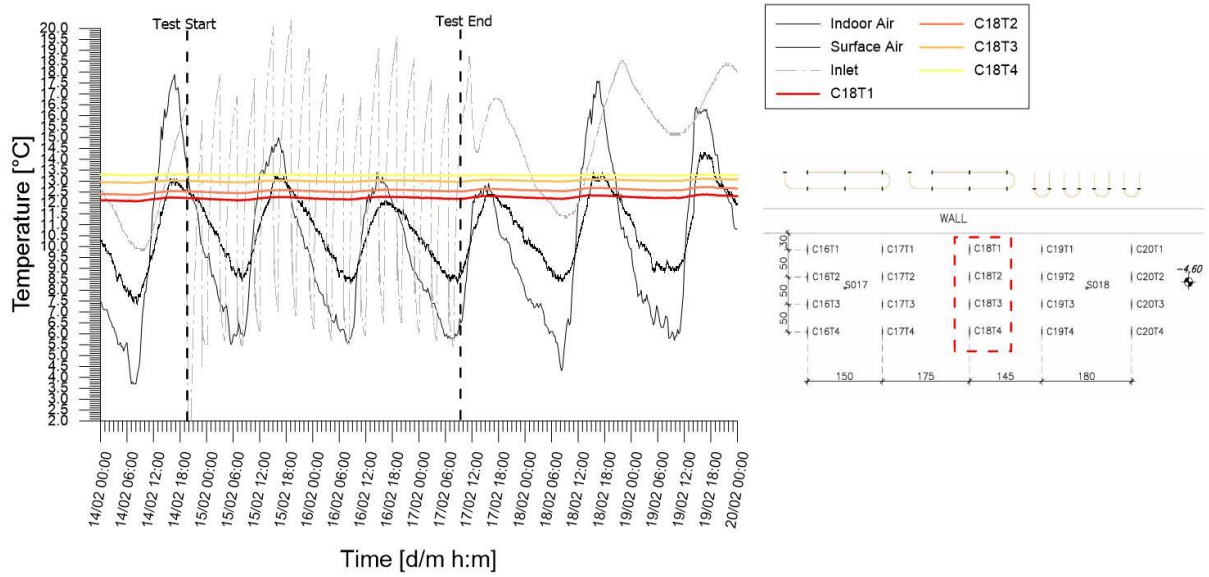


Figure A.67 Temperatures records from chain 18 of experimental test  
*H\_1+3\_20200214\_20200217*

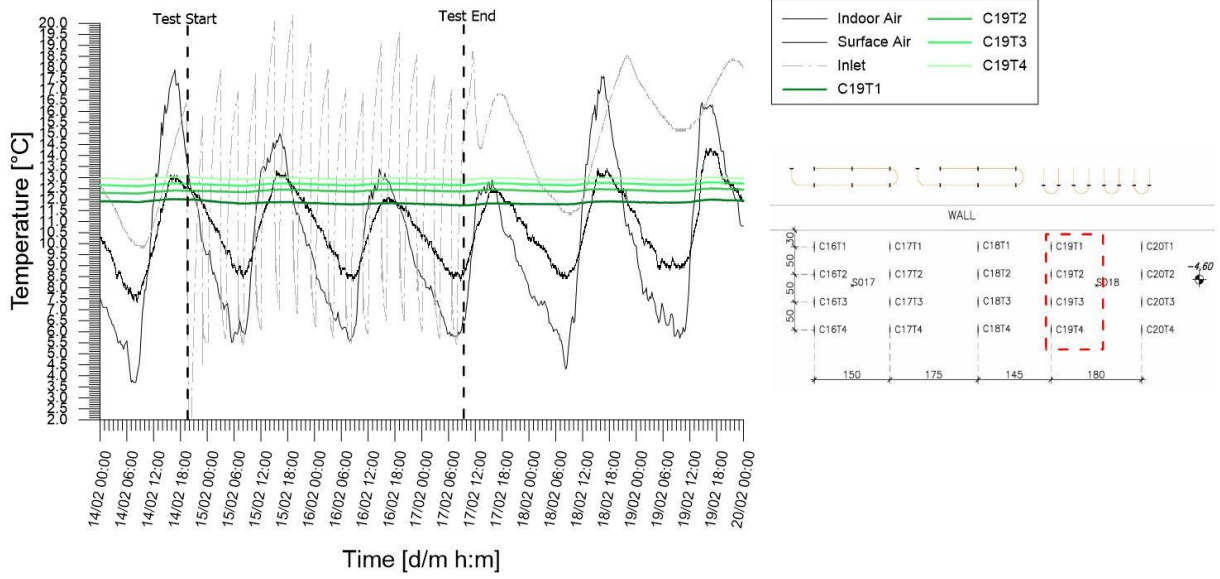


Figure A.68 Temperatures records from chain 19 of experimental test

H\_1+3\_20200214\_20200217

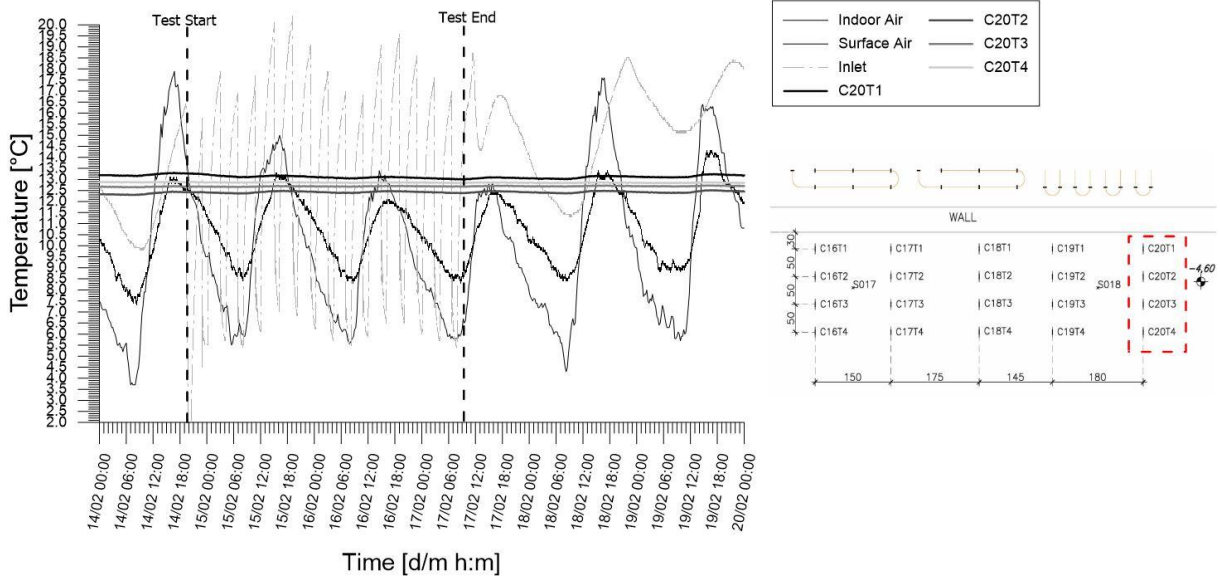


Figure A.69: Temperatures records from chain 20 of experimental test

H\_1+3\_20200214\_20200217

#### 4. Test H\_1+3\_20200221\_20200224

Table A.4: Main features of the test

|                                    |                |
|------------------------------------|----------------|
| Test start time                    | 21/02/20 18.04 |
| Test end time                      | 24/02/20 10.04 |
| Duration [h]                       | 64             |
| Operative mode                     | Heating        |
| Active circuit(s)                  | 1;3            |
| Circuit link                       | Parallel       |
| Target temperature user [°C]       | 45             |
| Flow rate at the ground side [l/h] | 930.7          |

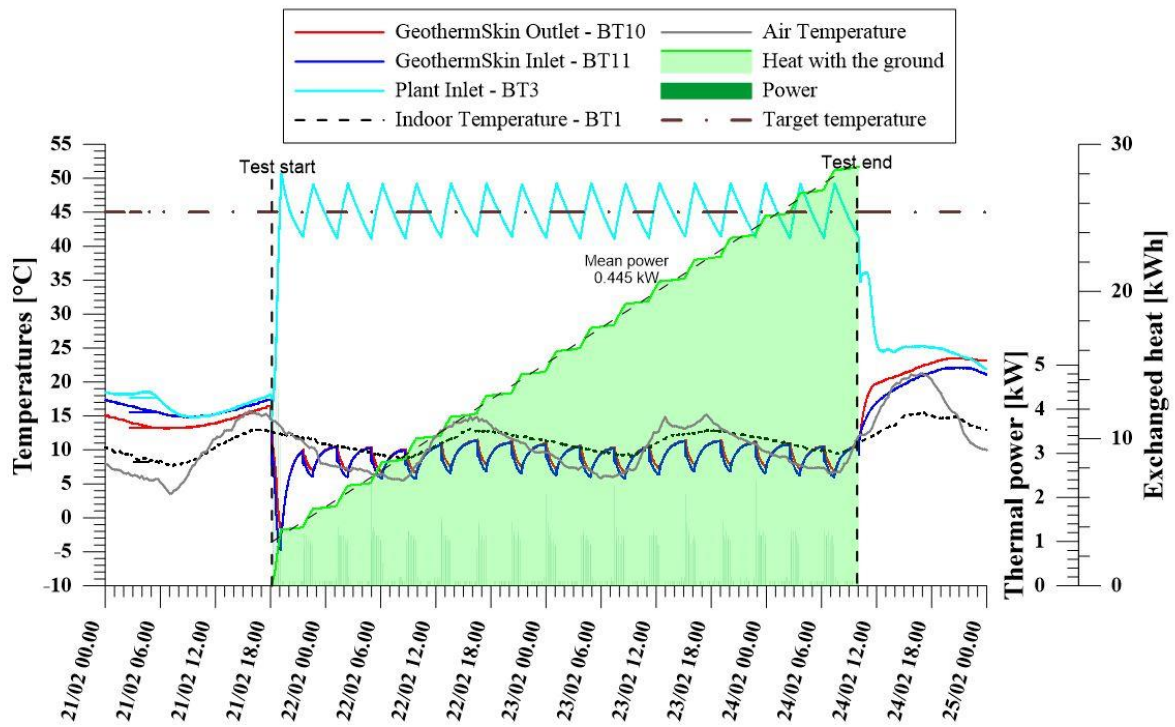


Figure A.70: Thermal performance interpretation of experimental test  $H_{1+3}_{20200221\_20200224}$  with parallel link of circuit 1 and 3 in heating mode.

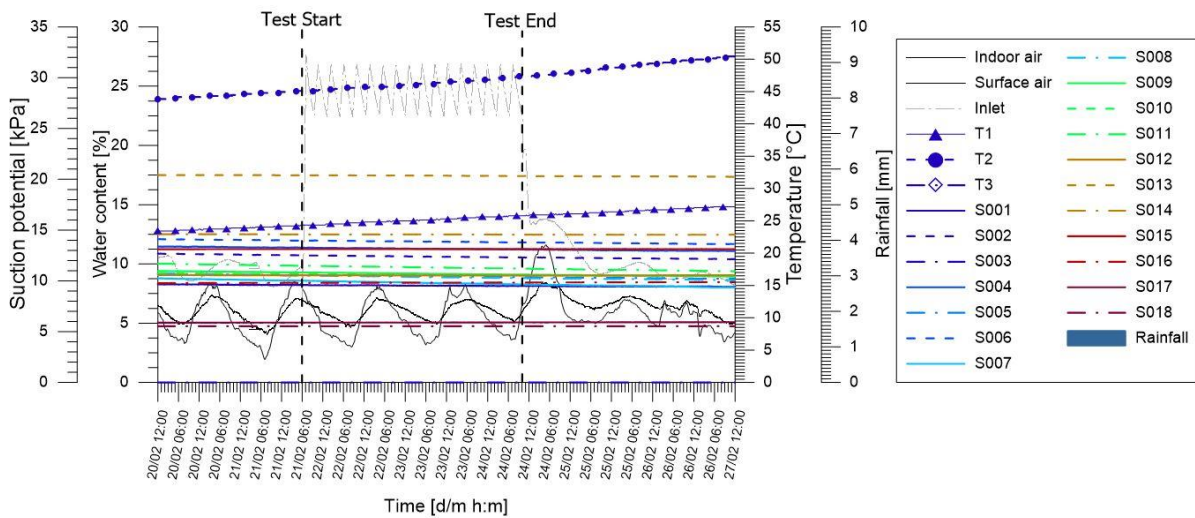


Figure A.71: Tensiometer and hygrometers records of experimental test  $H_{1+3}_{20200221\_20200224}$  together with monitored rainfall from Politecnico weather station.

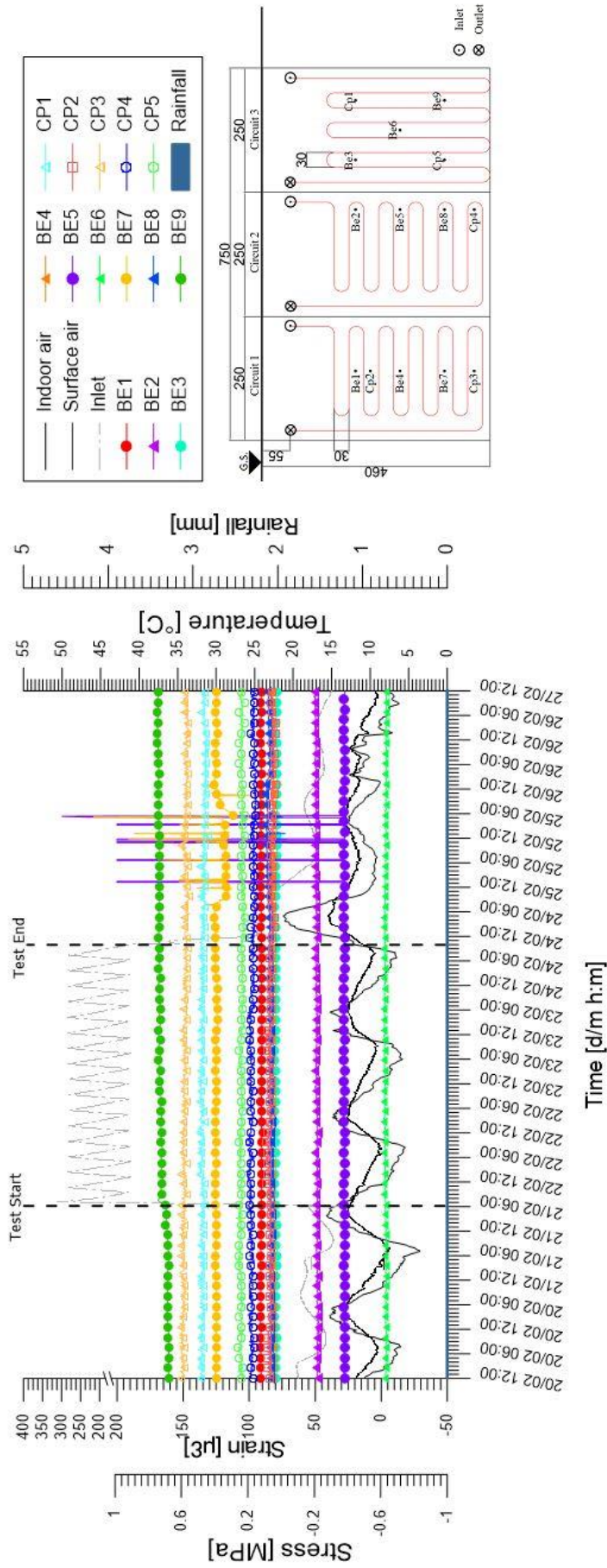


Figure A.72: Stresses and strains monitored at the wall external facade during experimental

test H\_I+3\_20200221\_20200224

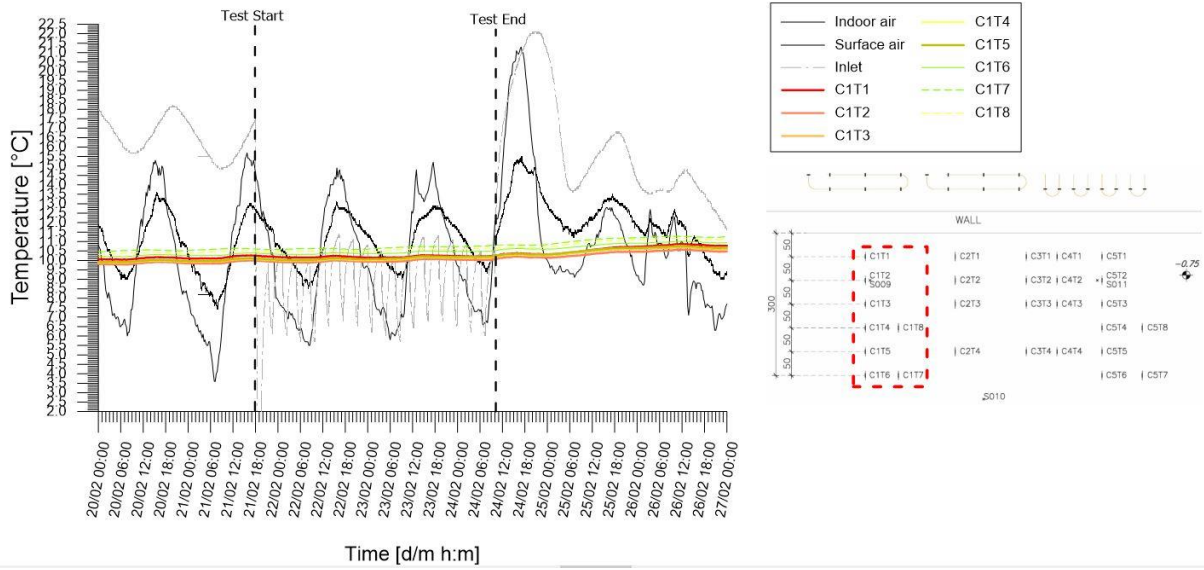


Figure A.73: Temperatures records from chain 1 of experimental test  
*H\_1+3\_20200221\_20200224*

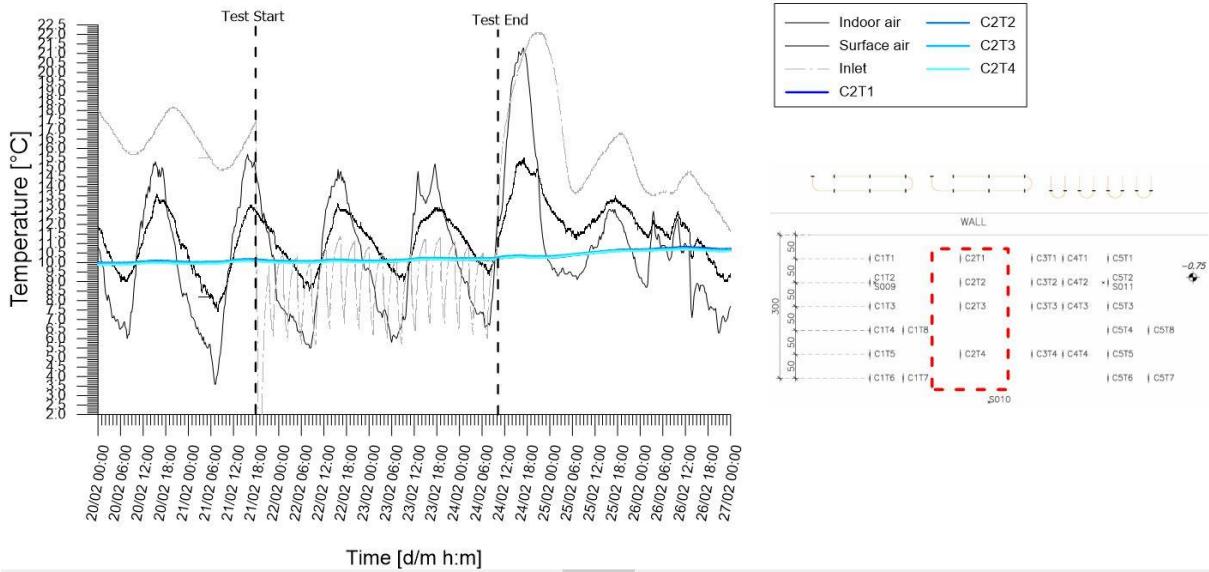


Figure A.74: Temperatures records from chain 2 of experimental test  
*H\_1+3\_20200221\_20200224*

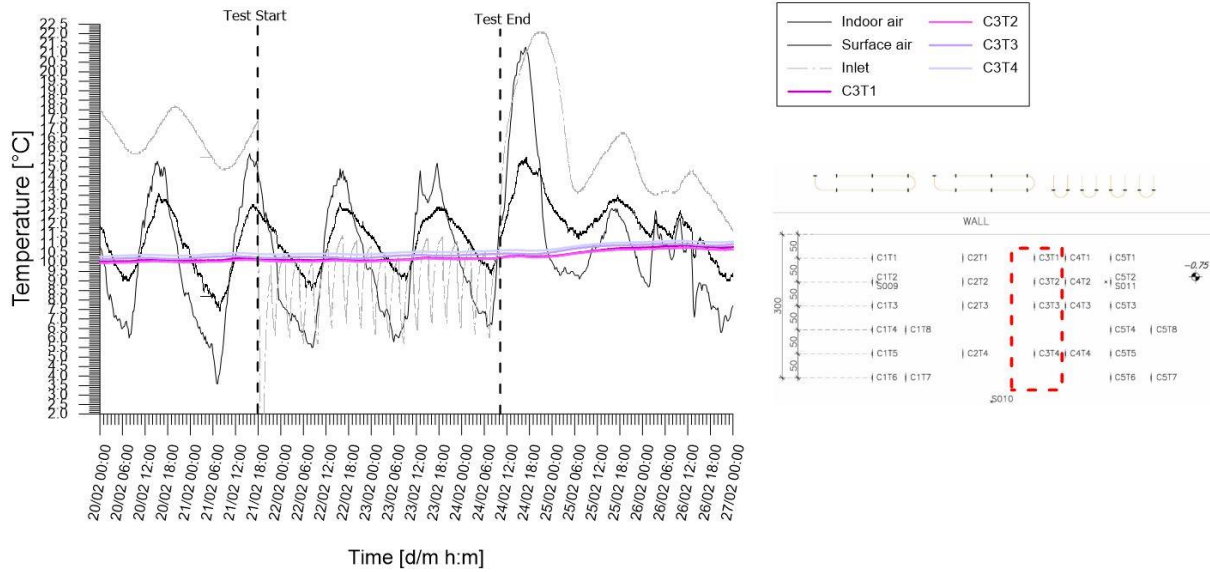


Figure A.75: Temperatures records from chain 3 of experimental test  
*H\_1+3\_20200221\_2020022*

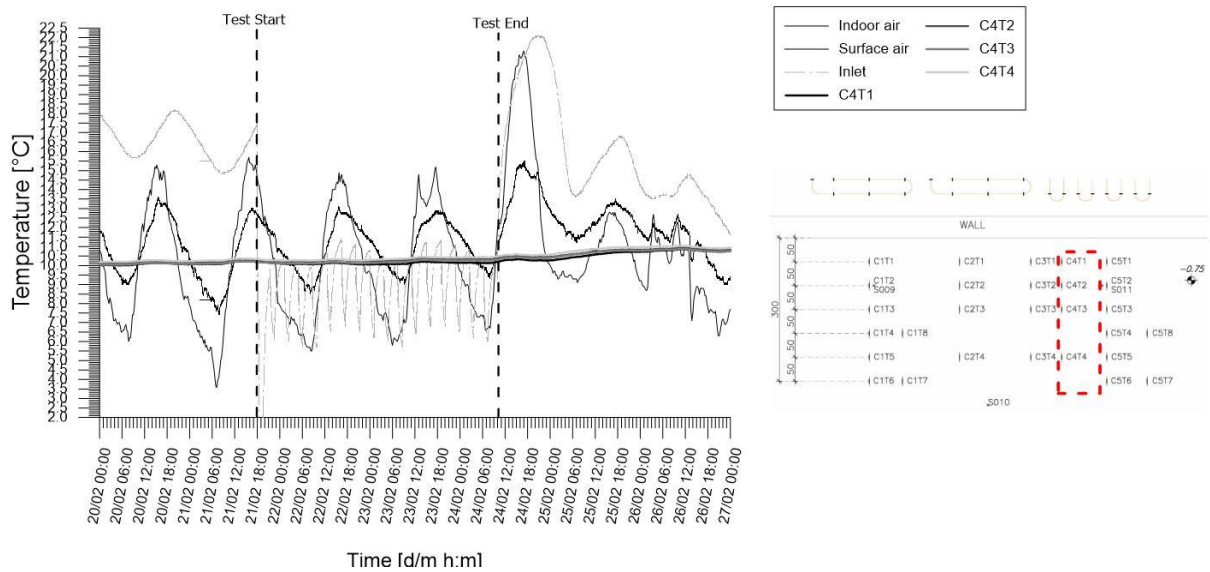


Figure A.76: Temperatures records from chain 4 of experimental test  
*H\_1+3\_20200221\_20200224*



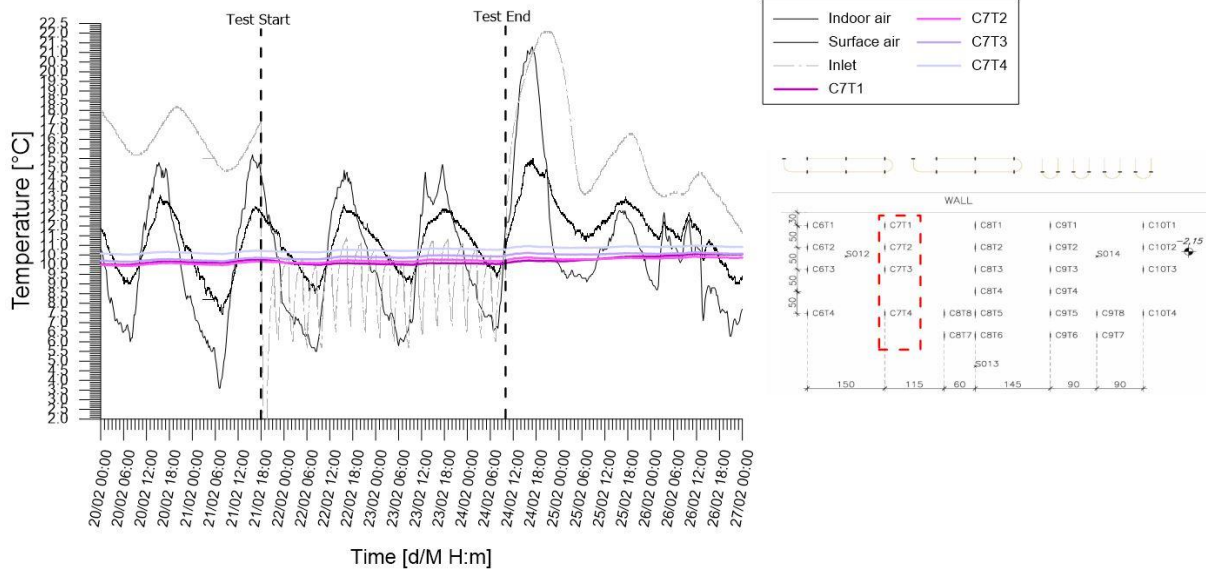


Figure A.79: Temperatures records from chain 7 of experimental test

H\_1+3\_20200221\_20200224

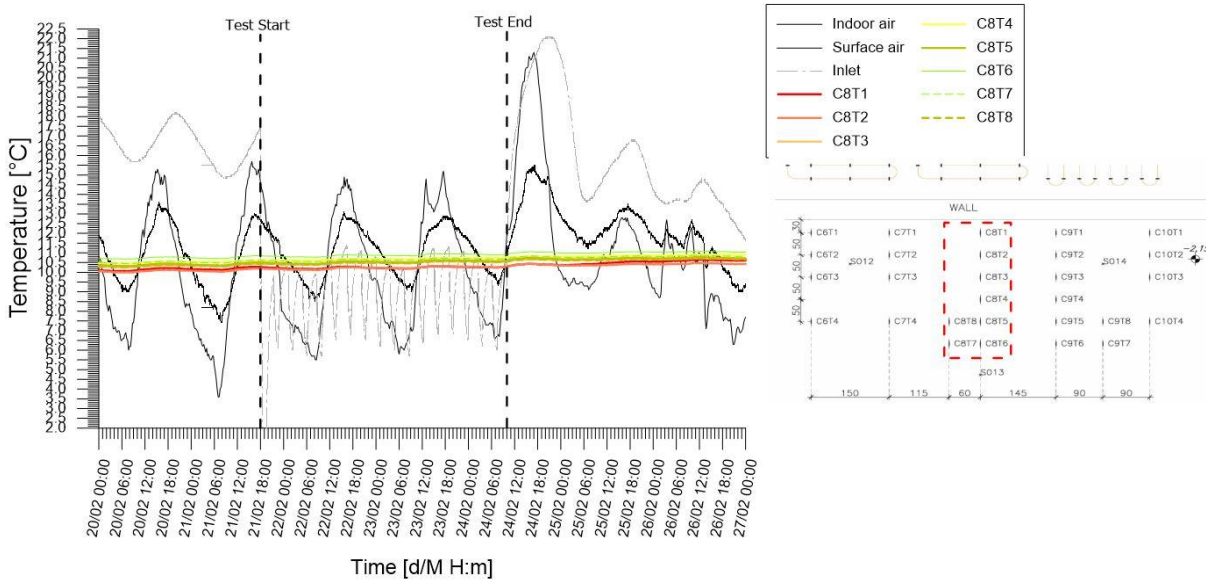


Figure A.80: Temperatures records from chain 8 of experimental test

H\_1+3\_20200221\_20200224

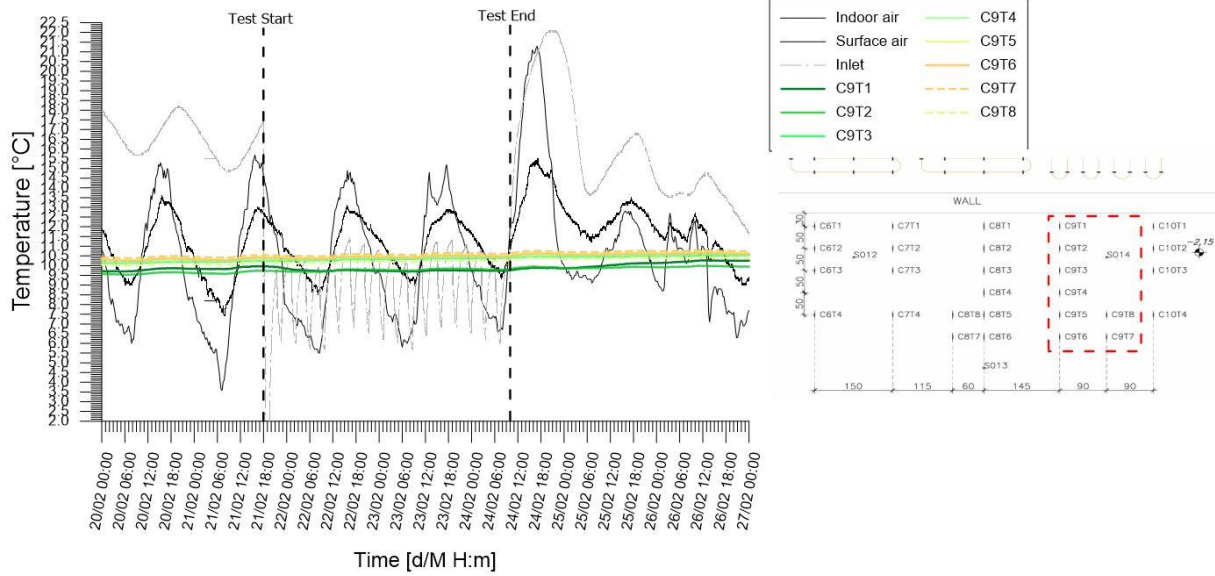


Figure A.81: Temperatures records from chain 9 of experimental test

H\_1+3\_20200221\_20200224

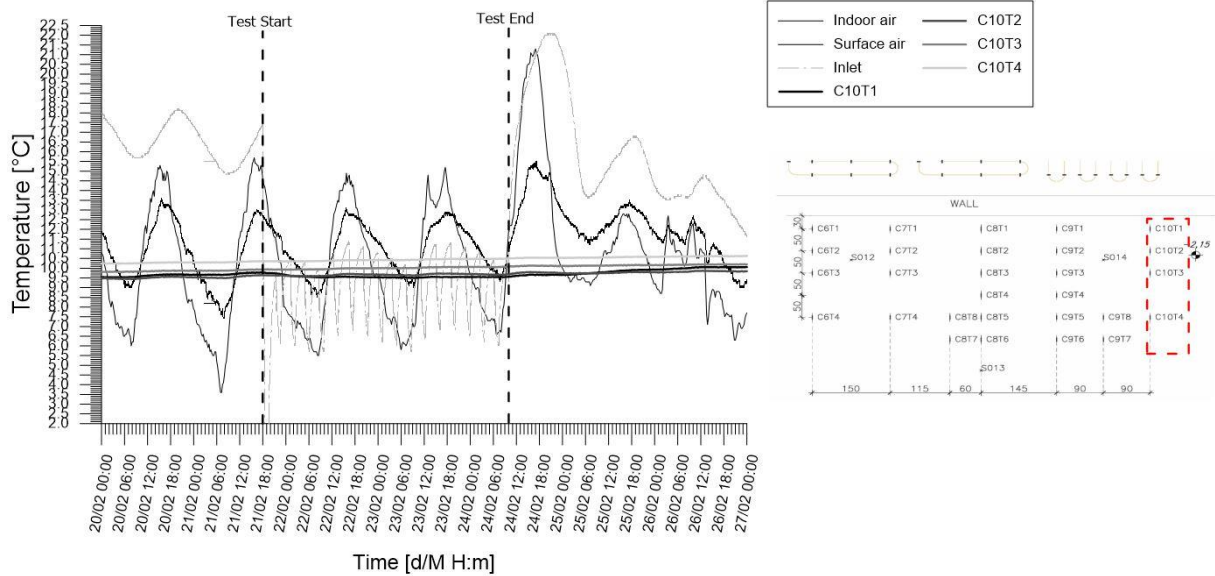


Figure A.82: Temperatures records from chain 10 of experimental test

H\_1+3\_20200221\_20200224

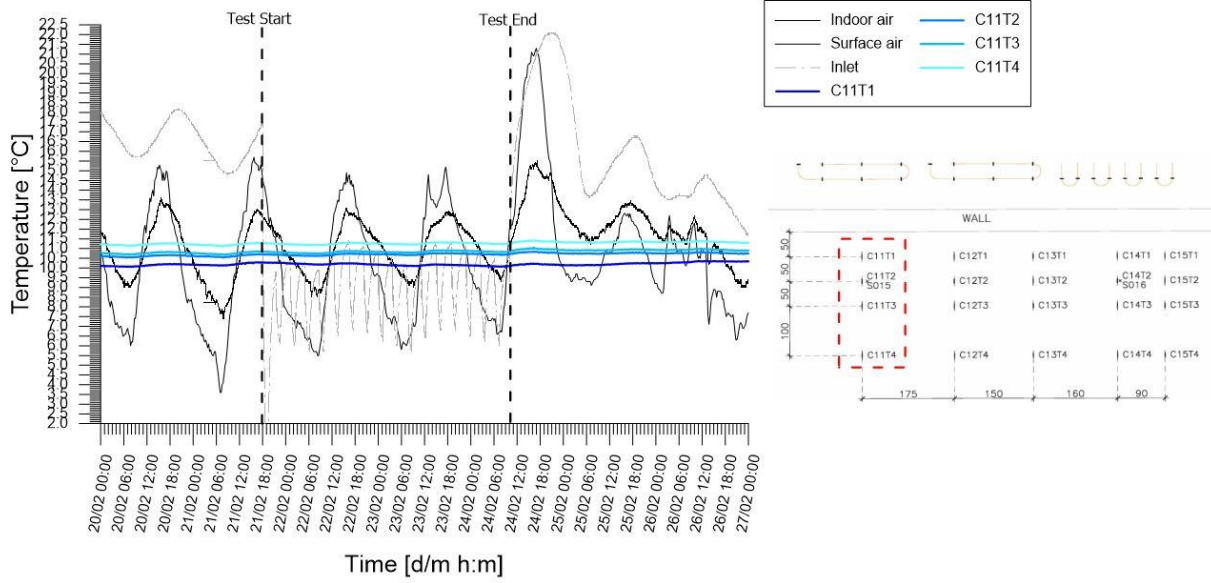


Figure A.83: Temperatures records from chain 11 of experimental test  
*H\_1+3\_20200221\_20200224*

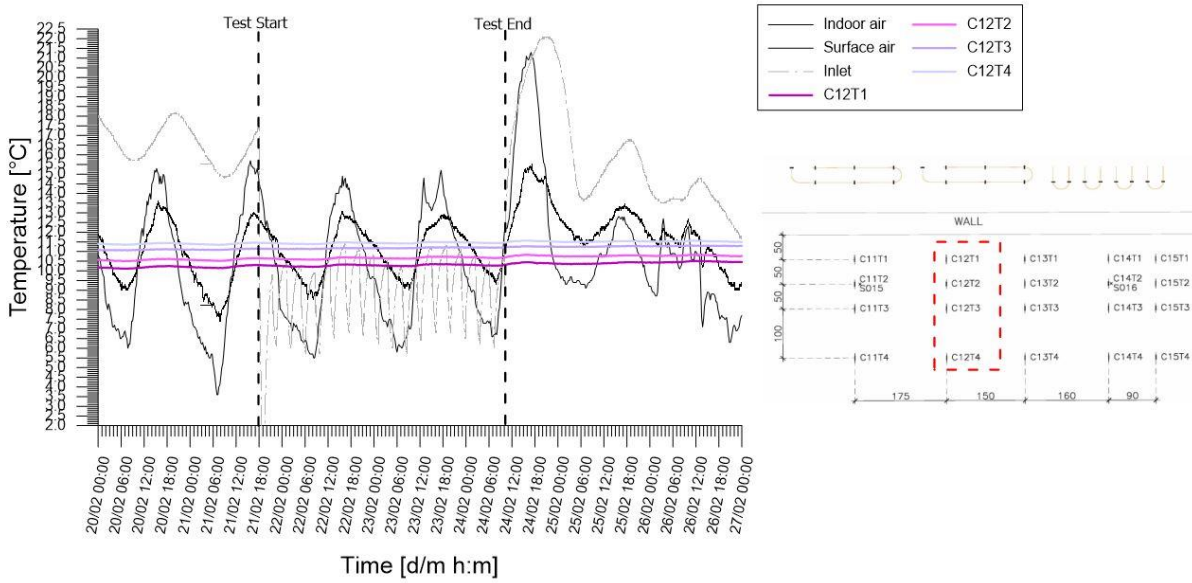


Figure A.84: Temperatures records from chain 12 of experimental test  
*H\_1+3\_20200221\_20200224*

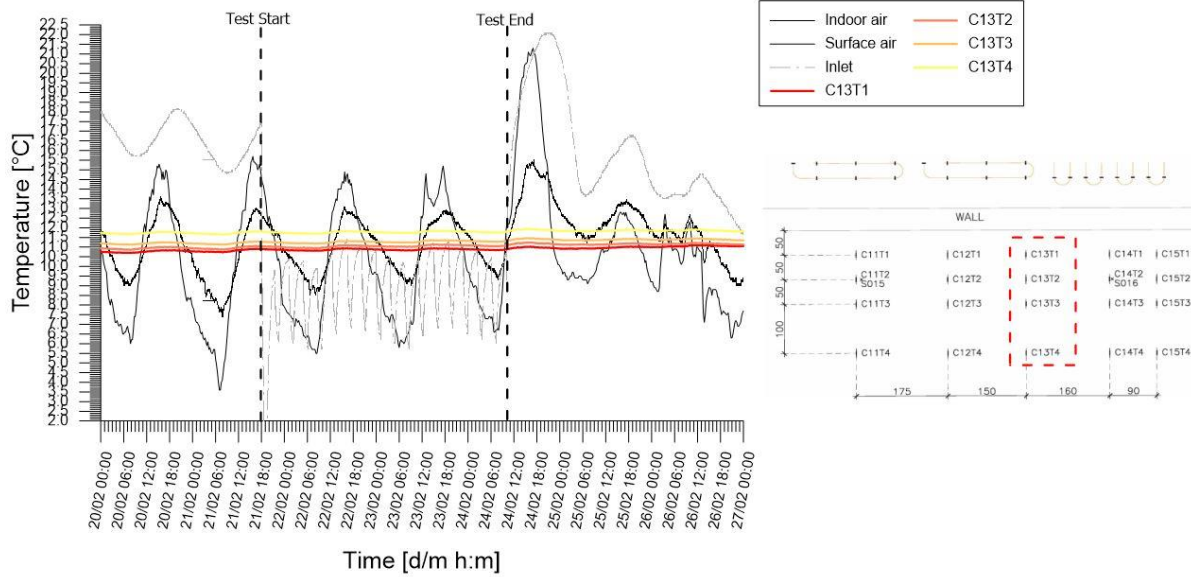


Figure A.85: Temperatures records from chain 13 of experimental test  
*H\_1+3\_20200221\_20200224*

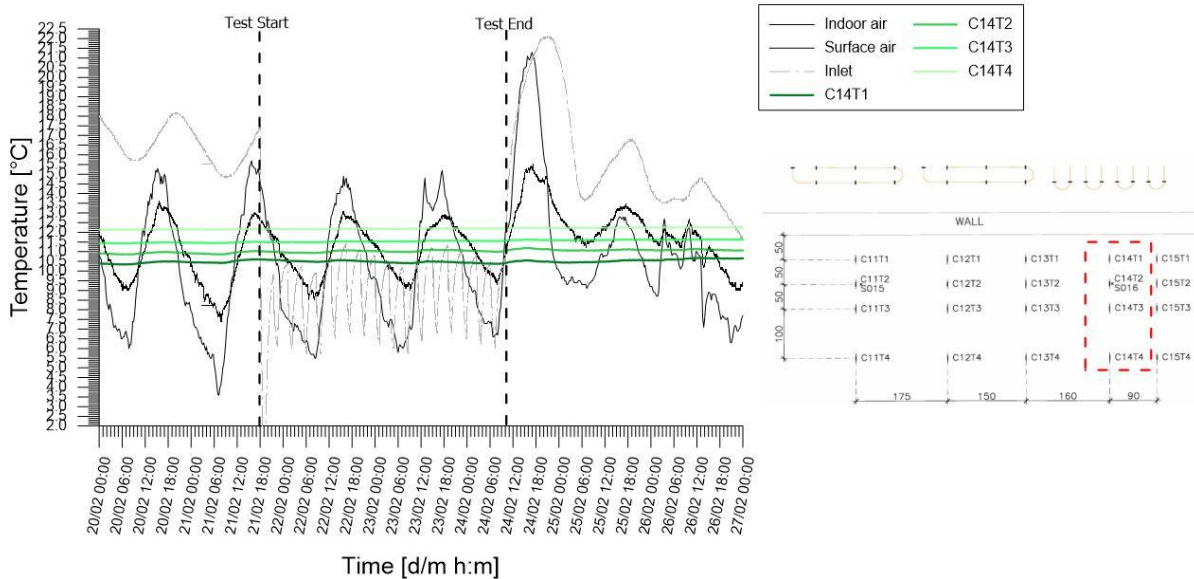


Figure A.86: Temperatures records from chain 14 of experimental test  
*H\_1+3\_20200221\_20200224*

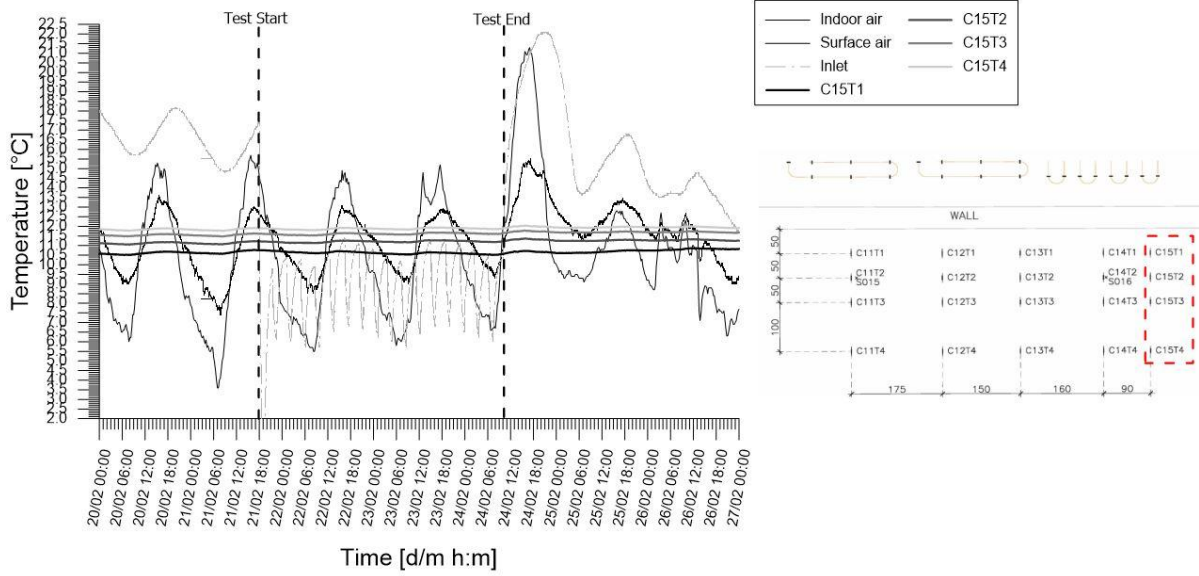


Figure A.87: Temperatures records from chain 15 of experimental test  
H\_1+3\_20200221\_20200224

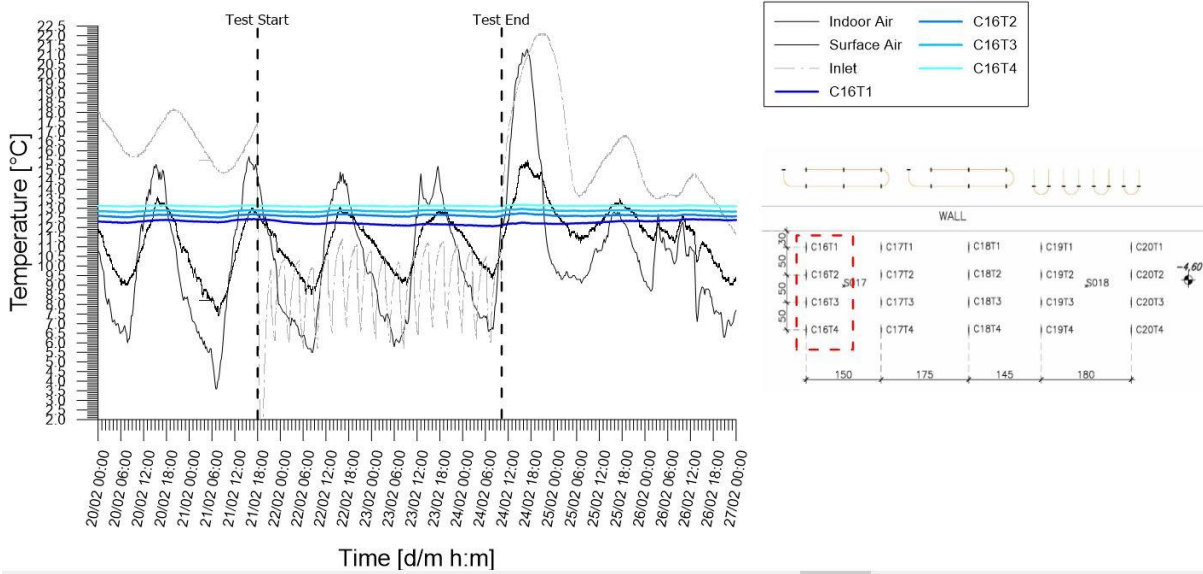


Figure A.88: Temperatures records from chain 16 of experimental test  
H\_1+3\_20200221\_20200224

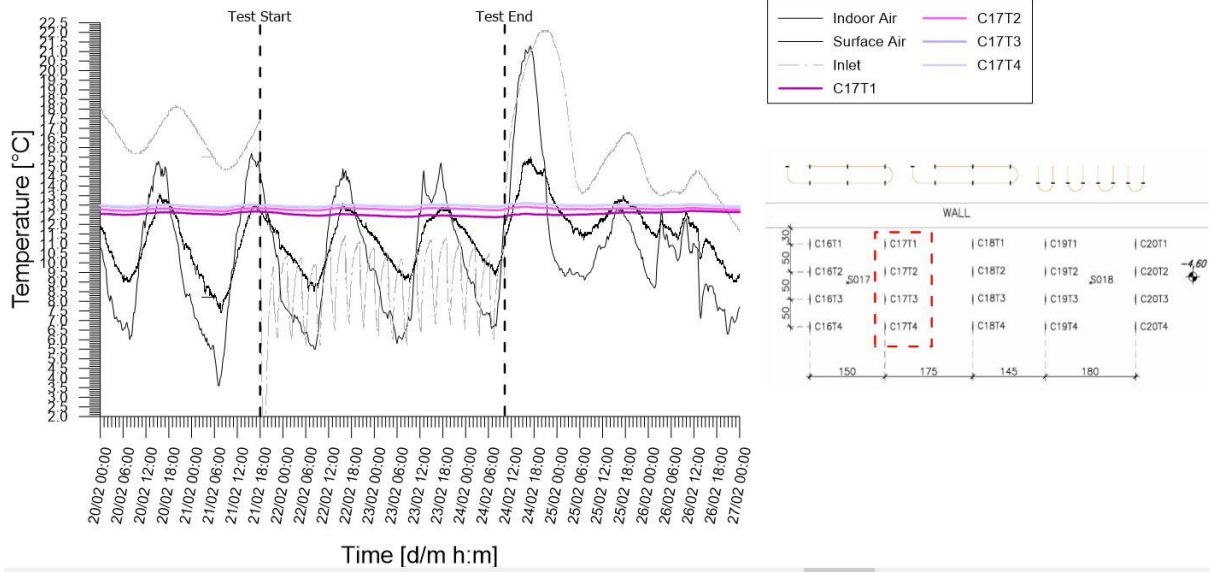


Figure A.89: Temperatures records from chain 17 of experimental test

H\_1+3\_20200221\_20200224

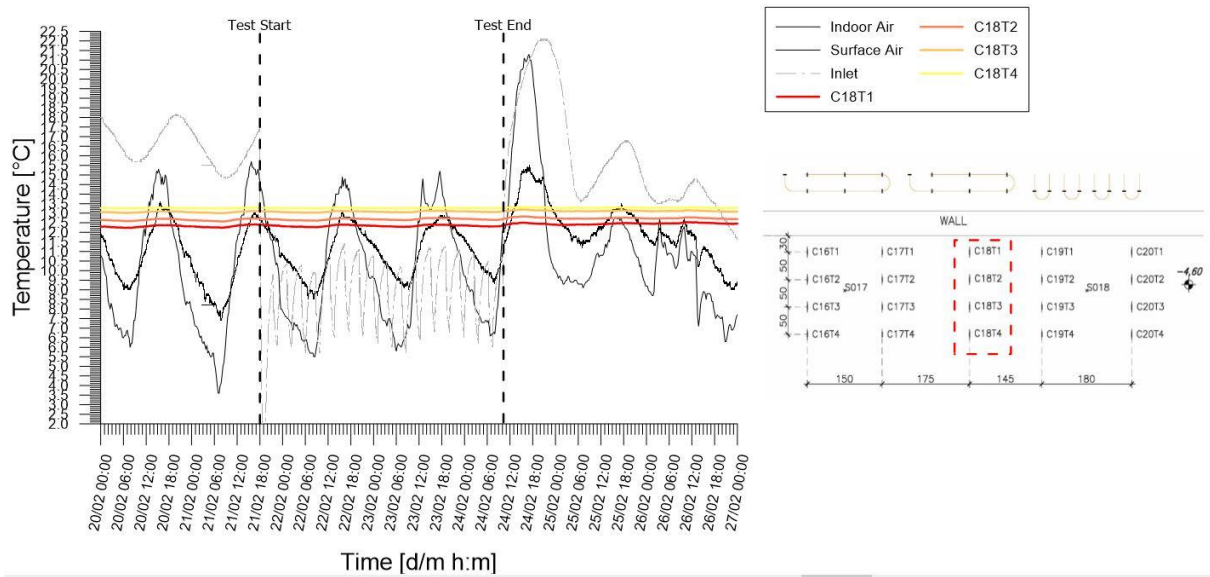


Figure A.90: Temperatures records from chain 18 of experimental test

H\_1+3\_20200221\_20200224

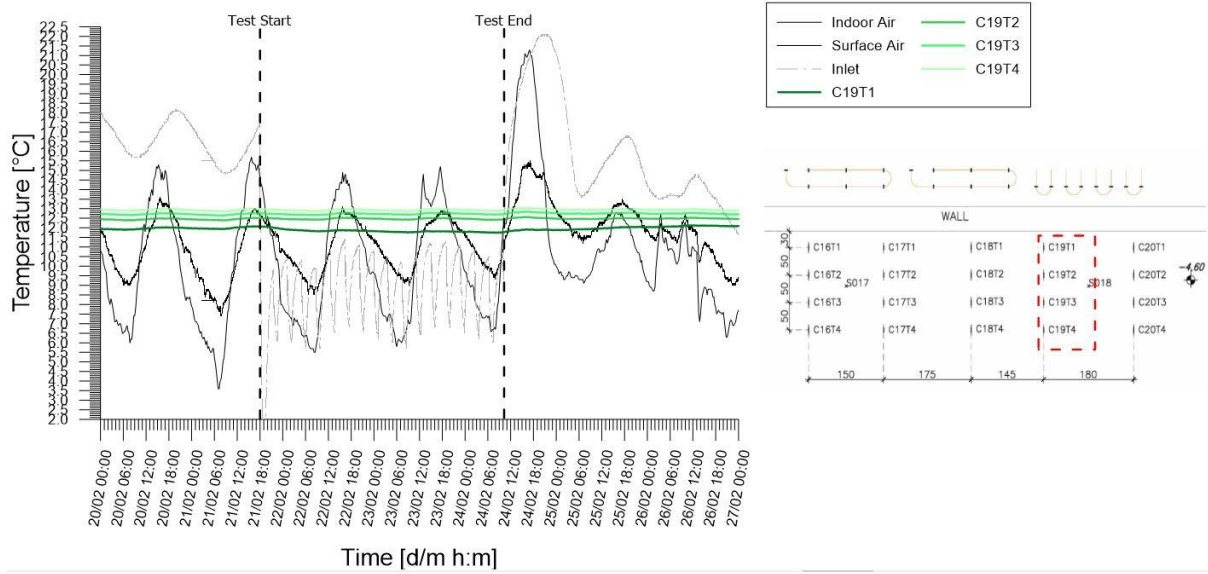


Figure A.91: Temperatures records from chain 19 of experimental test  
*H\_1+3\_20200221\_20200224*

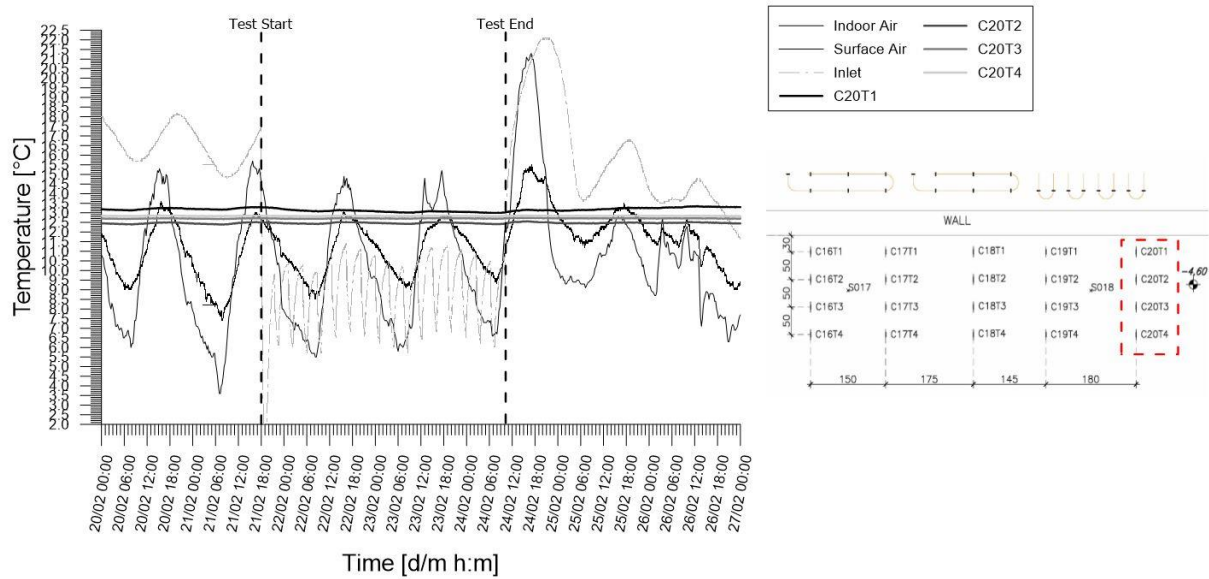


Figure A.92: Temperatures records from chain 20 of experimental test  
*H\_1+3\_20200221\_20200224*

## 5. Test H\_1+2+3\_20200228\_20200302

Table A.5: Main features of the test

|                                    |                |
|------------------------------------|----------------|
| Test start time                    | 28/02/20 18.40 |
| Test end time                      | 02/03/20 9.25  |
| Duration [h]                       | 62.75          |
| Operative mode                     | Heating        |
| Active circuit(s)                  | 1;2;3          |
| Circuit link                       | Parallel       |
| Target temperature user [°C]       | 45             |
| Flow rate at the ground side [l/h] | 1006           |

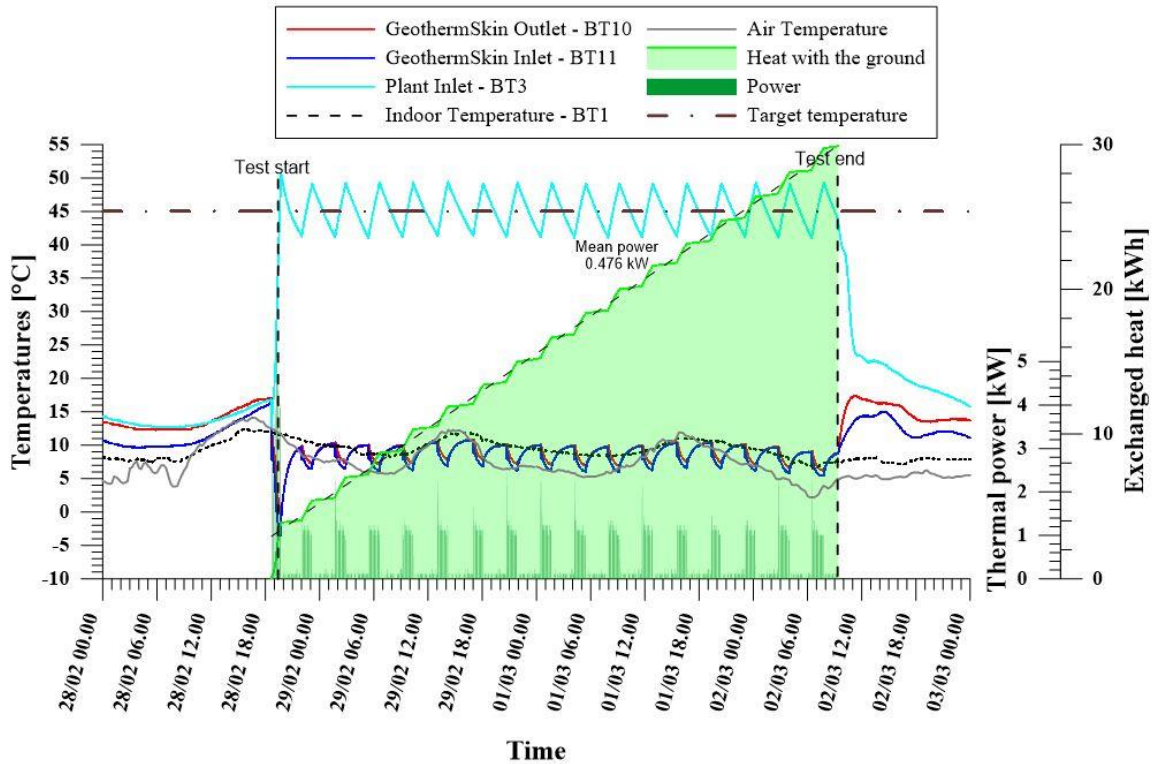


Figure A.93: Thermal performance interpretation of experimental test *H\_1+2+3\_20200228\_20200302* with parallel link of circuit 1, 2 and 3 in heating mode.

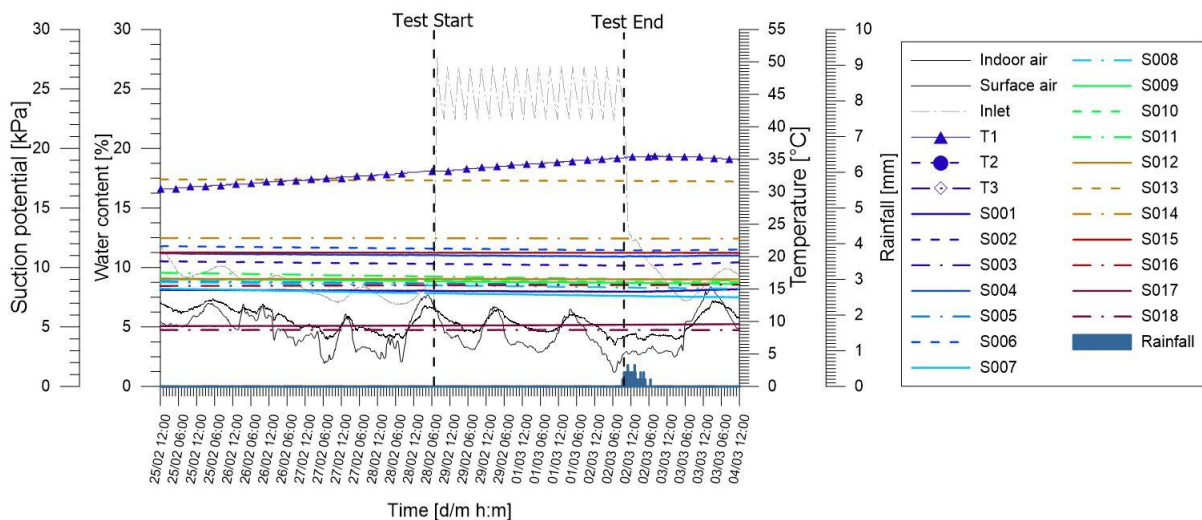


Figure A.94: Tensiometer and hygrometers records of experimental test *H\_1+2+3\_20200228\_20200302* together with monitored rainfall from Politecnico weather station.

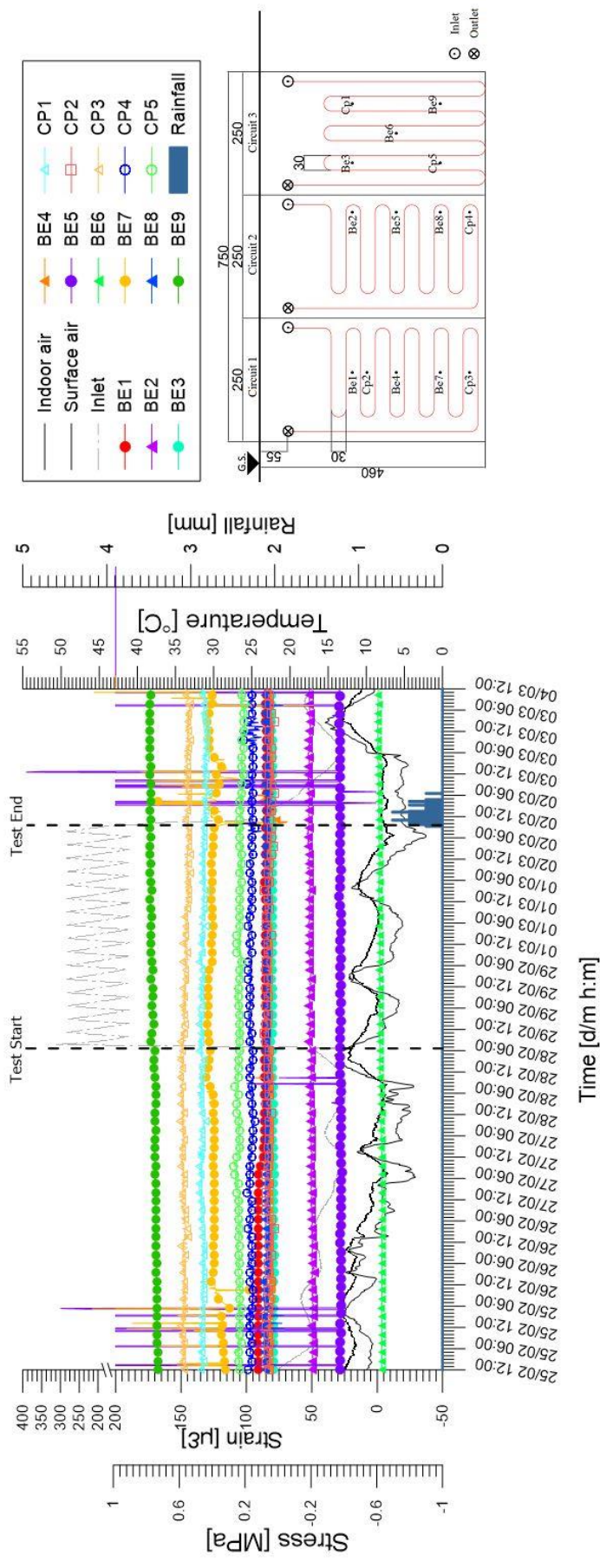


Figure A.95: Stresses and strains monitored at the wall external facade during experimental test

H\_1+2+3\_20200228\_20200302

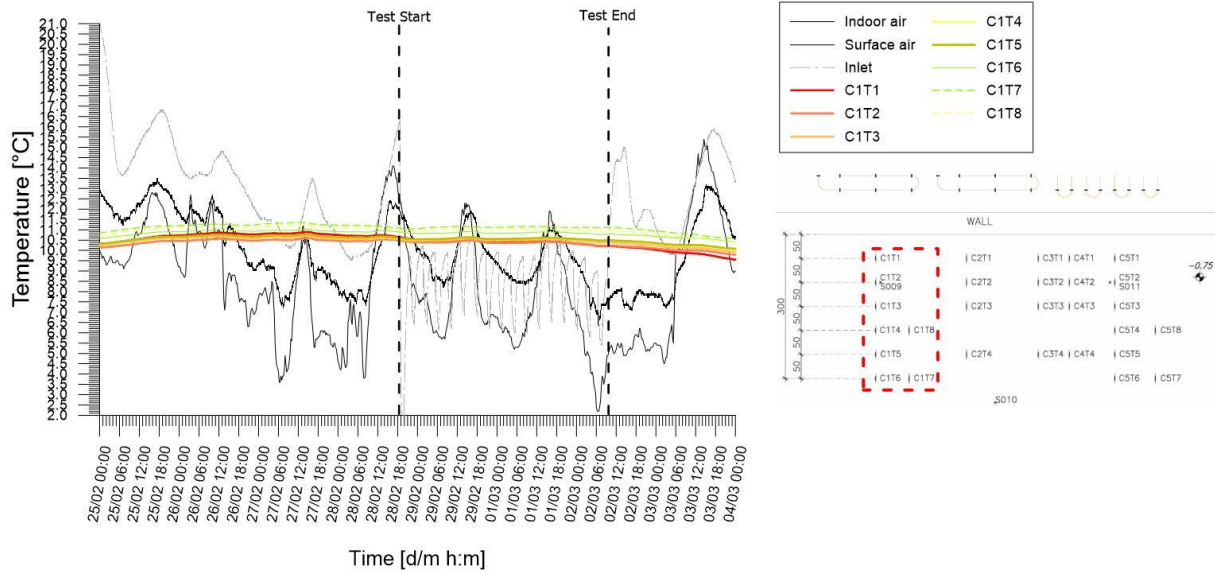


Figure A.96: Temperatures records from chain 1 of experimental test  
*H\_1+2+3\_20200228\_20200302*

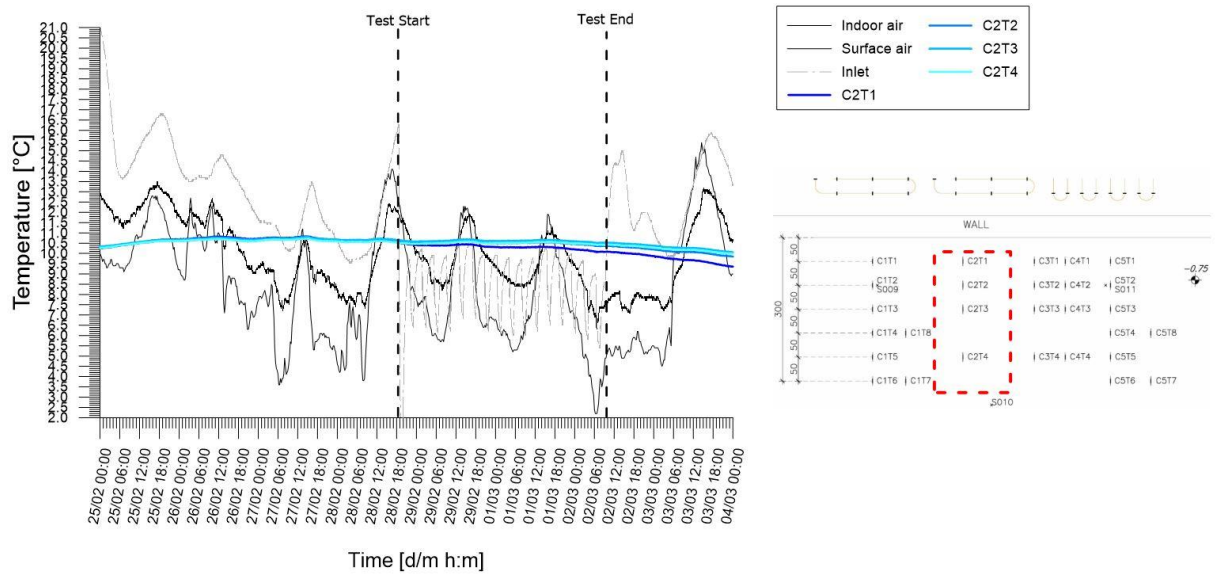


Figure A.97: Temperatures records from chain 2 of experimental test  
*H\_1+2+3\_20200228\_20200302*

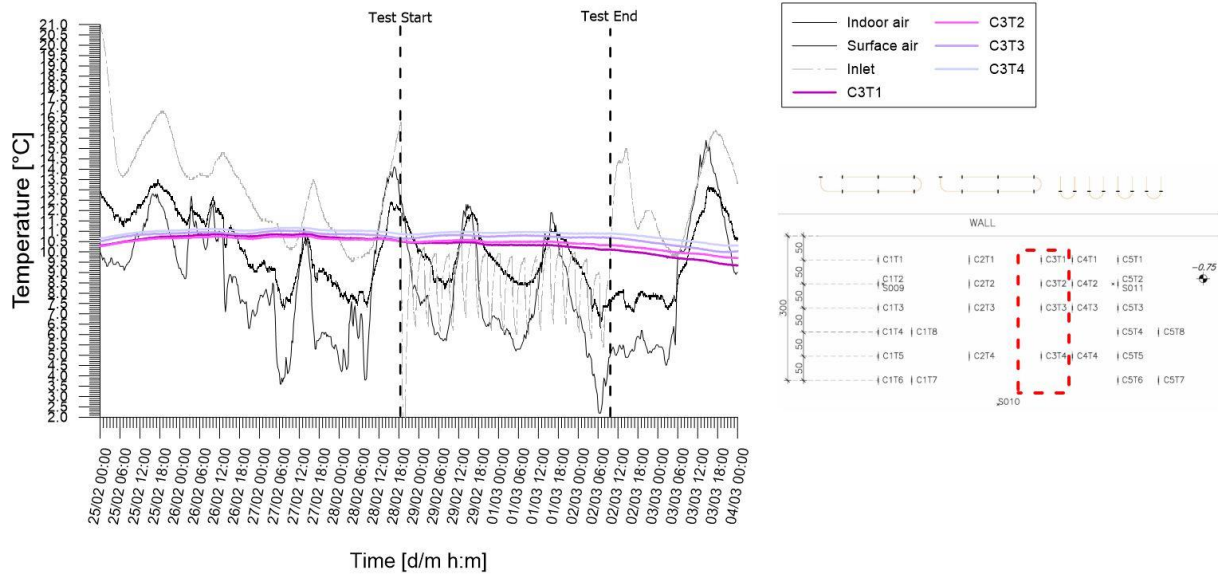


Figure A.98: Temperatures records from chain 3 of experimental test

H\_1+2+3\_20200228\_20200302

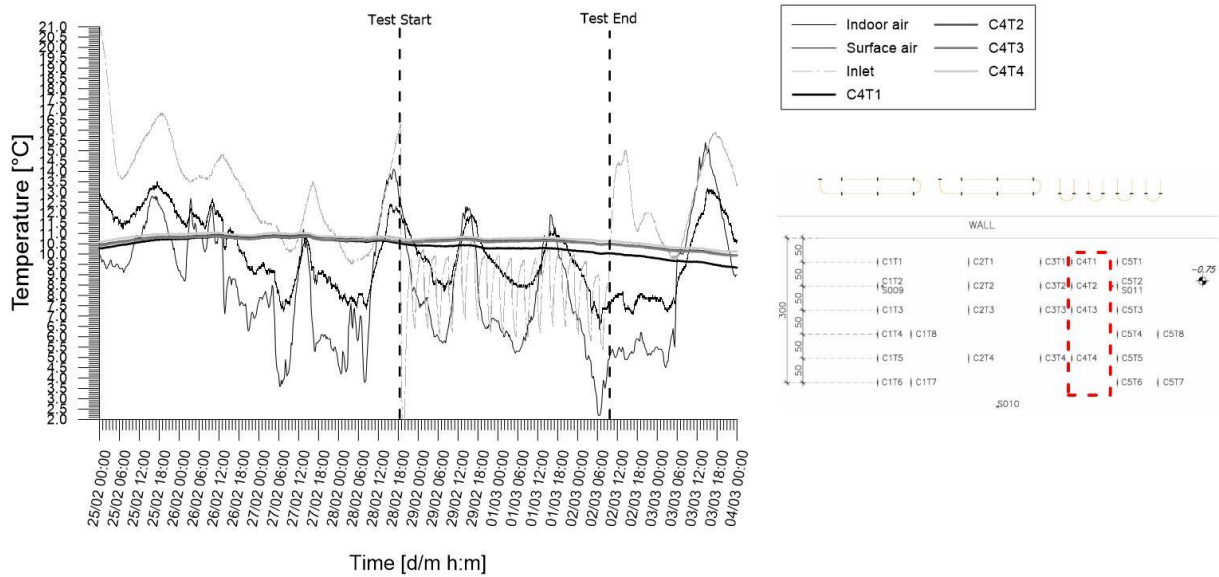


Figure A.99: Temperatures records from chain 4 of experimental test

H\_1+2+3\_20200228\_20200302

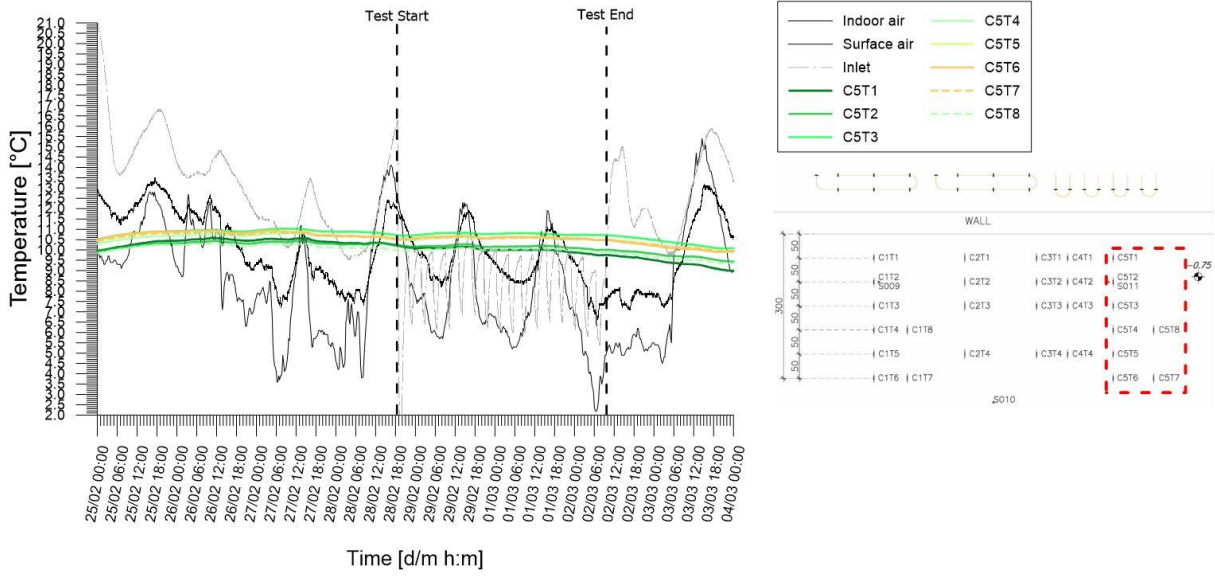


Figure A.100: Temperatures records from chain 5 of experimental test  
*H\_1+2+3\_20200228\_20200302*

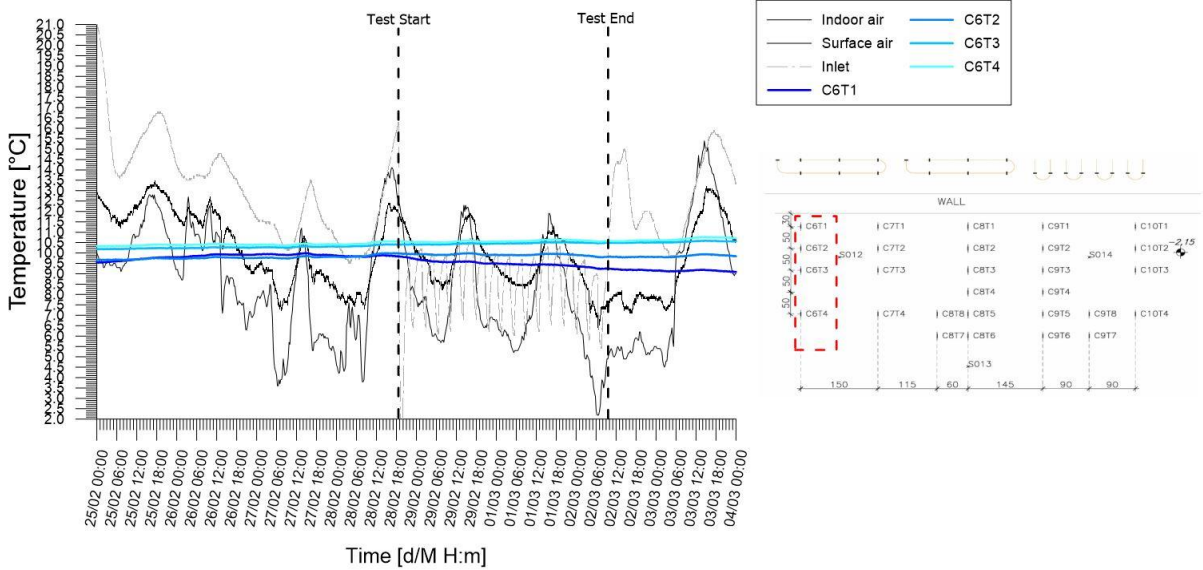


Figure A.101: Temperatures records from chain 6 of experimental test  
*H\_1+2+3\_20200228\_20200302*

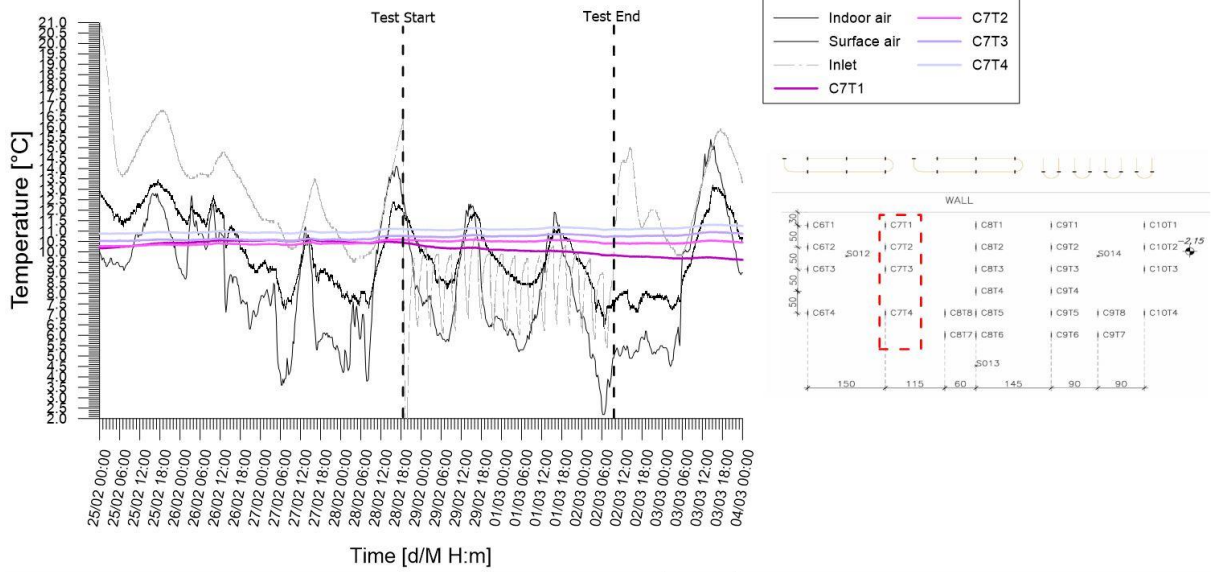


Figure A.102: Temperatures records from chain 7 of experimental test

H\_1+2+3\_20200228\_20200302

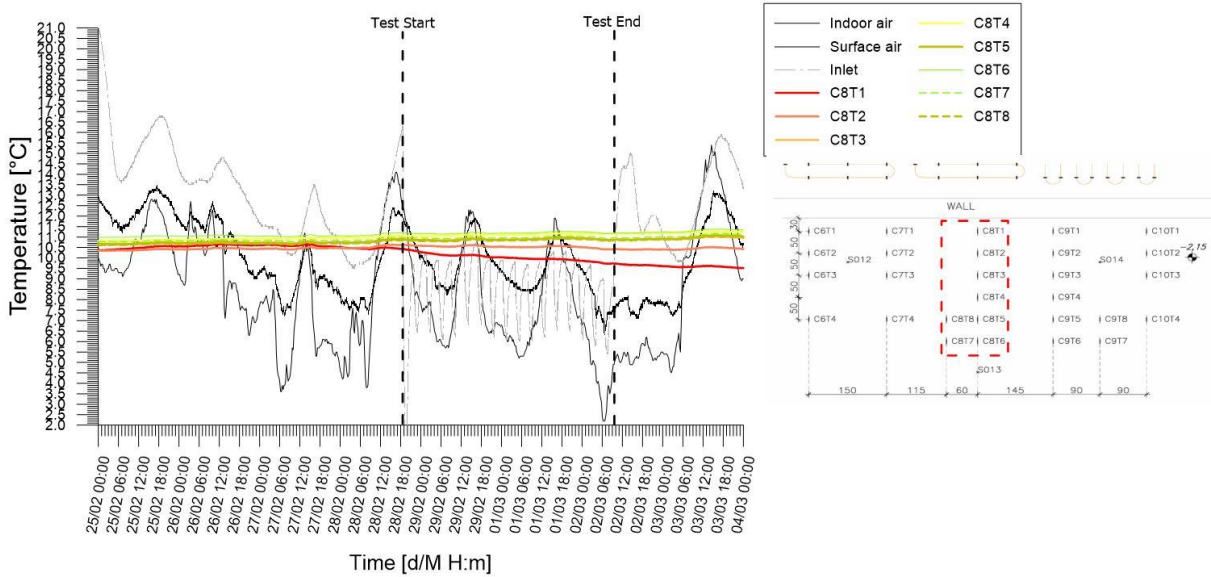


Figure A.103: Temperatures records from chain 8 of experimental test

H\_1+2+3\_20200228\_20200302

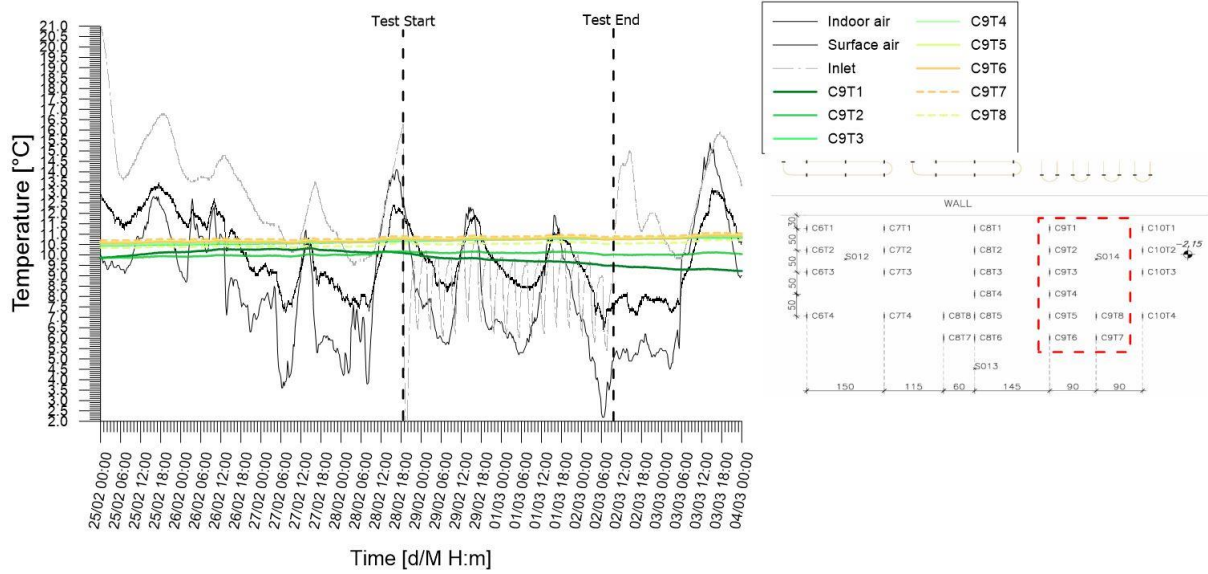


Figure A.104: Temperatures records from chain 9 of experimental test  
*H\_1+2+3\_20200228\_20200302*

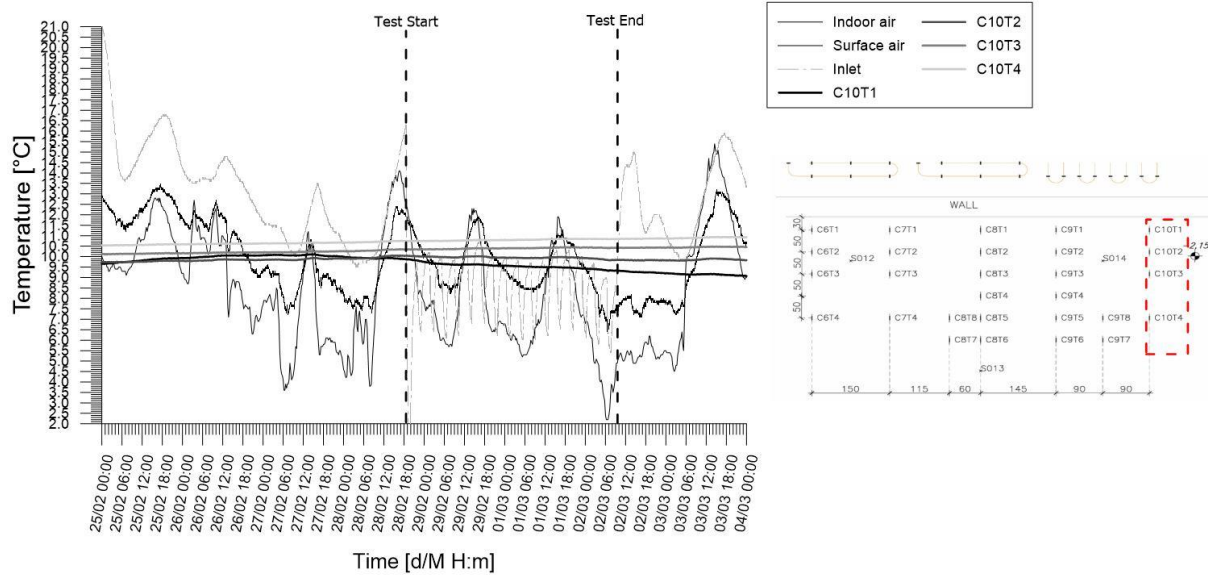


Figure A.105: Temperatures records from chain 10 of experimental test  
*H\_1+2+3\_20200228\_20200302*

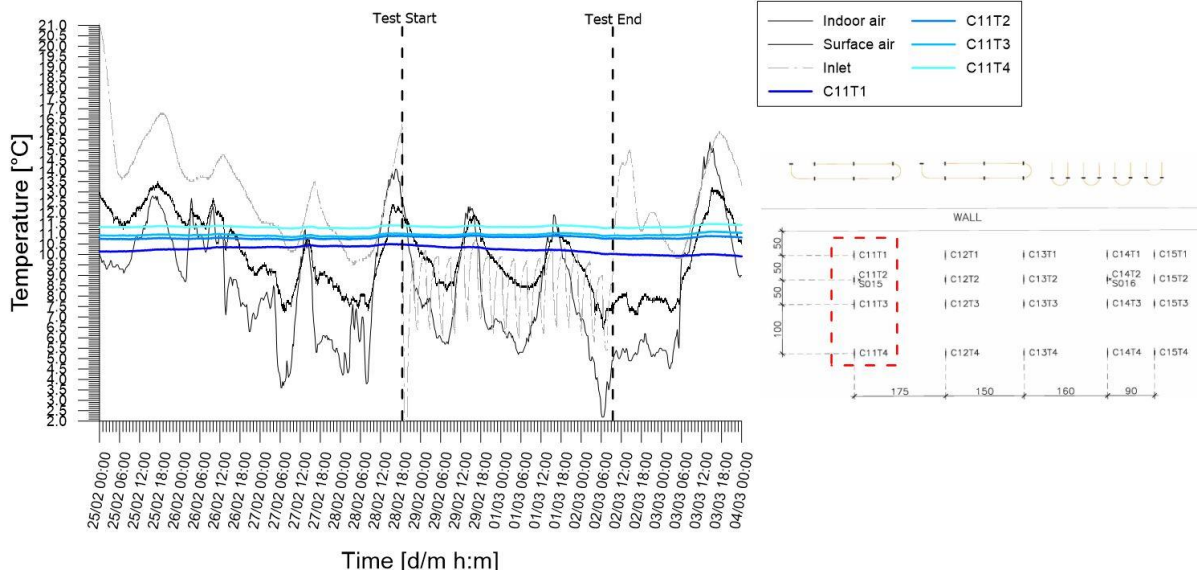


Figure A.106: Temperatures records from chain 11 of experimental test  
*H\_1+2+3\_20200228\_20200302*

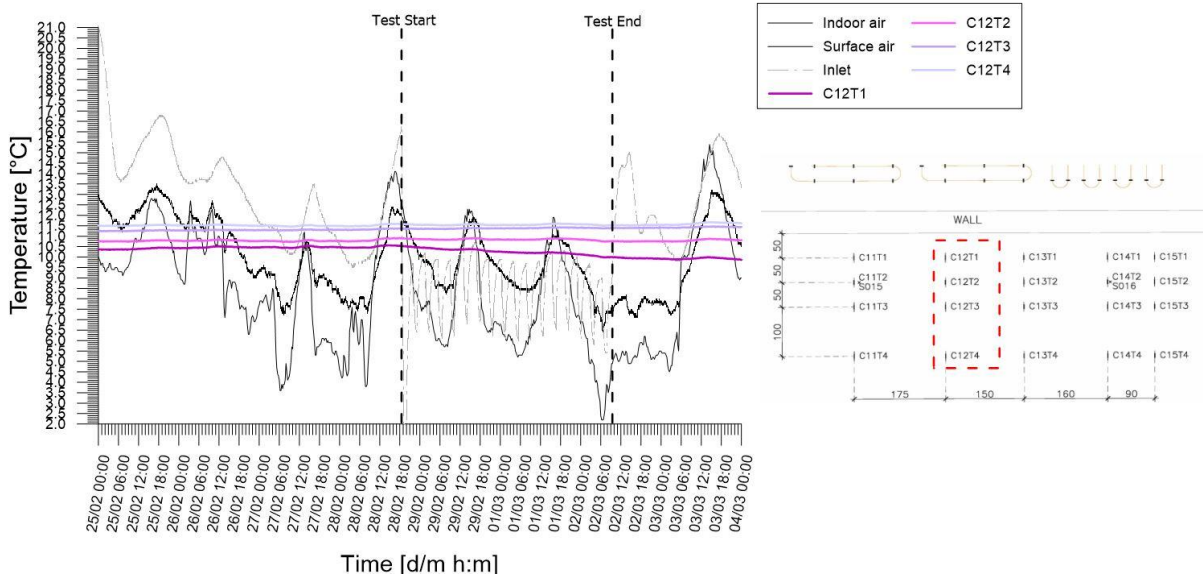


Figure A.107 Temperatures records from chain 12 of experimental test  
*H\_1+2+3\_20200228\_20200302*

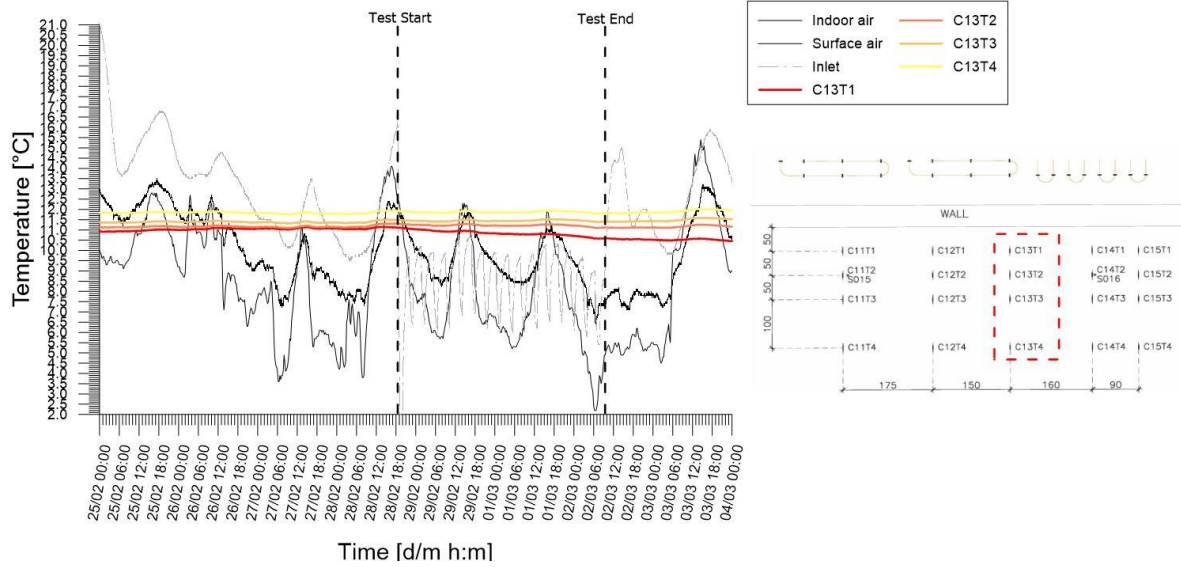


Figure A.108: Temperatures records from chain 13 of experimental test  
*H\_1+2+3\_20200228\_20200302*

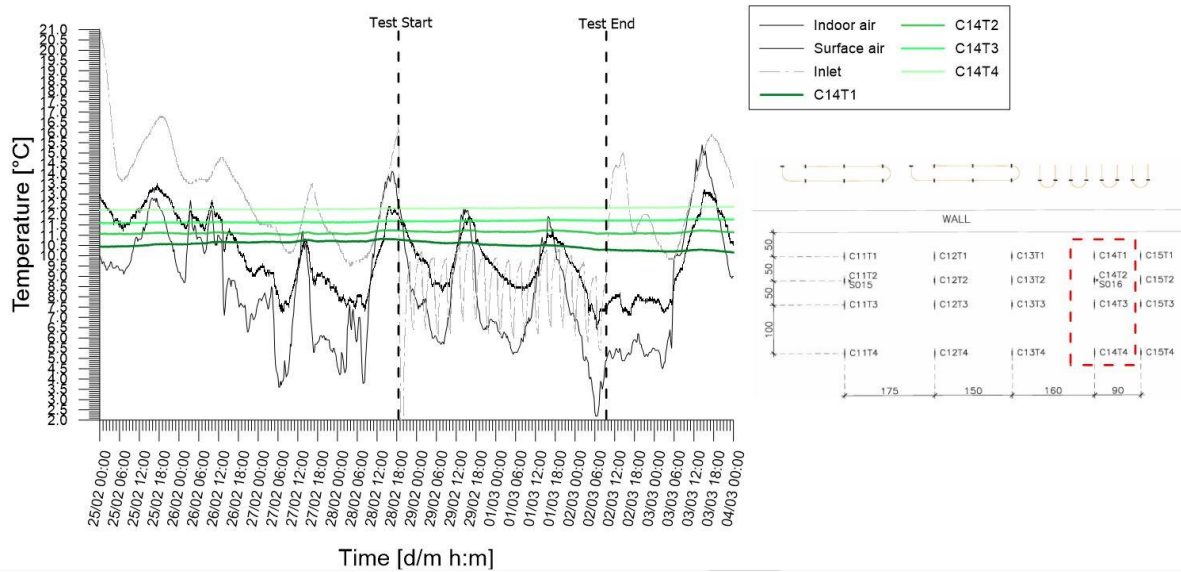


Figure A.109: Temperatures records from chain 14 of experimental test  
*H\_1+2+3\_20200228\_20200302*

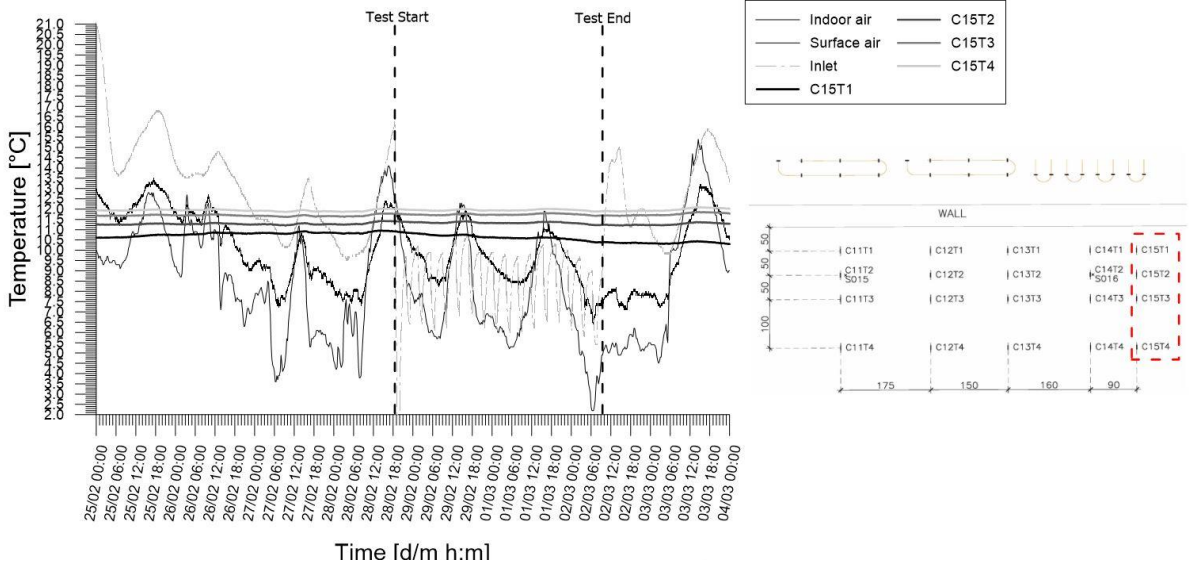


Figure A.110: Temperatures records from chain 16 of experimental test  
*H\_1+2+3\_20200228\_20200302*

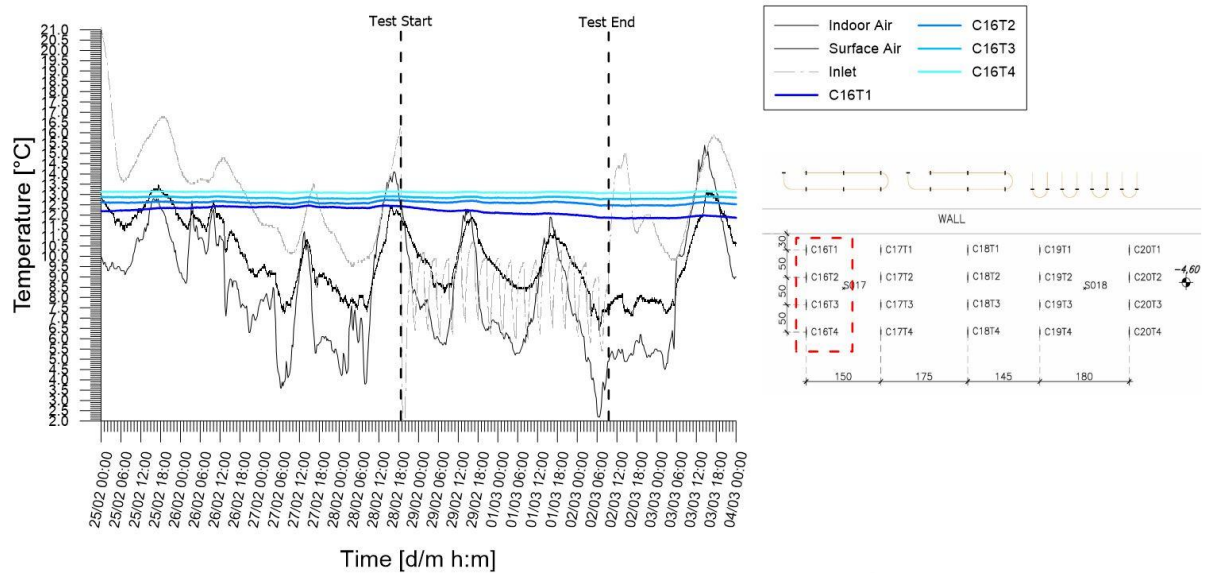


Figure A.111: Temperatures records from chain 17 of experimental test  
*H\_1+2+3\_20200228\_20200302*

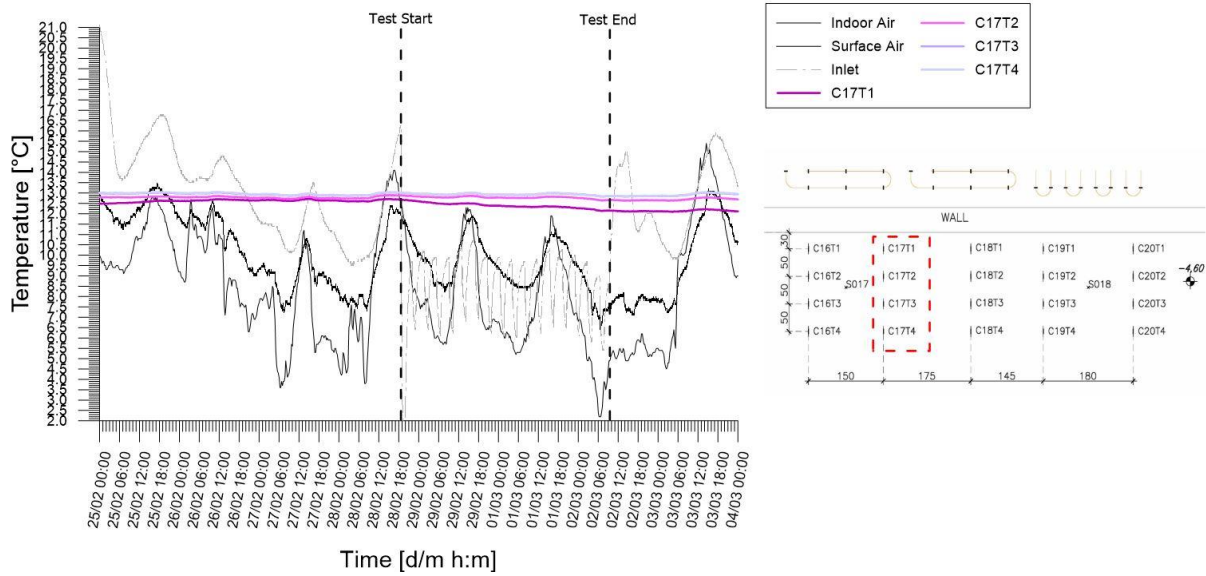


Figure A.112: Temperatures records from chain 17 of experimental test  
 H\_1+2+3\_20200228\_20200302

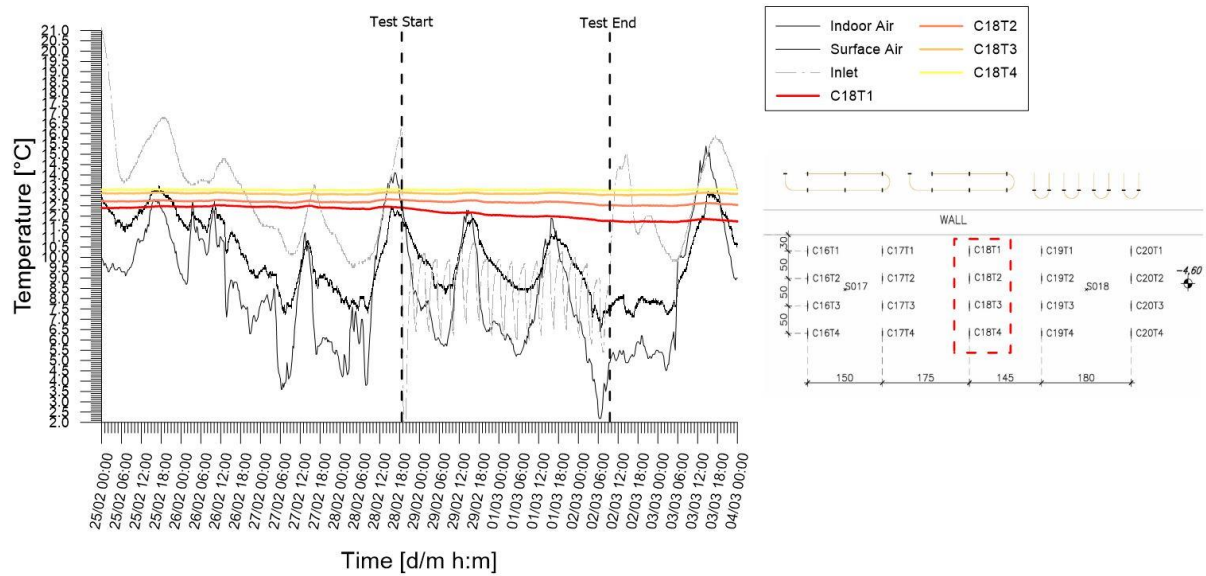


Figure A.113: Temperatures records from chain 18 of experimental test  
 H\_1+2+3\_20200228\_20200302

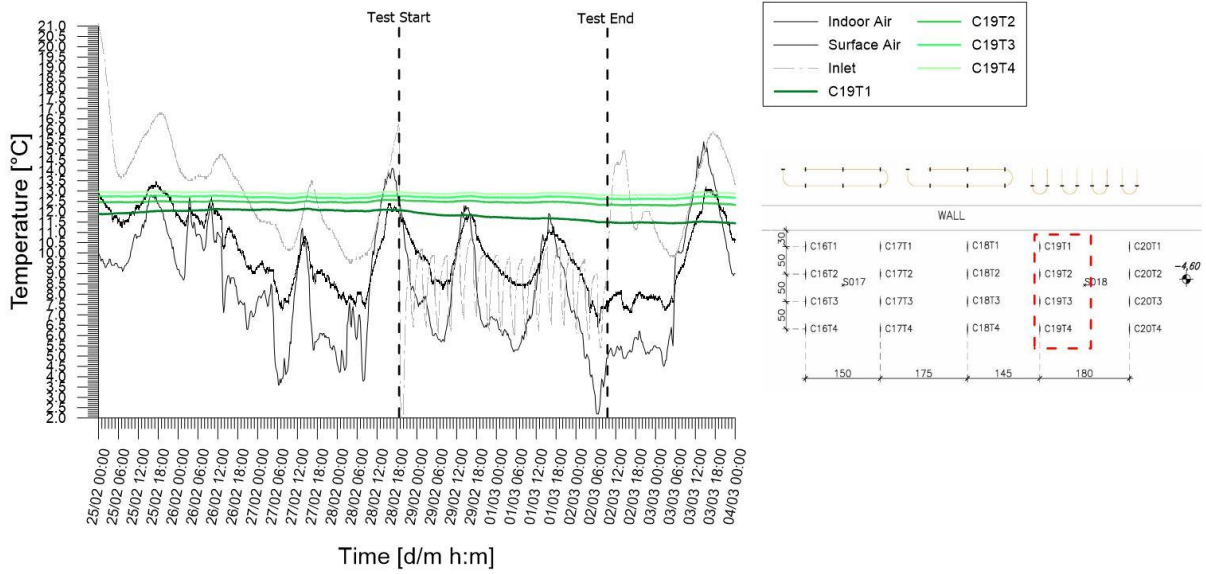


Figure A.114: Temperatures records from chain 19 of experimental test  
*H\_1+2+3\_20200228\_20200302*

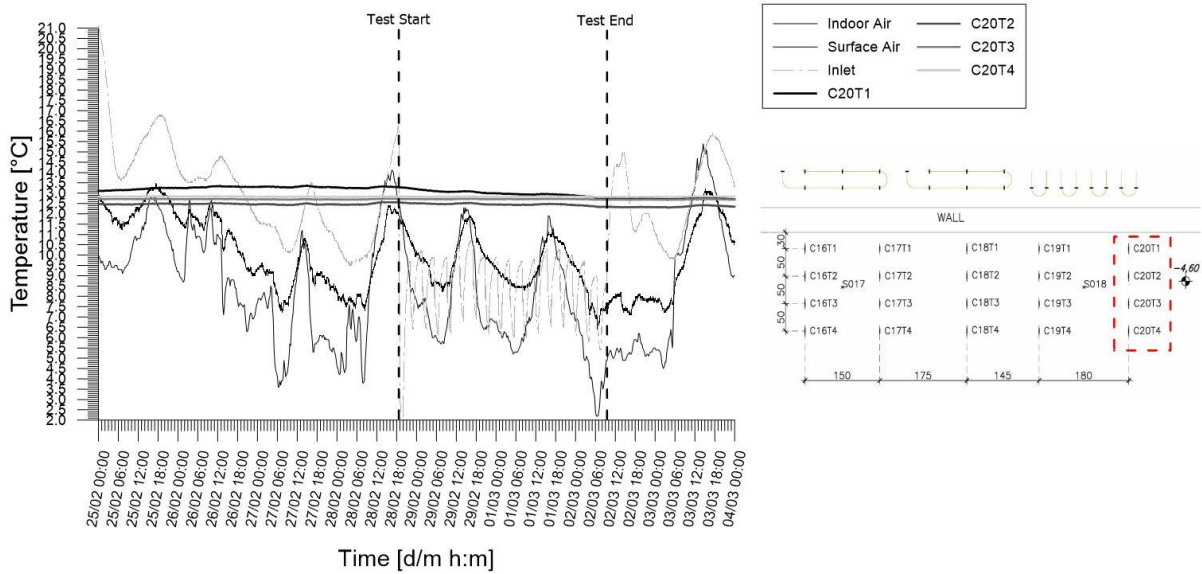


Figure A.115: Temperatures records from chain 20 of experimental test  
*H\_1+2+3\_20200228\_20200302*

## 6. Test H\_1\_20200305\_20200507

Table A.6: Main features of the test

|                                    |                |
|------------------------------------|----------------|
| Test start time                    | 05/03/20 19.25 |
| Test end time                      | 07/05/20 10.00 |
| Duration [h]                       | 1502.6         |
| Operative mode                     | Heating        |
| Active circuit(s)                  | 1              |
| Circuit link                       |                |
| Target temperature user [°C]       | 45             |
| Flow rate at the ground side [l/h] | 713.4          |

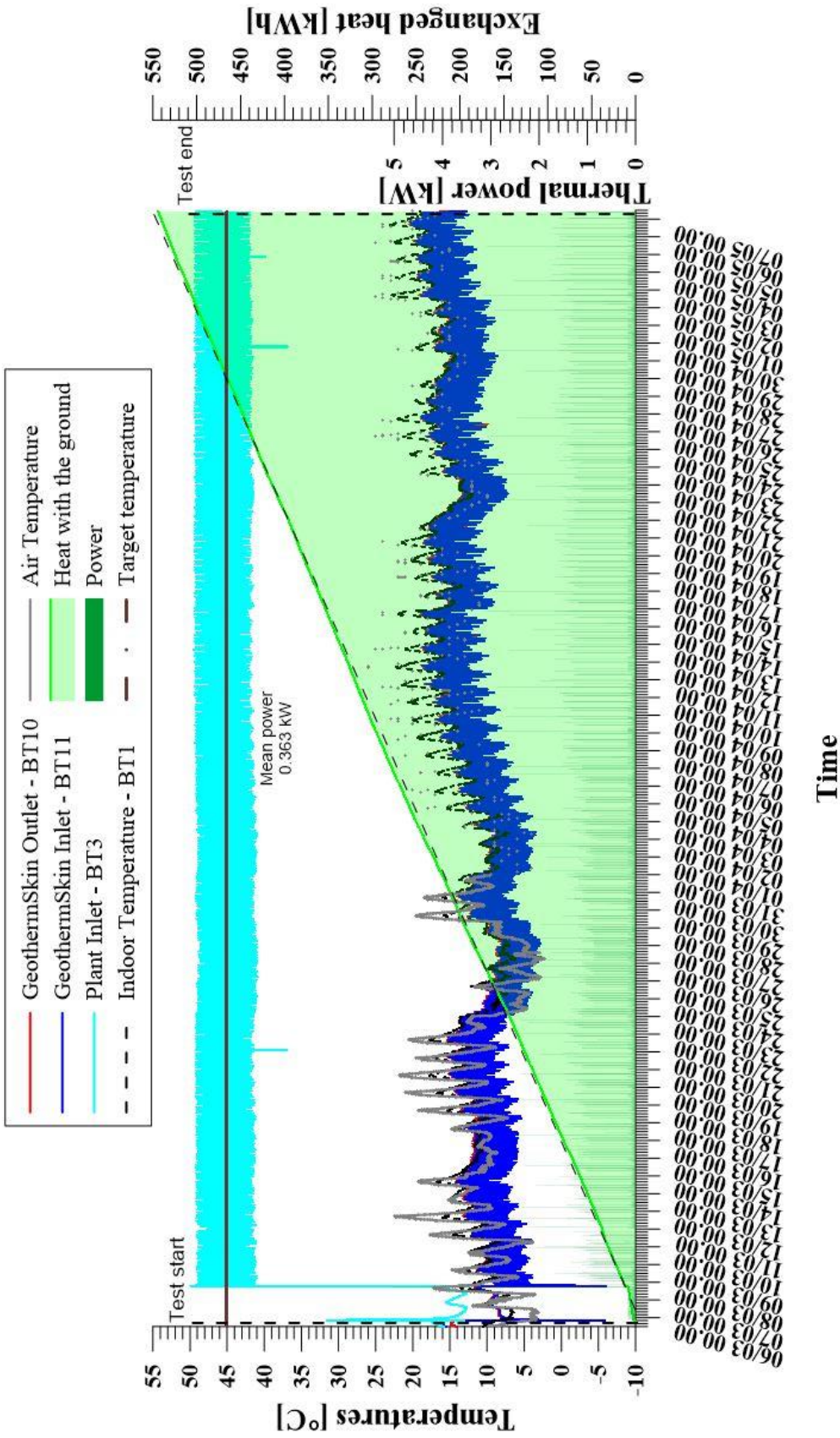


Figure A.116: Thermal performance interpretation of experimental test

H\_1\_20200305\_20200507of circuit 1 in heating mode.

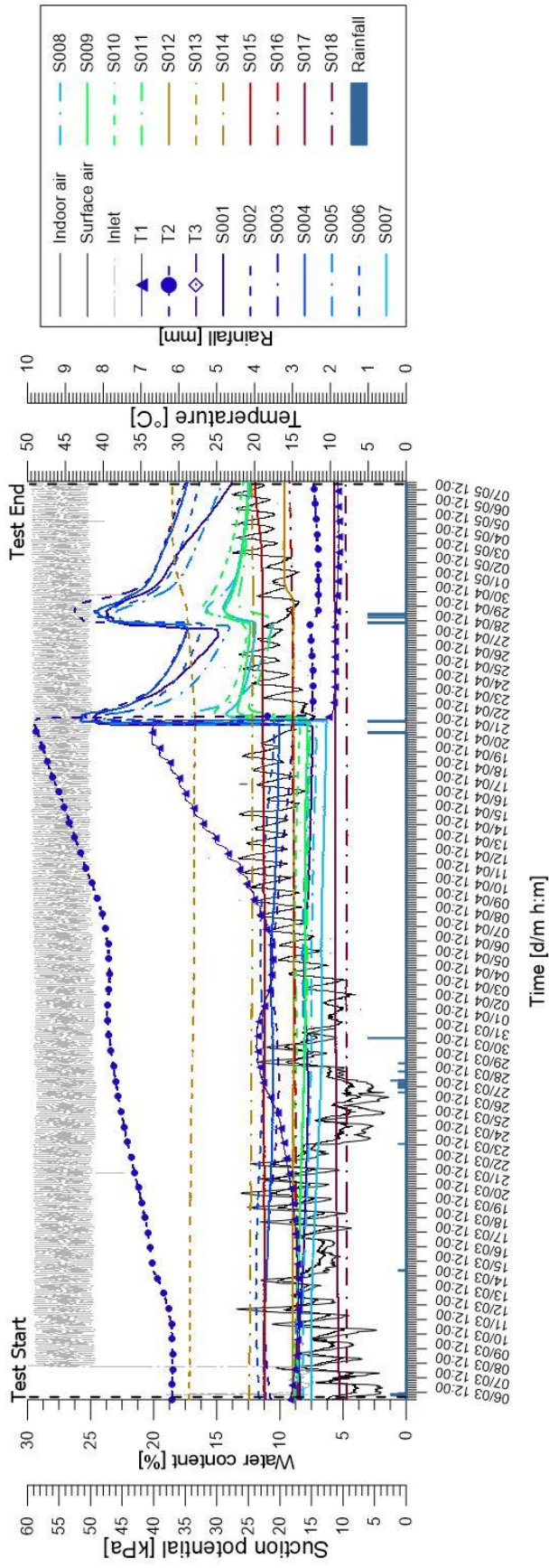


Figure A.117: Tensiometer and hygrometers records of experimental test  
 H\_1\_20200305\_20200507 together with monitored rainfall from Politecnico weather station.

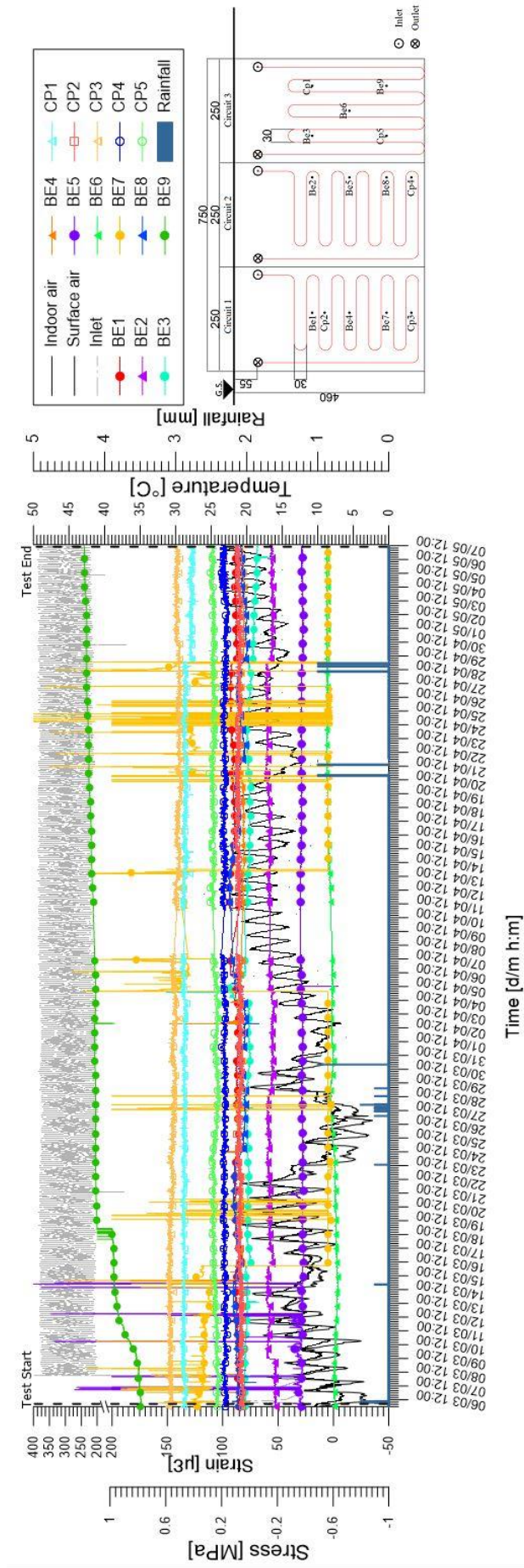


Figure A.118: Stresses and strains monitored at the wall external facade during experimental test

H\_1\_20200305\_20200507

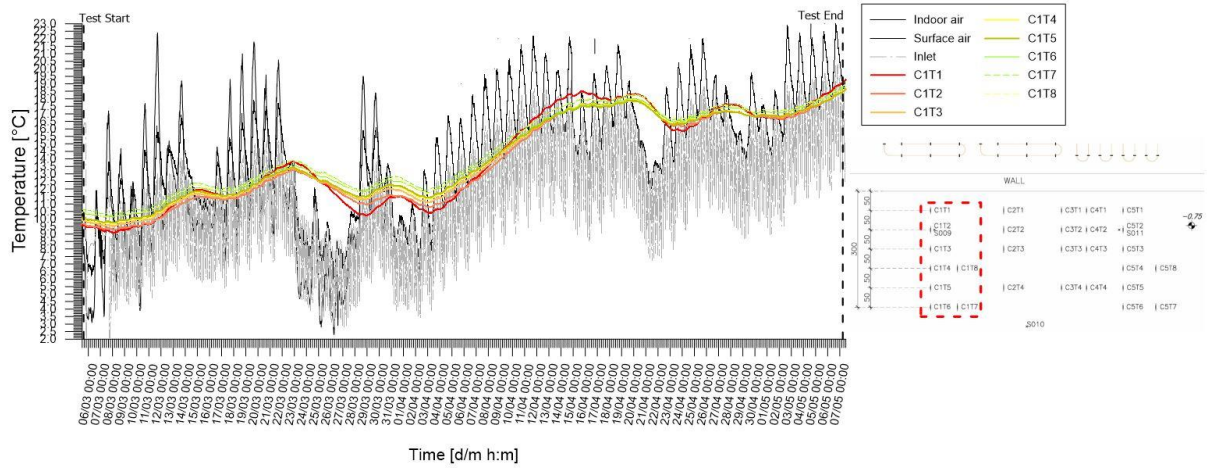


Figure A.119: Temperatures records from chain 1 of experimental test  
*H\_1\_20200305\_20200507*

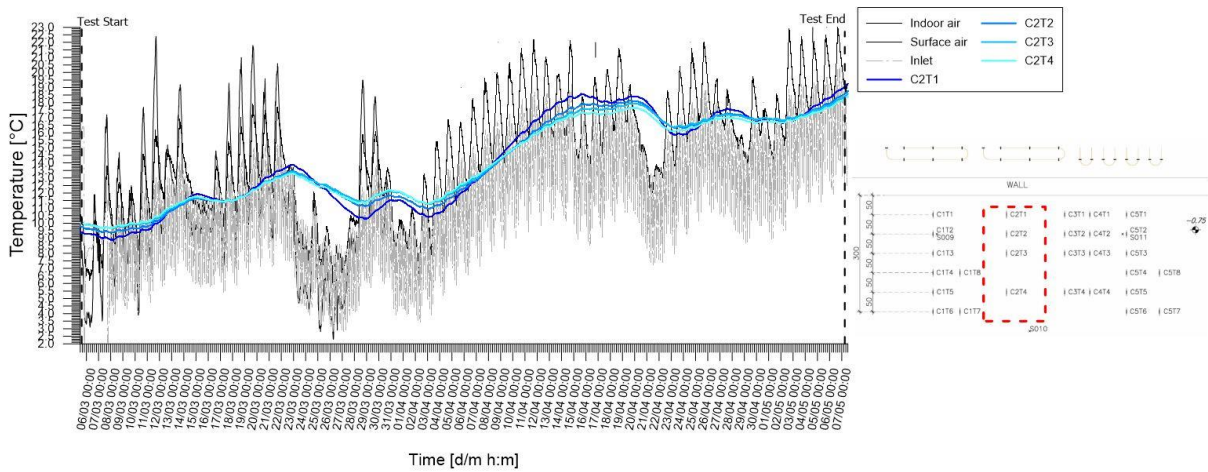


Figure A.120: Temperatures records from chain 2 of experimental test  
*H\_1\_20200305\_20200507*

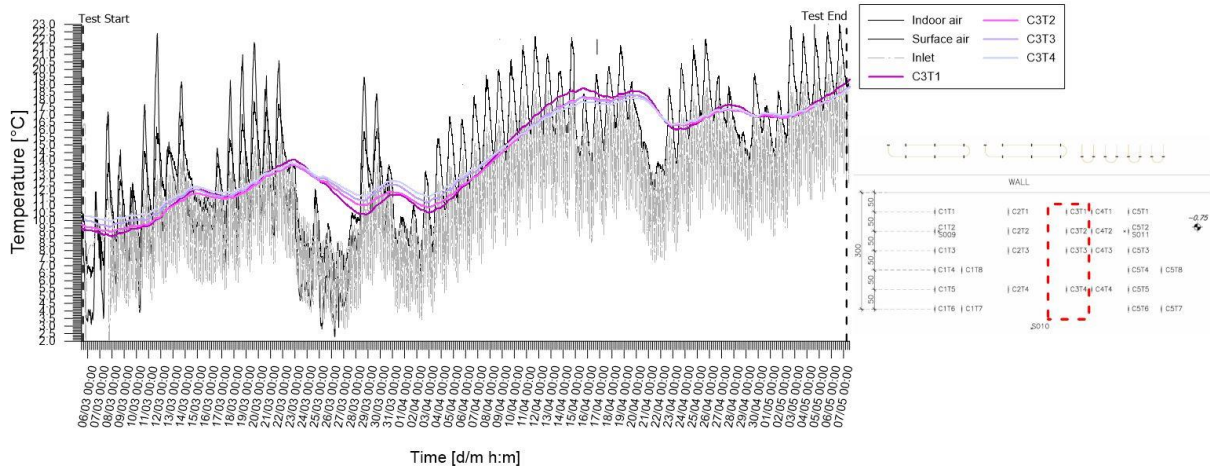


Figure A.121: Temperatures records from chain 3 of experimental test  
 H\_1\_20200305\_20200507

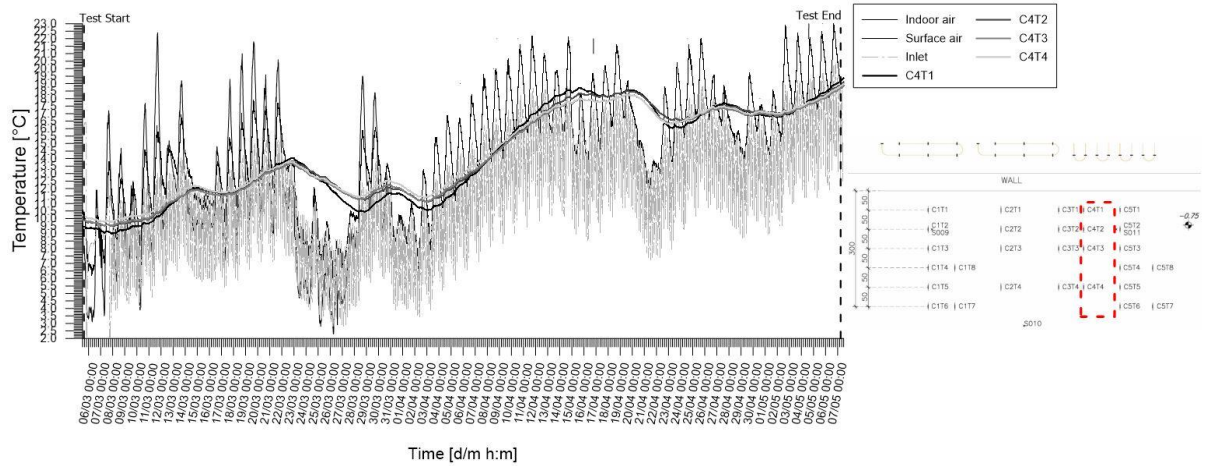


Figure A.122: Temperatures records from chain 4 of experimental test  
 H\_1\_20200305\_20200507

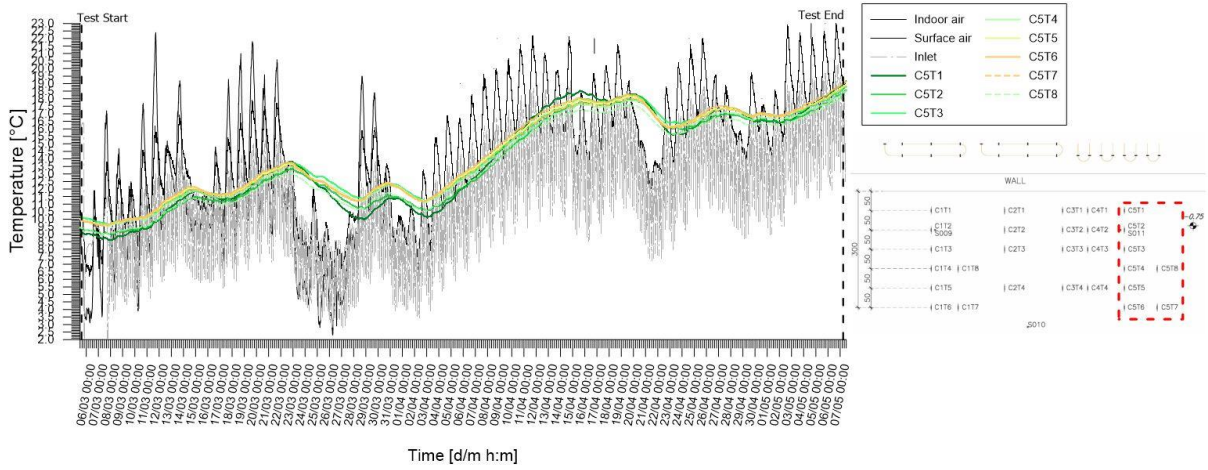


Figure A.123: Temperatures records from chain 5 of experimental test  
 H\_1\_20200305\_20200507

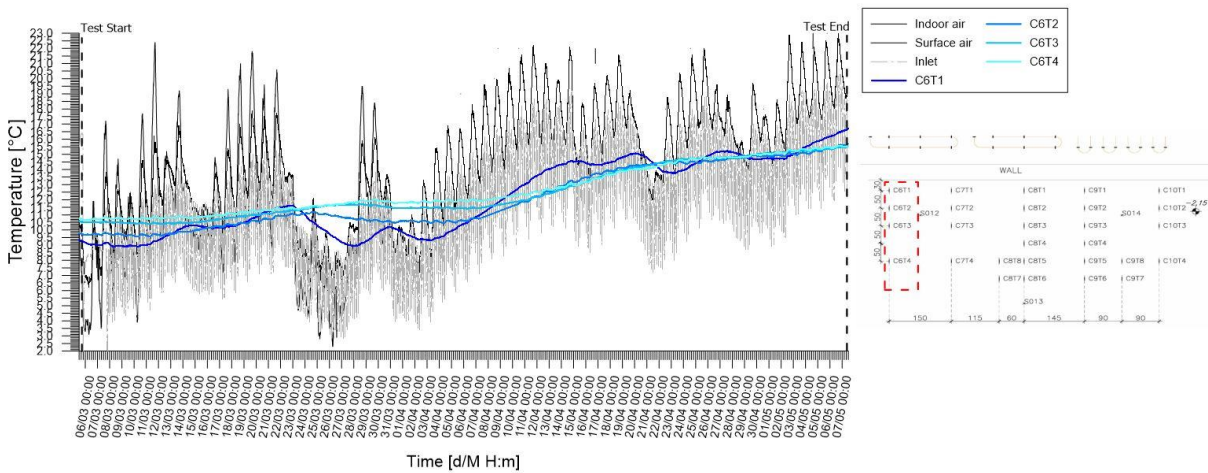


Figure A.124: Temperatures records from chain 6 of experimental test  
 H\_1\_20200305\_20200507

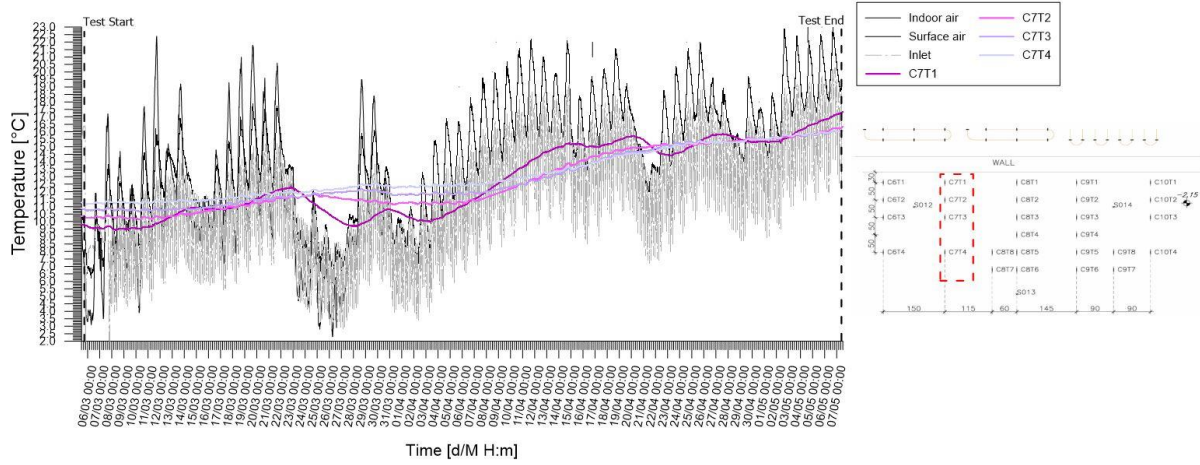


Figure A.125: Temperatures records from chain 7 of experimental test  
 H\_1\_20200305\_20200507

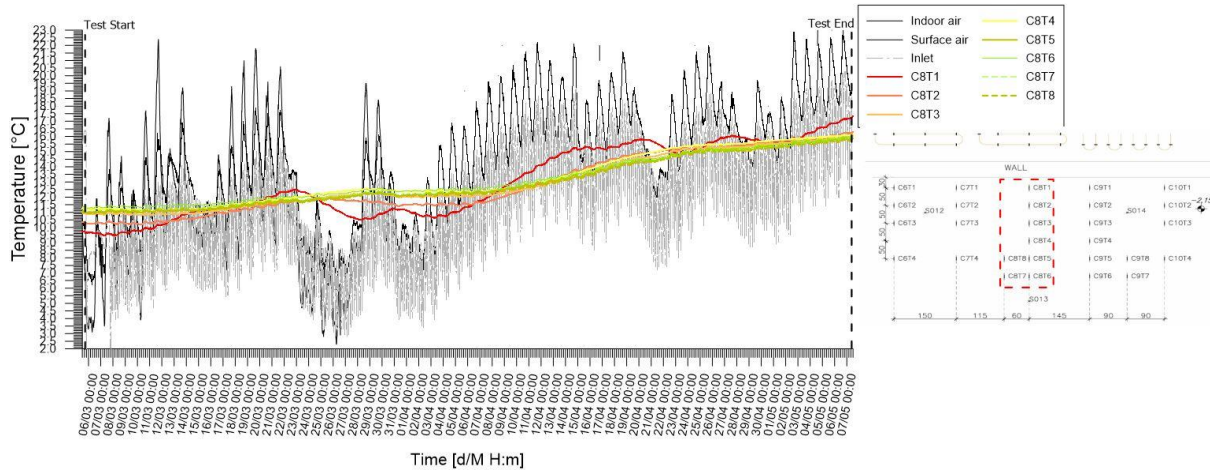


Figure A.126: Temperatures records from chain 8 of experimental test  
 H\_1\_20200305\_20200507

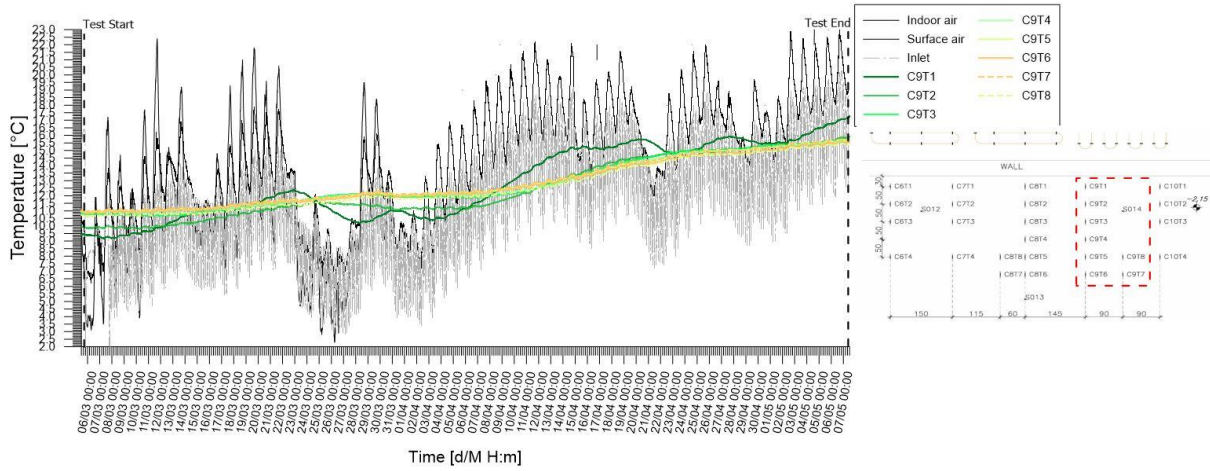


Figure A.127: Temperatures records from chain 9 of experimental test  
 H\_1\_20200305\_20200507

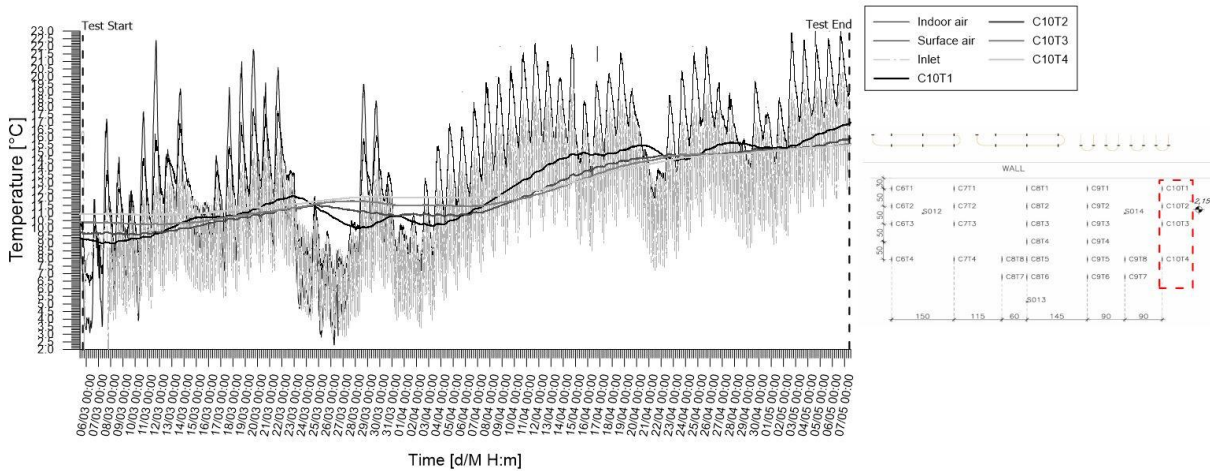


Figure A.128: Temperatures records from chain 10 of experimental test  
 H\_1\_20200305\_20200507

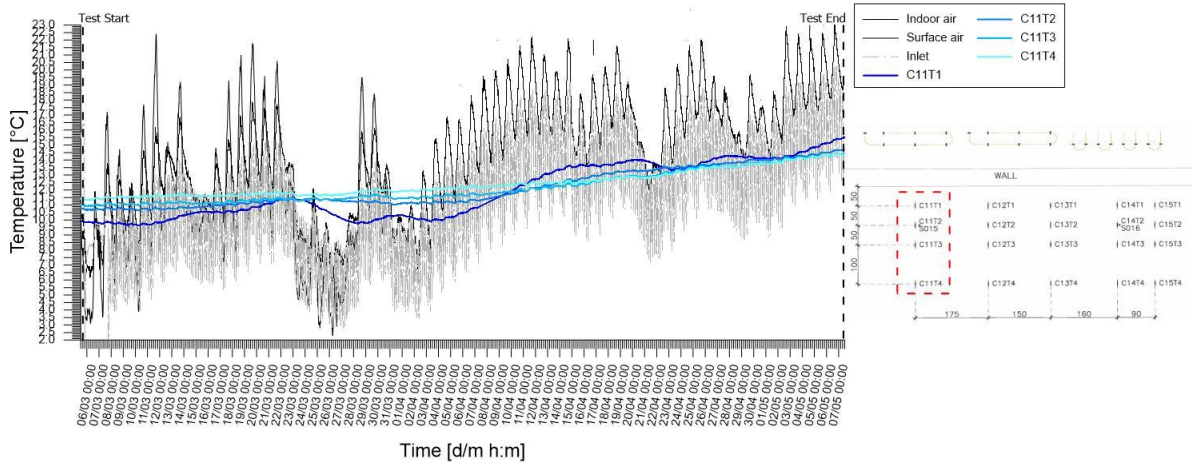


Figure A.129: Temperatures records from chain 11 of experimental test  
*H\_1\_20200305\_20200507*

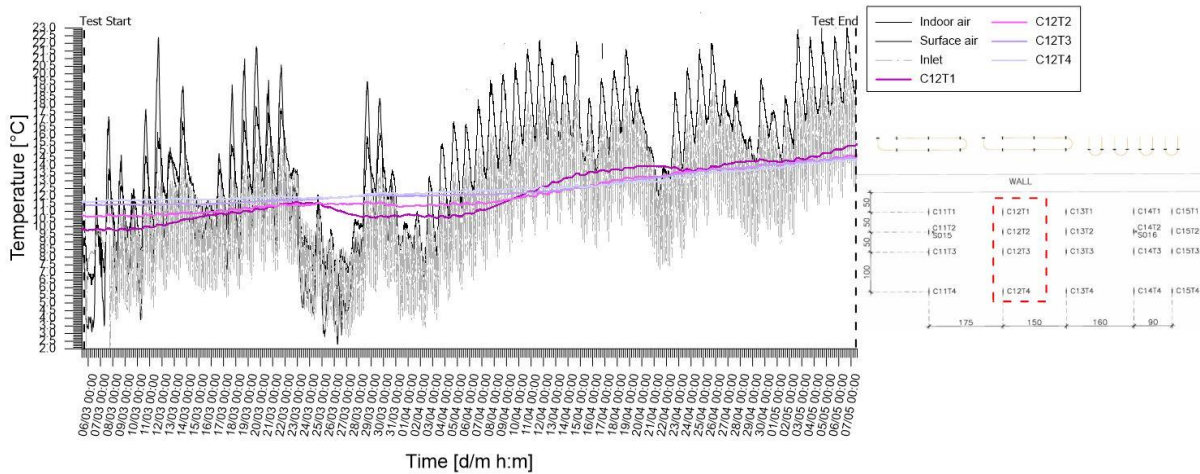


Figure A.130: Temperatures records from chain 12 of experimental test  
*H\_1\_20200305\_20200507*

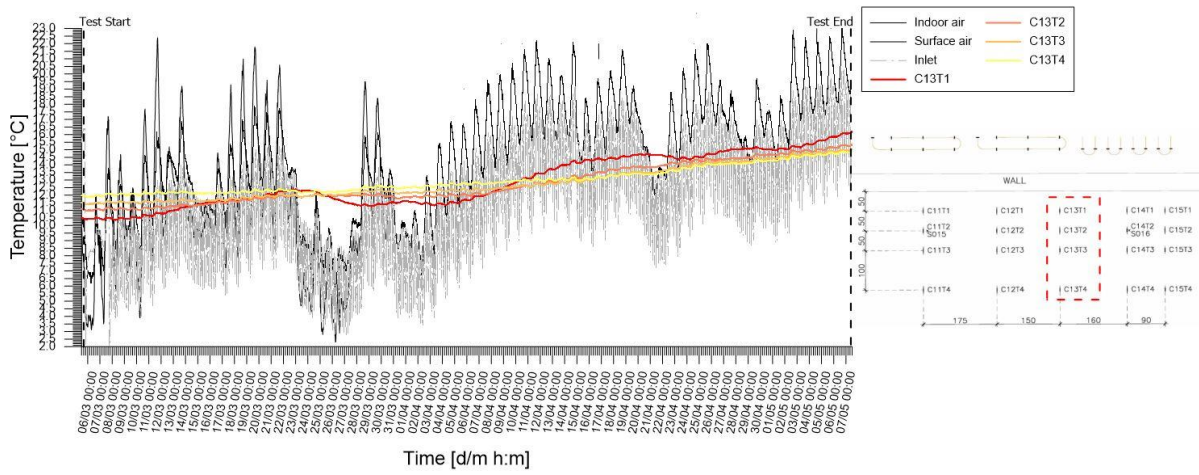


Figure A.131: Temperatures records from chain 13 of experimental test  
*H\_1\_20200305\_20200507*

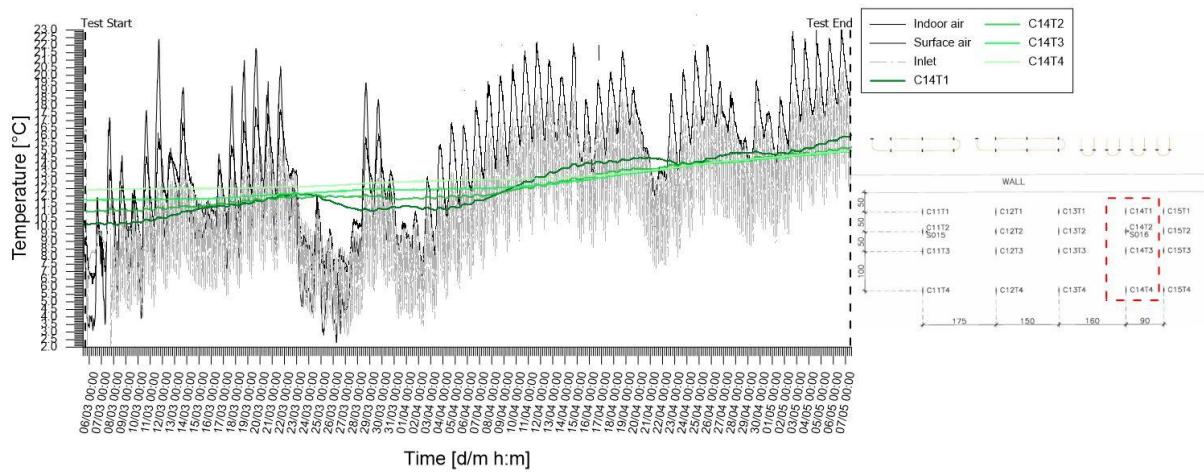


Figure A.132: Temperatures records from chain 14 of experimental test  
*H\_1\_20200305\_20200507*

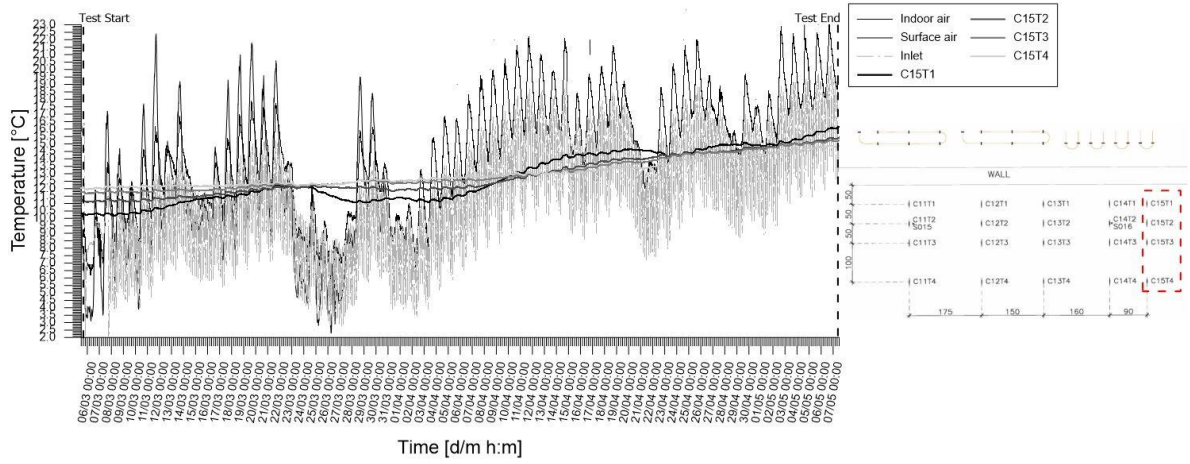


Figure A.133: Temperatures records from chain 15 of experimental test  
*H\_1\_20200305\_20200507*

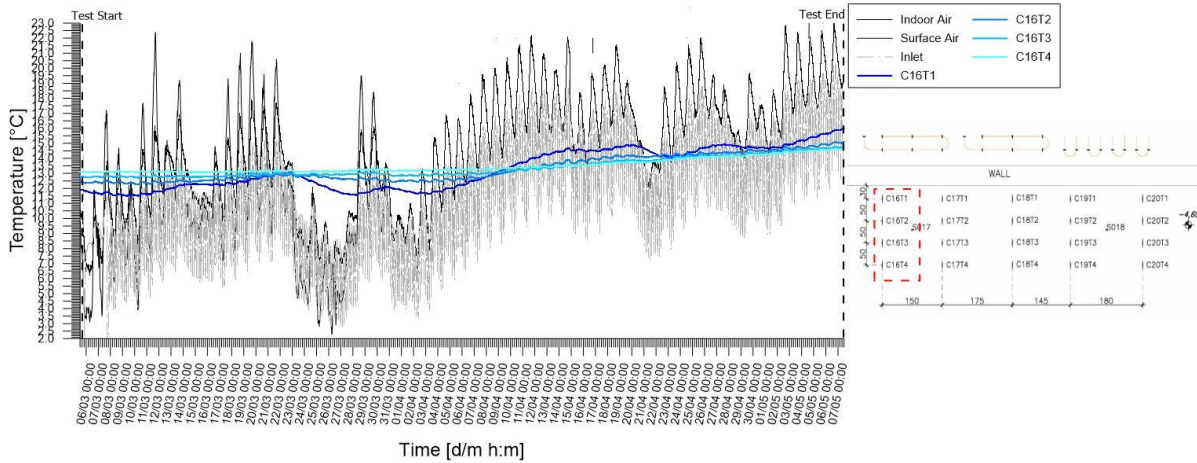


Figure A.134: Temperatures records from chain 16 of experimental test  
*H\_1\_20200305\_20200507*

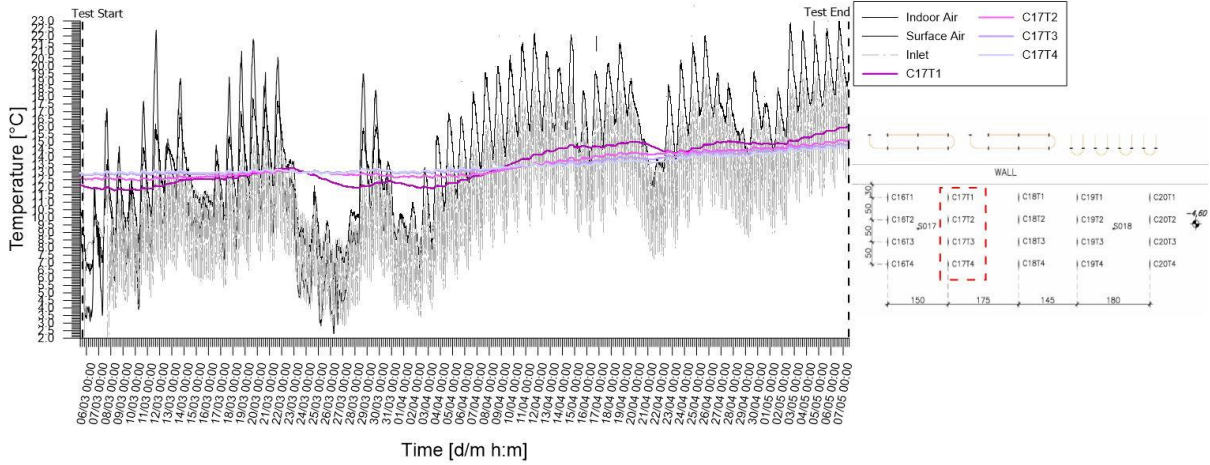


Figure A.135: Temperatures records from chain 17 of experimental test  
*H\_1\_20200305\_20200507*

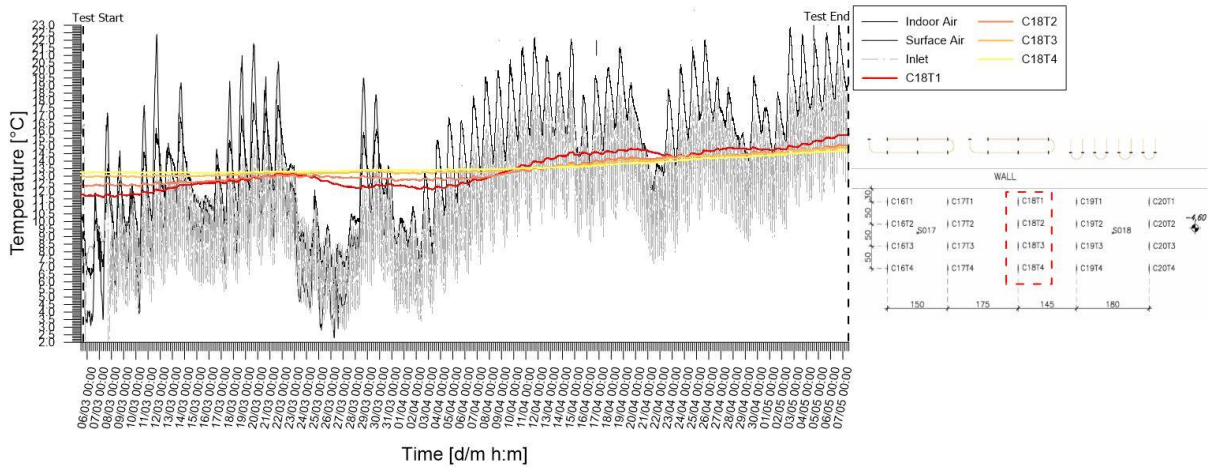


Figure A.136: Temperatures records from chain 18 of experimental test  
*H\_1\_20200305\_20200507*

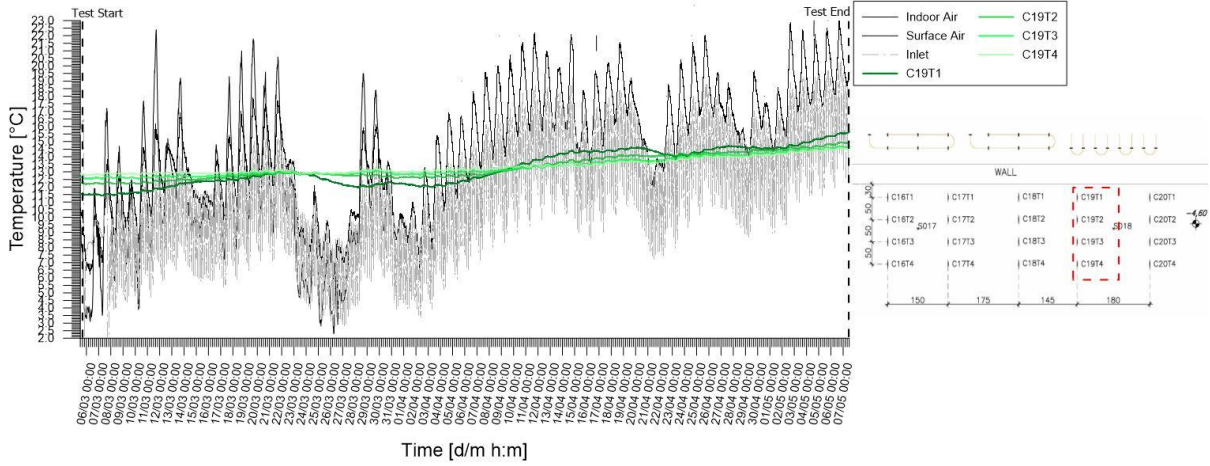


Figure A.137: Temperatures records from chain 19 of experimental test  
H\_1\_20200305\_20200507

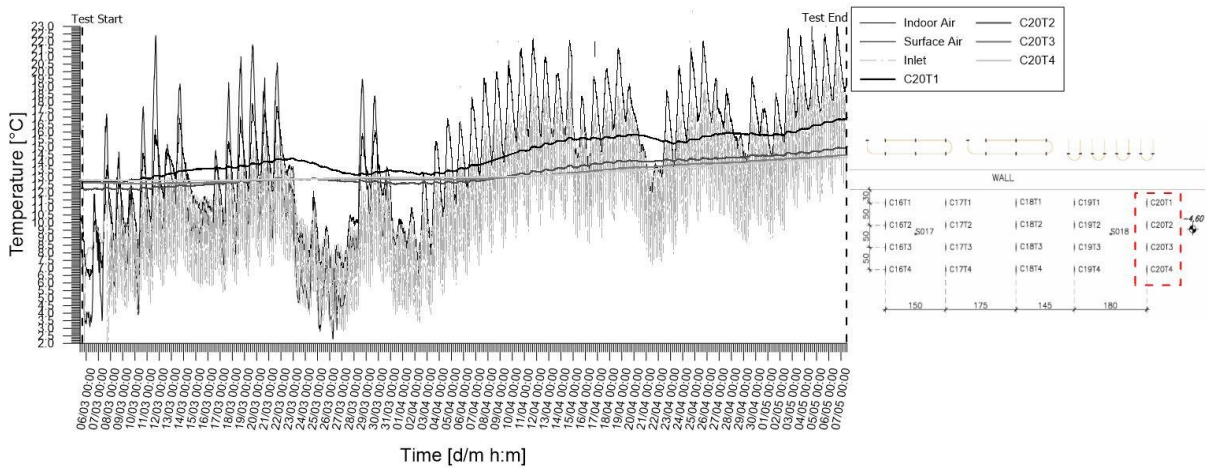


Figure A.138: Temperatures records from chain 20 of experimental test  
H\_1\_20200305\_20200507

## Reference:

- Adam, D. & Markiewicz, R. "Energy from earth-coupled structures, foundations, tunnels, and sewers" *Geotechnique*, Vols. 59, No. 3, pp. 229-236, 2009.
- Alice Di Donna, Fleur Loveridge, Francesco Cecinato, Marco Barla. "Energy performance of diaphragm walls used as heat exchangers" *Geotechnical Engineering*, vol. 170, no. GE3, pp. 232-245, 2016.
- Caichu Xia, Meng Sun, Guozhu Zhang, Suguang Xiao, Yichuan Zou "Experimental study on geothermal heat exchangers buried in diaphragm walls," *Energy and Buildings*, vol. 52, pp. 50-55, 2012.
- "Center for Climate and Energy Solutions" 2020. [Online]. Available: <https://www.c2es.org/content/international-emissions/>.
- D. Sterpi, A. Angelotti, D. Corti & M. Ramus, "Numerical analysis of heat transfer in thermo-active diaphragm walls," *Numerical Methods in Geotechnical Engineering – Hicks, Brinkgreve & Rohe (Eds)*, pp. 1043-1018, 2014.
- D. Sterpi, Tomaselli, Angelotti, "Energy performance of ground heat exchangers embedded in diaphragm walls: Field observations and optimization by numerical modelling," *Renewable Energy*, 2018.
- Geothermal Community, "Shallow Geothermal Systems" in *Geothermal Systems And Technology*, Concerto.
- GSHP Association, "Thermal Pile: Design, Installation & Materials Standards," 1 Oct 2012. [Online]. Available: [http://www.gshp.org.uk/pdf/GSHPA\\_Thermal\\_Pile\\_Standard.pdf](http://www.gshp.org.uk/pdf/GSHPA_Thermal_Pile_Standard.pdf).
- H. Brandl, "Energy foundations and other thermo-active ground structures" *Geotechnique*, Vols. 56, No. 2, pp. 81-122, 2006.
- Maria Alberdi-Pagola, Soren Madsen, Rasmus Lund Jensen, Soren Erbs Poulsen, "Thermo-mechanical aspects of pile heat exchangers: background and literature review" Department of Civil Engineering, Aalborg University, 2018.
- Mary H. Dickson and Mario Fanelli, "What is Geothermal Energy?", Pisa, Italy, 2004.
- M. Barla, Alice Di Donna, "Energy tunnels: concept and design aspects" *ScienceDirect*, 2018.
- M. Barla, Alice Di Donna, Andrea Perino, "Application of energy tunnels to an urban environment" *Geothermics*, vol. 61, pp. 104-113, 2016.
- M. Barla, A. Di Donna, A. Insana, "A novel real-scale experimental prototype of energy tunnel," *Tunnelling and Underground Space Technology*, vol. 87, pp. 1-14, 2019.
- M. Baralis, M. Barla, "Testing of a novel energy wall system in Torino" Torino, Italy, 2019.
- M. Sutman, "Thermo-Mechanical Behavior of Energy Piles: Full-Scale Field Testing and," Virginia Tech, 2016.

Tony Amis, Christopher A. W. Robinson, Samuel Wong, "Integrating geothermal loops into the diaphragm walls of the Bulgari Hotel Knightsbridge London project" *Research gate*, 2011.

Tony P. Suckling, Peter E.H. Smith, "Environmentally Friendly Geothermal Piles At Keble College, Oxford, UK," 2002.

"Union of Concerned Scientists," 20 Dec 2017. [Online]. Available: <https://www.ucsusa.org/resources/benefits-renewable-energy-use>.

## **Acknowledgments:**

A completed study would not be done without any assistance. Therefore, the author who conducted this research gratefully gives acknowledgement to their support and inspiration during the time of doing this thesis as a requirement of completing my Degree of Civil Engineering.

First of all, I would like to express my endless thanks and gratefulness to my supervisor Prof Marco Barla and Dr Matteo Baralis. Their kindly support and continuous advices went through the process of completion of my thesis. Their encouragement and comments had significantly enriched and improved my work. Without their motivation and instructions, the thesis would have been impossible to be done effectively.

Secondly, a special thanks goes to Italian Government and Italian Embassy in Vietnam, without the MAECI scholarship from them, I could not have a chance to study in Italy where I could expose to leading lecturers, good friends from around the world and perfect environment to study, absorb up-to-date knowledge. Besides, living experiences I got during the time in Italy are always in my mind and they will become one of the most valuable assets I have in my life.

Thirdly, I would like to thanks to my friends in Politecnico di Torino, especially Chan and Hydayat. Their kindly help, care, motivation gave me strength and lift me up all the trouble for the rest of my life

Last but not least, my special thanks approve to my parents for their endless love, care and have most assistances and motivation me for the whole of my life. I also would like to explain my thanks to my cousin, brother and sister-in-law for their support and care me all the time.